UNIVERSITÀ
DEGLI STUDI
FIRENZE

DOTTORATO DI RICERCA IN FISICA E ASTRONOMIA

CICLO XXIX

COORDINATORE Prof. Massimo Gurioli

Modeling magnetized neutron stars in general relativity

Settore Scientifico Disciplinare: FIS/05 Astronomia e Astrofisica

Dottorando
Antonio Graziano Pili

Tutori
Dott. Niccolò Bucciantini

Dott. Luca Del Zanna

Coordinatore
Prof. Massimo Gurioli

Anni 2013/2016

Ad Alessandra

Alla mia famiglia

Contents

Introduction

Neutron Stars (NSs) are the compact remnants left at the end of the evolutionary history of massive stars. Characterized by strong-gravity, supranuclear densities, fast rotation and super strong magnetic field, NSs are among the most exotic and fascinating objects in the Universe. They embody a physical environment where our knowledge of nature and its fundamental laws can be tested under extreme conditions that are not replicable on Earth. Nevertheless, their astronomical manifestation is extremely diverse and still today it is difficult to draw a unifying picture of the phenomenology of NSs. It is widely accepted that magnetic fields play a critical role in establishing and governing the observational behaviours of such stars. This holds particularly true for *magnetars*: slowly rotating young NSs endowed with surface magnetic fields of the order of 10^{14-15}G. Their extraordinary observational properties, characterized by a persistent X-ray emission with high luminosity and by sporadic and violent events releasing up to $\sim 10^{45}$ erg in less then few seconds, are explained in terms of a huge magnetic energy reservoir hidden in the interior of the star. It is precisely the rearrangement and the dissipation of the internal magnetic field that is though to sustain the observed phenomenology. Unfortunately, it is not well known how magnetar magnetic fields originate, and even less known are the requirements for their stability. We basically do not know how the magnetic field organizes inside the star since astronomical observations brings us information that directly concerns only the geometry of the external magnetic field or, at most, of the field in the outer crust.

An accurate and precise description of the magnetic field in magnetars and, in general, in NSs, represents a necessary tool to develop realistic physical models able to shed light on the physic and the phenomenology of these astrophysical objects. During the last years a vast effort has been devoted to different aspects of this subjects, such as the origin of the magnetic field and its morphology, both inside and outside the NS. Recent numerical simulations have shown that a strong amplification of the magnetic field during core collapse (Mösta et al. 2015) or merging events (Kiuchi et al. 2015, Giacomazzo et al. 2015) is possible. This may have important consequences on the study of *Gamma-Ray Bursts* (GRBs): a newly born, fast rotating and ultramagnetized NS can play as central engine driving the energetic emission of both Long (Metzger et al. 2011) and Short GRBs (Bucciantini et al. 2012). Concerning the equilibrium and morphology, the modelization of the outer magnetosphere (Tchekhovskoy et al. 2013) has been mainly motivated by the necessity to understand pulsed emission of canonical pulsars. On the other hand the interest in the interior structure of the NSs has been mostly driven by questions of nuclear and theoretical physics, expecially their Equation of State (EoS) (Lattimer 2012, Chamel et al. 2015) their cooling properties (Viganò et al. 2013), and the stability of the magnetic field itself (Mitchell et al. 2015). The effects of magnetar magnetic fields on the structure of the NS are important also from the point of view of Gravitational Wave (GW) astronomy (Lasky 2015): strong magnetic fields can deform the star, and such deformation, in conjunction with fast rotation, could lead to the emission of GWs (Cutler 2002, Dall'Osso et al. 2009, Lasky 2015). Due to the complexity of the problem, models have been realized either in the Newtonian regime (Lander and Jones 2009, Glampedakis et al. 2012a, Fujisawa and Eriguchi 2015) on in General Relativity (GR) either with a perturbative approach (Ciolfi et al. 2009, Gualtieri et al. 2011, Ciolfi and Rezzolla 2013) or assuming a simple morphology for the magnetic field itself (Bocquet et al. 1995, Kiuchi and Yoshida 2008, Frieben and Rezzolla 2012), with currents always confined inside the star. Only recently the possibility of currents extending outside in the magnetosphere has been investigated (Glampedakis et al. 2014, Fujisawa and Kisaka 2014, Akgün et al. 2016).

In general these studies have been limited to specific configurations representative of typical regimes, and on investigating a few quantities relevant for GWs emission such as the quadrupolar deformation. However, a detailed study of the parameter space is still partially lacking. In this Ph.D. thesis we present a comprehensive numerical study of magnetic configurations in NSs, derived in the GR regime, taking into account different magnetic field geometries that arise from different choices of the current distributions located both in core and in peripheral region inside the star, but also outside in the near magnetosphere. Our approach is based on the simultaneous solution of Einstein equations for the metric (under the simplifying assumption of conformal flatness), of the general-relativistic Euler equation for the hydro-magnetic equilibrium, and of the Grad-Shafranov equation or Maxwell equations for the magnetic field structure.

This thesis is organized as follows. In the first chapter we will broadly review the physics of NSs and recent attempts at their modeling with a particular emphasis to the magnetic field. We will also provide a quick review on the recent developments in modeling the equilibrium configurations of magnetized NSs. In Chap. 2 we will introduce the formalism and discuss the equations we solve through the XNS code which, during the last years has been updated to handle different magnetic field morphologies and which is discussed in the Appx. A (see also the website `http://www.arcetri.astro.it/science/ahead/XNS/` or Bucciantini et al. 2014). In Chap. 3 and 4 we begin by presenting respectively purely toroidal and purely poloidal configurations assuming both static and rotating NSs. In Chap. 5 we will discuss equilibria endowed with a mixed magnetic field, while Chap. 6 is devoted to twisted magnetosphere models. In all cases we present a qualitative discussion of the equilibrium models, of the current distributions and the associated magnetic field morphology. With a wide sampling of the parameter space, we characterize how some physical quantities of interest, such as the stellar deformation, change with mass, rotation, and magnetic field geometry. In particular, we will provide simple parametrizations of the deformation effects in terms of the magnetic field strength, the spin frequency, the current distribution and the associated energetic. Finally, in Chap. 7 we will present an application to the physics of GRBs. In particular we will explore the possible consequences of quark deconfinement in the phenomenology of long GRBs in terms of timescales and energetics, modeling the quasi-stationary spin-down evolution for both Hadron and Quark stars.

This thesis is partly based on results published by the Author: Chaps. from 3 to 5 are adapted from Pili et al. (2014), Bucciantini et al. (2015b) and Pili et al. (2017) (in preparation), Chap. 6 is closely based on Pili et al. (2015) and finally Chap. 7 refers to Pili et al. (2016).

List of publications

International peer-reviewed journals

- A. G. Pili , N. Bucciantini, A. Drago, G. Pagliara & Del Zanna, *Quark deconfinement in the proto-magnetar model of Long Gamma-Ray Bursts*, 2016, MNRAS Letters, 462, L26
- A. G. Pili , N. Bucciantini & L. Del Zanna, *General relativistic neutron stars with twisted magnetosphere*, 2015, MNRAS, 447, 2821
- N. Bucciantini, A. G. Pili & L. Del Zanna, *The role of currents distribution in general relativistic equilibria of magnetized neutron stars*, 2015, MNRAS, 447, 3278
- A. G. Pili , N. Bucciantini & L. Del Zanna, *Axisymmetric equilibrium models for magnetized neutron stars in General Relativity under the Conformally Flat Condition*, 2014, MNRAS, 439, 3541

Manuscripts currently in preparation

- A. G. Pili , N. Bucciantini & L. Del Zanna, *General relativistic models for rotating magnetized neutron stars*, 2017, to be submitted to MNRAS

Proceedings of international conferences

- N. Bucciantini, A. G. Pili & L. Del Zanna, *Modeling the structure of magnetic fields in Neutron Stars: from the interior to the magnetosphere*, Proceedings of the 10th International Conference on Numerical Modeling of Space Plasma Flows, 8-12 June 2015, Avignon, France
- A. G. Pili, N. Bucciantini, & L. Del Zanna *General relativistic equilibrium models of magnetized neutron stars*, International Journal of Modern Physics Conference Series, Volume 28, id. 1460202
- N.Bucciantini, A. G. Pili & L. Del Zanna, *Solving the 3+1 GRMHD equations in the eXtended Conformally Flat Condition: the XNS code for magnetized neutron stars*, Proceedings of the 8th International ASTRONUM Conference

1

Neutron stars

In this chapter we introduce the physics of NSs from a general viewpoint emphasizing, in particular, the importance of the magnetic field. After a brief historical introduction, we will discuss the different types of astronomical sources associated with NSs, detailing in particular how a different morphology of the magnetic field affects their phenomenology. We will focus on the possible origin of strong magnetic fields inside NSs considering also the possible observational implications for GRBs and GW emission. In the last section we will summarize the current status of magnetized NS modelization.

1.1 A brief history of discoveries

The early history of NSs dates back to 1931 when Lev Landau first speculated about the possible existence of a star resembling a gigantic nucleus (see Yakovlev et al. 2013). His work was published in February 1932, the same month of the announcement of the discovery of neutrons (Chadwick 1932). Two years later, Baade and Zwicky proposed the idea that the final outcome of a supernova (SN) explosion is a star whose hydro-static equilibrium is guaranteed by the degenerate pressure of neutrons. Later, Gamow (1937, 1938) and Landau (1938) discussed the possibility that the stellar radiation is powered by the accretion of matter on a neutron star core, while the first general relativistic approach to NS was developed by Tolman (1939) and Oppenheimer and Volkoff (1939). They separately derived the general relativistic equation of selfgravitating hydrostatic equilibrium, named "TOV equation" after them. The very small radii of these objects meant that they could not be observed with the instruments available at that time.

The interest for NSs was only renewed during 1950s when many efforts were made in order to obtain a description of dense stellar matter (Harrison et al. 1958) considering also nuclear interaction (Cameron 1959) through the new effective nucleon-nucleon potential developed by Skyrme (1959) and superfluidity (Migdal 1959). The first attempts to estimate the thermal emission of cooling NSs was made by Stabler (1960) and Chiu and Salpeter (1964) and at that point the advent of X-ray astronomy seemed to give the first real opportunity to detect NSs (Tsuruta and Cameron 1966). However, even if at the beginning of 1960s many extrasolar X-ray sources had already been discovered (Giacconi et al. 1962, 1964), their association with NSs (Shklovskii 1967) did not convince the astrophysical community. The very discovery of NSs arrived in a completely different way. In 1967 Pacini showed that rotating NSs, if endowed with strong magnetic field, would loose their rotational energy through electromagnetic dipole emission (Pacini 1967) and that such energy could be pumped into a Supernova Remnant (SNR). In August of the same year Susan Jocelyn Bell discovered a weak and variable radio-source, known today as pulsar PSR B1919+21, characterized by the emission of a highly periodic pulse with an astonishingly stable period: it was constant to better than 1 part over 10^7. After few months of observations it was proposed that the radiation may be associated with oscillations of white dwarfs stars (Hewish et al. 1968). However the first hypothesis on oscillating stars was soon ruled out by the lack of higher harmonics: this would imply that only one mode was excited, unlikely for an astrophysical source. Independently from Pacini, in that same year Gold (1968) proposed the so called "lighthouse model" suggesting that the pulsars are actually rotating NSs. The final evidence in its favor was given by the discovery of the Crab pulsar and the measure of its spin period: 33 ms, too short to be due to a white draft (Comella et al. 1969). Moreover since the Crab PSR is located within a SNR, this provided a striking confirmation of the Baade and Zwicky's idea.

Within a year from the discovery, Counselman and Shapiro (1968) realized that pulsars, because of the high stability of their periods, would be valuable tools to test GR. Then, in 1974, came the first discovery of a pulsar in a binary-NS system, the famous Hulse & Taylor pulsar (PSR B1913+16), which has provided the first indirect evidence of the existence of GWs: the orbital decay inferred from timing measures agrees with the value obtained in GR assuming gravitational radiation (Hulse and Taylor 1975).

At this point, although the interpretation of pulsars as strongly magnetized NS had been commonly accepted, there was no independent estimate confirming the presence of a strong magnetic field. This evidence came in 1976 when Trümper and collaborators observed strong cyclotron line emission in the spectrum of Hercules X-1, a binary system composed of a NS accreting matter from a normal star. The inferred magnetic field was 5.3×10^{12} G (Truemper et al. 1978). The most magnetized NSs, named *magnetars*, were casually discovered few years later, in 1979, as Soft Gamma Repeaters (SGRs). Initially labelled as a sub-class of Gamma Ray Bursts (GRBs), only in 1987 they were recognized as different objects. Indeed, unlike GRBs, SGRs are recurrent sources. The idea that SGRs represent a new kind of super-magnetized NSs was finally suggested by Duncan and Thompson (1992), Thompson and Duncan (1993). However, the first confirmation of the magnetar hypothesis arrived with the measurement of the dipole magnetic field of SGR 1900+14 by Kouveliotou et al. (1999). Since the '80s to nowadays the continuous development of space technology has enlarged our knowledge of NSs phenomenology. The Einstein X-ray observatory has allowed the discovery of a new class of NSs, the Anomalous X-ray Pulsars (AXPs) (Gregory and Fahlman 1980), which are now classified as a magnetar sub-class. *ROSAT*, *ASCA* and

BeppoSAX[1] have provided the first reliable detections of thermal radiation from isolated NSs (see Becker and Pavlov 2002 for a review). In the 21st century the new generation of satellites such as *Chandra*, *XMM-Newton*, *Swift*, *INTEGRAL*, *Fermi* and *AGILE*[2] have provided us unprecedented data on the high-energy emission of NSs. This together with ground-based observations (radio and optical) has significantly contributed to our understanding of NSs and their physical properties.

Among the many recent discoveries, it is worth to mention the discovery of $2M_\odot$ NSs (Demorest et al. 2010, Antoniadis et al. 2013) that has put an important constraint on the EoS describing NS matter that, still today, remains one of the biggest unknown of NS physics. Indeed, while experimental data obtained on Earth can be used to infer the composition and the structure of the outer layers of the NS, where density is well below the critical *nuclear density* $\rho_0 \simeq 3 \times 10^{14}$ g cm^{-3}, the same can not be done in the inner core. The *outer crust* is composed by degenerate electrons immersed in a Coulomb lattice of fully ionized atoms. Proceeding inward inside the star, β-captures make nuclei in the lattice more and more neutron rich until, at density $\sim 10^{11}$ g cm^{-3}, neutron drip sets in. This marks the beginning of the *inner crust* where the number-density of free neutron grows with depth. At densities in the range $0.5\rho_0 \leq \rho \leq 2\rho_0$, in the *outer core*, NS matter consists of a strongly degenerate plasma of neutrons, protons, electrons and possibly muons in beta equilibrium. The composition of the inner core, where density ranges from $2\rho_0$ up to $(10-15)\rho_0$, is almost completely unknown. Current theoretical models make different predictions with the appearance of hyperons, Bose condensate of pions or kaons, or possibly also deconfined quark matter.

1.2 The neutron stars bestiary

As discussed in the previous section, NSs manifest themselves as different classes of astronomical sources that can be broadly distinguished based on their observational properties. Their emission covers almost the entire electromagnetic spectrum and, in the majority of the cases, it shows pulses or modulation. Differences in the pulse profiles, in the spectral features of their emission and in the possible bursting activities are at the base of the observational classification of the NS families. In the following we will briefly introduce the main families of the currently identified "beasts" in the so called "Neutron Star Zoo". More exhaustive reviews can be found in Mereghetti (2011), Kaspi (2010), Harding (2013), Tauris et al. (2015).

From the pulsed/modulated emission of a NS we can directly measure both the NS rotational period P and its time derivative $\dot{P}$. According to the simple magnetic dipole model (Pacini 1967, Gold 1968) the spindown of NSs is mainly due to magnetic braking and hence

---

[1] ROSAT - RÖntgenSATellit; ASCA - Advanced Satellite for Cosmology and Astrophysics; Beppo-SAX - Satellite per Astronomia a raggi-X named in honour of Giuseppe "Beppo" Occhialini.

[2] XMM - X-ray Multi-Mirror; INTEGRAL - INTErnational Gamma-Ray Astrophysical Laboratory; AGILE - Astro-Rivelatore Gamma a Immagini LEggero.

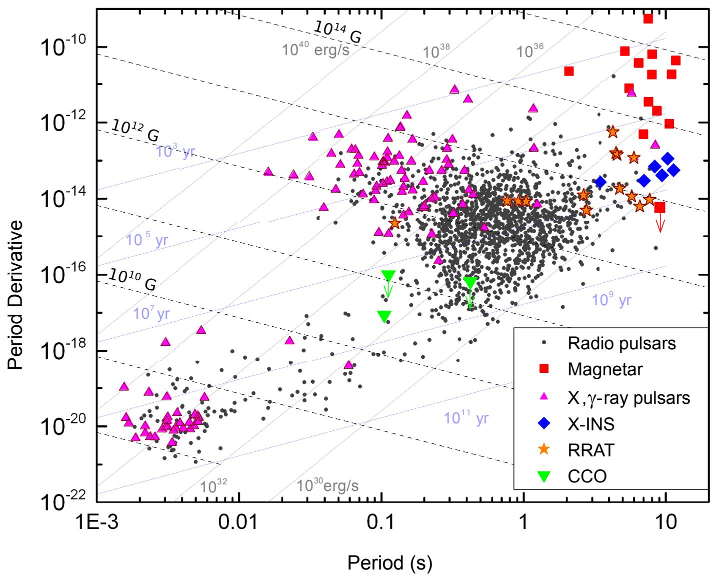

Figure 1.1: $P - \dot{P}$ diagram for the known population of isolated NSs. Blue lines are curves of constant characteristic age, grey lines of constant dipole spin-down luminosity, dashed lines of constant dipole magnetic field. Adapted from Harding (2013).

the values of P and $\dot{P}$ can be combined, assuming a typical NS radius, to provide an indirect estimate of the dipole magnetic field ($B_{\rm dipole} \propto \sqrt{P\dot{P}}$), of the characteristic age ($\tau = P/2\dot{P}$) and of the dipole spin-down luminosity ($\dot{E}_d \propto B^2 P^{-4}$). In Fig. 1.1 NSs are shown in terms of the measured P and $\dot{P}$.

- **Rotation-Powered Pulsars**
  The bulk of the observed NSs population, with period ranging from $\sim$ 1 ms up to $\sim$ 10 s, is represented by the Rotationally Powered Pulsars (RPPs). The emission of this kind of NSs is powered by the rotation of the NS itself. It is evident from Fig. 1.1 that RPPs can be divided in two subclasses: the *canonical pulsars* and the *millisecond pulsars* (MSPs). Canonical pulsars with $\sim 0.03{\rm s} \lesssim P \lesssim 10$ s and $B_{\rm dipole} \sim 10^{10} - 10^{14}$ G are thought to originate from core collapse SNe. MSPs, with $P \lesssim 10$ ms, $B_{\rm dipole} \lesssim 10^{10}$ G and characteristic age $\tau \gtrsim 100$ Myr, are the possible final outcome of a NS evolving in a close binary system. The majority of RPPs have been discovered thanks to their radio pulsation, but some of them are visible also as pulsating optical, X-ray or γ-ray sources. The spin frequency evolution of RPPs is typically very stable and predictable and unique exceptions are represented by *glitches*. Other irregularities are pulse nulling phenomena, i.e. abrupt cessations of the pulsed radio emission for up to $\sim 10^4$ s. The latter are particularly dramatic in a subclass of RPPs, the Rotating Radio Transient (RRATs), where no regular pulsar emission is observed between single pulses (Gajjar et al. 2012).

- **Magnetars**
  Magnetars are located in the up-right corner of the $P-\dot{P}$ diagram (Fig. 1.1). They are young (with a typical age of 10^4 yr), isolated NSs characterized by slow rotation ($P \sim 2-12$ s) and a surface magnetic field strength of the order of $10^{14}-10^{15}$ G. As anticipated in Sec. 1.1 the magnetar class is divided in two sub-classes: Soft Gamma Repeaters (SGRs) and Anomalous X-ray pulsars (AXPs). Both exhibit a persistent X-ray emission with luminosities $L_X \sim 10^{34}-10^{36}$ erg s^{-1} (that in the case of transient magnetar lowers to $L_X \sim 10^{32}$ in the quiescent phase). They are both characterized by flaring activity with X-ray bursts whose duration is $\sim 0.1-1$ s and peak luminosities $\sim 10^{40}-10^{41}$ erg s^{-1}. SGRs are sources of violent events, known as giant flares, during which an amount of energy $\sim 10^{44}-10^{46}$ erg is released in few seconds [for recent reviews, see Rea and Esposito (2011), Mereghetti et al. (2015), Turolla and Esposito (2013), Turolla et al. (2015)]. Since they are slow rotators, their emission can not be powered by spin-down energy losses but it is thought to come form the huge magnetic energy reservoir stored in the interior of the NS (Duncan and Thompson 1992, Thompson and Duncan 2001).

- **X-ray Isolated Neutron Stars**
  X-ray Isolated Neutron Stars (XINSs) are nearby NSs, with distances < 500 pc, characterized by slow rotation ($P \sim 3-11$ s) and strong magnetic fields (10^{13} G). Observed in the X-ray band, their emission is mainly thermal with a luminosity that can be even larger than the spin down luminosity (for a review on XINSs observational properties see Turolla 2009). Therefore, the XINSs emission is believed to be powered by the residual thermal energy supplied by the decay of an initially high magnetic field (Heyl and Kulkarni 1998). Because of the poor statistic (only 7 objects are classified as XINS), at the moment it is not clear if they can be connected with other families of the NSs zoo: XINS may be extreme RRATs (McLaughlin et al. 2006), high-B RPPs viewed off-beam or old magnetars (Pons et al. 2009).

- **Compact Central Objects**
  Compact Central Objects (CCOs) represent the most puzzling class of NS zoology and their nature is still largely debated. They owe their name to their central position in SNRs. Similarly to XINSs, they are seen as soft X-ray thermal sources without any apparent emission at other wavelengths.
  The unique feature of CCOs is that the characteristic age $\tau \sim 100$ Myr is much larger than the age of the SNR (10^4 yr). This may suggest that CCOs are born as slow rotators with a low initial magnetic field (Gotthelf and Halpern 2008). Indeed, when measurements of $\dot{P}$ are possible (just in three cases: RX J0822.0-4300 in Puppis A, CXOU J185238.6+004020 in Kes79 and 1E 1207.4-5209 in PKS 1209-51/52, see Gotthelf et al. 2013), the inferred magnetic field is of the order of $B_{\rm dipole} \sim 10^{10}$ G. Despite this, their pulse morphology indicates a strongly non-uniform surface temperature distribu-

tion which, in turn, seems to suggest the existence of a strong decaying magnetic field hidden in the interior. As proposed by Shabaltas and Lai (2012) the magnetic field could be submerged by mass fallback accretion during core collapse and re-emerge later in the NS lifetime. This scenario seems to be confirmed by recent observation regarding the Calvera X-ray source. Initially thought as a XINS, recent measurements of $\dot{P}$,inferring a spin-down magnetic field $B_{\rm dipole} \sim 10^{11}$ G, suggest to include Calvera among CCOs (Halpern et al. 2013). Finally a very puzzling CCO, 1E 1613485055, characterized by a very long periodicity of $\sim$ 6.67 hr, has shown an energetic flaring activity typical of magnetars phenomenology (Rea et al. 2016, D'Aì et al. 2016).

- **Accretion-powered Neutron Stars**
  NSs are found also in binary systems. When the system experiences accretion episodes due to mass transfer either through winds or an accretion disk the NS manifests itself as an accretion-powered NS. In this case the spin evolution is governed by the accretion rather than by the magnetic field. Measurements of the magnetic field are possible when cyclotron lines are present in the spectrum.

1.2.1 The neutron star emission and the magnetic field morphology

A key role in the diversification of the NS families is surely played by the magnetic field morphology. It is indeed commonly accepted that the magnetic field plays a crucial role in shaping their emission. For example, magnetars and high magnetic field RPPs share a comparable dipolar magnetic field strength but they behave in a completely different way: the former are almost radio-quiet (with the exception of transient periods of radio-activity McLaughlin et al. 2006) while the latter are detected as radio-PSRs. This may suggest that while RPPs are characterized by a mainly dipolar magnetic field, magnetar emission may originate from a more complex morphology.

The standard approaches made in the modelization of NS magnetospheric emission are based on the simplifying assumption of a vacuum dipole geometry (Deutsch 1955, Ruderman and Sutherland 1975, Arons and Scharlemann 1979, Cheng et al. 1986, Dyks and Rudak 2003). With this simple geometry it is however possible to explain the main electrodynamic properties of RPPs, reconstruct the properties of the source (such as the magnetic inclination and the rotation axis of the pulsar) and fairly reproduce the general shape of the pulse profile (Harding and Muslimov 2011, Ferdman et al. 2013, Guillemot et al. 2013, Perera et al. 2014, Seyffert et al. 2014). Nevertheless, a deeper understanding of the complex processes involved in RPPs emission requires more complex magnetic field morphologies as shown by Bai and Spitkovsky (2010). The anomalous braking index of some PSRs, and in particular of PSR J1640-4631 which is the unique PSR having a braking index > 3, can be explained in terms of a strong quadrupolar fields in the magnetosphere (Archibald et al. 2016). Asseo and Khechinashvili (2002) and Harding and Muslimov (2011) have shown that multipole fields can increase the pair cascade efficiency. This can justify why PSR J2144-3933, located beyond the death line according to standard models, emits radio-waves. Multipolar magnetic fields may be also important for a more accurate modelization of the pulse profile and phase diagrams (Bonazzola et al. 2015, Pétri 2015).

The morphology of the near magnetosphere is linked to the complex processes occurring inside the NS. These are particularly relevant for the other classes of NSs (XINSs, CCOs and magnetars) where the bulk of the emission appears to be powered by the dissipation of the internal magnetic field. In the case of CCOs, the large anisotropy of the surface temperature distribution, inferred by the pulse profile, requires the existence of a strong crustal toroidal field which is able to channel heat from the star interior to hot-spots on the surface (Shabaltas and Lai 2012). In the case of magnetars, readjustments of the internal magnetic field are usually invoked to explain their characteristic flaring and bursting activity (e.g. Thompson and Duncan 2001): while global rearrangements of the magnetic field, possibly depending on the coupled crust-core evolution, are expected to power giant-flares (Lander et al. 2015, Lander 2016), Hall drift and Ohmic diffusion occurring in the crust are thought to originate bursts (Viganò et al. 2013). Indeed, the evolution of the crustal magnetic stresses initially induces elastic deformations of the crust but, when the maximum strain is reached, plastic shear flows are produced (Perna and Pons 2011). This leads to quickly developing instabilities that dissipate the magnetic energy fueling the ignition of bursts (Beloborodov and Levin 2014). As initially suggested by Thompson et al. (2002) and Beloborodov and Thompson (2007) the dissipation of the energy inside the star can also induce a twist of the emergent magnetic field into a non-potential state which, in turn, is sustained by electric currents that, threading the magnetosphere, might interact with the thermal photons emitted by the surface of the NSs. This explains why magnetars persistent X-ray spectra are well fitted by a blackbody-like component at $kT \sim 0.5$ keV, joined with a power-law tail that becomes dominant above 10 keV (Kuiper et al. 2006). The latter indeed can be explained in terms of resonant cyclotron scattering of the thermal photons by magnetospheric particles (An et al. 2013, Beloborodov 2013). Such twisted magnetosphere scenario has been strengthened by the detection of a proton cyclotron feature in the X-ray spectrum of the 'low-field' magnetar SGR 0418+5729 which is compatible with a strong and localized field of the order of 10^{15} G (Tiengo et al. 2013). Phase-variable absorption features have been observed in other magnetars (Rodríguez Castillo et al. 2016, Makishima et al. 2016) but also in XINSs (Borghese et al. 2015).

At present, motivated also by the observation of transient behaviours, understanding the connections between the different NS families remains a fundamental question in the field. This is however a difficult task that requires a better understanding of how NSs form, how the initial magnetic field is configured, and how the NS evolves at later stages. Nowadays, magneto-thermal evolution models (Yakovlev and Pethick 2004, Arras et al. 2004, Pons and Geppert 2007, Pons et al. 2009, Viganò et al. 2013) represent the first important attempt to obtain a unified picture.

1.3 The birth of a NS and its magnetic field

The properties of neutron stars cannot be understood without considering their violent origin. Although there is a general consensus concerning the main aspects of the formation of a NS in core collapse events (see Janka 2012 for a recent review), we still lack a precise understanding of many key details of the physical processes involved, especially concerning the origin of the magnetic field.

NSs are believed to form after core collapse SN explosions of massive stars with typically $8M_{\odot} \lesssim M \lesssim 25M_{\odot}$. In such kind of stars, the standard theory of stellar evolution predicts that as nuclear burning proceeds an iron core is formed. Since iron has the highest binding energy per nucleon, no energy can be released by further thermonuclear fusions and, as it cools, the entire core is supported by the degeneracy pressure of electrons. As the mass of the iron core grows the Fermi energy of electrons increases and electron capture on iron nuclei becomes energetically favorable. The iron core becomes unstable to gravitational collapse. During the collapse the temperature in the core increases and when it exceeds the value $T \sim 10^9$K photo-dissociation of iron nuclei occurs. This subtracts thermal energy to the core accelerating the collapse. When the density of the core exceeds 10^{11} g cm^{-3} the diffusion time-scale of neutrinos becomes larger then the dynamical time-scale of the collapse so that neutrinos are trapped inside the iron core and form a Fermi sea together with electrons. At $\sim$ 100 ms since the collapse the density inside the core reaches the critical value of the nuclear density $\rho_0 \sim 10^{14}$ g cm^{-3} and nucleons are so close together that the repulsive component of nuclear strong force becomes dominant causing a sudden stiffening of the EoS. As a consequence the pressure now becomes high enough to stop the collapse and causes the inner core to bounce. The rebounding inner core triggers the formation of an outward shock wave that, sustained also by the neutrino flux coming from the inner core, expands into the external layers of the collapsing star. The shock wave blows off the entire star giving rise to a SN explosion.

The compact remnant left behind a successful SN explosion is a hot and neutron rich object, the so called proto-NS (PNS), whose complex evolution is characterized by large entropy gradients (Pons et al. 1999), instabilities (Urpin 2010), dynamo (Duncan and Thompson 1992, Bonanno et al. 2003), and intense neutrino-driven winds (Pons et al. 1999). It is only after a typical Kelvin-Helmholz tymescale, $\sim$ 100 s after core bounce, that the PNS becomes transparent to neutrinos, it rapidly cools, and reaches a state that is dynamically very close its final equilibrium (Burrows and Lattimer 1986), even if its thermal and magnetic evolution can last much longer (Viganò et al. 2013), and late phase transitions are still possible (Staff et al. 2006, Drago and Pagliara 2015). It is during this brief lapse of time that the magnetic properties of the resulting NS, such as the magnetic field strength, geometry and distribution, will be set. Once the crust begins to form, it will tend to "freeze" magnetic field lines in their position, and only dissipative effects might then affect its evolution (Viganò et al. 2013). Given that the dynamics of the core collapse is so fast that to first order

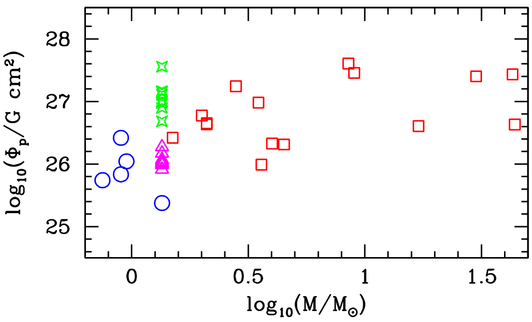

Figure 1.2: Magnetic flux ϕ_p for strongly magnetized main sequence stars (squares) white dwarfs (circles), high magnetic field pulsars (triangle), and magnetars (diamonds) (from Ferrario et al. 2015).

the core evolves as if it was detached from the outer layers of the surrounding star, it is reasonable to expect that the magnetic properties might be related to the conditions in the core of the progenitor, like its rotational profile (Duncan and Thompson 1992, Spruit 2009) or the presence of a seed field (Woltjer 1960, Ruderman 1972). However, given the complexity of the problem, it is difficult to establish a clear relation between them.

The origin of magnetars, among all NSs species, is a particularly puzzling problem. Because of their huge magnetic field, one naturally wonder how it originates and many evolutionary scenarios have been proposed so far (see Spruit 2009, Ferrario et al. 2015 and Popov 2015 for reviews): the magnetar magnetic field can be either completely inherited by a strongly magnetized progenitor star, as the fossil-field scenario suggests (Woltjer 1960, Ruderman 1972), or generated by dynamo mechanism during the proto-NS phase as proposed in the original magnetar model (Duncan and Thompson 1992). In the first hypothesis the final magnetic field results from the magnetic flux freezing during the core collapse. This is suggested in particular by the broad similarity of the magnetic flux of the most magnetized Main Sequence star with the magnetic flux of NSs (see Fig. 1.2 and Ferrario et al. 2015 and references therein for a discussion). This model has been investigated in Ferrario and Wickramasinghe (2006, 2008) through a population synthesis, showing that magnetars are probably descendants of massive and strongly magnetized OB stars with magnetic field of the order of 10^4 G. Nevertheless Spruit (2008) had pointed out that the paucity of suitable magnetized progenitors is inconsistent with the observational inferred magnetar birth-rate (Woods 2008, Keane and Kramer 2008). This suggests that in a large fraction of magnetars the core compression does not produce strong enough magnetic fields. However if the nascent NS rotates with a millisecond period, the inherited magnetic field can be further increased by the differential rotation acquired during core collapse that winds up the magnetic field lines (Burrows et al. 2007) and leads to possible dynamo effects (Bonanno et al. 2003, Rheinhardt and Geppert 2005, Braithwaite 2006a, Moiseenko et al. 2006). In principle, after the core bounce, there is enough free energy available to amplify the magnetic field up to 10^{17} G. In this case magnetars are the successors of rapidly rotating stellar cores. Nevertheless at present it is still not clear how the evolution of the star rotation proceeds before and after the collapse (Ott et al. 2006). As an example the association of AXP CXO

J164710.2-455216 with the young cluster Westerlund 1 (with an age of $\sim$ 4Myr Clark et al. 2005) suggests that some magnetars can even originate from very high mass $\gtrsim 40\mathrm{M}_\odot$ main sequence stars (Muno et al. 2006), that undergo consistent mass losses through powerful stellar winds or mass transfer onto a binary companion preventing the collapse into a Black Hole (BH). In the case of an isolated progenitor, the stellar core can be substantially spun-down by the magneto-frictional coupling with the outer layers during the Red Supergiant phase (Heger et al. 2005, Yoon 2015). In contrast, as suggested by Popov and Prokhorov (2006) and Popov (2015), a possible enhancement of rotation can occur if the progenitor star evolves in a close binary system undergoing mass accretion transfer and tidal synchronization. Recently, Clark et al. (2014) have provided a number of arguments in favor of the possible origin of CXO J164710.2-455216 in a massive binary system, identifying the putative pre-SN companion. Interestingly, recent 3D numerical simulations of core collapse SNe have shown that fast rotation can help the onset of neutrino driven explosions (see Nakamura et al. 2014, Takiwaki et al. 2016, Gilkis 2016 or Müller 2016 for a recent review). High resolution 3D MHD models by Mösta et al. (2015) show that the magneto-rotational instabilities can grow magnetar-strength magnetic fields with a strong toroidal component. Let us finally recall that ultra magnetized NSs can be formed also during NS merger events, as shown in the numerical simulations by Giacomazzo et al. (2015), where magnetic field of the order of 10^{16} G are reached. It remains open the question if such NSs can survive long enough to give observable signature, or if they are bound to collapse to BH on timescales of milliseconds (Giacomazzo and Perna 2013) .

Numerical studies, devoted to initial field amplification, typically follow the evolution of the magnetic field for, at most, few tens of milliseconds after the formation of the proto-NS. Nevertheless, at this time the magnetic field is still far from its final stable configuration, but it continues to evolve until, after $\sim$ 100 s (a Kelvin-Helmholtz time-scale), a crust begins to form, freezing the magnetic field on the NS surface (Pons et al. 1999). From now on the magnetic field evolves on the much longer diffusive time-scales (Braithwaite and Spruit 2006, Viganò et al. 2013, Gourgouliatos et al. 2013, 2016, Elfritz et al. 2016, Passamonti et al. 2016). In the case of a proto-magnetar, given that the Alfvénic crossing time ($\sim$ 0.01 s for a magnetic field of the order of 10^{16} G) is much smaller than the typical Kelvin-Helmholtz time-scale, the magnetic field can completely decay against instabilities, unless a stable equilibrium is reached before the crust forms (Spruit 2008). The stability problem has been investigated by Braithwaite and Nordlund (2006), Braithwaite and Spruit (2006), Braithwaite (2009) and Mitchell et al. (2015) by means of numerical simulations in the Newtonian MHD regime. They found that, in a stably stratified star, an initial random magnetic field with non vanishing helicity always relaxes to a characteristic geometry that persists for many Alfvén times (see Fig. 1.3). In the emerging configuration, usually dubbed as *Twisted-Torus* (TT), the poloidaly field is roughly axisymmetrically twined with a toroidal field, of comparable strength, into a ring-like region located just underneath the surface of the star. The exterior field they find is mainly a dipole with only smaller contributions from

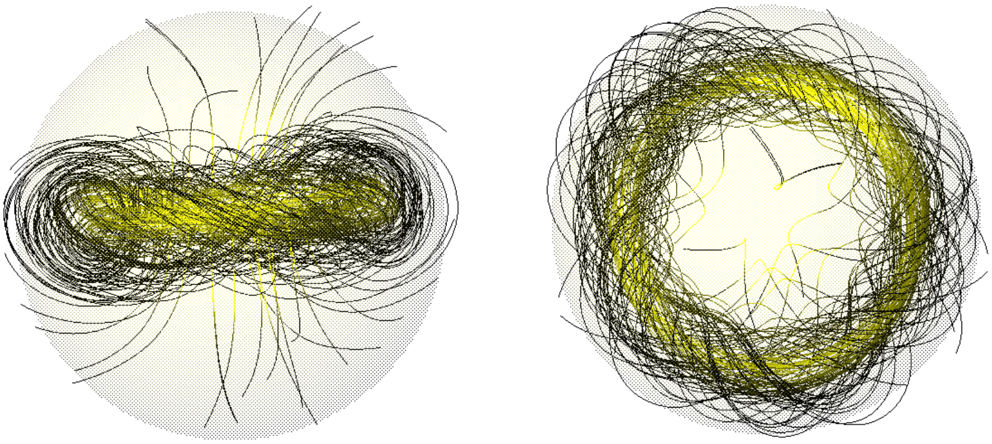

Figure 1.3: The shape of the TT magnetic field obtained by Braithwaite and Nordlund (2006), Braithwaite and Spruit (2006) viewed from different angles. The dotted surface represents the stellar surface, with stronger magnetic field in yellow, weaker in black.

higher-order multipoles (note however that they impose a potential field outside the NS surface, confining any current to the interior). A common conclusion of these works is that stability requires that the toroidal field is energetically dominant with respect to the poloidal one (for a discussion on recent developments see Sec. 1.4).

1.3.1 Gamma Ray bursts

The formation of a rapidly rotating magnetar can have important observational implications: magnetars could be fundamental to explain GRBs, the most luminous explosions known in the Universe.

While there is a compelling evidence that these events are associated with the core collapse of massive stars (Woosley 1993), in the case of long GRBs, merging event or accretion induced collapse (Paczynski 1986), in the case of short GRBs, it is not yet well established whether the burst is produced by a disk accreting onto a BH, within the so-called *Collapsar* model (Woosley 1993), or by the outflow emerging from a fast rotating and highly magnetized proto-neutron star in the so called *proto-magnetar* models (Usov 1992, Bucciantini et al. 2009, Metzger et al. 2011, Bucciantini et al. 2012). In the latter case, the combination of a rapid millisecond-like rotation with a magnetic field of typical magnetar strength can easily drive a relativistic outflow with energetics of the order of $\sim 10^{49-50}$ erg s^{-1}. This is enough to power both Short and Long GRBs, for a typical duration of $10-100$ s corresponding to the characteristic Kelvin-Helmholtz timescale of a newly formed NS.

It is possible that both these systems, BHs and magnetars, contribute in producing GRBs, depending on the initial condition of the progenitor (in particular its mass, spin frequency and magnetic field). With the discovery by Swift of GRB extended emission (for Long GBRs), and plateaus (for short GRBs) after the initial prompt phase (Nousek 2006, Zhang 2006), the magnetar models has grown in popularity. These late-time activities, lasting up to 10^4 s and present in a sizable fraction of GRBs, suggest a continuous energy injection by a long lasting central engine. In particular as shown by several authors (Troja et al. 2007, Dall'Osso et al. 2011, Rowlinson et al. 2013, 2014), the shape of the light-curves of many GRBs are more naturally interpreted within the proto-magnetar model as due to the pulsar-like energy injection powered by the residual rotational energy left after the prompt emission.

Within the proto-magnetar model an important ingredient, which regulates the temporal evolution of the jet and its gamma-ray luminosity, is the neutrino signal released by the star due to deleptonization (the gradual neutronization of matter) and cooling. In particular, neutrinos ablate baryonic matter from the surface and provide a tiny amount of baryonic load which is crucial for an efficient internal dissipation of the kinetic and magnetic energy of the jet into gamma-ray emission. When the neutrino luminosity drops below $\sim 10^{50}$ erg/s (after a few tens of seconds), the magnetization (or the Lorentz factor) grows too large and the prompt emission ends. Notice that in the case of short GRBs, originating from NS-NS binary merger, the presence of a highly baryon polluted environment left behind soon after the merging event could actually hinder the formation and the propagation of a relativistic jet (Murguia-Berthier et al. 2014, Just et al. 2016). An alternative model, the so-called "time-reversal" scenario has been proposed by (Ciolfi and Siegel 2015) and (Rezzolla and Kumar 2015). In this scenario, the jet is launched only few minutes after the merging event, once the proto-magnetar left behind the merger collapses into a BH[3].

Another known problem of the canonical proto-magnetar model is that it is not easy to reactivate the inner engine and therefore to describe multi-episodes of the prompt emission of long GRBs (e.g. Zhang et al. 2012) or X-ray flares occurring during the afterglow (Zhang et al. 2006). Possible solutions to overcome this limitation have been recently suggested, such as mass accretion (Penacchioni et al. 2013, Bernardini et al. 2014) but also delayed, spin-down induced, phase transition from a 'standard' NS to a quark star (Staff et al. 2006, Yasutake et al. 2010). In Chap. 7 we will explore the possible implications of quark deconfinement on the long GRB light-curves.

---

[3] In the "time-reversal" model for short GRBs the product of the binary-NS merger is a supramassive differentially rotating proto-magnetar that, losing its rotational energy through magnetic braking, collapses into a BH. The slow highly baryon loaded neutrino-driven wind emerging from the newly-born proto-magnetar is quenched when the star settles down to uniform rotation. At this point ($\lesssim 0.1-10$ s after the merger) the baryon density of the wind begins to drops and the wind, driven by the NS spin-down, becomes relativistic. The progressive loss of centrifugal support leads the NS to collapse into a BH, possibly surrounded by an accretion debris disk, after $1-10^3$ s since the merger, depending on the stability of the star. Since the fast magnetized wind has pushed outward the slow baryon rich wind, the BH-disk system is able to launch a relativistic jet producing the prompt emission. Within this picture, although the spin-down energy is injected into the environemnt by the NS before the jet formation, it is seen after the prompt emission because it takes a finite time to diffuse out of the optical thick ejecta, resulting in a delayed X-ray afterglow. Nevertheless, as pointed out by Margalit et al. (2015), it is not clear whether the collapse of the rigidly rotating NS creates a debris disk around the BH necessary to explain the retarded formation of the jet (see also Metzger 2016 for a discussion).

1.3.2 Gravitational waves from magnetized Neutron Stars

The recent detections of GWs by the *aLIGO* (advanced Laser Interferometer Gravitational-Wave Observatory) observatories heralds a new era in GW astronomy (Abbott et al. 2016b,a). Among the different possibilities, and in particular compact binary coalescences (BH-BH, BH-NS and NS-NS), also newly born millisecond magnetars from core collapse SNe have been often considered as a promising source of detectable GWs with the second generation of ground-based detectors, not only in the case of formation by binary NS mergers (Dall'Osso et al. 2015), but also in the more common case of core collapse SNe (Stella et al. 2005, Dall'Osso et al. 2009, Mastrano et al. 2011).

The super-strong magnetic field hosted in magnetars is able to induce substantial deformations in the structure of the NS itself, with typical ellipticities given by $|e| \approx 10^{-8}(B/10^{14}\mathrm{G})^2$ (i.e. Cutler 2002, Haskell et al. 2008, Mastrano et al. 2013 and references therein; see also Sec. 2.7 for the definition). Moreover if the initial magnetic magnetic field is energetically dominated by the toroidal component, as expected also from numerical simulations (Braithwaite and Nordlund 2006, Mösta et al. 2015), the resulting deformation is prolate. As initially pointed out by Cutler (2002) this geometry is the most favorable for the GW emission: in this case, even if the magnetic symmetry axis is initially aligned with the spin axis (and hence no GW is produced), the internal dissipative processes minimize the energy of the system driving the magnetic axis toward orthogonal rotation (Mestel and Takhar 1972, Jones 1976). Therefore this process, usually dubbed as 'spin-flip', maximizes the efficiency of the GW production and, in the context of the millisecond magnetar model, the release of energy through GWs enters in direct competition with the magnetic braking. In particular, Dall'Osso et al. (2009) have estimated that, if the newly-born magnetar has a toroidal magnetic field $\sim 10^{16}$ G but a poloidal magnetic field $\lesssim 10^{14}$ G, the magnetic braking is less efficient than the GWs emission that will carry away most of the rotational energy in the first day after formations. The resulting GW signal would be observable with advanced Ligo/Virgo up to Virgo cluster distances ($\sim$ 20 Mpc). Inside this horizon the magnetar birth rate is estimated to be 1 per yr (Stella et al. 2005).

Recent analyses of the light curves of short GRBs by Lasky and Glampedakis (2016) and super-luminous SNe by Moriya and Tauris (2016) have shown that, if interpreted in terms of energy injection by a rapidly rotating engine, the shape of such light curves indicates that most of the rotational energy losses are compatible with the hypothesis that magnetic braking prevails over GWs emission. This either implies small stellar ellipticities ($|e| \lesssim 10^{-3} - 10^{-4}$), constraining the toroidal field to be $\lesssim 10^{16}$ G, or inefficient spin-flip mechanism which is due, in turn, to the high temperature of the proto-magnetar or to a very large stellar deformation (Lasky and Glampedakis 2016). Lasky and Glampedakis (2016) conclude that the post-merger GW emission associated with magnetar phenomenology will probably be only marginally detectable even with third-generation Einstein Telescope (Punturo et al. 2010) within a horizon of 20 Mpc.

It is worth to remember that NSs are possible sources of GWs also at later time after their formation due to a number of mechanisms that include magnetic deformations, glitches, flares and superfluid turbulence (for recent reviews see Andersson et al. 2011 and Lasky 2015). Until now searches for GWs signals from targeted pulsar have produced no evidence of GW emission. This has been used to set upper limits on NSs ellipticities (Aasi et al. 2014, 2015). The strongest constraints have been obtained for millisecond pulsars J2124-3358 and J2129-5721 with $|e| \leq 6.7 \times 10^{-8}$ and $|e| \leq 6.8 \times 10^{-8}$ respectively while for radio pulsars the typical constraint is $|e| \lesssim 10^{-4} - 10^{-6}$ (Aasi et al. 2014). In the particular case of the Crab pulsar it was found that the GW luminosity is $\lesssim 1\%$ of the observed spin-down luminosity, thereby limiting the ellepticity to $|e| \leq 10^{-4}$ and the internal magnetic field to $\leq 10^{16}$G (Abbott et al. 2008, Aasi et al. 2014). In general the magnetic fields in the NS population are too weak to induce a sufficient deformation that would be currently observable. Moreover even in the case of magnetars, where stronger internal magnetic fields can induce suitable deformations[4], the characteristic slow rotation ($P \sim 1 - 10$ms) implies a low frequency GW emission that is not detectable with groud-based GW observatories. Interestingly, if NSs are endowed with exotic states of matter such as colour-superconducty, we expect larger deformations up to three order of magnitude with respect to ‘normal’ NS matter (Owen 2005, Haskell et al. 2007, Glampedakis et al. 2012b). Therefore, future detections of GW from magnetized NS could provide important clues on the fundamental state of nuclear matter.

1.4 Modeling magnetized neutron stars

Theoretical models for equilibria of Newtonian magnetized stars have a long tradition, dating back to Chandrasekhar and Fermi (1953) (also Ferraro 1954, Roberts 1955, Prendergast 1956, Woltjer 1960, Monaghan 1965, 1966, Ostriker and Hartwick 1968, Miketinac 1975, Roxburgh 1966), up to more recent developments (Tomimura and Eriguchi 2005, Yoshida et al. 2006, Akgün and Wasserman 2008, Fujisawa et al. 2012, Mastrano et al. 2013). Models for stars endowed with strong magnetic fields in GR have started to been published only in the last years, because the additional complexity of the equations can only be dealt with the use of numerical tools. Many of these models are limited to simple configurations of either a purely toroidal (Kiuchi and Yoshida 2008, Kiuchi et al. 2009, Yasutake et al. 2010, Frieben and Rezzolla 2012, Fujisawa 2015) or a purely poloidal magnetic field (Bocquet et al. 1995, Bonazzola and Gourgoulhon 1996, Konno 2001, Yazadjiev 2012, Cardall et al. 2001, Franzon et al. 2016a,b). In the latter case, equilibrium models has been computed also in perturbative $f(R)$-gravity (e.g. Cheoun et al. 2013, Astashenok et al. 2015, Bakirova and Folomeev 2016). The strongest driver in developing these models has been the investigation of the role played by the magnetic field, in conjunction with rotation, on the deformation of the NS. However, as originally suggested by Prendergast (1956), such

---

[4] Some recent claims of a free precession in magnetar 4U 0142+61 suggest a prolate deformation of the NS with $|e| \sim 10^{-4}$, possibly caused by a toroidal magnetic field of the order of 10^{16} G (Makishima et al. 2014, 2016) to be compared with the inferred dipole magnetic field of 10^{14} G.

simple configurations are expected to be unstable (Wright 1973, Tayler 1973, Markey and Tayler 1974, 1973, Flowers and Ruderman 1977). The instability of both purely poloidal and purely toroidal fields has been explored also numerically by Braithwaite (2006b, 2007), Lander and Jones (2011a,b), Asai et al. (2016) in the Newtonian regime or in GR by Kiuchi et al. (2008, 2011), Ciolfi et al. (2011), Lasky et al. (2011) and Ciolfi and Rezzolla (2012). All these works confirm that both configurations are always subject to Parker and/or Tayler instability (Parker 1955, 1966, Tayler 1973) and the rotation of the star can only marginally stabilize the system. While poloidal fields are particularly vulnerable in the region of closed field lines around the neutral line, the toroidal magnetic field develops instability at the center of the star (see also Ciolfi 2014 or Braithwaite and Spruit 2015 for a discussion).

As anticipated in Sec. 1.3, Braithwaite and collaborators have shown that TT configurations are likely to be stable. This appears natural considering that the toroidal magnetic field acts to stabilize the poloidal field in the closed field lines region while the poloidal field stabilizes the toroidal one at the centre of the star. In particular, they found a stability condition in terms of the toroidal-to-poloidal magnetic field energy ratio, that has been recently refined in a semi-analytical study in non-barotropic star by Akgün et al. (2013)

$$2a(E_{\rm mag}/E_{\rm grav}) < H_{\rm pol}/H_{\rm tor} \lesssim 0.8 \tag{1.1}$$

where $E_{\rm mag}/E_{\rm grav}$ is the magnetic to gravitational energy ratio, $H_{\rm pol}/H_{\rm tor}$ is the toroidal-to-poloidal magnetic field energy ratio, and a is a constant depending on the stellar stratification.

Inspired by these results, many authors have presented TT equilibrium models in order to evaluate the deformations induced by a mixed field configuration. Due to the complexity of the problem, this has been done either assuming Newtonian gravity by Yoshida et al. (2006), Lander and Jones (2009, 2012), Glampedakis et al. (2012a), Fujisawa et al. (2012), Armaza et al. (2014, 2015) or within GR following a perturbative approach (Ciolfi et al. 2009, 2010). Only recently the fully GR non-linear regime has been explored under the assumption of conformally flat spacetime (by the Author, see Chaps. 2-5) or solving the full set of Einstein-Maxwell equations (Uryū et al. 2014). Interestingly in all these works, where the equilibrium solution is obtained solving the 2D axisymmetric Euler equation and Grad-Shafranov (GS) equation (Grad and Rubin 1958, Shafranov 1956, 1966) on top of a barotropic star, a common outcome is that the toroidal field remains always energetically sub-dominant with respect to the poloidal one with $H_{\rm pol}/H_{\rm tor} < 0.1$. The main reason for this is that to increase the toroidal magnetic field, one needs to rise also the toroidal currents (the two being related due to equilibrium requirement in the GS equation), which act to change the structure of the poloidal field, reducing the volume occupied by the toroidal field. To circumvent this problem, Ciolfi and Rezzolla (2013), Fujisawa and Eriguchi (2013, 2015) have designed very *ad-hoc* prescriptions for the current distribution and boundary conditions that we will discuss in Chapt. 5. Another possibility to obtain higher $H_{\rm tor}/H_{\rm pol}$ is to relax the barotropicity requirement, related to the integrability of Euler equation, and consider a multifluid NS as shown in Glampedakis et al. (2012a). It is important to mention, that stratification, and hence non-barotropicity, is expected to be important in the stability of the system (Reisenegger 2009): even if the toroidal component is energetically dominant, a mixed magnetic field configuration may be always unstable in a barotropic star. This conjecture is strongly supported by a recent numerical investigation by Mitchell et al. (2015) where the authors compare the evolution of an initial random magnetic field in a barotropic and in a non barotropic star. In the former case, where buoyancy force due to stratification are absent, the magnetic field always decay in few Alfvén times through an axially symmetric instability in which the toroidal flux flows radially out of the star where, because they assume a poorly conductive atmosphere, the twist is dissipated.

From an observational point of view, we have no direct access to the morphology of the internal magnetic field. As discussed in Sec. 1.2.1, all the hypotheses are based on indirect evidences (i.e. hot-spots, anomalous braking indexes, bursts etc.) that can be interpreted in terms of a complex internal magnetic field morphology. On the other hand, the bulk of the NS emission is controlled by the exterior magnetic field. For this reason, in the astrophysical community, a vast effort has been devoted to the modelization of the physics of the exterior magnetic field. As pointed out in the seminal work by Goldreich and Julian (1969) rotating NSs are surrounded by a magnetosphere filled by a charge-separated plasma, where the dynamics is completely controlled by the electromagnetic field, while the pressure and the inertia of the fluid are ineffective. Michel (1973a), Scharlemann and Wagoner (1973) found that in the case of axisymmetric force-free equilibria the magnetosphere is described by the so-called *pulsar equation* which was numerically solved for the first time for a dipole by Contopoulos et al. (1999). In the subsequent years, MHD models of NS magnetosphere have been generalized to include non-axisymmetric geometries (Spitkovsky 2006, Philippov et al. 2014, Melrose and Yuen 2014), GR effects (Gralla and Jacobson 2014, Gralla et al. 2016, Bonazzola et al. 2015, Pétri 2016a), quantum effects (Pétri 2016b). Recently particle-in-cell simulations have started to appear as well (Chen and Beloborodov 2014, Philippov and Spitkovsky 2014, Philippov et al. 2015a,b, Belyaev 2015), motivated by the fact that the MHD description does not allow one to model particle acceleration that occurs in the so called ‘gaps’.

As discussed in Sec. 1.2.1 there is a growing observational evidence that, in the vicinity of the NS and especially in the case of magnetars, the magnetic field can host a large twist associated with a strong component of the toroidal field. This twisted magnetosphere scenario has been successfully validated by calculation of synthetic spectra (Lyutikov and Gavriil 2006, Fernández and Thompson 2007, Nobili et al. 2008, Taverna et al. 2014). Typically, the standard reference model is the one discussed in Thompson et al. (2002) where the magnetosphere is described in terms of a self-similar, globally twisted, dipolar magnetic field. This model has been refined to account for higher order multipoles by Pavan et al. (2009), in response to observational indications of a local, rather than global, twist (Woods et al. 2007, Perna and Gotthelf 2008). More general equilibrium models have been obtained by Viganò et al. (2011) using a magneto-frictional method, originally developed for the study of the

Solar corona (Yang et al. 1986, Roumeliotis et al. 1994), or by Parfrey et al. (2013) who, with time-dependent numerical simulations, investigated the response of the magnetosphere to different shearing profiles of the magnetic footpoints. More recently, Akgün et al. (2016) presented magnetospheric models based on the solution of the Grad-Shafranov equation.

Due to the complexity of the problem, studies have been limited either on the internal field structure (assuming a prescription for the magnetosphere) or on the external magnetosphere (assuming an internal current distribution). It is obvious that the two cannot be worked out independently, and global models are a necessary step forward. A first attempt in this direction has been recently made in Glampedakis et al. (2014). Considering non-rotating stars in Newtonian regime, they show that a “Grad-Shafranov approach” to the problem can be used to obtain global equilibrium configurations, with twists and currents extending from the interior to the magnetosphere. A similar modelization as been presented also by the author (see Chap. 6) and by Fujisawa and Kisaka (2014) who include a surface current distribution at the core-crust interface. A different approach was used in Ruiz et al. (2014) where, for the first time, detailed GR models of inside-out pulsar magnetosphere were developed. In particular they search for steady state configurations by evolving in time the NS and by matching the interior field, evolved according to ideal MHD equations, to the exterior solution modeled in the force-free regime.

2

The Mathematical Framework

In order to obtain GR models of magnetized NSs we have to solve, simultaneously, both Einstein's equation and the magnetohydrodynamic (MHD) equations. The major difficulties in this task come from the complexity of Einstein's equation itself. Indeed they are a set of non-linear partial differential equations for the metric that in general, apart from some specific cases, must be solved numerically. However, even in that case, due to the complexity of the equations involved it is convenient to introduce some simplifications.

To a first approximation for the typical inferred magnetic field strengths, a magnetized rotating NS is described as a stationary and axisymmetric fully degenerate compact object. Since the symmetry of the physical system must reflect on the geometry of the spacetime we can assume that also the spacetime is stationary and axisymmetric[1]. Unfortunately, in the case of magnetized NSs, imposing such symmetries on the spacetime does not lead to a sufficient simplification of Einstein's equation and one has to resort either to a perturbative approach or to limit himself to simple configurations of the magnetic field. Since we want to model magnetic fields of general morphology, also in the fully non-linear regime, we have adopted a particular strategy in order to simplify Einstein's equation: we assume the spacetime to be *conformally-flat*.

In this chapter we will introduce the general formalism we have adopted to construct our equilibrium models. We will present and justify our assumptions on the symmetries and properties of the spacetime, that we have chosen. We will show how, under those assumptions, given a distribution of momentum-energy, one can solve Einstein's equation, and determine the associated metric. Then we will illustrate how to derive an equilibrium configuration, for the matter and the electromagnetic field, on a given metric.

In the following we assume a signature $(-,+,+,+)$ for the spacetime metric. We adopt

---

[1] Real NSs are neither axisymmetric nor stationary systems. NSs constantly spin down because of magnetic braking, so that they cannot be considered as strictly stationary objects. Their magnetic field, which is only roughly axisymmetric, induces non axisymmetric deformations in the structure of the NS itself (Lasky and Melatos 2013). Moreover, in some extreme cases of rapidly rotating and/or strongly magnetized NSs, different kinds of instabilities may drive the star into an approximately triaxial configuration (see Uryū et al. 2016 and references therein for a discussion). However since the magnetic field strength inside a NS is at most $\sim 10^{16}$ G, magnetic perturbation to the equilibrium configurations can be, in principle, accurately described as (asymmetric) perturbations to a spherical/axi-symmetric star (depending on the rotational rate). In this thesis we assume that also the magnetic field is axisymmetric in order to simplify the problem.

the standard convention with Greek indices running from 0 to 3, while latin indices run from 1 to 3. Quantities are expressed in geometrized units where $c = G = M_\odot = 1$, unless otherwise stated, and all $\sqrt{4\pi}$ factors entering Maxwell's equations are absorbed in the definition of the electromagnetic field.

2.1 The 3+1 formalism

Our approach to the numerical modelization of magnetized NSs is based on the so called 3 + 1 formalism of GR (e.g. Alcubierre 2008, Baumgarte and Shapiro 2010, Gourgoulhon 2012). The major advantage provided by this approach is that it allows one to recover a more intuitive picture of the physics of gravity. Indeed, while in the fully covariant formulation of GR time and space are indistinguishable since they are treated on an equal footing, in the 3+1 formulation time regains a distinct and preferential role and the geometry of the spacetime itself is described as a continuous 'time-lapse' evolution of the geometry of three-dimensional spaces. Within this formalism the evolution of the gravitational field is formulated in the form of a initial value problem. Indeed, the first works that mark the origin of the 3+1 formalism were mainly devoted to the Cauchy problem in GR and the study of its initial conditions (Darmois 1927, Lichnerowicz 1939, Fourès-Bruhat (Choquet-Bruhat) 1952). Further improvements arose from the development of an Hamiltonian formulation of GR by Arnowitt et al. (1962) and Dirac (1958) inspired by the first attempts to unify quantum theory and gravity. Finally during the '70s the 3+1 formalism became a primary tool for the development of the nascent Numerical Relativity (York 1973, 1979, Nakamura et al. 1987). Nowadays most of the numerical codes for the evolution of Einstein's equation, or for the evolution of fluid/MHD quantities within a fixed or evolving spacetime, are built on top of the 3+1 formalism.

Considering a globally-hyperbolic spacetime endowed with a metric tensor $g_{\mu\nu}$, the basic idea at the origin of the 3+1 formulation is to provide a foliation of the space time itself. This mathematical structure is obtained defining a smooth and regular scalar field t all over the manifold. The latter is chosen so that its level surfaces slice the four-dimensional manifold into a family of spacelike three dimensional surfaces $\{\Sigma_t\}$, with time-like unit normal n^μ. By construction n^μ is colinear with the gradient of t:

$$n^\mu = -\alpha(\mathrm{d}t)^\mu, \tag{2.1}$$

where α is known as the *lapse function* and ensures the correct normalization of n^μ. Notice that n^μ defines the four-velocity of the so called *Eulerian observers*. If we promote the role of t as the global time coordinate, the lapse function measures the proper time of the Eulerian observer.

The induced three-metric that measures proper distances within each Σ_t is given by:

$$\gamma_{\mu\nu} = g_{\mu\nu} + n_\mu n_\nu. \tag{2.2}$$

Actually, $\gamma_{\mu\nu}$ defines also the projection operator onto the spatial hyper-surfaces Σ_t: in order to decompose any generic tensor field into a normal and spatial component, it is sufficient to contract its indexes with $-n^\mu$ or with $\gamma^\mu{}_\nu$. As an example the *extrinsic curvature* $K_{\mu\nu}$, which measures the curvature of Σ_t as an embedded manifold, can be defined as the spatial projection of the covariant derivative ∇ of n^μ:

$$K_{\mu\nu} := -\gamma^\rho{}_\mu \nabla_\rho n_\nu. \tag{2.3}$$

Since $n^\mu K_{\mu\nu} = n^\nu K_{\mu\nu} = 0$, the extrinsic curvature is a purely spatial tensor. A completely equivalent definition of the extrinsic curvature can be given in terms of the induced metric as:

$$K_{\mu\nu} = \mathcal{L}_{\mathbf{n}} \gamma_{\mu\nu}, \tag{2.4}$$

where $\mathcal{L}_{\mathbf{n}}$ stands for the Lie derivative[2] along the vector field n^μ.

If $x^\mu := \{t, x^i\}$ are the spacetime coordinates adapted to the foliation introduced above, the generic line element is rewritten as

$$ds^2 = -\alpha^2 dt^2 + \gamma_{ij}(dx^i + \beta^i dt)(dx^j + \beta^j dt), \tag{2.6}$$

where β^i, a purely spatial vector field, is known as *shift vector* and describes how the spatial coordinates x^i change from a slice to another. It can be also viewed as the relative velocity between the Eulerian observer and the lines of constant spatial coordinates. With this choice for the coordinates, the unit normal field has components $n^\mu = (1/\alpha, -\beta^i/\alpha)$ and $n_\mu = (-\alpha, 0)$.

As already discussed, the aim of the 3 + 1-formalism is to cast Einstein's equation in the form of a Cauchy problem. Starting from the full covariant expression of the Einstein field equation

$$G^{\mu\nu} = 8\pi T^{\mu\nu}, \tag{2.7}$$

where $G^{\mu\nu}$ is the *Einstein tensor* and $T^{\mu\nu}$ is the *stress-energy tensor*, and considering the different projections obtained contracting the previous equation with the unit normal vector and $\gamma^\mu{}_\nu$, it is possible to show that Einstein's field equation splits into an evolutionary equation for the extrinsic curvature

$$\begin{aligned}\partial_t K_{ij} = \beta^k \mathrm{D}_k K_{ij} + K_{ik} \mathrm{D}_j \beta^k + K_{jk} \mathrm{D}_i \beta^k - \mathrm{D}_i \mathrm{D}_j \alpha + \\ \alpha[R_{ij} + K K_{ij} - 2K_{ik} K^k_j] + 4\pi\alpha[\gamma_{ij}(S - E) - 2S_{ij}], \end{aligned} \tag{2.8}$$

---

[2] The Lie derivative of a generic tensor field $\mathbf{T}$ of type (k, l) with respect to the vector field $\mathbf{v}$ is defined as:

$$(\mathcal{L}_{\mathbf{v}}\mathbf{T})^{\alpha_1\ldots\alpha_k}{}_{\beta_1\ldots\beta_l} = v^\mu \partial_\mu T^{\alpha_1\ldots\alpha_k}{}_{\beta_1\ldots\beta_l} - \sum_{i=1}^{k} T^{\alpha_1\ldots\overset{i\downarrow}{\sigma}\ldots\alpha_k}{}_{\beta_1\ldots\beta_l} \partial_\sigma v^{\alpha_i} + \sum_{i=1}^{l} T^{\alpha_1\ldots\alpha_k}{}_{\beta_1\ldots\overset{i\downarrow}{\sigma}\ldots\beta_l} \partial_{\beta_i} v^\sigma, \tag{2.5}$$

where i indicates the position of the σ index to be saturated with $\partial_\sigma v^{\alpha_i}$ or $\partial_{\beta_i} v^\sigma$.

plus a set of constraints that must be satisfied at all times

$$R + K^2 - K_{ij}K^{ij} = 16\pi E, \tag{2.9}$$

$$\mathrm{D}_j(K^{ij} - K\gamma^{ij}) = 8\pi S^i, \tag{2.10}$$

that are know, respectively, as the *Hamiltonian constraint* and the *momentum constraint*. Here $\mathrm{D}_i := \gamma^{\mu}{}_i \nabla_\mu$ is the covariant derivative with respect to the 3-metric γ_{ij} (so that $\mathrm{D}_k\gamma_{ij} = 0$), R_{ij} is the Ricci tensor, again with respect to γ_{ij}, $R := R^i{}_i$ the corresponding Ricci scalar, $K := K^i{}_i$ is the trace of the extrinsic curvature. As far as the fluid sources are concerned $E := n_\mu n_\nu T^{\mu\nu}$, $S^i := -n_\mu\gamma^i{}_\nu T^{\mu\nu}$, and $S^{ij} := \gamma^i{}_\mu\gamma^j{}_\nu T^{\mu\nu}$ (of trace $S := S^i{}_i$) are, respectively, the energy density, momentum density, and the stress-energy tensor as measured by the Eulerian observers. Finally, to close the system we need also an evolutionary equation for the three metric which descends directly from the definition 2.4 of the extrinsic curvature

$$\partial_t\gamma_{ij} = -2\alpha K_{ij} + \mathrm{D}_i\beta_j + \mathrm{D}_j\beta_i. \tag{2.11}$$

The evolutionary equations Eq. 2.8 and Eq. 2.11 plus the constraints 2.9 and 2.10 are known as the ADM equations. Notice that while the tensor fields K_{ij} and γ_{ij}, are the true dynamical fields, both the lapse function α and the shift vector β^i are gauge functions and can be specified freely by choosing the foliation build on top of the manifold. Therefore it is natural that Einstein's equation does not provide any evolutionary equation for these scalar fields.

In order to find a solution to this system of equations one has to specify the initial data and then evolve the dynamical fields K_{ij} and γ_{ij} in time. However, the initial condition can not be specified arbitrarily but they must satisfy both the hamiltonian and momentum constraint. These constraints indeed select the geometry γ_{ij} of the three dimensional slice Σ_t which is compatible with the matter content of the spacetime T^{ij}. Notice, however, that for a given energy-matter content of the spacetime, such equations form a system of four differential equations in the twelve dynamical quantities γ_{ij} and K_{ij}. This implies that eight of the initial data are freely specifiable in order to solve the constraints. Nevertheless there is no natural and unique procedure to separate the dynamical fields from the constrained components. A common approach to this task lies in the conformal decomposition of the constraint equations (Lichnerowicz 1944, York 1971, 1972). The starting idea is to define an auxiliary metric $\tilde{\gamma}_{ij}$ on the slice Σ_t which is related to the induced metric through a conformal transformation

$$\gamma_{ij} = \psi^4\tilde{\gamma}_{ij} \tag{2.12}$$

where ψ is a strictly positive scalar field. It is then possible to define a Levi-Civita connection $\tilde{\mathrm{D}}$ associated with the conformal metric ($\tilde{\mathrm{D}}_k\tilde{\gamma}_{ij} = 0$), and the curvature tensor can be expressed in terms of conformal quantities. In particular the Ricci scalar appearing in the

Hamiltonian constraint is related to its conformal counterpart $\tilde{R}$ by the relation:

$$R = \frac{1}{4}\tilde{R} - \frac{8}{\psi^5}\tilde{\Delta}\psi \tag{2.13}$$

where $\tilde{\Delta}$ is the conformal Laplacian $\tilde{\Delta} := \tilde{\gamma}^{ij}\tilde{\mathrm{D}}_i\tilde{\mathrm{D}}_j$. The next step is to separate the extrinsic curvature in its trace K plus a traceless part:

$$K^{ij} = A^{ij} - \frac{1}{3}\gamma^{ij}K. \tag{2.14}$$

and finally decompose the traceless part in a transverse (divercence free) and longitudinal component:

$$A^{ij} = A^{ij}_{\mathrm{TT}} + (\mathbb{L}W)^{ij}, \tag{2.15}$$

where $\mathbb{L}$ is the *conformal Killing operator* defined as

$$(\mathbb{L}X)^{ij} := \mathrm{D}^iX^j + \mathrm{D}^jX^i - \frac{2}{3}\gamma^{ij}\,\mathrm{D}_kX^k. \tag{2.16}$$

Finally another conformal transformation is applied to the trace free part of the extrinsic curvature (Pfeiffer and York 2003, Cordero-Carrión et al. 2009):

$$A^{ij} = \psi^{\zeta-8}\left(\frac{1}{\tilde{\sigma}}(\tilde{\mathbb{L}}W)^{ij} + \tilde{A}^{ij}_{\mathrm{TT}}\right), \tag{2.17}$$

where $\tilde{\mathbb{L}}$ is expressed in term of the covariant derivative $\tilde{\mathrm{D}}_i$, ζ is a free parameter and $\tilde{\sigma}$ is a free weight function. Different choices for ζ and the weight function $\tilde{\sigma}$ lead to different reformulations of the momentum constraint but, in all cases, constraints are cast into a set of four elliptic equations for the four unknown quantities ψ and W^i, that can be solved with the appropriate boundary conditions. The other quantities such as the conformal metric $\tilde{\gamma}$, the trace K, the tensor $\tilde{A}^{ij}_{TT}$, the weight function $\tilde{\sigma}$ together with the source term E and S^i are specified as free data. Notice that, within this approach it is not possible to provide any input on the possible evolution of the spatial metric. This can be done within the Conformal Thin Sandwich (CTS) approach (York 1999). Without going into the details the main idea is to provide not only the conformal metric but also its time derivative on the initial slice Σ_t. The resulting decomposition of the extrinsic curvature is analogous to the one shown in Eq. 2.17, and can be then obtained by choosing $\zeta = -2$ and identifying $W^i = \beta^i$, $\tilde{\sigma} = 2\psi^{-6}\alpha$. Finally the transverse traceless part of the estrinsic curvature is expressed in terms of the time derivative of the conformal metric. Within this approach the momentum and Hamiltonian constraints translate into four differential equation for ψ and β^i. An extra equation for α can be obtained from the trace of Eq. 2.8 specifying also $\partial_t K$ in the initial conditions. Notice that the CTS approach seems to be particularly suitable for the construction of stationary (or quasistationary) configurations as initial data.

As soon as the solution to the constraints is provided, one can evolve in time the initial condition thus obtained. From the mathematical point of view, if the constraints are satisfied at a specific time, due to the Bianchi identities, they will be satisfied at any time. From a numerical point of view, once the equations are discretized to be solved, this is no longer true and initial small deviations and round-off errors can be amplified catastrophically during the evolution. Different computational methods have been developed and they are divided in two main classes: *free evolution schemes*, where constraints are explicitly solved only at the beginning and their violations is minimized through an appropriate reformulation of the evolution equations (Shibata and Nakamura 1995, Baumgarte and Shapiro 1999), eventually with the addition of propagating modes and damping terms (Bona et al. 2003, Bernuzzi and Hilditch 2010); *costrained schemes*, where one solves some or all the constraints at every time-step (Bonazzola et al. 2004), imposing, in some cases, also extra conditions on the metric in order to simplify the equations (Wilson and Mathews 2003, Isenberg 2008).

Since we are interested in modeling stationary equilibrium configurations for magnetized NSs we will not perform a time evolution, but we will exploit the fully constrained scheme developed by Wilson and Mathews (2003), Isenberg (2008) and extended by Cordero-Carrión et al. (2009) to obtain our models as we will discuss in Sec. 2.3.

2.1.1 The energy-momentum content of the spacetime

A standard approach in the modelization of rotating magnetized NSs, in the context of GRMHD, is to assume that the star can be described as an ideal magnetized plasma. Such approximation can be considered suitable only within ~ 100 s from the birth of the NS, when it is too hot to form a crystalline crust and allow a superfluid/superconducting phase (Chamel and Haensel 2008, Potekhin et al. 2015). Even if both the presence of the crust and superfluidity are crucial ingredients that should be taken into account in a realistic modelization of NSs, since they both affects the long term evolutionary (Arras et al. 2004, Yakovlev et al. 2008, Glampedakis et al. 2011, Viganò et al. 2013, 2015) and observational properties (Glampedakis et al. 2012b) as well as the structure of the magnetic field (Gourgouliatos et al. 2013, Palapanidis et al. 2015, Glampedakis and Lasky 2015, 2016, Gourgouliatos et al. 2016), but they are less relevant to the problem of the dynamical magneto-equilibrium in newly-born NSs, which we have investigated in this thesis.

The energy-momentum tensor can be separated in two contributions:

$$T^{\mu\nu} = T^{\mu\nu}_{\text{fluid}} + T^{\mu\nu}_{\text{EM}}. \tag{2.18}$$

The perfect fluid component can be written as

$$T^{\mu\nu}_{\text{fluid}} = \rho h u^{\mu} u^{\nu} + p g^{\mu\nu}, \tag{2.19}$$

where ρ is the mass density, $h := (e + p)/\rho$ is the specific enthalpy with the energy density e and the pressure $p = p(\rho, e)$ (provided by some form of the EoS), as measured by the comoving observer with four-velocity given by u^μ; the electromagnetic part instead reads

$$T^{\mu\nu}_{\text{EM}} = F^{\mu}{}_{\lambda}F^{\nu\lambda} - \frac{1}{4}(F^{\lambda\kappa}F_{\lambda\kappa})g^{\mu\nu}, \tag{2.20}$$

where the antisymmetric tensor $F^{\mu\nu}$, the *Faraday tensor*, encodes all the information about the electromagnetic field. In particular $F^{\mu\nu}$ can be decomposed, with respect to the comoving observer, into an electric component, parallel to u^μ, and a magnetic component, orthogonal to u^μ. In particular, if e^μ and b^μ are the electric field and the magnetic field experienced by the comoving observer then

$$F_{\mu\nu} = u_{[\mu}e_{\nu]} + \epsilon_{\mu\nu\alpha\beta}u^\alpha b^\beta, \tag{2.21}$$

where $\epsilon_{\mu\nu\alpha\beta}$ is the Levi-Civita tensor (related to the Levi-Civita alternating symbol $\varepsilon_{\mu\nu\alpha\beta}$ through the relations $\epsilon_{\mu\nu\alpha\beta} = \sqrt{-g}\varepsilon_{\mu\nu\alpha\beta}$) and the square brackets denote antisymmetrization over the enclosed indices (i.e. $u_{[\mu}e_{\nu]} = u_\mu e_\nu - e_\mu u_\nu$).

The equations of motion regulating the behaviors of the fluid and the magnetic field are given by the baryon number conservation:

$$\nabla_\mu(\rho u^\mu) = 0, \tag{2.22}$$

the local covariant conservation of the energy momentum

$$\nabla_\mu T^{\mu\nu} = 0, \tag{2.23}$$

and the homogeneus Maxwell's equations

$$\nabla_\mu\ {}^*F^{\mu\nu} = 0, \tag{2.24}$$

where the $*$ operator is the standard Hodge dual such that ${}^*F^{\mu\nu} = \epsilon^{\mu\nu\alpha\beta}F_{\alpha\beta}$. The system is then closed by the relativistic *Ohm's Law* for a perfectly conducting plasma, which corresponds to the condition of a vanishing comoving electric field (for more general forms of Ohm's law see Bucciantini and Del Zanna 2013)

$$e^\mu := u_\nu F^{\mu\nu} = 0. \tag{2.25}$$

The Ohm's Law substantially replaces the inhomogeneous Maxwell's equation

$$\nabla_\mu F^{\mu\nu} = -j^\nu, \tag{2.26}$$

where j^μ is the four-current density[3]. Just as in the Newtonian MHD, the four current can be considered a derived quantity.

---

[3] In the general formulation of Maxwell's equations in material medium , such as in superfluid-superconducting NS plasma (Glampedakis et al. 2011, Gusakov and Dommes 2016), the electromagnetic field is described using an additional antisymmetric tensor, the so called excitation tensor $H_{\mu\nu}$ which is related to the electric displacement d^μ and the magnetic field h^μ (the magnetic field denoted with b^μ introduced in the main

As far as concerns Eq. 2.23 notice that this is true for the total $T^{\mu\nu}$: since the fluid and the electromagnetic field can in principle exchange energy and momentum the divergence of $T^{\mu\nu}_{\rm fluid}$ or $T^{\mu\nu}_{\rm EM}$ separately does not vanishes. In particular since $\nabla_\mu T^{\mu\nu}_{\rm EM} = -F^{\mu\nu} j_\mu$, Eq. 2.23 can be written as

$$\nabla_\mu T^{\mu\nu}_{\rm fluid} = F^{\mu\nu} j_\mu := L^\nu \tag{2.31}$$

where L^μ is the Lorentz force. Now, considering that $u_\mu L^\mu = 0$ because of the ideal MHD condition (Eq. 2.25) and using the continuity equation, Eq. 2.22, the orthogonal projection of the previous equation with respect to u^μ provides the GR expression of the *Euler equation*

$$\rho h a_\mu + u_\mu u^\nu \partial_\nu p + \partial_\mu p = L_\mu \tag{2.32}$$

where we have introduced the four-acceleration field $a^\mu = u^\nu \nabla_\nu u^\mu$.

In the context of the 3+1 formalism, we have to decompose all quantities in their spatial and temporal component. In the case of the electric and magnetic field, in analogy with the definition of e^μ and b^μ, the electric and magnetic field seen by the Eulerian observer are simply given by

$$E^\mu = F^{\mu\nu} n_\nu \quad \text{and} \qquad B^\mu = {}^*F^{\mu\nu} n_\nu, \tag{2.33}$$

where both E_μ and B_ν are purely spatial four-vector since $n^\mu E_\mu = n^\mu B_\mu = 0$. Substituting this expression in Eqs. 2.24 and 2.26 , after few calculations one obtains the 3+1 splitting of the Maxwell's equations (Thorne and MacDonald 1982, Baumgarte and Shapiro 2003, Gourgoulhon 2012):

$$\mathrm{D}_i B^i = 0 \tag{2.34}$$

$$\partial_t B^i = -\epsilon^{ijk}\, \mathrm{D}_j(\alpha E_k) + \alpha K B^i + \mathcal{L}_\beta B^i \tag{2.35}$$

$$\mathrm{D}_i E^i = \rho_e \tag{2.36}$$

---

body of the text is actually the induced magnetic field) with:

$$H_{\mu\nu} = u_{[\mu} d_{\nu]} + \epsilon_{\mu\nu\lambda\sigma} u^\lambda h^\sigma. \tag{2.27}$$

The Maxwell's equations are now written as

$$\nabla_{[\lambda} F_{\mu\nu]} = 0 \quad \text{and} \quad \nabla_{[\lambda} H_{\mu\nu]} = I_{\lambda\mu\nu}, \tag{2.28}$$

where $I_{\lambda\mu\nu}$ is the free charge-current density tensor. The two tensor $F_{\mu\nu}$ and $H_{\mu\nu}$ are not independent but they are linked through the *constitutive relation*

$$F_{\mu\nu} = \kappa_{\mu\nu}{}^{\alpha\beta} H_{\alpha\beta} \tag{2.29}$$

where $\kappa^{\mu\nu\alpha\beta}$ is the so called *constitutive tensor* that encodes the electric and magnetic properties of the medium, such as the magnetic and electric susceptibilities, the polarization and magnetization vector. However, in a vacuum spacetime or in the case of ideal plasma, with zero electric and magnetic susceptibilities, the constitutive tensor is exclusively related to the metric through

$$\kappa_{\alpha\beta}{}^{\mu\nu} = \frac{1}{2}\sqrt{-g}\,\varepsilon_{\alpha\beta\lambda\sigma}(g^{\lambda\mu} g^{\sigma\nu} - g^{\lambda\nu} g^{\sigma\mu}) \tag{2.30}$$

where $\varepsilon_{\alpha\beta\lambda\sigma}$ is the Levi-Civita symbol. Hence the constitutive tensor reduces to the standard Hodge dual so that $H_{\mu\nu} = {}^*F_{\mu\nu}$ and we recover the formulation given in Eqs. 2.24 and 2.26.

$$\partial_t E^i = \epsilon^{ijk}\,\mathrm{D}_j(\alpha B_k) + \alpha K E^i + \mathcal{L}_\beta E^i - \alpha J^i \tag{2.37}$$

where again D_i is the covariant derivative associated with the induced metric and ϵ^{ijk} is the alternating tensor in three dimensions (related to the four-dimensional Levi-Civita tensor by $\epsilon_{ijk} = n^0\epsilon_{0ijk}$). Finally $\rho_\mathrm{e} = n^\mu j_\mu$ is the charge density and $J^i = \gamma^i_{\ \mu} j^\mu$ is the current vector.

Regarding the fluid quantities the components of the four-velocity u^μ can be written in terms of the Lorentz factor Γ and the three velocity v^i of the fluid relative to the Eulerian observer through

$$u^\mu = \frac{\Gamma}{\alpha}(1, \alpha v^i - \beta^i). \tag{2.38}$$

From the normalization $u_\mu u^\mu = -1$ it follows $\Gamma = (1 - v_i v^i)^{-1/2}$ which justifies its identification with the Lorentz factor. Notice also that the three velocity v^i is related to the coordinate velocity u^i/u^t by the relation $v^i = \alpha^{-1}(u^i/u^t + \beta^i)$. With this choice for the four-velocity decomposition, the 3+1 counterpart of the MHD condition in Eq. 2.25 takes the familiar form

$$E_i = -\epsilon_{ijk} v^j B^k. \tag{2.39}$$

Here, we post-pone the discussion of the 3+1 decomposition of the Euler equation to Sec. 2.5 when we will exploit the spacetime symmetries assumed for our equilibrium models.

We conclude this section providing explicitly the source terms of Eistein's equation, Eqs. 2.8-2.10,

$$E := n_\mu n_\nu T^{\mu\nu} = (e+p)\Gamma^2 - p + \tfrac{1}{2}(E^i E_i + B^i B_i), \tag{2.40}$$

$$S^i := -n_\mu \gamma^i_\nu T^{\mu\nu} = (e+p)\Gamma^2 v^i + \epsilon^{ijk} E_j B_k, \tag{2.41}$$

$$S^{ij} := \gamma^i_\mu \gamma^j_\nu T^{\mu\nu} = (e+p)\Gamma^2 v^i v^j - E^i E^j - B^i B^j + [p + \tfrac{1}{2}(E^i E_i + B^i B_i)]\gamma^{ij}. \tag{2.42}$$

2.2 Choice for the metric

Our equilibrium models for magnetized NSs are based on the assumption that the matter distribution and the magnetic field content of the spacetime is *stationary* and *axisymmetric*. As a consequence, also the spacetime itself must retain the same symmetries. These imply the existence of two *Killing vectors*: a timelike Killing vector $\boldsymbol{\xi}$ associated with the time invariance of the system, and a spacelike Killing vector $\boldsymbol{\chi}$ which is instead associated with the rotational invariance (Carter 1970, 1973). At this point, it seems natural to adopt a coordinate system adapted with the spacetime symmetries. In particular, considering spherical-like coordinates $[t, r, \theta, \phi]$ the two Killing vector are promoted to the role of coordinate fields, i.e. $\boldsymbol{\xi} = \boldsymbol{\partial}_t$ and $\boldsymbol{\chi} = \boldsymbol{\partial}_\phi$. With this choice all the quantities defined on the spacetime manifold depend only on (r, θ), while (t, ϕ) are ignorable variables.

In a stationary and axisymmetric spacetime the timelike surfaces $\mathcal{S}$, parametrized as $r = \mathrm{cost}, \theta = \mathrm{cost}$ are known as *surfaces of transitivity*. At every point of $\mathcal{S}$ its tangent space Π is spanned by the two Killing vector, so that $\Pi := \mathrm{Vect}(\boldsymbol{\xi}, \boldsymbol{\chi})$. Any vector $\mathbf{V}$ is said to be *toroidal* if $\mathbf{V} \in \Pi \Rightarrow V^\mu = c_t \xi^\mu + c_\phi \chi^\mu$ (with $c_\phi \neq 0$), and *poloidal* (or *meridional*) if it lies in the spacelike 2-plane perpendicular to Π. Additional properties are valid for the subset of *circular* spacetimes, for which the coordinates (r, θ) span the two-surfaces orthogonal to Π, leading to the simplification $g_{tr} = g_{t\theta} = g_{r\phi} = g_{\theta\phi} = 0$. This type of metric is generated by configurations of matter-energy for which the momentum-energy tensor $T^{\mu\nu}$ is also circular, and this happens when

$$\xi_\mu T^{\mu[\nu}\xi^\kappa\chi^{\lambda]} = 0, \quad \chi_\mu T^{\mu[\nu}\xi^\kappa\chi^{\lambda]} = 0. \tag{2.43}$$

Consider now the case of rotating, magnetized compact objects to be described as equilibrium solutions of the GRMHD system. The stress-energy tensor reads

$$T^{\mu\nu} = (e + p + b^2)u^\mu u^\nu - b^\mu b^\nu + (p + \tfrac{1}{2}b^2)g^{\mu\nu}, \tag{2.44}$$

where we have used the MHD condition (Eq.2.25). With this form of the momentum-energy tensor, the circularity condition holds provided the 4-velocity is toroidal, that is $\mathbf{u} \in \Pi \Rightarrow u^\mu := u^t(\xi^\mu + \Omega\chi^\mu)$, due to $\xi_\mu u^\mu \neq 0$, where $\Omega := u^\phi/u^t = d\phi/dt$ is the fluid angular momentum as measured by an observer at rest at spatial infinity. If one looks for magnetic configurations independent of the flow structure, in the limit of ideal MHD, circularity requires that the comoving magnetic field must be either purely toroidal, $b^\mu \in \Pi$, with $b_\mu u^\mu = 0 \Rightarrow b_t = -\Omega b_\phi$, or purely poloidal, that is $b^\mu\xi_\mu = b^\mu\chi_\mu = 0$. In the latter case, stationarity requires solid body rotation $u^\phi/u^t = \text{const}$ (Oron 2002), or Ω must be a constant on *magnetic surfaces* (Gourgoulhon et al. 2011), as we will discuss in Sect. 2.5. For mixed magnetic fields configurations the circularity of the spacetime does not hold.

In the case of circular spacetimes and spherical-like coordinates, the line element can be further simplified to:

$$\mathrm{d}s^2 = -\alpha^2\mathrm{d}t^2 + \gamma_{ij}\mathrm{d}x^i\mathrm{d}x^j + R^2(\mathrm{d}\phi - \omega\mathrm{d}t)^2, \tag{2.45}$$

where $R = \sqrt{\gamma_{\phi\phi}}$ is knows as *quasi-isotropic radius*, $\omega = -\beta^\phi$ is the *frame dragging potential*, and the *poloidal* two-metric with $(i, j = r, \theta)$ can always be orthogonalized introducing a *conformal factor* ψ, so that $\gamma_{r\theta} = 0$, $\gamma_{rr} = \psi^4$, $\gamma_{\theta\theta} = r^2\psi^4$. The determinant of the three-metric is then $\sqrt{\gamma} = Rr\psi^4$. Models of stationary and axisymmetric equilibria of rotating NSs are generally built on top of this metric (e.g. Gourgoulhon 2010), even in the magnetized case (Bocquet et al. 1995, Kiuchi and Yoshida 2008, Frieben and Rezzolla 2012) for either purely poloidal or purely toroidal fields. However, in the mixed field case, even if the above form of the metric is no longer appropriate, sensible deviations from circularity are expected to arise only for unrealistically large values of the magnetic field of $\sim 10^{19}$ G (Oron 2002). Moreover, it has been verified (Shibata and Sekiguchi 2005, Dimmelmeier et al. 2006, Ott et al. 2007, Bucciantini and Del Zanna 2011), that even for highly deformed star, up to the *mass shedding limit*, the difference between R and $\psi^2 r\sin\theta$ is at most of the order of 10^{-3} (see also Appx. A for a discussion), and the metric can be further simplified to

$$ds^2 = -\alpha^2dt^2 + \psi^4[dr^2 + r^2d\theta^2 + r^2\sin^2\theta\,(d\phi - \omega dt)^2]. \tag{2.46}$$

with the volume element of the three-metric given by $\sqrt{\gamma} = \psi^6 r^2 \sin\theta$. Under this latter assumption, the spatial three-metric is *conformally flat*, and the spherical coordinates can be identified with the canonical *isotropic coordinates*. This form is particularly suitable to be solved numerically, as it is described in the following section.

2.3 Solving Einstein's equation

The assumption of conformal flatness implies that the induced metric is related to the flat Remannian three-metric f_{ij} by a conformal transformation

$$\gamma_{ij} = \psi^4 f_{ij}. \tag{2.47}$$

where the conformal factor satisfies $\psi = (\gamma/f)^{1/12}$, with $f := \det f_{ij}$. This assumption was initially adopted by Isenberg (2008) and Wilson and Mathews (1989) in order to provide a waveless approximation to general relativity, which is now known as the IWM approximation or as the *Conformally Flat Condition* (CFC). With this choice the covariant derivative associated to the flat three-metric f_{ij} is the standard *nabla* operator in flat spacetime $\tilde{\mathrm{D}}_i = \nabla_i$, while the scalar curvature (see Eq. 2.13) simply reduces to

$$R = -8\psi^{-5}\Delta\psi, \tag{2.48}$$

in which $\Delta := \nabla_i \nabla^i$ is the usual Laplacian of flat space. A second assumption made in the context of the CFC is to demand maximal slicing

$$K = 0. \tag{2.49}$$

Notice that while this last requirement can always be satisfied by selecting a maximal slicing for the foliation, Eq. 2.47 is exact only in the case of a spherical symmetric spacetime (Gourgoulhon 2012). In the other cases the requirements in Eq. 2.47 represent an approximation of the correct metric.

The conformal decomposition adopted in the CFC approximation can be obtained from Eq. 2.17 by a CTS-like decomposition with $\zeta = 4$, $\sigma = 2\alpha$ and $A^{ij}_{\mathrm{TT}} = 0$ so that the extrinsic curvature is

$$K^{ij} = \psi^{-4}\tilde{A}^{ij} \quad \text{with} \quad \tilde{A}^{ij} = \frac{1}{2\alpha}(\mathbb{L}\beta)^{ij}, \tag{2.50}$$

where the conformal operator $\mathbb{L}$ is now associated to the flat metric. Notice that in the CTS approach the transverse traceless component A^{ij}_{TT} can be expressed in terms of the time derivative of the conformal metric.

The final set of CFC elliptic equations may be written in terms of the sources and of $\tilde{A}^{ij}$ (containing α and first derivatives of β^i) as

$$\Delta\psi = -[2\pi E + \tfrac{1}{8} f_{ik} f_{jl} \tilde{A}^{ij}\tilde{A}^{kl}]\,\psi^5, \tag{2.51}$$

$$\Delta(\alpha\psi) = [2\pi(E + 2S) + \tfrac{7}{8} f_{ik} f_{jl} \tilde{A}^{ij} \tilde{A}^{kl}]\, \alpha\psi^5, \tag{2.52}$$

$$\Delta_L \beta^i = 16\pi\alpha\psi^4 S^i + 2\psi^6 \tilde{A}^{ij}\, \nabla_j(\alpha\psi^{-6}), \tag{2.53}$$

where

$$\Delta_L \beta^i := \nabla_j (L\beta)^{ij} = \Delta\beta^i + \tfrac{1}{3}\, \nabla^i(\nabla_j \beta^j), \tag{2.54}$$

is the so-called *conformal vector Laplacian* operator, associated to the flat 3-metric f_{ij} and applied to β^i.

The CFC approximation has been often used to study gravitational collapses (Dimmelmeier et al. 2002a,b, Cerdá-Durán et al. 2005), quasi-equilibrium configurations of binary NSs (Baumgarte et al. 1997, 1998, Bonazzola et al. 1999, Oechslin et al. 2004), or to investigate the stability and evolution of NSs (Saijo 2004, Cerdá-Durán et al. 2008, Abdikamalov et al. 2009)[4]. However in some highly relativistic situations, the CFC system may suffer of non-uniqueness issues that prevent numerical codes to converge (Cordero-Carrión et al. 2009). This problem has been however solved in Cordero-Carrión et al. (2009), considering a slightly different approach named XCFC (eXtended CFC), which is in turn based on a different choice for the extrinsic curvature decomposition. In particular one requires a *conformal transverse traceless* (CTT) decomposition with $\zeta = -2$ and $\sigma = 1$, resulting in

$$K^{ij} = \psi^{-10} \hat{A}^{ij}, \quad \text{with} \quad \hat{A}^{ij} := (\mathbb{L}W)^{ij} + \hat{A}^{ij}_{TT}. \tag{2.57}$$

Consistency between the CTS and CTT decompositions (notice that $\hat{A}^{ij} = \psi^6 \tilde{A}^{ij}$) requires a non-vanishing $\hat{A}^{ij}_{TT}$. However it has been demonstrated (Cordero-Carrión et al. 2009) that this quantity is even smaller than the non-conformally flat part of the spatial metric within the CFC approach, and hence it can be safely neglected on the level of the CFC approximation. Thus we set, as an additional hypothesis

$$\hat{A}^{ij}_{TT} = 0 \Rightarrow \hat{A}^{ij} = (\mathbb{L}W)^{ij}, \tag{2.58}$$

so that $\hat{A}^{ij}$ is defined in terms of the auxiliary vector W^i alone. The latter is derived from the momentum constraint that becomes

$$\nabla_j \hat{A}^{ij} = \Delta_L W^i = 8\pi\, \psi^{10} S^i, \tag{2.59}$$

---

[4] In the main body of this section we have derived the conformal rescaling given in Eq. 2.50 starting from CTS. Nevertheless, CFC is actually a fully constrained approach to GR. The same scaling, indeed, can be obtained noticing that under the assumption of $K = 0$ the trace of Eq. (2.11) and its traceless part respectively become

$$\partial_t \ln \gamma^{1/2} \equiv \partial_t \ln \psi^{1/6} = \mathrm{D}_i \beta^i, \tag{2.55}$$

$$2\alpha K_{ij} = \mathrm{D}_i \beta_j + \mathrm{D}_j \beta_i - \tfrac{2}{3}(\mathrm{D}_k \beta^k) \gamma_{ij} = (\mathbb{L}\beta)^{ij}. \tag{2.56}$$

where $\partial_t \gamma = 0$ if, and only if, $\mathrm{D}_i \beta^i = 0$, and the extrinsic curvature can be expressed in terms of derivatives of the shift vector alone. Then, adopting a *time-evolution rescaling* of the extrinsic curvature $K^{ij} = \psi^{-4} \tilde{A}^{ij}$, the conformal Killing operator associated with the initial metric γ_{ij} coincides with the one associated with the flat metric.

to be added to the other CFC equations.

The final *augmented* set of CFC elliptic equations, also known as XCFC equations, is then the following (Cordero-Carrión et al. 2009)

$$\Delta_L W^i = 8\pi f^{ij}\hat{S}_j, \tag{2.60}$$

$$\Delta\psi = -2\pi\hat{E}\,\psi^{-1} - \tfrac{1}{8}f_{ik}f_{jl}\hat{A}^{kl}\hat{A}^{ij}\,\psi^{-7}, \tag{2.61}$$

$$\Delta(\alpha\psi) = [2\pi(\hat{E}+2\hat{S})\,\psi^{-2} + \tfrac{7}{8}f_{ik}f_{jl}\hat{A}^{kl}\hat{A}^{ij}\,\psi^{-8}]\,\alpha\psi, \tag{2.62}$$

$$\Delta_L\beta^i = 16\pi\,\alpha\psi^{-6}f^{ij}\hat{S}_j + 2\hat{A}^{ij}\,\nabla_j(\alpha\psi^{-6}), \tag{2.63}$$

where for convenience we have introduced rescaled fluid source terms of the form

$$\hat{S}_j := \psi^6 S_j, \quad \hat{E} := \psi^6 E, \quad \hat{S} := \psi^6 S, \tag{2.64}$$

and we remind that

$$\hat{A}^{ij} = \nabla^i W^j + \nabla^j W^i - \tfrac{2}{3}(\nabla_k W^k)f^{ij}. \tag{2.65}$$

Notice that while in CFC all the equations were strongly coupled, here the equations can be solved hierarchically one by one, in the given order, since each right hand side just contains known functions or the variable itself and of previously computed quantities. Moreover, the mathematical structure of the Poisson-like equations for ψ and α guarantees the *local uniqueness* of the solution. Indeed, it can be demonstrated that for a differential equation of the form

$$\Delta u = s u^q \tag{2.66}$$

where s is the source term and q provides the exponent of non-linearity, only the condition $sq \geq 0$, which is verified by both Eqs. 2.61 and 2.62, ensures that the solution u is locally unique.

Even if the XCFC formulation, just as the CFC, represents an approximation to ‘exact’ GR, it is possible to show that the solutions obtained for both rotating and/or magnetized NSs are compatible with that obtained in full GR. Differences, indeed, are of the order of 0.1% (see Appx. A). Given the great simplification of the equations involved, the XCFC equations are at the base of the XNS metric solver (Bucciantini and Del Zanna 2011), which provides equilibrium models for axisymmetric NSs. Notice that in the case of static NSs, one has to solve only the equation for α and ψ, being $\beta^i = 0$. In the case of purely rotational flows ($\beta^r = \beta^\theta = 0$), one has to solve only the azimuthal components of Eqs. 2.60-2.63.

2.4 Electromagnetic Fields

In the hypothesis of conformal flatness or circular spacetime the stationary Maxwell’s equations, Eqs. 2.34-2.37, can be written in a compact form, using standard 3-dimensional vector quantities and the related divergence and curl operators defined with respect to the 3-metric γ_{ij}, as

$$\mathbf{D}\cdot\mathbf{B} = 0, \tag{2.67}$$

$$\mathbf{D}\times(\alpha\mathbf{E}) + (\mathbf{B}\cdot\mathbf{D})\boldsymbol{\beta} = 0, \tag{2.68}$$

$$\mathbf{D}\cdot\mathbf{E} = \rho_e, \tag{2.69}$$

$$\mathbf{D}\times(\alpha\mathbf{B}) - (\mathbf{E}\cdot\mathbf{D})\boldsymbol{\beta} = \alpha\mathbf{J}, \tag{2.70}$$

where we have used the notation $(\mathbf{D}\times\mathbf{V})^i = \epsilon^{ijk}\,\mathrm{D}_j V_i$ for the curl operator.

Eq. 2.67 implies that the magnetic field can be written as the curl of a vector potential $\mathbf{A}$ such that $B^i = \epsilon^{ijk}\partial_j(A_k)$. This, together with the assumption of axisymmetry, $\partial_\phi = 0$, implies that the poloidal (r,θ) components of the magnetic field can be expressed in terms of the gradient of a scalar function $\Psi(r,\theta) \equiv A_\phi$, called *magnetic flux function*. Analogously the ϕ-component of the magnetic field can be written using another scalar function $\mathcal{I}$, such that $B_\phi = \alpha^{-1}\mathcal{I}$ for later convenience, known as the *current function*. By introducing the orthonormal triad $\mathbf{e}_{\hat{i}} = \boldsymbol{\partial}_i/\sqrt{\gamma_{ii}}$, with $\mathbf{e}_{\hat{i}}\times\mathbf{e}_{\hat{j}} = \varepsilon_{\hat{i}\hat{j}\hat{k}}\mathbf{e}_{\hat{k}}$, the magnetic vector field can be expressed as

$$\mathbf{B} = \frac{\mathbf{D}\Psi}{R}\times\mathbf{e}_{\hat{\phi}} + \frac{\mathcal{I}}{\alpha R}\mathbf{e}_{\hat{\phi}}. \tag{2.71}$$

where $R := \sqrt{\gamma_{\phi\phi}} = \psi^2 r\sin\theta$ and $\mathbf{D}\Psi$ is the vector field associated with the gradient of Ψ, with components given by $(\mathbf{D}\Psi)^{\hat{i}} = \partial_i\Psi/\sqrt{\gamma_{ii}}$. The isosurfaces $\Psi(r,\theta) = cost$, are known as *magnetic surfaces*, and they contain the magnetic poloidal field-lines. Moreover any scalar function f satisfying $\mathbf{B}\cdot\mathbf{D}f = 0$ will be constant on them: $f = f(\Psi)$. It is possible to show, starting from Eq. 2.70, that the poloidal component of the 3-current is related to the curl of the azimuthal magnetic field, $\alpha J^i = \varepsilon^{ij\phi}\partial_j(\alpha B_\phi)$, such that

$$\mathbf{J} = \frac{\mathbf{D}\mathcal{I}}{\alpha R}\times\mathbf{e}_{\hat{\phi}} + J_{\hat{\phi}}\mathbf{e}_{\hat{\phi}}, \tag{2.72}$$

where the toroidal component is given by

$$\frac{\alpha}{R}J_{\hat{\phi}} = -\mathbf{D}\cdot\left(\frac{\alpha}{R^2}\mathbf{D}\Psi\right) + \mathbf{E}\cdot\mathbf{D}\omega. \tag{2.73}$$

From the other sourceless Maxwell's equation, Eq. 2.68, under the same constraints of stationarity, axisymmetry and circularity/conformal-flatness, one finds $\alpha E_\phi = 0$. By noticing that with our assumptions $(\mathbf{B}\cdot\mathbf{D})\boldsymbol{\beta} = -\mathbf{D}\times(\boldsymbol{\beta}\times\mathbf{B})$, the same equation implies that the poloidal components of the electric field are related to the gradient of a new scalar function $\Phi \equiv A_t$ as:

$$\alpha\mathbf{E} + \boldsymbol{\beta}\times\mathbf{B} = \alpha\mathbf{E} - \omega\,\mathbf{D}\Psi = \mathbf{D}\Phi. \tag{2.74}$$

Specializing our choice to a conformally flat metric, in Eq. 2.46, $R = \psi^2 r\sin\theta$ and the components of the magnetic field in local coordinate read:

$$B^r = \frac{\partial_\theta \Psi}{\sqrt{\gamma}}, \quad B^\theta = -\frac{\partial_r \Psi}{\sqrt{\gamma}}, \quad B^\phi = \frac{\mathcal{I}}{\alpha \psi^4 r^2 \sin\theta}; \tag{2.75}$$

instead the components of the electric field are given by:

$$E^r = \frac{1}{\alpha\psi^4}(\partial_r \Phi + \omega \partial_r \Psi), \quad E^\theta = \frac{1}{\alpha r^2 \psi^4}(\partial_\theta \Phi + \omega \partial_\theta \Psi), \quad E^\phi = 0. \tag{2.76}$$

Finally the Maxwell-Gauss equation, Eq. 2.69, can be written as an elliptical PDE for the electromagnetic potentials Φ and Ψ, as a function of the charge and current density.

$$\begin{aligned}\Delta\Phi \;=\; & \psi^4\left[\alpha\rho_e + \omega\psi^4 r^2 \sin^2\theta J^\phi\right] - \frac{\omega\psi^4 r^2 \sin^2\theta}{\alpha^2}\partial\omega\partial\Phi \\ & \left[1 + \frac{\omega^2\psi^4 r^2\sin^2\theta}{\alpha^2}\right]\partial\omega\partial\Psi - \partial\ln(\alpha^{-1}\psi^2)\left[\partial\Phi + 2\omega\partial\Psi\right] - \\ & \frac{2\omega}{r}\left[\partial_r\Psi + \frac{1}{r\tan\theta}\partial_\theta\Psi\right].\end{aligned} \tag{2.77}$$

The same can be done for the Maxwell-Ampère equation Eq. 2.70:

$$\tilde{\Delta}_3\tilde{\Psi} = \psi^4 r\sin\theta\left(\frac{\partial\omega\partial\Phi + \omega\partial\omega\partial\Psi}{\alpha^2} - \psi^4 J^\phi\right) + \partial\ln(\alpha^{-1}\psi^2)\partial\Psi, \tag{2.78}$$

where, for convenience, we have introduced the quantity $\tilde{\Psi} := \Psi/(r\sin\theta)$. The new operators are defined as:

$$\partial f \partial g := \partial_r f \partial_r g + \frac{1}{r^2}\partial_\theta f \partial_\theta g, \tag{2.79}$$

$$\tilde{\Delta}_3 := \Delta - \frac{1}{r^2\sin^2\theta}. \tag{2.80}$$

These equations completely define the electromagnetic field in the entire space, once the charge and current distribution are known, independently of the fluid properties.

2.5 Matter

Let us discuss here the equilibrium condition for the matter distribution under the simultaneous action of gravity and electromagnetic field. Assuming purely rotational flow, the three-dimensional velocity is given by

$$\mathbf{v} = \frac{\Omega - \omega}{\alpha} R \mathbf{e}_{\hat{\phi}}, \tag{2.81}$$

where $\Omega := u^\phi/u^t$ is the angular velocity of the fluid as seen by an observer at rest at spatial infinity. Here we will consider for simplicity rigid rotation so that $\Omega = \text{cost}$.

As discussed in Sec. 2.1.1 the dynamics of matter is described by the Euler Eq. 2.32.

Recalling that $u^i = 0$, $(i = r, \theta)$ and $\partial_t = \partial_\phi = 0$, so that $u^\nu \partial_\nu = 0$, the four-acceleration reduces to

$$a_\mu = -\tfrac{1}{2} u^\nu u^\lambda \partial_\mu g_{\nu\lambda}, \tag{2.82}$$

and its spatial projection in the 3 + 1 formulation is

$$a_i = \frac{\Gamma^2}{2\alpha^2}[\partial_i(\alpha^2 - R^2\omega^2) + 2\Omega\partial_i(R^2\omega) - \Omega^2\partial_i R^2]. \tag{2.83}$$

Recalling the definition of $\mathbf{v}$ in Eq. 2.81, and given the relation $v^2\Gamma^2\partial_i \ln v = \partial_i \ln\Gamma$, one finally gets:

$$\frac{\partial_i p}{\rho h} + \partial_i \ln\alpha - \partial_i \ln\Gamma = \frac{L_i}{\rho h}. \tag{2.84}$$

Notice that axisymmetry implies necessarily $L_\phi = 0$.

In order cast this equation into an integrable form, suitable for numerical solutions, two assumptions are required:

- a barotropic EoS $p = p(\rho)$, as in the case of a polytropic law

  $$p = K_{\rm a}\rho^{1+1/n} \Rightarrow h = 1 + (n+1)K_{\rm a}\rho^{1/n}, \tag{2.85}$$

  where $K_{\rm a}$ is the *polytropic constant*, n is the *polytropic index*, such that $\partial_i p/(\rho h) = \partial_i \ln h$;

- an external conservative force with potential $\mathcal{M}$

  $$\mathbf{L} = \rho h \mathbf{D}\mathcal{M}. \tag{2.86}$$

The first one is usually justified by the fact that matter in neutron stars can be considered fully degenerate (zero temperature). The second one, on the other hand, restricts the possible choices of current distribution (see e.g. Akgün et al. 2013 for examples where this constrain is relaxed), but is the only one that permits to compute equilibria in the fully non perturbative regime.

Under those two assumptions one can integrate Euler's equation to derive the so called *Bernoulli integral*

$$\ln\frac{h}{h_c} + \ln\frac{\alpha}{\alpha_c} - \ln\frac{\Gamma}{\Gamma_c} - = \mathcal{M} - \mathcal{M}_c, \tag{2.87}$$

where we have indicated with the label c a reference position, for instance the center of the NS.

Inside the star the ideal MHD condition guarantees that the electric field is always orthogonal to the magnetic field, i.e. $\mathbf{E}\cdot\mathbf{B} = 0$, so that $\mathbf{B}\cdot\mathbf{D}\Phi = 0$ and the electric potential can be expressed as a function of the magnetic potential, $\Phi = \Phi(\Psi)$. In particular the ideal MHD condition provides the following relation between the two potentials (see e.g. Gourgoulhon et al. 2011)

$$\mathbf{D}\Phi = -\Omega\,\mathbf{D}\Psi, \tag{2.88}$$

that in the case of rigid rotation can be easily integrated in

$$\Phi = -\Omega\Psi + C \tag{2.89}$$

where C is an integration constant, that can be shown to correspond to an arbitrary net charge. The other possible integrability condition for equation Eq. 2.88 is $\Psi = \Psi(\Omega)$; however, as pointed out by Bonazzola et al. (1993), this latter condition can not be fulfilled in general since Ψ has to solve also the stationary Maxwell-Ampère equation, Eq. 2.78. Indeed, as anticipated in Sec. 2.2, the strict requirement arising from stationarity is that the rotational rate should be constant on the magnetic surfaces. For example the simplest prescription of *constant specific angular momentum* leads to a rotation largely stratified on cylinders, known as *von Zeipel cylinders* (von Zeipel 1924), while the simplest prescriptions for the current distribution typically used in NS modelization (Lander and Jones 2009, Ciolfi et al. 2009) lead to dipole-like magnetic surfaces.

From Eq. 2.39, one can then express the electric field and the associated charge density in terms of the magnetic flux function

$$\mathbf{E} = -\frac{\Omega-\omega}{\alpha}\mathbf{D}\Psi, \tag{2.90}$$

$$\rho_e = -\mathbf{D}\cdot\left(\frac{\Omega-\omega}{\alpha}\mathbf{D}\Psi\right). \tag{2.91}$$

Using these results, the Lorentz force per unit volume acting on the plasma is

$$\mathbf{L} = \rho_e\mathbf{E} + \mathbf{J}\times\mathbf{B} = (\mathbf{J} - \rho_e\mathbf{v})\times\mathbf{B}, \tag{2.92}$$

which, using also Eq. 2.71 and Eq. 2.72, becomes:

$$\mathbf{L} = \left(\frac{J_{\hat\phi}}{R} - \rho_e\frac{\Omega-\omega}{\alpha}\right)\mathbf{D}\Psi - \frac{\mathcal{I}\,\mathbf{D}\mathcal{I}}{\alpha^2R^2} + \frac{\mathbf{D}\mathcal{I}\times\mathbf{D}\Psi\cdot\mathbf{e}_{\hat\phi}}{\alpha R^2}\mathbf{e}_{\hat\phi}. \tag{2.93}$$

As required by axisymmetry the aximuthal component of the Lorentz force must vanish. This corresponds to require that $\mathcal{I} = \mathcal{I}(\Psi)$, and we can write

$$\mathbf{L} = \left(\frac{J_{\hat\phi}}{R} - \frac{\mathcal{I}}{\alpha^2R^2}\frac{\mathrm{d}\mathcal{I}}{\mathrm{d}\Psi} - \rho_e\frac{\Omega-\omega}{\alpha}\right)\mathbf{D}\Psi. \tag{2.94}$$

Finally equating it to Eq. 2.86 and requiring the integrability condition $\mathcal{M} = \mathcal{M}(\Psi)$ one obtains

$$\frac{J_{\hat\phi}}{R} = \rho h\frac{\mathrm{d}\mathcal{M}}{\mathrm{d}\Psi} + \frac{\mathcal{I}}{\alpha^2R^2}\frac{\mathrm{d}\mathcal{I}}{\mathrm{d}\Psi} + \rho_e\frac{\Omega-\omega}{\alpha}. \tag{2.95}$$

By making use of Eq. 2.73 this can be written as a single equations for Ψ and, after some algebra, one obtains the relativistic *Grad-Shafranov* (GS) equation

$$\mathbf{D}\cdot\left[\frac{\alpha}{R^2}\left(1-v^2\right)\mathbf{D}\Psi\right]+\frac{\mathcal{I}}{\alpha R^2}\frac{\mathrm{d}\mathcal{I}}{\mathrm{d}\Psi}+\alpha\rho h\frac{\mathrm{d}\mathcal{M}}{\mathrm{d}\Psi}=0. \tag{2.96}$$

Notice that since we have used the Ideal MHD condition, the GS equation is strictly valid only inside the NS. On the other hand if one assumes the existence of a low density plasma that, without affecting the dynamics, can provide the required charges and currents, the condition $\mathbf{E}\cdot\mathbf{B}=0$ can be extended also outside the NS. This is the base of the so called *force-free degenerate electro-dynamic* (or magnetodynamic, Komissarov 2011), and is the prescription generally adopted in magnetospheric models that focus just on the exterior (Michel 1973b, Contopoulos et al. 1999, Timokhin 2006, Spitkovsky 2006, Tchekhovskoy et al. 2013, Pétri 2016b), and that has been recently extended to global models (Ruiz et al. 2014). In this case, given the negligible dynamical effects of the plasma, the Lorentz force must vanishes. Hence the force-free limit of the GS equation can be obtained with $\mathcal{M}(\Psi)=$ cost or equivalently with $\rho\rightarrow 0$. One obtains

$$\mathbf{D}\cdot\left[\frac{\alpha}{R^2}\left(1-v^2\right)\mathbf{D}\Psi\right]+\frac{\mathcal{I}}{\alpha R^2}\frac{\mathrm{d}\mathcal{I}}{\mathrm{d}\Psi}=0. \tag{2.97}$$

which is also known as the *pulsar equation*.

Notice that the force-free GS equation could have also been derived requiring $\mathbf{L}=0$ with the assumption that Ω is the rotational rate of the magnetic field lines, namely $\Omega=-\mathrm{d}\Phi/\mathrm{d}\Psi$, so that the velocity $\mathbf{v}=\alpha^{-1}(\Omega-\omega)R\mathbf{e}_{\hat{\phi}}$ refers to the motion of the immaterial field-lines as measured by the Eulerian observer. In this case there is nothing to prevent $v>1$ once the *Light Cylinder*, defined by $R=R_L=\alpha^{-1}(\Omega-\omega)$, is crossed. On the contrary, in the case $\mathbf{v}$ is associated with the fluid rotation then $v<1$ everywhere and we do not have a transition at the generalized Light Cylinder. Moreover, there is a net energy flow along those field-lines that cross the Light Cylinder which is not strictly consistent with our assumption of stationarity.

In order to preserve the stationarity requirement one can force the poloidal fields lines to be contained inside the star, adding an *ad hoc* singular toroidal current at the stellar surface (Tomimura and Eriguchi 2005). The other possibility, which is often adopted in literature (see for example Bocquet et al. 1995, Franzon et al. 2016a), is to consider an electrovacuum approximation, assuming that field-lines extend also outside the NS surface into a 'vacuum'. In this case one cannot define any meaningful reference frame in the exterior, such that it is not possible to enforce any relation between Ψ and Φ. Indeed there are regions where $\mathbf{E}\cdot\mathbf{B}\neq 0$, which are known as *vacuum gaps* (Goldreich and Julian 1969, Michel and Li 1999, Cheng et al. 1986). In this case one cannot use a single GS equation over the entire space but one should solve the potentials separately inside and outside the NS with the requirement of continuity at the stellar surface. While the vacuum corresponds to the simple assumption $\rho_e=J^{\phi}=0$, inside the ideal MHD condition, together with the requirement of integrability, can be easily translated into a condition on the charge and current distribution

$$\rho_e = -\frac{\alpha v^2}{\omega - \Omega}\rho h \Gamma^2 \frac{\mathrm{d}\mathcal{M}}{\mathrm{d}\Psi} + \frac{\omega - \Omega}{\alpha \psi^4 v^2}\partial \ln \Gamma^2 \partial \Psi - \frac{1}{\psi^4}\partial\omega\partial\Psi, \tag{2.98}$$

$$J^\phi = \rho h \Gamma^2 \frac{\mathrm{d}\mathcal{M}}{\mathrm{d}\Psi} - \frac{1}{\psi^8 r^2 \sin^2\theta}\partial \ln \Gamma^2 \partial \Psi + \frac{\omega - \Omega}{\alpha^2 \psi^4}\partial\omega\partial\Psi. \tag{2.99}$$

Note however that it is not sufficient to impose these forms for the source terms into Eq. 2.77 in order to ensure ideal MHD inside the NS, because Eq. 2.77 defines the electromagnetic field minus an arbitrary harmonic function. This harmonic function (which guarantees ideal MHD inside) corresponds to a singular source term (a surface charge), that have been neglected in deriving the integrability conditions, where we only considered distributed forces. Moreover the solution is not unique but depends on the arbitrary constant of integration C in Eq. 2.89, which regulates the global net charge of the NS.

2.6 Choices for the currents function

The morphology of the magnetic field is controlled by the form of the free functions $\mathcal{M}$ and $\mathcal{I}$. As discussed in the previous section the magnetization function $\mathcal{M}$ is associated with the Lorentz force appearing in the Euler equation, Eq. 2.84. The current function $\mathcal{I}$, instead, is related only to the toroidal component of the magnetic field.

If the magnetic field has a poloidal component then $\Psi \neq 0$ and $\mathcal{M}$ can be expressed as a function of the magnetic potential Ψ alone because of the orthogonality relation $\mathbf{f}_L \cdot \mathbf{B} = 0$. A common choice is to express $\mathcal{M}$ as the sum of a linear function of Ψ plus a non-linear term (Bocquet et al. 1995, Ciolfi et al. 2009, Lander and Jones 2009), namely

$$\mathcal{M}(\Psi) = k_{\mathrm{pol}}\Psi\left(1 + \frac{\xi}{\nu + 1}\Psi^\nu\right) \tag{2.100}$$

where k_{pol} is the so-called *poloidal magnetization constant*, ξ is the *non-linear magnetization constant* and ν is the *poloidal magnetization index* of the non linear term. The functional form for $\mathcal{I}$ is instead chosen as

$$\mathcal{I}(\Psi) = \frac{a}{\zeta + 1}\Theta[\Psi - \Psi^{\mathrm{max}}](\Psi - \Psi^{\mathrm{max}})^{\zeta + 1}, \tag{2.101}$$

where $\Theta[.]$ is the Heaviside function, Ψ^{max} is the maximum value the ϕ component of the vector potential reaches on the stellar surface or at a certain distance from the stellar surface, a is the *twisted torus magnetization constant* and ζ is the *twisted torus magnetization index*. This functional form allows one to limit the domain of the toroidal magnetic field. The value of Ψ_{max} fixes the last magnetic surface bonding the region where the toroidal magnetic field is confined. For example choosing Ψ_{max} as the maximum value of Ψ at the surface, allows one to confine the toroidal magnetic field all within the star, obtaining TT configurations. On the other hand one can select different prescriptions for $\Psi_{\rm max}$ that allow twisted magnetopsheres, where the toroidal field exists also outside the star. These choices are again quite usual in literature (Ciolfi et al. 2009, Lander and Jones 2009, Glampedakis et al. 2014, Fujisawa et al. 2013, Fujisawa and Kisaka 2014, Uryū et al. 2014). Alternative formulation of Eqs. 2.100-2.101 will be discussed in Chapter 4 and 5.

In the case of a purely toroidal field, most of the formalism leading to the Grad-Shafranov equation does not apply, since $\Psi = 0$ and we cannot define the usual free functions on magnetic surfaces. However, since Eq. 2.84 is still valid, we can look for a scalar function $\mathcal{M}$ (though no longer a function of Ψ) such that $L_i = \rho h \partial_i \mathcal{M}$. Then, using Eq. 2.93 with $\Psi = 0$, the integrability condition in Eq. 2.86 reads:

$$\mathbf{D}\mathcal{M} = -\frac{\mathcal{I}\,\mathbf{D}\mathcal{I}}{\rho h \alpha^2 R^2}. \tag{2.102}$$

Defining a new quantity $G = \rho h \alpha^2 R^2$, the previous equation can be easily integrated if we assume a barotropic-like dependency for the current function $\mathcal{I} = \mathcal{I}(G)$, namely

$$\mathcal{I} = K_m G^m \tag{2.103}$$

where K_m is the *toroidal magnetization constant* and $m \geq 1$ is the *toroidal magnetization index*. With this assumption the magnetization function $\mathcal{M}$ is given by (Kiuchi and Yoshida 2008, Kiuchi et al. 2009, Yasutake et al. 2010, Frieben and Rezzolla 2012)

$$\mathcal{M} = -\frac{m K_m^2}{2m-1} G^{2m-1}, \tag{2.104}$$

and the magnetic field is related to the enthalpy per unit volume through

$$B_\phi = \alpha^{-1} K_m G^m = \alpha^{-1} K_m (\rho h\, \alpha^2 R^2)^m. \tag{2.105}$$

Here the magnetization constant K_m regulates the strength of the magnetic field (more specifically the magnetic flux through the meridional plane), while the magnetization index m governs to the distribution of the magnetic field inside the star.

2.7 Global quantities

In order to characterize each equilibrium model we have computed a wide set of global physical quantities. Here we give their definition assuming CFC.
The relevant quantities are: the gravitational mass

$$M := \int \left[2p + \rho h \Gamma^2 \left(1 + v^2 + 2R^2 v \omega \right) + B^2 + E^2 - \epsilon_{\phi ij} \frac{\omega}{\alpha} E^i B^j \right] \alpha \psi^6 \sin\theta \, dr d\theta d\phi; \tag{2.106}$$

the baryonic mass

$$M_0 := \int \rho\Gamma\psi^6 r^2 \sin\theta \, dr d\theta d\phi; \tag{2.107}$$

the proper mass

$$M_p := \int e\Gamma\psi^6 r^2 \sin\theta \, dr d\theta d\phi; \tag{2.108}$$

the total electromagnetic energy

$$H := \frac{1}{2}\int (B^2 + E^2)\psi^6 r^2 \sin\theta \, dr d\theta d\phi; \tag{2.109}$$

the magnetic energy in the toroidal component

$$H_{\rm tor} := \frac{1}{2}\int B^\phi B_\phi \psi^6 r^2 \sin\theta \, dr d\theta d\phi; \tag{2.110}$$

the magnetic energy in the poloidal component

$$H_{\rm pol} := \frac{1}{2}\int (B^r B_r + B^\theta B_\theta)\psi^6 r^2 \sin\theta \, dr d\theta d\phi; \tag{2.111}$$

the Komar angular momentum:

$$\mathcal{J} = \int (e + p)\Gamma^2 v \psi^8 r^3 \sin^2\theta \, dr d\theta d\phi; \tag{2.112}$$

the rotational kinetic energy

$$K := \frac{1}{2}\mathcal{J}\Omega \tag{2.113}$$

and the absolute value of the binding energy

$$W := |M - M_p - H - K|, \tag{2.114}$$

where the integrals are defined over the all three-dimensional space.

In order to characterize the geometrical properties of the magnetic field, other quantities must be introduced. For a purely toroidal magnetic field , the magnetic flux through a meridional half-plane which, analogously to Kiuchi and Yoshida (2008), is given by

$$\Phi_B := \int_0^\pi d\theta \int_0^\infty \sqrt{B^\phi B_\phi}\psi^4 r \, dr. \tag{2.115}$$

In the presence of a poloidal magnetic field we can estimate the magnetic dipole moment μ of the star. This is usually defined (see Bocquet et al. (1995)) by the leading term of the asymptotic behavior of the magnetic field components at $r \to \infty$, where the spacetime metric is flat. However this definition is not well suited for our numerical scheme XNS, where the numerical domain is not compactified but extends only over a few stellar radii outside the NS. Therefore we have evaluated the magnetic dipole moment at finite distance ($\sim$ 3 stellar radii) from the star verifying that this is constant in a curved spacetime. In particular, from a multipole expansion of Eq. (2.125), assuming that outside the star the line element is well approximated by the Schwarzschild solution and selecting the dipole term ($\ell = 1$), one can find a simple relation that connects the dipole moment μ to the ϕ−component of the vector potential $\tilde{\Psi}$, the gravitational mass M and the radial coordinate r, namely

$$\tilde{\Psi} = \mu\left(1 + \frac{M}{4r}\right)\frac{\sin\theta}{r^2}. \tag{2.116}$$

Finally there are global quantities related exclusively to the shape and deformation of the star. These are the equatorial radius r_e, the polar radius r_p, and the circumferential radius

$$R_\mathrm{circ} := \psi^2(r_e, \pi/2) r_e. \tag{2.117}$$

In the majority of cases, the surface of the star is well fitted by a super-ellipsoid generated by the rotation of

$$r = \left[\left(\frac{\cos\theta}{r_\mathrm{p}}\right)^{n_\mathrm{s}} + \left(\frac{\sin\theta}{r_\mathrm{e}}\right)^{n_\mathrm{s}}\right]^{-\frac{1}{n_\mathrm{s}}}, \tag{2.118}$$

where n_s, the *index of ellipticity*, regulates the shape of the ellipse. Other important quantities related to the deformation of the star are the surface ellipticity, given by

$$e_\mathrm{s} := \frac{r_\mathrm{e}}{r_\mathrm{p}} - 1 \tag{2.119}$$

and the mean deformation that, following Kiuchi and Yoshida (2008), is defined by

$$\bar{e} := \frac{I_{zz} - I_{xx}}{I_{zz}}, \tag{2.120}$$

where I_{zz} and I_{xx} are the moment of inertia, respectively in the parallel and orthogonal direction to the axis of symmetry

$$I_{zz} := \int e r^4 \sin^3\theta dr d\theta d\phi \tag{2.121}$$

$$I_{xx} := \frac{1}{2}\int e r^4 \sin\theta(1 + \cos^2\theta) dr d\theta d\phi. \tag{2.122}$$

The deformation rate $\bar{e}$ has the advantage that it can be computed as an integral over the star, but it is strictly a Newtonian quantity (we have however verified that the inclusion of magnetic and kinetic energy gives negligible contributions being them dominated by the matter distribution). In GR, the relevant quantity for the emission of GWs is the quadrupolar ellipticity e_q, defined as

$$e_\mathrm{q} = -\frac{3}{2}\frac{\mathcal{I}_{zz}}{I} \tag{2.123}$$

where $\mathcal{I}_{zz}$ is the gravitational quadrupole moment and I is the moment of inertia. The gravitational quadrupole moment can not be computed as an integral over the star but must be derived from the asymptotic structure of the metric terms (Bonazzola and Gourgoulhon 1996) in the limit $r \to \infty$. The moment of inertia can be properly defined only for rotating stars as the ratio of the Komar angular momentum over the rotational rate $I := \mathcal{J}/\Omega$ (Bonazzola and Gourgoulhon 1996, Frieben and Rezzolla 2012). In the case of a non rotating stars, it can be evaluated in the limit $\Omega \to 0$

$$I \simeq \lim_{\Omega\to 0} \frac{\mathcal{J}}{\Omega} = \int (e+p)\frac{\psi^{10}}{\alpha^{-1}} r^4 \sin^3\theta dr d\theta d\phi. \tag{2.124}$$

Interestingly, we find that in almost all our models the quadrupolar ellipticity scales as the deformation ratio: $e_\mathrm{q}/\bar{e} = 0.40 \pm 0.05$ (see also Frieben and Rezzolla 2012). In the following chapters we will consider $\bar{e}$ rather that e_q since with our numerical approach $\bar{e}$ is a more robust quantity being the result of an integration over a confined domain.

2.8 Modeling magnetized Neutron Stars

In the previous sections we have introduces all the formalism at the base of our numerical models. While the details of the XNS code are discussed in Appx. A, here we summarize the equations the we have to solve depending on the specific choice for the morphology of the magnetic field. In the remainder of this thesis we will consider static configurations with purely toroidal, purely poloidal or mixed magnetic field. For the rotating configurations we will consider exclusively purely poloidal or purely toroidal magnetic fields with all the current terms confined inside the star, since mixed field morphologies leads to configurations where the Poynting flux does not vanishes contradicting the requirement of stationarity (see also Sec. 2.5). In particular, Einstein's equation as well as the Bernoulli integral are obviously solved for each configuration, the Lorentz force contribution to the Bernoulli integral $\mathcal{M}$ is evaluated through different methods:

- in the case of NSs endowed with a purely toroidal field the magnetic $\mathcal{M}$ is simply given by Eq. 2.104;
- in the case of static configurations with poloidal or mixed magnetic field, the magnetic potential Ψ in the expression of $\mathcal{M}$ (Eq. 2.100) and $\mathcal{I}$ (Eq. 2.101) is obtained by solving the non-rotating limit of the GS equation which in local coordinates reads

  $$\tilde{\Delta}_3\tilde{\Psi} + \frac{\partial\Psi\partial\ln(\alpha\psi^{-2})}{r\sin\theta} + \psi^8 r\sin\theta\left(\rho h\frac{\mathrm{d}\mathcal{M}}{\mathrm{d}\Psi} + \frac{\mathcal{I}}{\alpha^2R^2}\frac{\mathrm{d}\mathcal{I}}{\mathrm{d}\Psi}\right) = 0, \tag{2.125}$$

  where Δ_3 is given in Eq. 2.80;
- for rotating NSs with a purely poloidal field the electromagnetic potentials are obtained solving the Maxwell-Gauss Eq. 2.77 for Ψ and the Maxwell-Ampère Eq. 2.78 for Φ, with the source terms given by Eqs. 2.98 and 2.99 (see also Appx. A for a detailed discussion).

Given that our work focuses on the role of magnetic field only, in this thesis we have adopted a simple polytropic EoS (with the exception of Chap. 7 where we consider more physically motivated EoS), with a polytropic index $n = 1$ and a polytropic constant $K_\mathrm{a} = 110$ (in geometrized units[5]). These values are commonly used in literature and allow us a straightforward comparison with previous results (Kiuchi and Yoshida 2008, Frieben and Rezzolla 2012). In the unmagnetized case, for a central density $\rho_c = 8.576 \times 10^{14}\mathrm{g\ cm}^{-3}$, this EoS gives an equilibrium configuration characterized by a baryonic mass $M_0 = 1.680\mathrm{M}_\odot$, a gravitational mass $M = 1.551\mathrm{M}_\odot$, and a circumferential radius $R_\mathrm{circ} = 14.19\mathrm{km}$. This will be our reference model for comparison to magnetized and rotating cases.

---

[5] This corresponds to $K_a = 1.6 \times 10^5 \mathrm{cm}^5 \mathrm{g}^{-1} \mathrm{s}^{-2}$.

3

Purely Toroidal Magnetic Fields

The morphology of the magnetic field might strongly depend on the details of the NS formation. It is natural to expect that, after a merging event or after the gravitational collapse of a rapidly rotating progenitor, the resulting NS is characterized by an appreciable degree of differential rotation (Janka and Moenchmeyer 1989). This differential rotation, in turn, can reshape the initial configuration of the magnetic field leading to the formation of a strong toroidal component. Then, as already discussed in Chap. 1, if the toroidal magnetic field is energetically dominant, it induces a prolate deformation of the structure of the NS, favoring the possible spin-flip mechanism (Cutler 2002) necessary to make the NS itself an efficient gravitational waves emitter.

In this chapter we will present a detailed study of various equilibrium configurations endowed with a purely toroidal magnetic field. We will analyze how the structure of the NS changes with the magnetic field strength, the distribution of the associated currents and the centrifugal effects. In particular, in the first section of this chapter, which is based on Pili et al. (2014), we will focus only on static configurations at fixed baryonic mass. This allows us to investigate the role of the magnetic field alone. In the second section we will introduce rotation. The remaining part of the chapter is devoted to the study of global trends and to the possible parametrization of the magnetic field effects.

3.1 Static configurations

Configurations with a purely toroidal magnetic field are obtained with the barotropic-type expression for $\mathcal{M}(G)$ in Eq. 2.104 which we recall here for convenience:

$$\mathcal{M} = -\frac{mK_{\rm m}^2}{2m-1}G^{2m-1},$$

where $K_{\rm m}$ regulates the strength of the magnetic field while m is linked to the distribution of currents inside the star. Configurations with higher m are characterized by currents more concentrated in narrower regions.

Let us first compare equilibrium configurations with different values of m. In Fig. 3.1

we show the strength of the magnetic field and the distribution of the baryonic density for two equilibrium configurations characterized by the same baryonic mass $M_0 = 1.68\mathrm{M}_\odot$, the same maximum value of the internal magnetic field strength $B_{\max} = 6.134 \times 10^{17}$ G, but with different values of the toroidal magnetization index: $m = 1$ and $m = 2$ respectively. In Tab. 3.1 we list some physical properties of these models. Concerning the distribution of magnetic field, the two models look qualitatively very similar: as expected for a toroidal field arising from our choice for $\mathcal{M}$, in both cases the magnetic field vanishes on the axis, reaches a maximum at 20%-30% of the NS radius and then decreases moving toward the surface where it vanishes. Quantitatively, however, there are significative differences. In the case $m = 1$ the magnetic field strength goes to zero on axis as $r \sin\theta$, while the ratio B^2/p, a monotonically increasing function of radius, tends to a constant at the stellar surface (the magnetic field decreases as fast as the pressure). On the other hand in the case $m = 2$ the magnetic field strength goes to zero on axis $\propto (r \sin\theta)^3$, while the ratio B^2/p reaches a maximum inside the star, and then goes to zero at the stellar surface.

Table 3.1: Global physical quantities of the equilibrium models displayed in Fig. 3.1 with baryonic mass $M_0 = 1.68\mathrm{M}_\odot$ and maximum magnetic field strength $B_{\max} = 6.134 \times 10^{17}$ G.

Model	ρ_c $[10^{14}\mathrm{g\,cm^{-3}}]$	M $[\mathrm{M}_\odot]$	r_e [km]	r_p/r_e	R_{circ} [km]	H/W $[10^{-1}]$	$\bar{e}$ $[10^{-1}]$	Φ_{B} $[10^{30}\,\mathrm{G\,cm^2}]$
$K_{\mathrm{m}} = 0$	8.576	1.551	12.08	1.000	14.19	0.000	0.000	0.000
$m = 1$	8.430	1.596	18.10	1.139	20.15	2.013	-8.130	1.538
$m = 2$	8.588	1.577	14.01	1.104	15.92	1.246	-3.730	0.862

Similar considerations hold for the distribution of the baryonic density (Fig. 3.1). In both cases the magnetic stresses lead to a prolate deformation of the star. This affects the internal layers even more than the outer ones. Indeed, the typical prolateness of the iso-density surfaces in the core is larger than the deformation of the stellar surface, and the external low-density layers. Interestingly, to this axial compression of the internal layers corresponds an expansion of the outer part of the star to larger radii, due to the extra pressure support provided by the magnetic field. There are two noticeable differences between the $m = 1$ and $m = 2$ cases, in this respect. For $m = 1$ the iso-density surfaces are, to a good approximation, prolate ellipsoids, while in the $m = 2$ case they tend to be more barrel-shaped. More important, despite the internal maximum magnetic field being the same, the $m = 2$ case shows smaller deformation. This can be explained in terms of the energetics of the magnetic field that for higher m is reduced by the shrinkage of the magnetic field distribution toward the stellar surface. As we will discuss in Sec. 3.4, even comparing models with the same magnetic energy, the deformation is slightly reduced for higher m at most by 5%. This can be justified recalling that the action of the magnetic tension, responsible for the anisotropy, is $\propto B^2/R$ (R is now the radius of curvature of the magnetic field line). For higher values of m the magnetic field reaches its maximum at increasingly larger radii, resulting in a relatively smaller tension. This can be rephrased in terms of currents, suggesting that currents in the

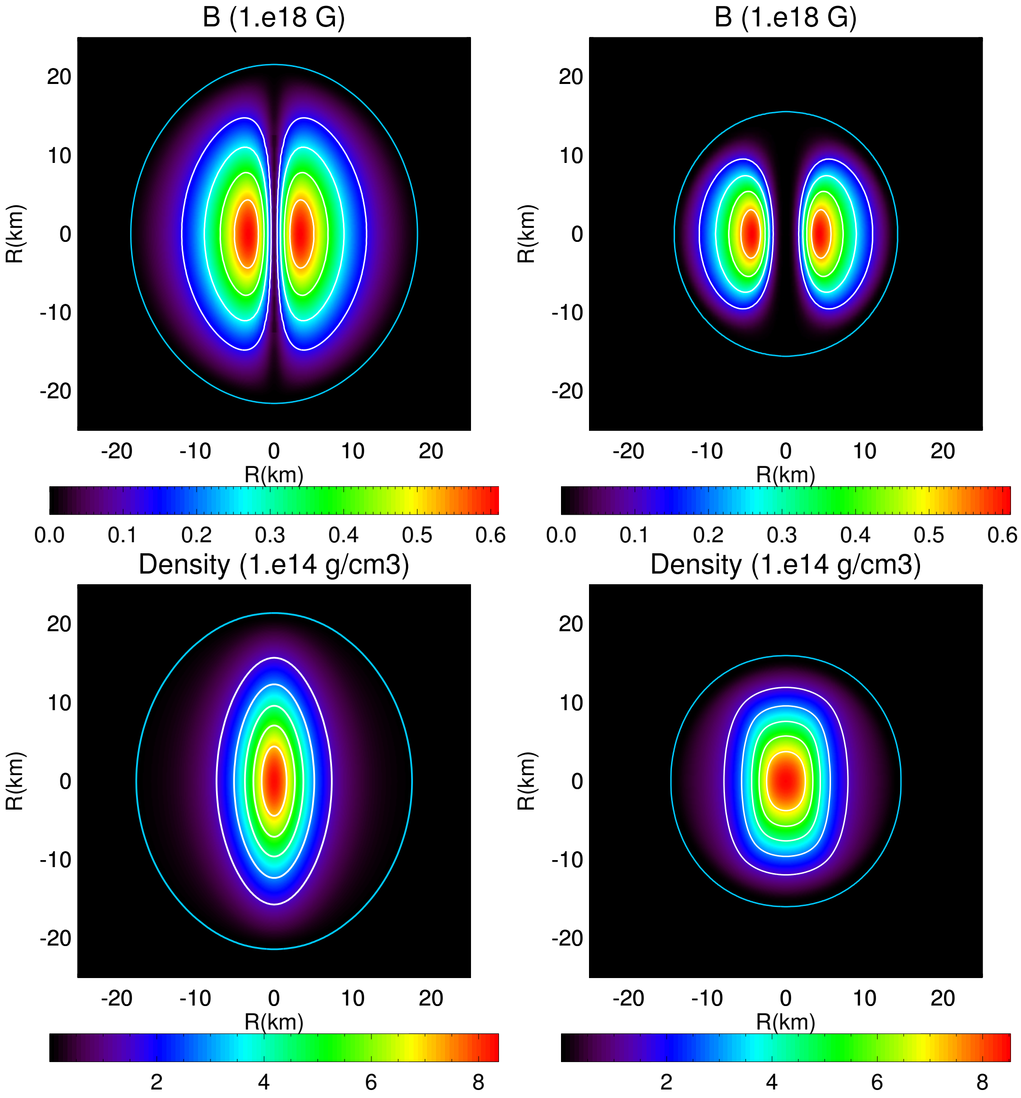

Figure 3.1: Meridional distribution and isocontours of the magnetic field strength $B = \sqrt{B^{\phi}B_{\phi}}$ (top) and of the baryonic density (bottom) for models with baryonic mass $M_0 = 1.68\mathrm{M}_{\odot}$, maximum magnetic field strength $B_{\rm max} = 6.134 \times 10^{17}$ G, with magnetic index $m = 1$ (left) and $m = 2$ (right). Blue curves represent the surface of the star. Other global quantities related to these configurations are listed in Table 3.1.

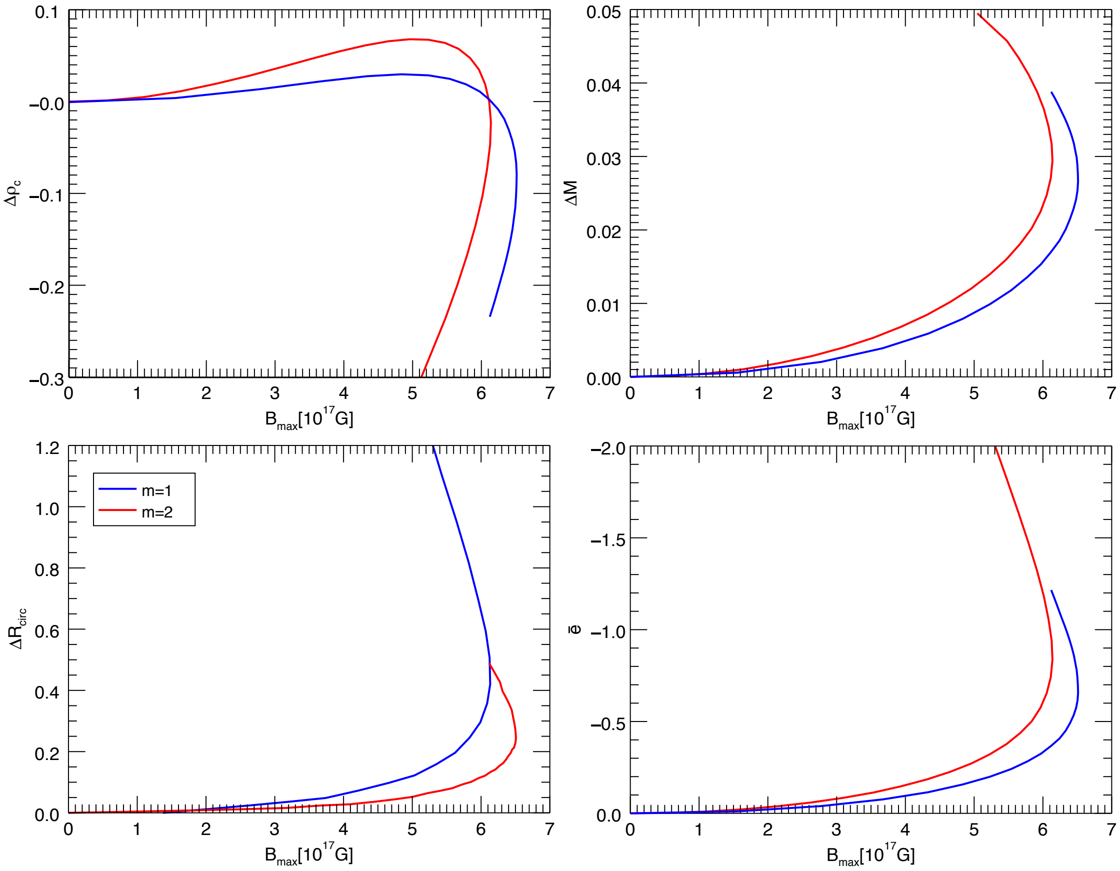

Figure 3.2: Variation, with respect to the unmagnetized equilibrium model, of the central baryon density ρ_c, of the gravitational mass M, of the circumferential radius $R_{\rm circ}$ and of the mean deformation rate $\bar{e}$ along the equilibrium sequence of magnetized non-rotating configurations with constant $M_0 = 1.68 M_\odot$ and $m = 1$ or $m = 2$.

outer layers have minor effects with respect to those residing in the deeper interior.

Apart from a qualitative analysis of the structure and shape of these equilibrium models, it is possible to investigate in detail the parameter space as a function of various quantities and to check how they are related. In particular, following Kiuchi and Yoshida (2008) and Frieben and Rezzolla (2012) we compute sequences of magnetized equilibrium models characterized by a constant baryonic mass $M_0 = 1.68 M_\odot$, evaluating how global quantities change increasing the magnetization of the star $K_{\rm m}$. In Fig. 3.2 we plot the deviation of the central baryonic density ρ_c, the gravitational mass M, the circumferential radius $R_{\rm circ}$ and the deformation rate $\bar{e}$, with respect to the unmagnetized case, as a function of the maximum value of the magnetic field strength for both the $m = 1$ and $m = 2$ configurations. Here, the deviation of the generic quantity Q is defined as:

$$\Delta Q = \frac{[Q(B_{\rm max}, M_0) - Q(0, M_0)]}{Q(0, M_0)}. \tag{3.1}$$

The comparison between our results and those by Kiuchi and Yoshida (2008) and Frieben and Rezzolla (2012) is performed in Appx. A. The first thing to notice in Fig. 3.2, is that $B_{\rm max}$ is not a monotonic function of the magnetization constant K_m: $B_{\rm max}$ initially increases with

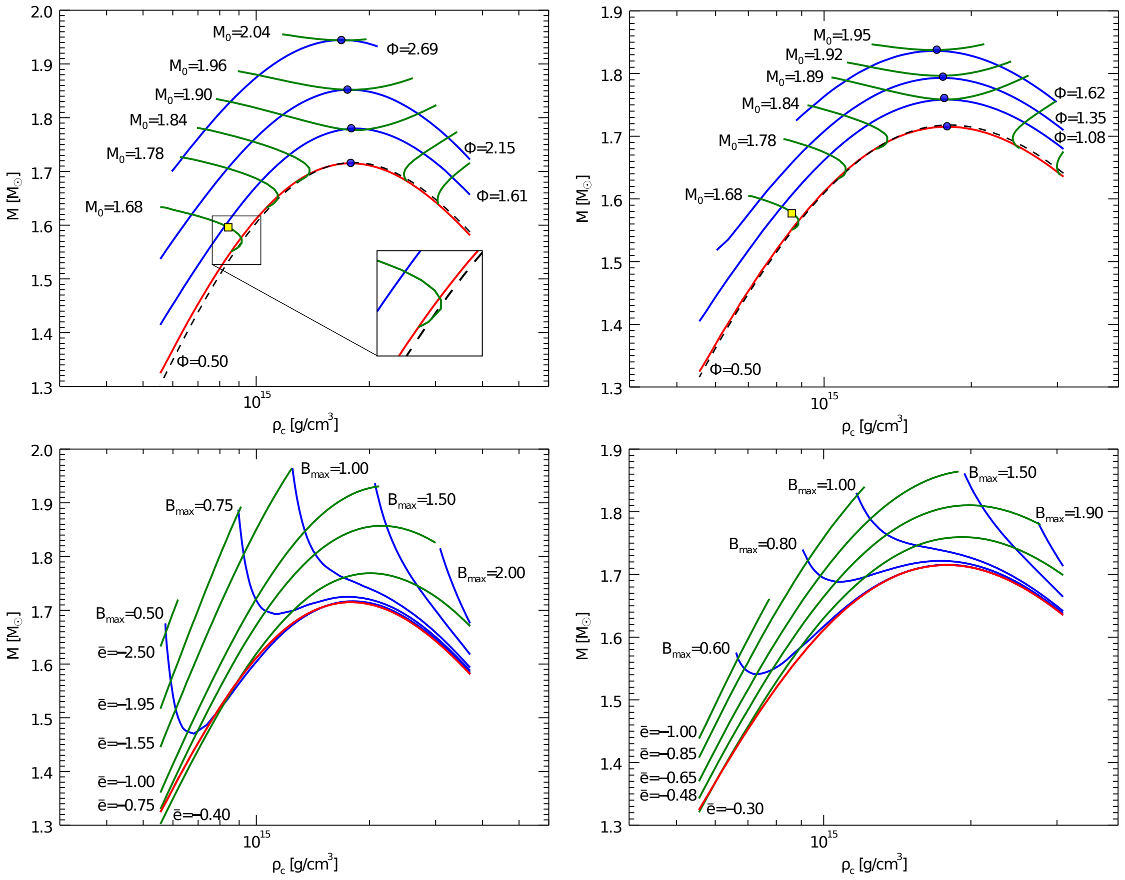

Figure 3.3: Sequences of equilibrium stellar models with purely toroidal field. Top panel: with fixed baryonic mass M_0 and fixed magnetic flux Φ_{B}. Bottom panel: with fixed mean deformation rate $\bar{e}$ and fixed maximum magnetic field strength B_{max}. Left panels show configurations with $m = 1$ while right ones show configurations with $m = 2$. M_0 is expressed in unit of solar masses $\mathrm{M}_{\odot}$, Φ_{B} in unity of $10^{30}\mathrm{G\,cm}^2$ and B_{max} in unity of 10^{18}G. The red line is the unmagnetized sequence while the black dashed lines represent equilibrium configurations with low magnetic flux Φ_{B}. The filled circles locate the models with the maximum gravitational mass at fixed magnetic flux. Details of these models are listed in Table 3.2. The yellow squares represent the models shown in Fig. 3.1.

K_m, till it reaches a maximum value, and then for higher values of K_m it drops. This is due to the expansion of the star. For small values of K_m, the stellar radius changes marginally, and an increase in K_m translates simply into a stronger field. However at higher values of K_m, the radius of the star is largely inflated and any further increase in K_m translates into an expansion of the star and a consequent reduction of the maximum internal field. This also reflects on the magnetic energy H, which initially grows but at large K_m it saturates and begins to drop. A similar effect shows up in the behaviour of the central density. For small values of K_m the magnetic tension tends to compress the matter in the core, increasing its density. However as soon as the magnetic field becomes strong enough to cause the outer layer of the star to expand, the central density begins to drop (recall that the sequence is for a fixed baryonic mass).

In order to quantify these effects and to search for global trends we have carried out a full sampling of the parameter space. In Fig. 3.3 we plot the gravitational mass M as a function of the central density ρ_c both for sequences with a constant baryonic mass M_0 and

Table 3.2: Global quantities of the maximum mass models shown in Fig. 3.3.

Model	ρ_c $[10^{14}\mathrm{g\,cm^{-3}}]$	M $[\mathrm{M_\odot}]$	M_0 $[M_\odot]$	R_circ [km]	r_p/r_e	H/W $[10^{-1}]$	$\bar{e}$ $[10^{-1}]$	B_max $[10^{18}\,\mathrm{G}]$	Φ_B $[10^{30}\,\mathrm{G\,cm^2}]$
$B = 0$	17.91	1.715	1.885	11.68	1.000	0.000	0.000	0.000	0.000
$m = 1$	18.65	1.780	1.901	14.84	1.088	1.670	-4.587	1.129	1.613
	17.50	1.852	1.960	17.74	1.107	2.373	-7.833	1.216	2.150
	16.85	1.945	2.041	20.86	1.138	2.956	-11.36	1.265	2.690
$m = 2$	17.69	1.761	1.890	13.22	1.067	1.330	-3.041	1.133	1.080
	17.78	1.795	1.916	13.98	1.094	1.747	-4.311	1.262	1.350
	17.00	1.838	1.950	15.07	1.115	2.158	-5.944	1.291	1.620

with a constant magnetic flux Φ_B. The first thing to notice is that the gravitational mass generally grows with the magnetic flux Φ_B. This trend is reversed only in a small region of the parameter space characterized by a weak magnetization, with $\Phi_\mathrm{B} \lesssim 5 \times 10^{30}\mathrm{G\,cm^2}$, and low central density, $\rho_\mathrm{c} \lesssim 1 - 1.5 \times 10^{15}\mathrm{g\,cm^{-3}}$. This is a manifestation of the same effect discussed above in relation to the trend of the central density in Fig. 3.2. This effect was already present to a lesser extent in Kiuchi and Yoshida (2008), but not discussed.

Along sequences with fixed Φ_B, the configurations with the highest gravitational mass are very close to those having the highest value for the baryonic mass M_0 (they are coincident within the accuracy of our code), as can be seen in Fig. 3.3, where the filled circles locate the maximum gravitational mass models in the sequences of constant Φ_B. The global quantities related to these configurations are summarized in Table 3.2. Similarly, for a given M_0 the model with the minimal gravitational mass has also the minimum magnetic flux.

Our set of models allows us also to construct sequences characterized by a constant magnetic field strength B_max or a constant deformation rate $\bar{e}$. It is evident that models with a higher central density, which usually correspond to more compact stars, can harbor a higher magnetic field with a smaller deformation.

It is important to remark that the deformation ratio $\bar{e}$ is a Newtonian quantity and that the relevant quantity for the GW physics is instead the quadrupolar ellipticity e_q (see Sec. 2.7). However we have found that, as in Frieben and Rezzolla (2012), in almost all our models the quadrupolar ellipticity is a constant fraction of the deformation ratio: $e_\mathrm{q}/\bar{e} = 0.40 \pm 0.05$ where the uncertainty is mostly due to the asymptotic extrapolation of the metric terms. As anticipated in Sec. 2.7, in the following we will mainly consider $\bar{e}$, instead of e_q, since it is a robust quantity within our numerical scheme.

3.2 Rotating configurations

The analysis presented previously has been extended to rigidly rotating configurations where again we have computed a large set of equilibria varying the central density, the magnetization, the magnetic field profile, and the rotation frequency. The latter is however main-

Table 3.3: Global quantities for the configuration shown in Fig. 3.5 with gravitational mass $M = 1.55\mathrm{M}_{\odot}$.

B_{max} 10^{17} G	Ω $10^{3}\mathrm{s}^{-1}$	ρ_{c} $10^{14}\mathrm{g/cm}^{3}$	M_0 $M_{\odot}$	R_{circ} km	$r_{\mathrm{p}}/R_{\mathrm{e}}$	$\bar{e}$	n_{s}	H/W 10^{-1}	T/W 10^{-1}	H/M 10^{-2}	T/M 10^{-2}
0.51	3.045	7.31	1.67	10.5	0.90	0.09	2.00	0.01	0.50	0.02	7.62
4.63	2.030	8.24	1.66	16.9	1.00	-0.23	2.00	0.13	0.21	1.32	0.31
5.20	2.030	6.63	1.62	28.9	0.90	-0.79	1.76	2.30	0.38	2.44	0.41

tained below $\Omega = 5.1 \times 10^{3}\mathrm{s}^{-1}$ (corresponding to $\Omega = 2.5 \times 10^{-2}$ in geometrized units). At this frequency the space of models is quite narrow due to mass shedding, and mostly limited to very compact configurations, while less compact stars are more prone to magnetic and rotational deformation.

The parameter space is shown in Fig. 3.4, for $m = 1$, for different values of the constant rotation rate Ω. As in Fig. 3.3, models are given in terms of the central density ρ_c and the gravitational mass M. At each value of the rotation rate Ω we plot sequences of constant baryonic mass M_0 and of constant magnetic flux Φ_{B} and sequences of constant deformation ratio $\bar{e}$ and constant maximum magnetic field strength B_{max}. Notice that at low central density the space of solutions is limited by two physical boundaries: the unmagnetized limit (red line), and the mass shedding limit (yellow line).

Let us begin by discussing the general interplay between rotation and magnetic field. As already pointed out by Frieben and Rezzolla (2012), depending on the strength of the magnetic field versus the rotation rate we can obtain three main typologies of deformation, as shown in Fig. 3.5 and Tab. 3.3: if the rotation is dominant the resulting configuration is purely oblate with both positive surface ellipticity e_{s} and mean deformation rate $\bar{e}$ (left panel of Fig. 3.5); conversely, if the effects due to the magnetic field prevail the star is purely prolate with $\bar{e} < 0$ and $e_{\mathrm{s}} < 0$, or at most $e_{\mathrm{s}} = 0$ (central panel of Fig. 3.5); for intermediate configurations, when magnetization and rotation can counterbalance, the morphology of the star is only apparently oblate, with $e_{\mathrm{s}} > 0$, but globally prolate, with $\bar{e} < 0$ (right panel of Fig. 3.5).

While the Lorentz force squeezes the star in the direction of the magnetic axis inflating also the outer stellar layers (increases its prolateness), rigid rotation flattens the star toward the equatorial plane (increases its oblateness). Moreover while the rotation acts mainly in the outer region, where the specific rotational energy is larger, the magnetic field affects mainly the inner regions where its strength peaks. As a result, close to mass shedding, the star shows a peculiar diamond-like shape. In general the surface can be approximated by standard ellipsoids Eq. 2.118 with n_s in the range $1.9 - 2.1$. It is only for these peculiar diamond-shaped surfaces that the super-ellipsoid index lowers to ~ 1.7.

For the rotating models the trends of M_0, M and $\bar{e}$ with Φ_{B} and ρ_c remain the same as in the static case. However, comparing the same sequences for different values of the rotational frequency Ω, it is clear that also the rotation contributes to increase both the gravitational and the baryonic mass. For example the maximum mass on the unmagnetized sequences $\Phi_{\mathrm{B}} = 0$,

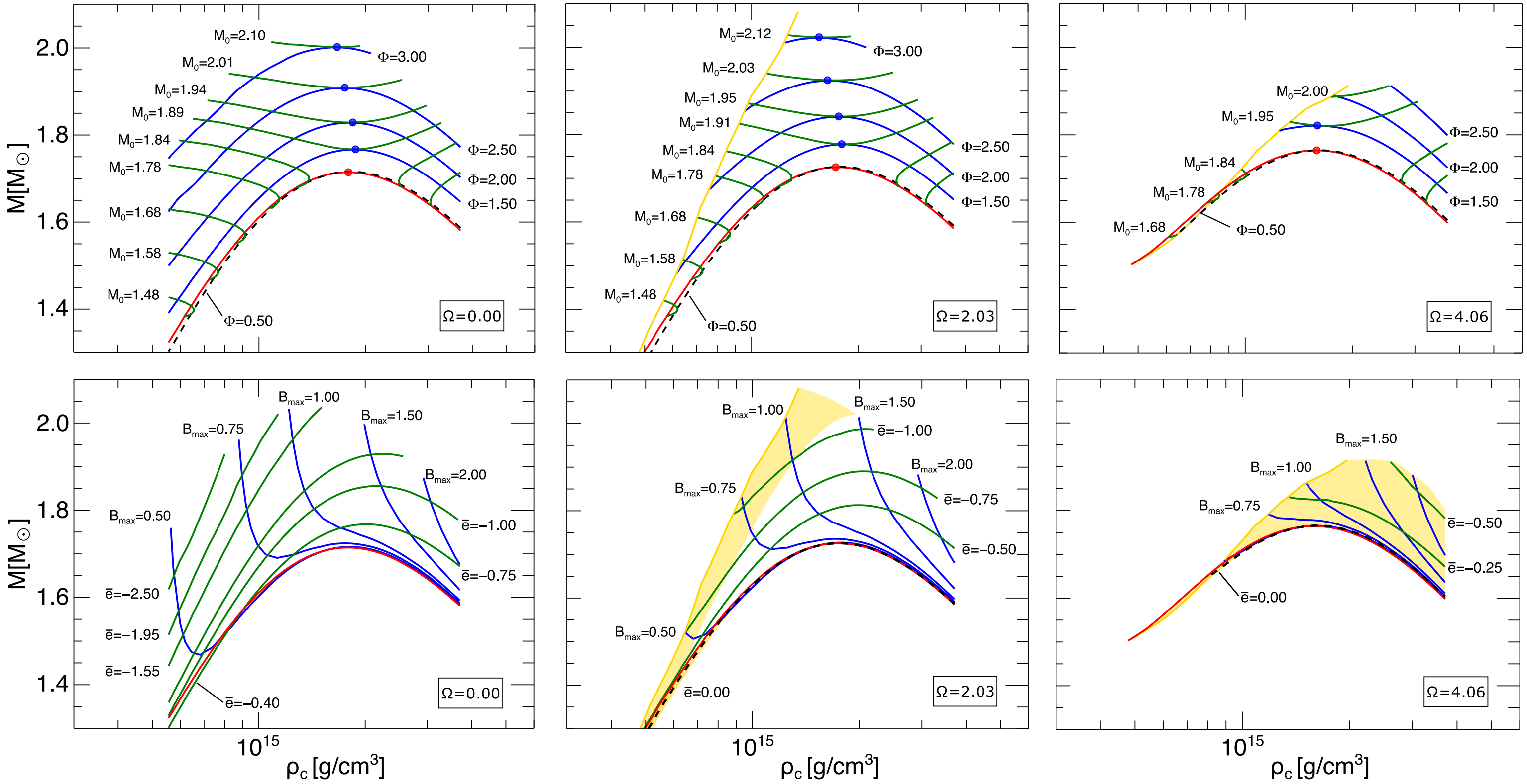

Figure 3.4: Space of physical solutions for magnetized NSs with magnetic index $m = 1$. Top row: equilibrium sequences with fixed baryonic mass M_0(green lines) and fixed magnetic flux Φ_B (blue lines) for different values of the rotational rate Ω. The black dashed lines represent configurations with low value of the magnetic flux. Bottom row: equilibrium sequences at fixed maximum magnetic field strength $B_{\max}$ (blue lines) and fixed deformation rate $\bar{e}$. Here the black dashed line represents magnetized configurations with vanishing $\bar{e}$, while the yellow shaded regions correspond to those configurations having positive surface ellipticity. In all cases the red lines represent the unmagnetized sequences. The baryonic mass M_0 is expressed in unity of $M_{\odot}$, Φ_B in unity of 10^{30}G cm^2, $B_{\max}$ in unity of 10^{18} G and the rotational rate is expressed in 10^3s^{-1}.

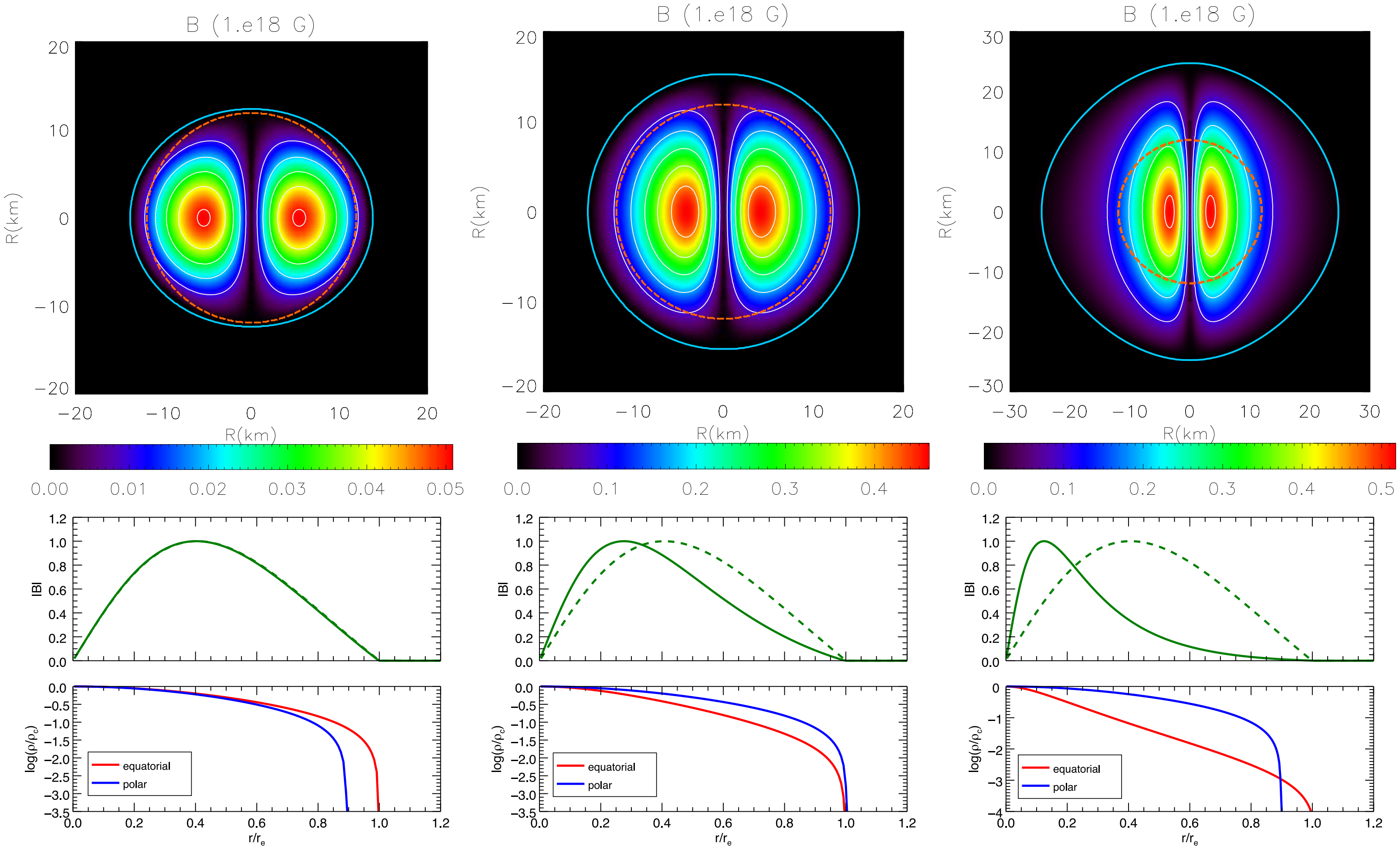

Figure 3.5: Top panels: distribution and isocontours of the magnetic field strength $B = \sqrt{B^\phi B_\phi}$ for equilibrium configurations with the same gravitational mass $M = 1.55\mathrm{M}_\odot$ but different rotational rate: $\Omega = 3.05 \times 10^3 \mathrm{s}^{-1}$ (left panel), $\Omega = 2.03 \times 10^3 \mathrm{s}^{-1}$ (central and right panel). The blue lines represent the stellar surface while the dashed lines represent the surface of the non rotating and unmagnetized model with the same gravitational mass. Bottom panels: profiles of the magnetic field strength and of the baryon density normalized to the peak value along the equatorial direction $\theta = \pi/2$. The green dashed lines represent the magnetic field distribution in the weak magnetization limit. Radii are normalized to the equatorial radius r_e. Global physical quantities for these equilibrium configurations are listed in Table 3.3.

changes from $M = 1.710\mathrm{M}_\odot$ in the non rotating case to $M = 1.805\mathrm{M}_\odot$ for $\Omega = 5.3 \times 10^3\mathrm{s}^{-1}$ while the related central density drops by $\sim 30\%$ (and from $M = 1.770\mathrm{M}_\odot$ in the non rotating case to $M = 1.820\mathrm{M}_\odot$ for $\Omega = 4.2\times10^3\mathrm{s}^{-1}$ if $\Phi_\mathrm{B} = 2.0$). The increase of the gravitational and the baryonic mass, at a given central density, is a simple volume effect. It is mainly linked to the growth of the stellar radius caused by the rotation and the magnetic field; indeed the magnetic energy and the rotational energy contribute together to the value of the gravitational mass for at most few percents.

The locus of points with $\bar{e} = 0$ is shown in the bottom panels of Figure 3.5 as a black dashed line. Configurations that are found below this line, characterized by weaker magnetization, have $\bar{e} > 0$. In the same figure we also show the region of the parameter space where the equatorial radius of the star is larger than the polar one: $e_\mathrm{s} > 0$. This yellow shaded region includes not only the purely oblate configurations with $\bar{e} > 0$ but also strongly magnetized equilibria located in proximity of the mass shedding limit. Notice that for rapid rotators with $\Omega \gtrsim 3 \times 10^3\mathrm{s}^{-1}$ almost all the obtained equilibria appear as oblate ellipsoids. Finally, at higher magnetization the mass shedding limit occurs at higher densities with respect to the non-magnetized case. This happens because the toroidal magnetic field significantly expands and rarefies the outer layers of the star making them volatile to the centrifugal effects.

In analogy with the static case of the previous section, in Fig. 3.6 we show the variations $\Delta\rho_c$, ΔM_0, ΔR_circ together with $\bar{e}$ as a function of B_max, for different values of the rotational rate Ω at fixed gravitational mass $M = 1.55\mathrm{M}_\odot$. As expected, as the rotational rate increases, the central density together with the baryonic mass drops, while the equatorial circumferential radius R_c expands. Interestingly, the effect of the magnetic field along these equilibrium sequences is qualitatively independent from the specific value of Ω, tracing the same behaviors of static equilibria discussed in Sec 3.1. Notice, that here we are considering sequences with fixed gravitational mass: since the central density ρc diminishes with increasing magnetization, also the baryonic mass M_0 is a decreasing function of the magnetic field. The rotation acts in two ways: it produces an offset, which can be safely computed for unmagnetized models, and it increases the effectiveness of the magnetic field (at higher rotations a lower value of B_max is required to achieve the same deviation). Indeed we verified that the curves can be superimposed adding an offset corresponding to the unmagnetized rotators ($B_\mathrm{max} = 0$), and rescaling slightly the magnetic field with the rotation rate. Obviously at higher rotation rate, when the unmagnetized star is already close to the *mass shedding limit*, the magnetic field can be increased only marginally, and the magnetic non-linear regime of highly inflated stars is never reached. We found that while at $\Omega = 2 \times 10^3\mathrm{s}^{-1}$ the star reaches the mass shedding when $B_\mathrm{max} = 5.1 \times 10^{17}$ G, and $H/M = 0.0245$, at $\Omega = 4 \times 10^3\mathrm{s}^{-1}$ this happens for $B_\mathrm{max} = 1.1 \times 10^{17}$ G, and $H/M = 0.001$.

Another interesting parameter, that describes the joint effect of magnetic field and rotation is the apparent ellipticity. We find that as the rotation rate increases, this shows a peculiar trend. At low magnetization, the surface shape is always oblate, as expected for an unmagnetized rotator. As the magnetic field increases, the oblateness diminishes and the

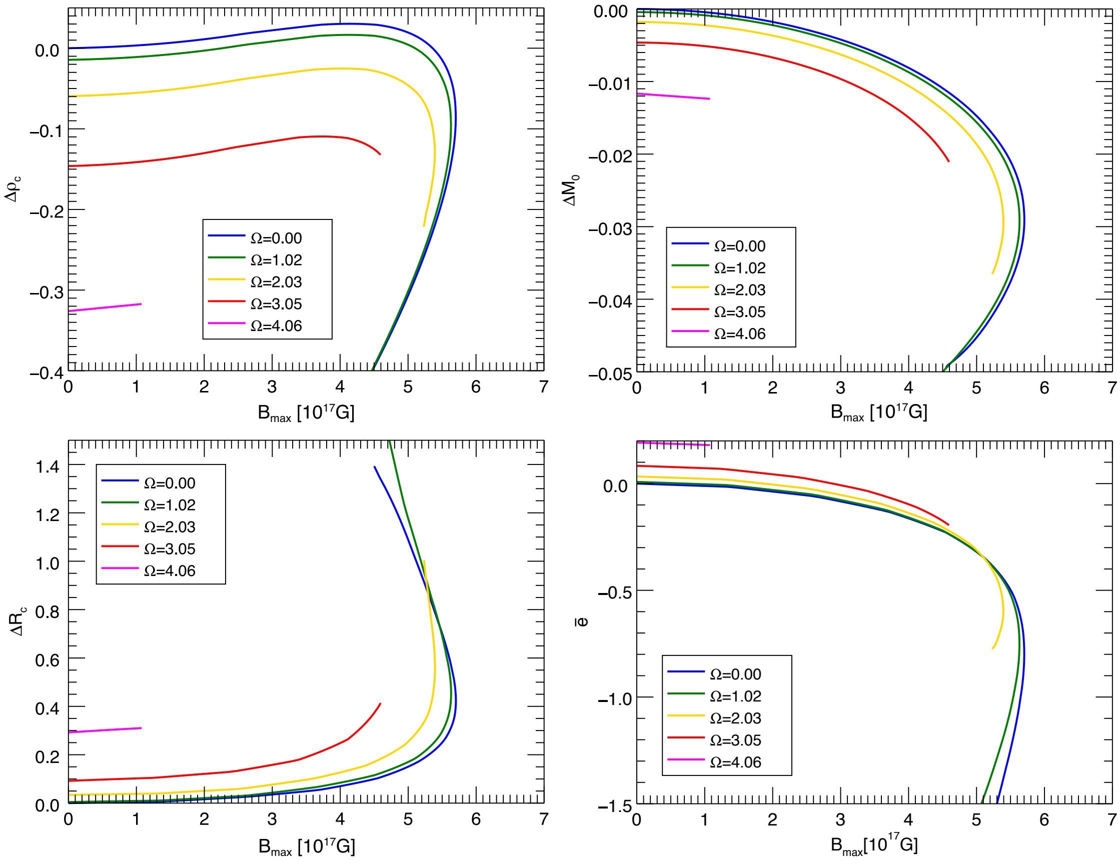

Figure 3.6: Variation with respect to the unmagnetized and static reference model of the baryon central density ρ_c, of the baryon mass M_0, of the circumferential radius $R_{\rm circ}$ and of the deformation $\bar{e}$, along the equilibrium sequences with fixed gravitational mass $M = 1.55 \mathrm{M}_\odot$, fixed magnetization index $m = 1$ but with different rotational rates expressed in unity of 10^{-3} s^{-1}.

shape can become prolate (this happens only for $\Omega < 2.5 \times 10^3 \mathrm{s}^{-1}$). Then as the magnetic field begins to inflate the outer layer of the star, the local centrifugal support is enhanced, and the star becomes oblate again (we observe this already at $\Omega = 10^3 \mathrm{s}^{-1}$). It was suggested by Frieben and Rezzolla (2012), that at the mass shedding all models show apparent oblateness: $R_{\mathrm{eq}} > R_{\mathrm{pol}}$. Indeed we find this to be consistent with our findings. For example models with $\Omega = 10^3 \mathrm{s}^{-1}$ have $e_s = -0.02$ at mass shedding. At lower rotation rates the accuracy with which we sample the surface, does not allow us to draw any conclusion. However this second transition toward apparent oblateness, only takes place in a range of magnetic energy extremely close to the threshold for mass shedding, when the circumferential radius almost doubles its size.

3.3 Trends at fixed gravitational mass and magnetic polytropic index

The trends shown in Fig. 3.7, suggest that it should be possible to find a global functional form able to describe with accuracy how global quantities change with similarity variables, such as the energy ratios H/M and H/W. We focus our analysis on the study of the induced deformation because this is the key physical parameter for GWs as discussed in Chap. 1. In the Newtonian case, in the limit $\Omega, B_{\max} \rightarrow 0$, it can be shown that deviations should scale bilinearly in H/W and T/W (Cutler 2002). These ratios represent, in fact, the relative energies of terms leading to deformations (magnetic field and rotation) with respect to the gravitational binding energy that tends to sphericize the star. We find for example that quantities like the baryon mass variation ΔM_0, the change in central density $\Delta\rho_{\mathrm{c}}$, the change in circumferential radius ΔR_{circ}, and the deformation ratio $\bar{e}$ can be fitted at fixed M and m for all values of Ω and $B_{\max}$ as:

$$\Delta q = \mathcal{G}_q(\Omega, H = 0) + \mathcal{F}_q\left([1 + a_q \Omega_{\mathrm{ms}}^2] H/W\right), \tag{3.2}$$

as shown in Fig. 3.7. Here Ω_{ms} is the rotation rate in units of the frequency of a millisecond rotator. The function $\mathcal{F}$ is linear in H/W in the limit $H \rightarrow 0$, as expected. a_q represents the non-linear coupling between magnetic field and rotation. This non-linear coupling term is small because rotation and magnetization cannot be increased independently in an arbitrary way, due to mass shedding. In the case of $\bar{e}$, we find $a_{\bar{e}} = -0.96$.

Within this parametrization the role of rotation is completely factored out in $\mathcal{G}$ (even if the kinetic energy enters also in the definition of W), which is linear in Ω^2 in the limit $\Omega \rightarrow 0$. It is remarkable that this self-similar scaling holds for highly deformed star in the full GR regime.

Interestingly we found that the deformation $\bar{e}$, can be fitted equivalently, as a function of

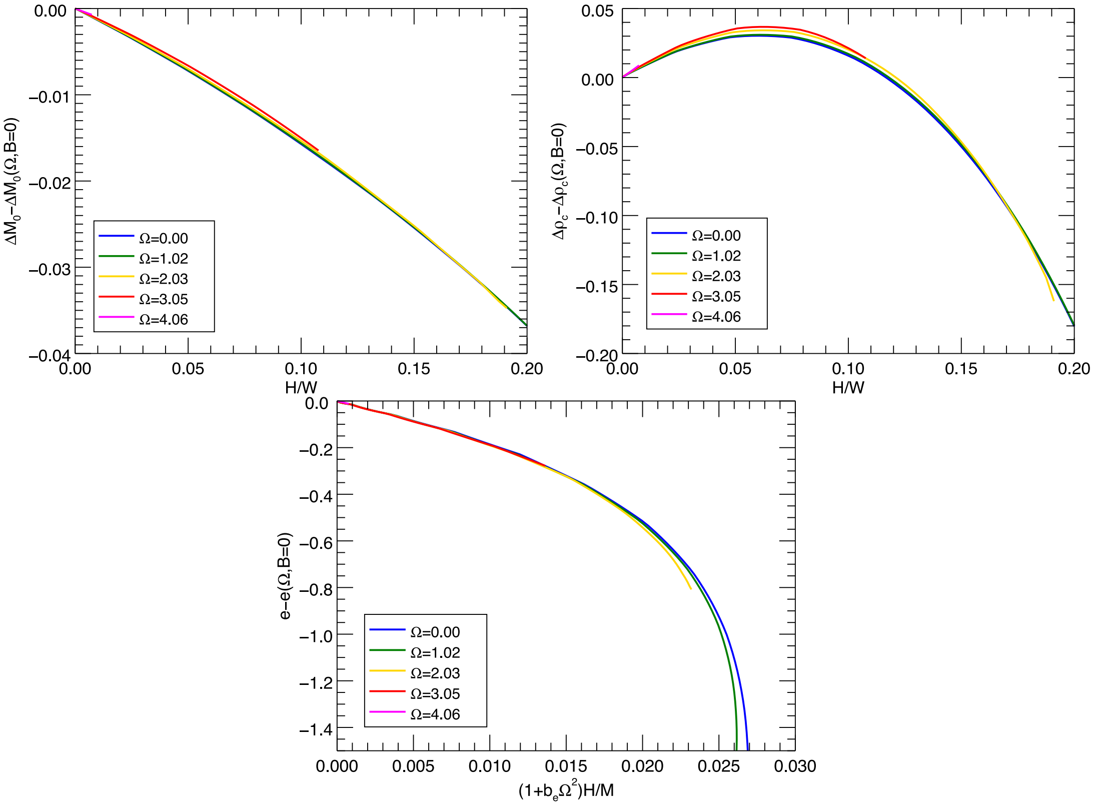

Figure 3.7: Variation of the baryonic mass, of the central density and of the deformation rate $\bar{e}$ with respect to the unmagnetized rotating reference model, as a function of the magnetic energy to binding energy ratio H/W or to gravitational mass H/M. The equilibrium sequences with different Ω are computed holding constant the gravitational mass $M = 1.55\mathrm{M}_{\odot}$.

H/M as:

$$\bar{e} = \mathcal{G}_{\bar{e}}(\Omega, H = 0) + \mathcal{B}_{\bar{e}}\left(\frac{H(1 + b_{\bar{e}}\Omega^2_{\rm ms})}{M}\right), \tag{3.3}$$

with $b_{\bar{e}} = -0.48$, as shown in Fig. 3.7. This reflects the fact that the non-linear coupling between rotation and magnetic field is negligible.

The bilinear approximation for the deformation is found to hold, with an error $< 10\%$ in the range $H/M \lesssim 0.01$, $T/M \lesssim 0.006$ (equivalently $H/W \lesssim 0.07$, $T/W \lesssim 0.04$ or $B_{\rm max} \lesssim 4 \times 10^{17}$ G, $\Omega \lesssim 0.001$), where one can write:

$$\bar{e} \simeq -d_B\, B^2_{17} + d_\Omega\, \Omega^2_{\rm ms}, \tag{3.4}$$

with $d_B \simeq 9 \times 10^{-3}$ and $d_\Omega \simeq 0.3$ (B_{17} is the maximum magnetic field strength in units 10^{17} G). In this linear regime the effects induced by rotation and magnetic field on the global deformation of the star $\bar{e}$ cancel if $B_{17} \simeq 6\,\Omega_{\rm ms}$, corresponding to a ratio of magnetic to kinetic energy $H/T \simeq 1.2$.

In the same limit $\Omega, B_{\rm max} \rightarrow 0$, also the apparent ellipticity of the surface can be fitted with a similar bilinaer dependence:

$$e_S \simeq -s_B\, B^2_{17} + s_\Omega\, \Omega^2_{\rm s}, \tag{3.5}$$

with $s_B \simeq 2.5 \times 10^{-3}$ and $s_\Omega \simeq 0.4$. Note that in terms of apparent ellipticity the effects induced by rotation and magnetic field cancel at $B_{17} \simeq 13\Omega_{\rm ms}$, corresponding to a ratio of magnetic to kinetic energy $H/T \simeq 6.8$. This is about a factor 5 higher than for $\bar{e}$, indicating that apparently oblate star, can in fact have a matter distribution that gives a net prolate quadrupole.

It is evident that in terms of deformation ratio, the contribution of the magnetic energy is analogous (even if acting in the opposite way) to that of the rotational energy, and the two tend to compensate each other close to equipartition, while rotational energy is slightly more efficient in determining the shape of the surface. This because magnetic field tends to act in the interior, while rotation mostly affects the outer layers. Note that while formally a parametrization in terms of Ω^2 and $B^2_{\rm max}$ is equivalent to one in T and H, the latter holds with the same accuracy for a $\sim 50\%$ larger range of magnetic field strengths and rotation rates.

3.4 The role of magnetic field distribution at fixed gravitational mass

In this section we discuss in more detail the effect of the different magnetic field distribution in order to generalize the scaling laws that we have found in the previous section in order to include also the contribution of the magnetic polytropic index m.

In Fig. 3.8 we show a comparison between rotating equilibria with the same gravitational

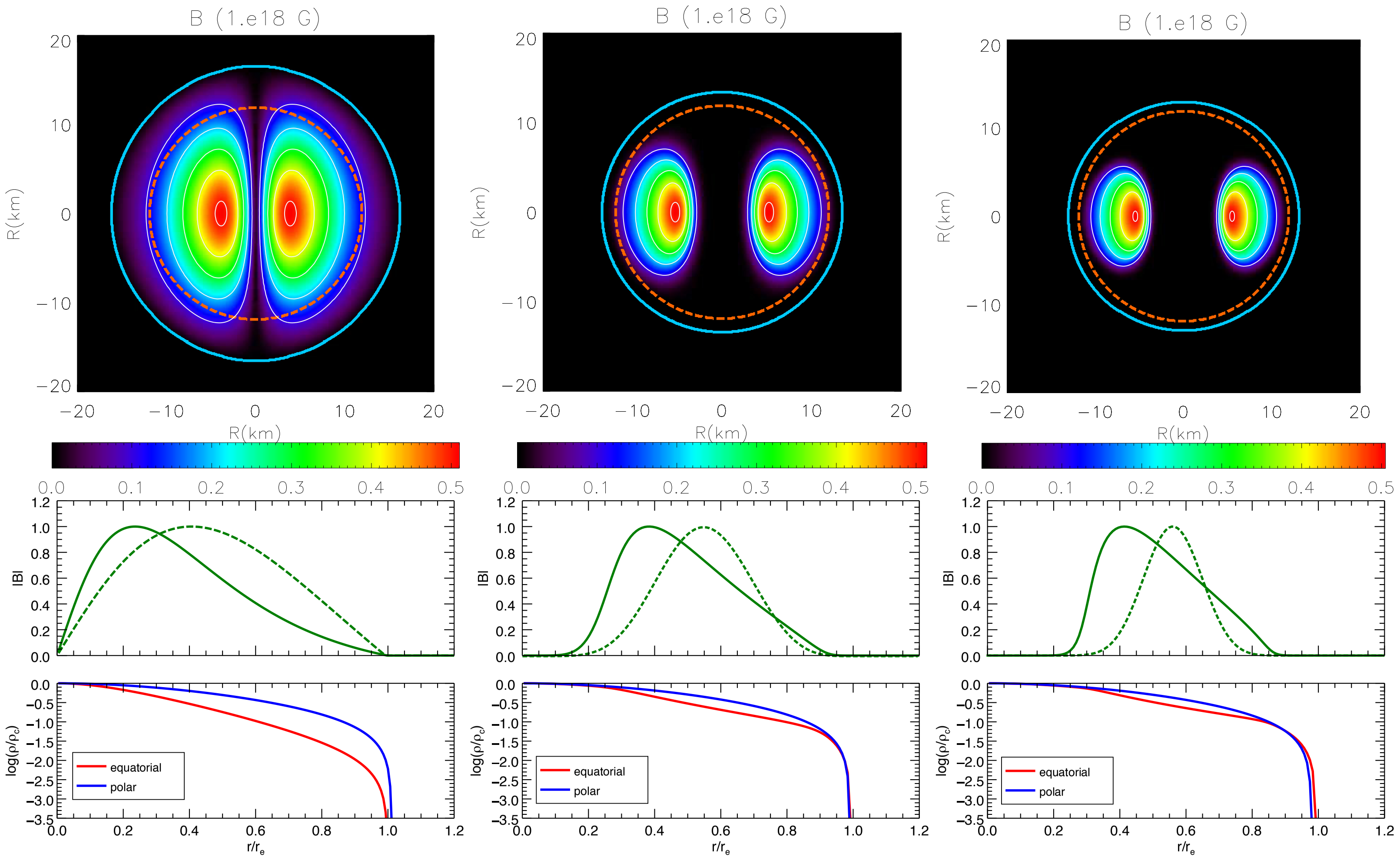

Figure 3.8: Top panels: distribution and isocontours of the magnetic field strength $B = \sqrt{B^{\phi}B_{\phi}}$ for equilibrium configurations with the same gravitational mass $M = 1.55\mathrm{M}_{\odot}$ and rotational rate $\Omega = 1.015 \times 10^{3}\mathrm{s}^{-1}$ but with different values of the magnetization index: $m = 1$ (left), $m = 4$ (middle) and $m = 10$ (right). The blue line is the stellar surface. Bottom panels: radial profiles of the magnetic field strength and of the baryon density normalized to peak values along the equatorial direction $\theta = \pi/2$ and the polar direction $\theta = 0$. The green dashed lines represent the magnetic field radial profile in the weak magnetization limit. Radii are normalized to the equatorial value r_{e}. Global physical quantities for these equilibrium configurations are listed in Table 3.4.

mass and the same value of the maximum magnetic field strength but with different values of m. A detailed quantitative characterization of these configurations is given in Tab. 3.4. As the value of m increases the magnetic field distribution becomes more concentrated toward the surface of the star, with a larger fraction of the star that behaves as if it was essentially unmagnetized. As a consequence the magnetic energy (at fixed maximum magnetic field strength) is smaller. This effect however is progressively less pronounced at higher magnetization, as shown by the comparison with the perturbative regime in Fig. 3.8, where we plot the magnetic field distribution in the radial direction at the equator for both the strong and weak field regime.

Table 3.4: Global quantities for the configuration shown in Fig. 3.8 with gravitational mass $M = 1.55 M_\odot$ and rotation frequency $\Omega = 2.03 \times 10^{-3} s^{-1}$.

	$B_{\rm max}$ 10^{17} G	Ω $10^3 s^{-1}$	ρ_c $10^{14} g/cm^3$	M_0 $M_\odot$	$R_{\rm circ}$ km	r_p/r_e	$\bar{e}$	n_s	H/W 10^{-2}	T/W 10^{-2}	H/M 10^{-2}	T/M 10^{-3}
m=1	5.12	2.3	8.07	1.65	18.3	1.01	-0.35	2.00	12.8	2.32	1.76	3.16
m=2	5.15	2.3	7.93	1.66	16.2	1.01	-0.20	2.00	9.00	2.16	1.29	3.10
m=4	5.15	2.3	7.95	1.66	15.6	1.03	-0.12	2.00	6.65	2.10	0.98	3.10
m=10	5.07	2.3	7.98	1.67	15.3	1.03	-0.07	2.00	4.81	2.06	0.72	3.09

Hence, if parametrized in terms of magnetic field strength, the effects against rotation are strongly reduced at higher m, leading to a smaller deformation and ellipticity. This is also evident from Fig. 3.10 where we plot the space of physical solutions in the case $m = 2$. Indeed, with respect to the $m = 1$ case (see Fig. 3.4), the mass-shedding line moves to lower densities and the region characterized by $e_s > 0$ shrinks toward models with lower compactness. In good part this is due to the fact that the inflationary effect on the outer layers of the star is also suppressed. In Fig. 3.9, we compare how some global quantities of interest change with m, in particular $\bar{e}$, ΔM_o and $\Delta \rho_c$, along the usual equilibrium sequences with $M = 1.551 M_\odot$ considering cases with $m = 1, 2, 4$. We find that, in terms of $B_{\rm max}$, the various cases show clearly distinct trends, as already discussed in Sec.3.1. We also found that for ΔM_0, once parametrized in terms of H/W the dependence on m becomes negligible (less than at most 5% for the fastest rotating configurations). Instead the parametrization Eq. 3.2 for the quadrupolar deformation leaves a residual dependence on m (at most 15%). This can be reabsorbed defining an effective energy ratio:

$$\bar{e} = \mathcal{G}_{\bar{e}}(\Omega, H = 0) + \mathcal{F}_{\bar{e}}\left([1 + a_{\bar{e}} \Omega^2_{\rm ms}] \left[0.84 + \frac{0.16}{m} \right] \frac{H}{W} \right), \tag{3.6}$$

which now generalizes Eq. 3.2 for different magnetic field distributions. The same holds for the apparent ellipticity, with major differences arising only close to the saturation fields, $B_{\rm max} \gtrsim 4 \times 10^{17}$ G.

Interestingly we found that, once parametrized in terms of H/M as in Eq. 3.3, both $\bar{e}$ and e_S show only a weak dependency (within 5%) on the parameter m even in the non-linear phase. Moreover from an observational point of view, one may prefer a parametrization in

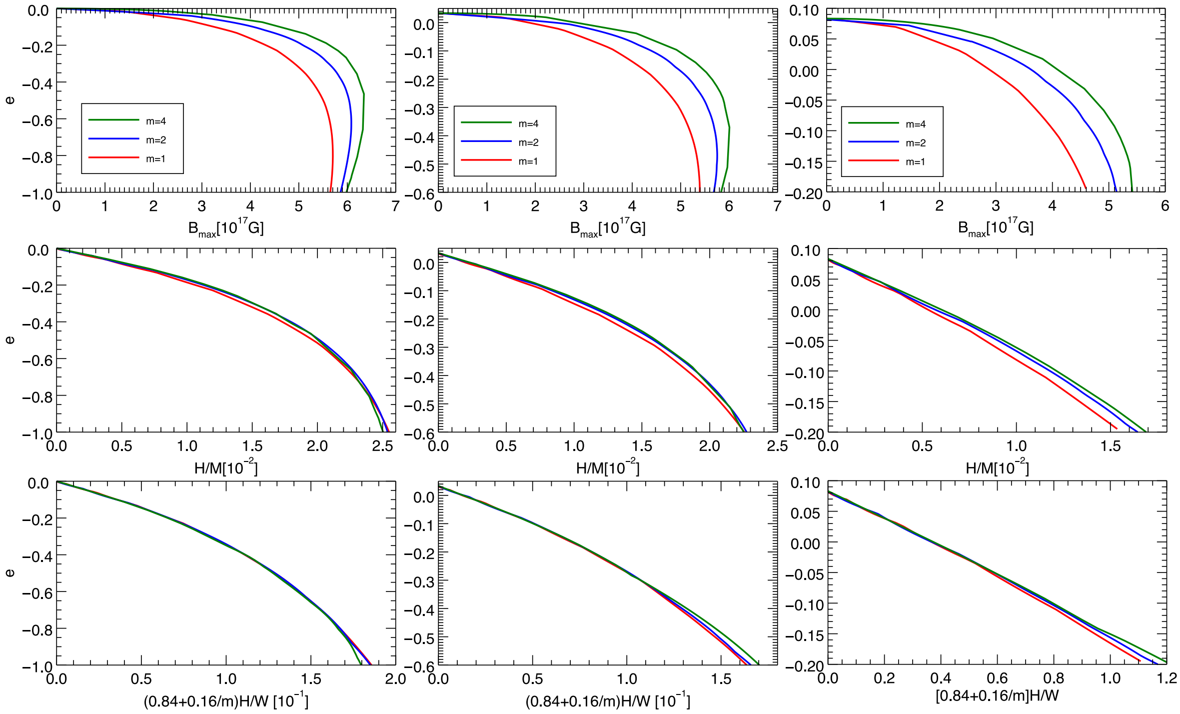

Figure 3.9: Mean deformation rate $\bar{e}$ as a function of the maximum magnetic field strength (top), of the magnetic energy to gravitational mass ratio (middle) and of the the effective magnetic energy ratio $[H/W]_{\rm eff}$ for different values of the magnetization index $m \in \{1, 2, 4\}$ along sequences of fixed gravitational mass $M = 1.55\mathrm{M}_\odot$ in the static case (left), with $\Omega = 2.03 \times 10^3\mathrm{s}^{-1}$ (centre) and $\Omega = 3.05 \times 10^3\mathrm{s}^{-1}$(right).

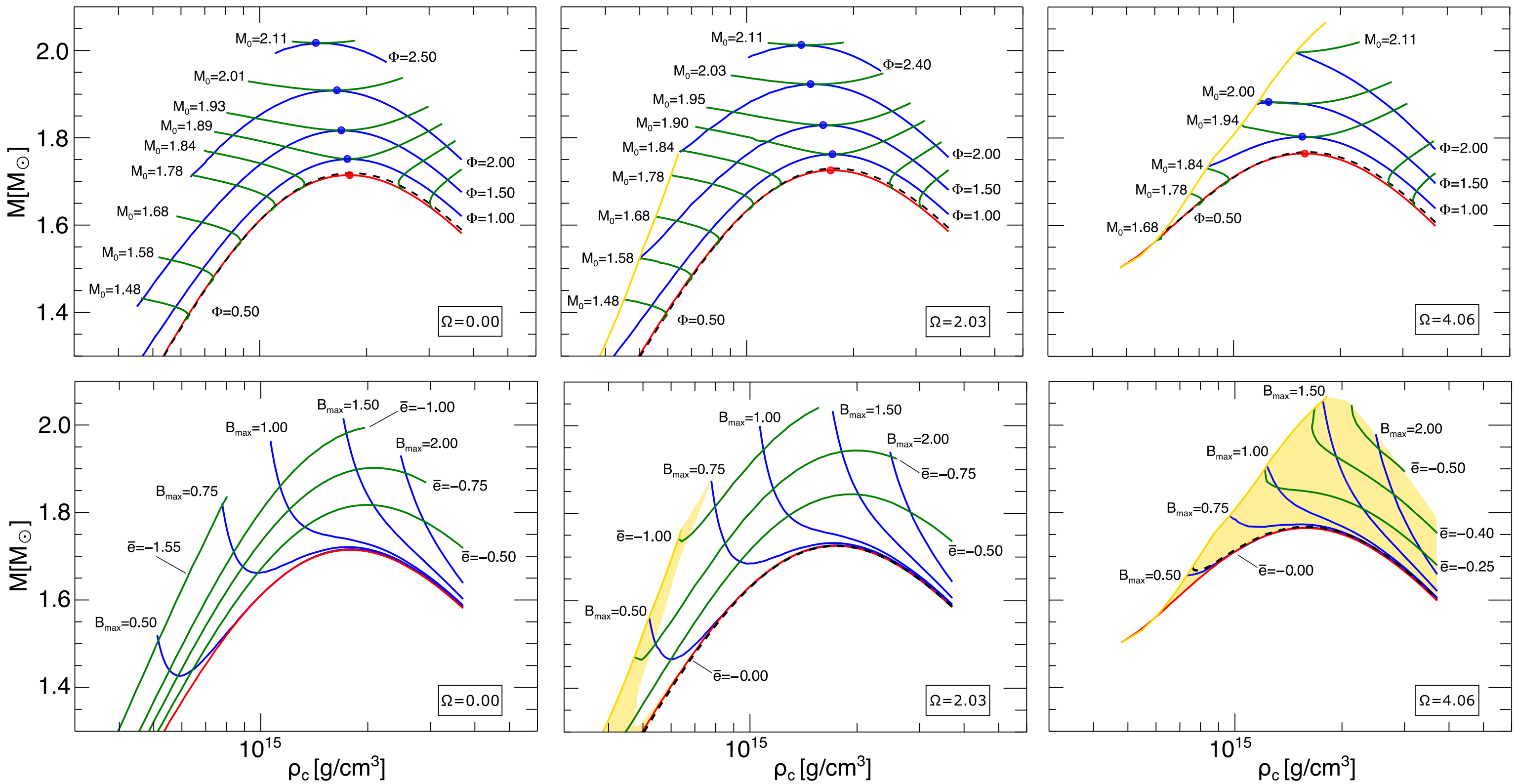

Figure 3.10: Space of physical solutions for magnetized NSs with magnetic index $m = 2$ and rigid rotation. Top row: equilibrium sequences with fixed baryonic mass M_0(green lines) and fixed magnetic flux Φ_B (blue lines) for different values of the rotational rate Ω. The black dashed lines represent configurations with a low value of the magnetic flux. Bottom row: equilibrium sequences at fixed maximum magnetic field strength $B_{\max}$ (blue lines) and fixed deformation rate $\bar{e}$. Here the black dashed line represents magnetized configurations with $\bar{e} = 0$. The yellow shaded regions indicate those configurations having $e_s > 0$. The red lines represent the unmagnetized sequences. The baryonic mass M_0 is expressed in unity of $M_\odot$, Φ_B in unity of 10^{30}G cm^2 and $B_{\max}$ in unity of 10^{18} G.

terms of the gravitational mass which is indeed a measurable quantity.

In the bilinear regime, the parametrization given by Eqs. 3.4-3.5, of the quadrupolar deformation $\bar{e}$ and of the surface ellipticity e_s, can be generalized as:

$$\bar{e} \simeq -\frac{d_B}{m} B_{17}^2 + d_\Omega \Omega_{\rm ms}^2, \tag{3.7}$$

$$e_{\rm s} \simeq -\frac{s_B}{m} B_{17}^2 + s_\Omega \Omega_{\rm ms}^2, \tag{3.8}$$

with the same values for d_B, and s_B. Now, since in the bilinear regime $\bar{e} \propto 17H/M$, Eq. 3.7 also implies that $B_{17} = 1.3 \times 10^2 \sqrt{mH/M}$.

Given the small residual effect due to m, it is reasonable to conclude that the quadrupolar and surface deformation gives only a direct indication of the magnetic energy content rather than of the current distribution, at least in the case of purely toroidal magnetic fields.

3.5 Trends at different mass

This section focuses on how the results depend on the mass and/or compactness of the NS. In general we found that the trends and scalings found in the previous sections, still hold at different masses in stable branches of the mass density relation. Obviously at lower gravitational mass (corresponding also to a lower compactness) the effects of rotation and magnetic field are enhanced.

For the deformation ratio $\bar{e}$, in the case of unmagnetized rotators, it is possible to reabsorb the mass differences in the term due to rotation by using as variable T/W, instead of Ω^2 or T/M. We also found that the trend is linear in T/W almost all the way up to the fastest rotators.

For the effects of the magnetic field on $\bar{e}$, and e_S, we find that they can be rescaled defining effective normalized (with respect to our fiducial model with $M = 1.55{\rm M}_\odot$) magnetic energy ratio, and rotational coupling term, such that:

$$\left[\frac{H}{W}\right]_{\rm eff} = \left[0.84 + \frac{0.16}{m}\right] \frac{1.55{\rm M}_\odot}{M} \frac{H}{W}, \tag{3.9}$$

$$a_{\bar{e}\,\rm eff} = -\left(3.94 - 2.98 \frac{M}{1.55{\rm M}_\odot}\right). \tag{3.10}$$

This behavior was already found to hold in the linear regime, for different EoS at fixed mass by Frieben and Rezzolla (2012). We prove here that it can be also generalized to the non linear regime for different masses and magnetic field distributions. It is interesting to notice that, while the rotational energy effects scales as T/W, the magnetic effects go as H/WM. This might be related to the way mass stratification couples with rotation and magnetic field: for a rigid rotator, the rotational stratification is independent of density and mass, while, given the magnetic barotropic law Eq. 3.1, as mass and stratification change so does the

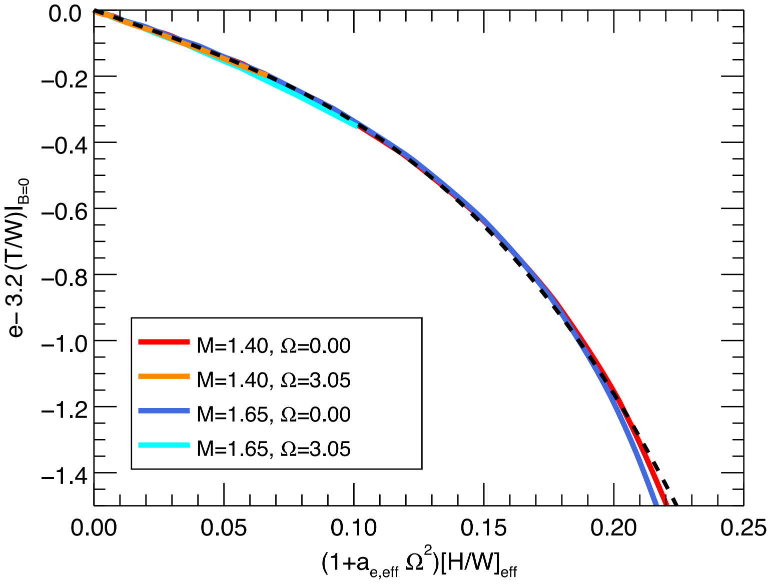

Figure 3.11: Deformation ratio $\bar{e}$ with respect to the unmagnetized model in terms of the effective magnetic energy mass ratio $[H/W]_{\rm eff}$ for configurations having gravitational mass 1.40 – 1.65 $\mathrm{M}_\odot$ and rotational frequency $\Omega = 0.0 - 3.05 \times 10^3\,\mathrm{s}^{-1}$. The black dashed line represents Eq. 3.11.

Table 3.5: Mass dependency for the $\bar{e}$ expansion coefficients.

M $\mathrm{M}_\odot$	d_Ω 10^{-1}	$d_{\rm B}$ 10^{-3}	s_Ω 10^{-1}	$s_{\rm B}$ 10^{-3}
1.40	4.2	17	6.0	4.8
1.45	3.8	14	5.1	4.1
1.50	3.4	12	4.6	3.6
1.55	3.0	9.5	3.8	2.6
1.60	2.6	7.4	3.5	2.2
1.65	2.2	5.5	3.1	1.5

magnetic field distribution.
We find that the following functional form:

$$\bar{e} \simeq 3.2 \frac{T}{W}\bigg|_{B=0} + \mathcal{F}\left(\left[1 + a_{\bar{e},\rm eff}\Omega^2_{\rm ms}\right]\left[\frac{H}{W}\right]_{\rm eff}\right) \tag{3.11}$$

$$\text{with} \quad \mathcal{F}(x) = -2.71x - 0.068(10x)^{3.2} \tag{3.12}$$

fits the deformation ratio for all values of Ω, H, M and m up to $\bar{e} \simeq 1$, with an error less than 5% as shown in Fig. 3.11.

In the bilinear regime, the coefficients in Eq. 3.7 will of course be functions of mass, as shown in Tab. 3.5, and one can immediately see that they show an almost linear trend with M, and both d_Ω and $d_{\rm B}$ decrease as M grows. Interestingly, the ratio $d_\Omega/d_{\rm B}$ grows with M.

The bilinear relation can be generalized to different masses also by using the magnetic and kinetic energy H and T, and recalling that for $H, T \to 0$ one has $W \to W_o = \text{const}$, we

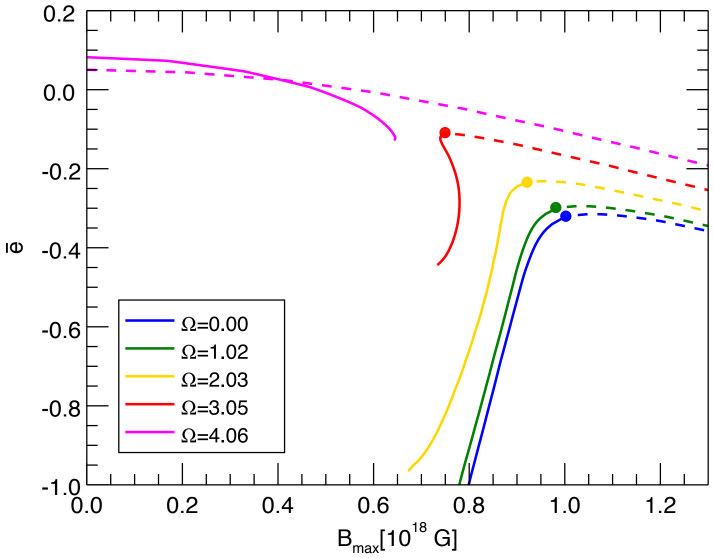

Figure 3.12: Variation of the mean deformation ratio $\bar{e}$ along equilibrium sequences characterized by fixed gravitational mass $M = 1.75\mathrm{M}_\odot$ and different value of Ω with $m = 1$. Filled circles represent the configurations with highest M_0 and they split each sequence into a low ρ_c (solid lines) and high ρ_c (dashed lines) branch.

obtain

$$\bar{e} \simeq \frac{C_{\bar{e}}}{W_o}\left[T - 1.3\frac{H}{M/\mathrm{M}_\odot}\right], \tag{3.13}$$

where the coefficient $C_{\bar{e}}$ depends on the specific EoS and the mass of the reference unmagnetized stationary configuration: for our fiducial model with $M = 1.551\mathrm{M}_\odot$ we have $C_{\bar{e}} = 3.2$ and $W_0 = 0.25M_\odot$. We recall that even the coefficient 1.3 in general has a residual dependence on m, but it can be taken as constant with an accuracy $\sim 10\%$.

We can conclude that, in the perturbative regime, the deformation ratio is linear in the quantity $T - 1.3H/(M/\mathrm{M}_\odot)$, which can be considered as a self-similarity variable, with all the information about the EoS, factored out in a single proportionality coefficient.

We can repeat the same analysis for the surface deformation in the bilinear regime. We found that the coefficients s_B and s_Ω in Eq. 3.8 also depend on mass and they both show a linear trend in accord with what was found for the deformation ratio. Coefficients are given in Tab. 3.5. Obviously a parametrization in terms of Ω^2 and B^2_max is not optimal, once different masses are taken into consideration (at fixed mass $\Omega^2 \propto T$ and $B^2_\mathrm{max} \propto H$, so it is equivalent to a parametrization in terms of kinetic and magnetic energies). We found that using the effective magnetic energy defined by Eq. 3.9, and T/W for the rotational contribution, the mass dependence can be reabsorbed analogously to Eq. 3.13, with an accuracy $\lesssim 10\%$

$$e_\mathrm{S} \simeq \frac{C_{e_\mathrm{s}}}{W_0}\left[T - 0.23\frac{H}{M/\mathrm{M}_\odot}\right], \tag{3.14}$$

with $C_{e_\mathrm{s}} \sim 4.2$. Note that given the accuracy of our solution, the surface deformation of our models cannot be determined better than 0.01, and models with $e_\mathrm{S} \gtrsim 0.05$ are already in the non-linear regime.

Up to this point we limited our investigations to equilibrium sequences with gravitational mass below the maximum mass of the static and unmagnetized sequences ($1.72\mathrm{M}_\odot$ for our choice of EoS). Moreover we have considered only equilibrium models with central density below the central density of the configuration with maximum mass ($\rho_\mathrm{c} < 1.8 \times 10^{15}\mathrm{g\,cm}^{-3}$). This corresponds to selecting sequences that are connected to the stable unmagnetized static branch and for which a comparison with a static unmagnetized reference model is meaningful.

The trends are more complex if one considers supramassive sequences (see Kiuchi and Yoshida (2008) for discussion). As an example we show in Fig. 3.12 the variation of the deformation ratio $\bar{e}$ in the case $M = 1.75\mathrm{M}_\odot$ for different values of Ω. No static configuration with such gravitational mass exists for magnetic flux $\Phi_\mathrm{B} < 1.31 \times 10^{30}\mathrm{G\,cm}^2$, neither unmagnetized configurations with $\Omega \lesssim 4 \times 10^3\mathrm{s}^{-1}$.

The trends of $\bar{e}$ shown in Fig. 3.12 can be understood by looking also at Fig. 3.4: the configurations with the minimal deformation is very close to the one that at fixed gravitational mass has the highest M_0 Moving away from this configuration, either toward lower or higher central densities, the deformation rises. At lower densities, despite the fact that the magnetic field also diminishes, the deformation rises because the star becomes less compact. At higher density, despite the star becoming more compact the magnetic field rises and its effect on the deformation becomes stronger. As one can see the interplay between the magnetic field, and the compactness can be quite different depending on the branch in the mass density sequence.

For a rotation rate $\Omega \gtrsim 4 \times 10^3\mathrm{s}^{-1}$, two unmagnetized configurations become possible (one stable one unstable) and the $\bar{e}$ sequence splits in two branches. The one connected with the unmagnetized configuration with lower ρ_c, the other connected with the unmagnetized configuration with higher ρ_c. Being this latter one more compact, both the effect of rotation and of the magnetic field are less pronounced.

3.6 Summary

During the evolution of the proto-NS the magnetic field is expected to relax toward a morphology characterized by a magnetic field with a toroidal component that is energetically dominant. The phenomenology of magnetars seems to confirm this picture: the extraordinary energetic activity of AXPs and SGRs may be sustained by the rearrangement and dissipation of a strong toroidal magnetic field buried inside the NS.

In this chapter we have explored a large sample of equilibrium models endowed with a purely toroidal field in both the static and rotating case. Our results are in agreement with those of Frieben and Rezzolla (2012). We find that the deformation of the star is always prolate if the magnetic energy is larger with respect to the rotational one. Consequently for very rapid rotators near the mass shedding, or for weakly magnetized rotators, the induced deformation is oblate. The threshold for oblate/prolate transition of the deformation ratio does not coincide with the transition between apparently prolate and apparently oblate NS: while the transition to $\bar{e} < 0$ happens very close to the equipartition when $H/T \sim 0.8M/\mathrm{M}_{\odot}$ the transition to $e_{\mathrm{s}} < 0$ is at $H/T \sim 4M/\mathrm{M}_{\odot}$. This reflects the different action of magnetic field (mostly affecting in the inner layers) and rotation (mostly affecting the outer ones).

In the static case, comparing configurations with the same mass, the deformation grows as the magnetic energy increases; the magnetic field strength instead reaches a maximum $\sim 6 \times 10^{17}$ G. Saturation is reached when the star begins to inflate to larger radii. While in the static case the outer layers can apparently inflate without limit, the rotation sets a limit to the size of the star. Since the magnetic field makes the outer layer more volatile, the mass shedding frequency reduces with respect to the unmagnetized case. As an example, considering our reference model with $M = 1.55\mathrm{M}_{\odot}$, the mass shedding frequency is $\Omega \sim 4 \times 10^{3}\mathrm{s}^{-1}$ in the unmagnetized case but $\Omega \sim 2 \times 10^{3}\mathrm{s}^{-1}$ with $B_{\mathrm{max}} \sim 5 \times 10^{17}$ G. As expected these effects are more pronounced in low mass stars, while more compact configurations, of higher central density, show smaller deformations, can support a stronger magnetic fields and more rapid rotations. As an example configurations with $\rho_c \gtrsim 10^{15}\mathrm{g\,cm}^{-3}$ can support magnetic field up to $\sim 10^{18}$G even for rapid rotation $\Omega \sim 4 \times 10^{3}\mathrm{s}^{-1}$ with deformations $\bar{e} \sim -1$; conversely, configurations with $\rho_c \lesssim 10^{15}\mathrm{g\,cm}^{-3}$ are characterized by a weaker magnetic field, always below $\sim 10^{18}$G, but they can show larger prolate deformations, with $|\bar{e}| > 2$ in the case of slow rotations.

The origin of the toroidal component of the magnetic field, is most likely to be found in the presence of large amount of differential rotation at birth, which itself is related either to the rotational profile of the core of the progenitor in core collapse events, or on the dynamics of merger in binary systems. For this reason we have investigated various current distributions, looking for possible signatures that the conditions at formation might leave on the remnant NS. In particular we have found that, at fixed maximum magnetic field strength, more concentrated currents (higher m), located in the outer layers of the star, induce weaker effects than those obtained with a more diffuse current extending deeper inside. This is clear if one looks at the energetics of the two configurations: being the strength of the magnetic field fixed, a more concentrated current corresponds to a lower value of the magnetic energy contained inside the star. Apart from small residual effects, the deformation ratio and the surface deformation of the star give only a direct indication of the magnetic energy content rather than the current distribution. Therefore they are more likely linked to the energetics of the differential rotation rather then its profile.

In literature the deformation is parametrized either in terms of B_{max} and Ω, or in terms of the rotational and magnetic energy. This is equivalent in the bilinear regime, but not so once the deformation exceeds $|\bar{e}| \sim 0.3$. For this reason we have investigated both parametrizations using a large and detailed sample of the parameter space. We have seen that, in opposition to a parametrization in terms of B_{max} and Ω, a parametrization in terms of the ratios H/W and T/W allows us to reabsorb the role of the current distribution, the rotation and the compactness of the star in a unique scaling law, that holds up to the fully non-linear regime with accuracy $\lesssim 5\%$. In particular we have seen that the effects of the rotation on various stellar quantities can be mainly described as a combination of a net effect (corresponding to the effect of the rotation on the unmagnetized models) plus an enhancement of the magnetic field effectiveness. Indeed the addition of rotation, diminishing the compactness of the star, makes the configuration more prone to the effects of the magnetic field itself.

In the case of $M = 1.4\mathrm{M}_\odot$, we can compare our result with those obtained by Cutler (2002) and Frieben and Rezzolla (2012) in the Newtonian limit (a comparison with GR results by Frieben and Rezzolla (2012) is not straightforward since they use a different parametrization based on the mean value of the magnetic field strength inside the star). In particular for the relation $\bar{e} = a_\Omega T/W + a_\mathrm{B} H/W$ we obtain $a_\Omega = 3.2$ and $a_\mathrm{B} = 2.97$ (see Eq. 3.13) which are similar to those obtained by Frieben and Rezzolla (2012), $a_\Omega = 3.8$ and $a_\mathrm{B} = 3.5$, and those obtained by Cutler (2002) with $a_\Omega = a_\mathrm{B} = 3.75$. Differences between distortion coefficients depends on the choices for the EoSs: while both Cutler (2002) and Frieben and Rezzolla (2012) adopt as reference model a NS having stellar radius $R = 10$ km, the former adopts an incompressible fluid and the latter a polytropic with $n = 1$; in our case we use $n = 1$ as well, but with a different polytropic constant leading to a NS with $R = 15$ km (see Sec. 2.8). Notice that our choice, leading to less compact configuration, should in principle imply higher value for a_Ω and a_B. However our calculations are made in GR and as pointed out by Frieben and Rezzolla (2012), a Newtonian treatment overestimates the correct distortion coefficient. Interestingly, for $M = 1.4M_\odot$, we find a ratio $a_\Omega/a_\mathrm{B} \sim 1.078$, similar to the value 1.085 found by Frieben and Rezzolla (2012) in the Newtonian limit. This suggests that the relative contributions of the magnetic field and of the rotation are the same independently from the compactness of the star, that only affect their absolute values.

4 Purely Poloidal Magnetic Field

Having investigated purely toroidal configurations, where however the magnetic field is fully confined inside the star, and has no other observational signatures than the NS deformation, in this chapter we consider equilibria with purely poloidal geometry, where the magnetic field extends also outside, where it is accessible through direct electromagnetic observations. As already anticipated in the introduction, the structure of the magnetic field near the surface of the NS may significantly differ from a purely dipole magnetic field, depending on the current distribution. Going beyond the pure dipole approximation, it is crucial to develop a reliable picture of local phenomenology (i.e. the spectral features of PSR J0821-4300 Gotthelf et al. 2013) that takes place near the surface of the star, and bears the signature of the higher-order multipoles. This in turn reflects the morphology of the current distribution inside the star, such that one can hope to use observations to constrain the latter.

This chapter, that focuses on modeling poloidal magnetic fields, is organized as follows: in Sec. 4.1 we analyze static configurations in order to isolate the effects of the magnetic field and the associated current distribution; we also discuss how different choices for the current distribution manifest themselves at the surface of the star; in Sec. 4.2 we study the interplay between rotation and electromagnetic field; in the remaining sections we present a quantitative analysis of the parameter space and show that even in the case of poloidal magnetic field it is possible to derive self-similar scalings. This chapter is based on Pili et al. (2014), Bucciantini et al. (2015b), Pili et al. (2017).

4.1 Static Models

Equilibrium configurations with purely poloidal magnetic field are obtained by choosing the current function $\mathcal{M}$ as in Eq. 2.100, i.e.

$$\mathcal{M}(\Psi) = k_{\rm pol}\Psi\left(1 + \frac{\xi}{\nu+1}\Psi^{\nu}\right),$$

where $k_{\rm pol}$ regulates the magnetization of the equilibrium configuration, ξ can be chosen such that the non-linear term leads to subtractive currents ($\xi < 0$) or additive currents ($\xi > 0$),

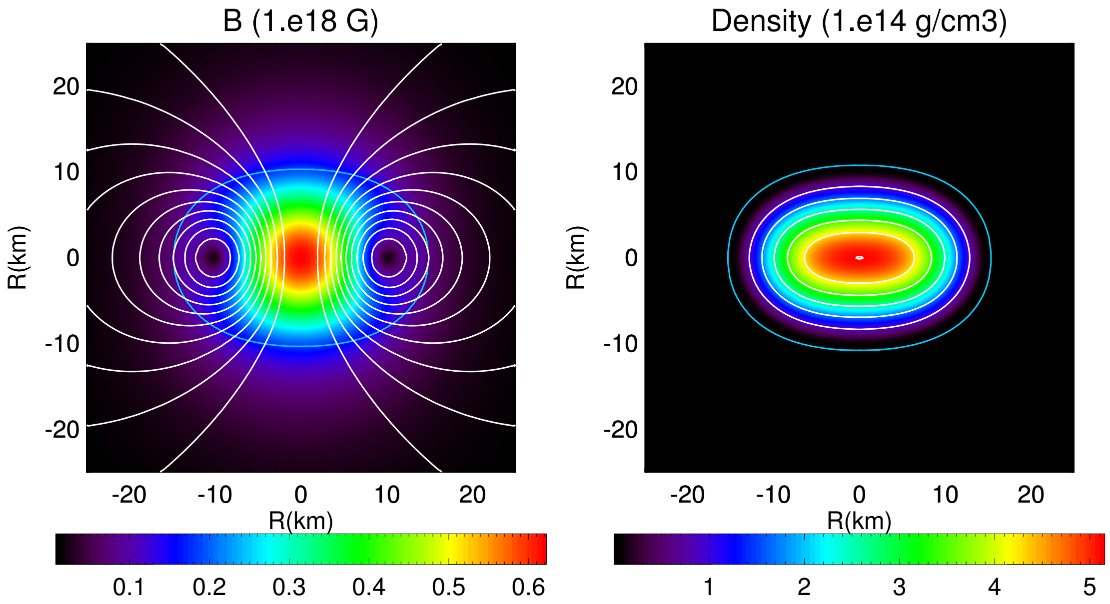

Figure 4.1: Left panel: *magnetic field surfaces* (isocontours of $\tilde{\Psi}$) and distribution of the magnetic strength $B = \sqrt{B^r B_r + B^\theta B_\theta}$. Right panel: baryonic density distribution. The blue curves represent the surface of the star. The model is characterized by $M_0 = 1.68 M_\odot$, $B_{\rm max} = 6.256 \times 10^{17}$ G and magnetic dipole moment $\mu = 2.188^{35}$ erg G^{-1}.

while the value of ν sets how much concentrated these currents are. Notice that the properties of the magnetic configuration are controlled exclusively by $\mathcal{M}(\Psi)$ since we set $\mathcal{I} = 0$ so that the conduction current is purely toroidal

$$J^\phi = \rho h k_{\rm pol} (1 + \xi \Psi^\nu) \, . \tag{4.1}$$

In Fig. 4.1 with present a model obtained with $\xi = 0$ so that only linear currents are present. This model shares the same baryonic mass $M_0 = 1.68 M_\odot$ and similar value of the maximum magnetic field strength $B_{\rm max} = 6.256 \times 10^{17}$G with the models shown in Fig. 3.1 for the purely toroidal case. In contrast to the toroidal case, for a purely poloidal magnetic field the NS acquires an oblate shape. The magnetic field threads the entire star and reaches its maximum at the very center. The pressure support provided by the magnetic field, leads to a flattening of the density profile in the equatorial plane. It is possible, for highly magnetized cases, to build also equilibrium models where the magnetic forces are able to redistribute the core density by moving the maximum value of ρ from the centre into a ring located in the equatorial plane (see Fig. 4.2). Because our numerical scheme is less accurate in this regime, in the following sections we will exclude this kind of configurations from the analysis of the parameter space. Moreover, as pointed out by Cardall et al. (2001) that adopt a numerical scheme similar to ours, at even higher magnetization no convergent numerical solution can be found because the magnetic field pushes off-center a sufficient amount of mass that the gravitational force, near the center of the star, points outward. Qualitatively, these effects are analogous to those produced by rotation. Rotation leads to oblate configurations, and for a very fast rotator, to doughnut-like density distribution. The main difference however, is

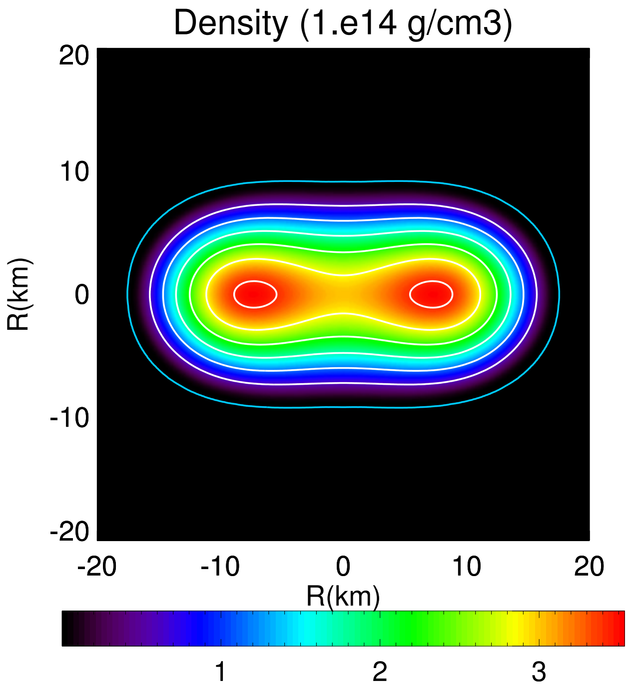

Figure 4.2: Baryonic density distribution for an extremely deformed configuration with a toroidal-like shape. This configuration is characterized by a baryonic rest mass $M_0 = 1.749 M_\odot$, a gravitational mass $M = 1.661 M_\odot$, a maximum field strength $B_{\rm max} = 5.815 \times 10^{17}\,{\rm G}$, a magnetic dipole moment $\mu = 3.595 \times 10^{35}\,{\rm erg\,G^{-1}}$, a circumferential radius $R_{\rm circ} = 19.33{\rm km}$ and a mean deformation rate $\bar{e} = 0.386$.

that rotation acts preferentially in the outer stellar layers, leaving the central core unaffected in all but the most extreme cases. A poloidal magnetic field instead acts preferentially in the core, where it peaks.

Another difference with respect to cases with a purely toroidal field, is the fact that the magnetic field extends smoothly outside the NS surface. Surface currents are needed to confine it entirely within the star (Tomimura and Eriguchi 2005). As a consequence, from an astrophysical point of view, the dipole moment μ is a far more useful parameter than the magnetic flux $\Phi_{\rm B}$, because it is in principle an observable (it is easily measured from spin-down).

Similarly to what was done in the case of a purely toroidal magnetic field, we have built an equilibrium sequence at fixed baryonic mass $M_0 = 1.680 M_\odot$. Changes in the various global quantities are shown as a function of the maximum magnetic field inside the star $B_{\rm max}$. The results in Fig 4.3 show that the central density ρ_c decreases with $B_{\rm max}$ while the gravitational mass M, the circumferential radius $R_{\rm circ}$ and the mean deformation ratio $\bar{e}$, which is now positive (oblateness), grow. As in the toroidal case, the equilibrium sequence is characterized by a turning point in the maximum magnetic field strength corresponding to $B_{\rm max} \approx 6.3 \times 10^{17}$ G. Along the sequences, the oblateness initially grows due to a rise of the magnetic field but, as soon as the maximum is reached, a further increase of the magnetization causes a rapid expansion of the equatorial radius and a rapid drop in the central density to which corresponds also a diminution of the polar radius. In the end, this leads to

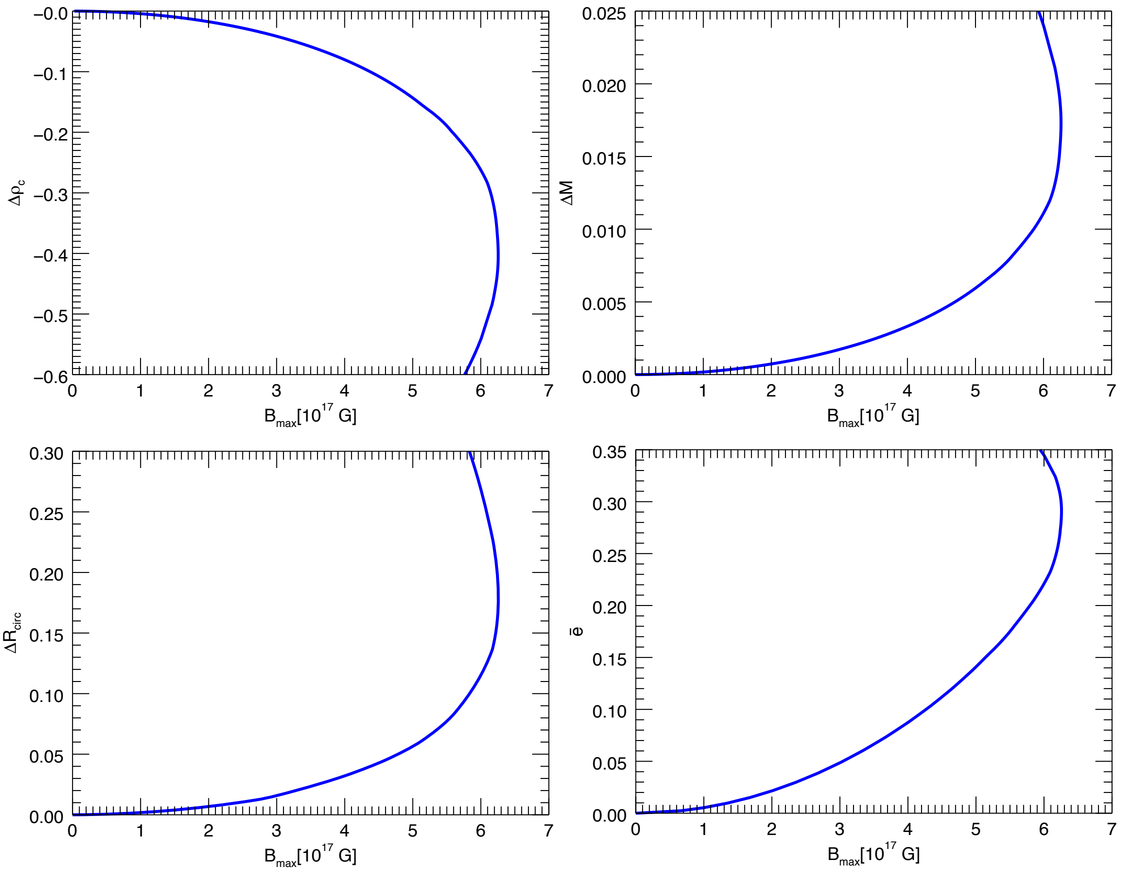

Figure 4.3: Variations of stellar quantities with respect to a non-magnetized configuration along an equilibrium sequence at fixed baryon mass $M_0 = 1.680 M_\odot$, for models with a purely poloidal magnetic field. Notation is the same as in Eq. 3.1.

Table 4.1: Global quantities from the poloidal models with maximum gravitational mass in sequences with fixed magnetic dipole moment μ, shown in Fig. 4.5.

ρ_c $[10^{14}\,\mathrm{g\,cm^{-3}}]$	M $[M_\odot]$	M_0 $[M_\odot]$	$R_{\rm circ}$ [km]	H/W $[10^{-2}]$	$B_{\rm max}$ $[10^{17}\,\mathrm{G}]$	$\bar{e}$ $[10^{-1}]$	r_p/r_e $[10^{-1}]$	μ $[10^{35}\,\mathrm{erg\,G^{-1}}]$
17.29	1.725	1.892	11.96	1.821	6.162	0.481	9.551	0.543
17.19	1.740	1.903	11.89	4.275	9.406	1.036	8.961	0.833
16.76	1.757	1.916	11.93	6.647	11.70	1.481	8.442	1.041
16.45	1.785	1.938	12.00	10.17	14.45	2.012	7.922	1.290

configurations with an off-centered density distribution. Notice that, unlike the toroidal field, the poloidal one does not inflate the outer layers, where the density profile remains similar to the unmagnetized case. In Fig. 4.4 we also display the variation of the magnetic dipole moment μ as a function of the maximum field strength $B_{\rm max}$. We notice that the trend is linear up to $\sim 10^{17}$ G and then increases rapidly once the field approaches its maximum.

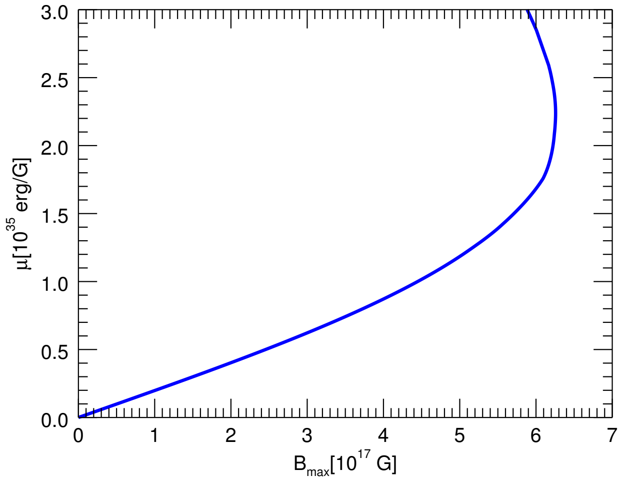

Figure 4.4: Magnetic dipole moment μ as a function of the maximum field strength inside the star $B_{\rm max}$ for an equilibrium sequence with the purely poloidal magnetic field and fixed baryon mass $M_0 = 1.680 M_\odot$.

Finally we have repeated a detailed parameter study, in analogy to what has been presented in the previous section, to explore the space $(\rho_c, k_{\rm pol})$. In Fig. 4.5 we show various sequences characterized by a constant baryonic mass M_0, or a constant magnetic dipole moment μ, or a constant maximum field strength $B_{\rm max}$, or a constant deformation ratio $\bar{e}$. As in the purely toroidal case, it is found that systems with lower central densities are in general characterized by larger deformations, for a given magnetic field and/or magnetic dipole moment. Notice also that, in contrast with the purely toroidal case, here the unmagnetized sequence is the one characterized by the smallest gravitational mass at fixed central density: there is no inversion trends with the magnetization $k_{\rm pol}$.

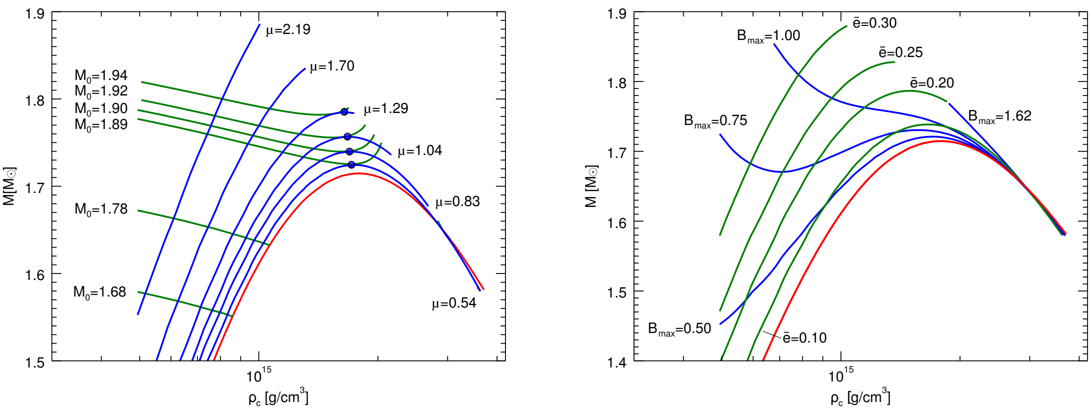

Figure 4.5: Left panel: equilibrium sequences with fixed magnetic field moment μ and fixed baryonic mass M_0. Right panel: equilibrium sequences with fixed deformation rate $\bar{e}$ and maximum field strength $B_{\rm max}$. The baryonic mass is expressed in units of $M_\odot$, the magnetic dipole moment in units of $10^{35}\,{\rm erg\,G^{-1}}$ and the maximum field strength in units of 10^{18}G. The red line shows the unmagnetized sequence while the filled dots locate the configurations with maximum mass for a given dipole moment μ. Parameters for these configurations are listed in Tab. 4.1.

4.1.1 Non linear current

Our choice for the magnetic function $\mathcal{M}$, allows us to investigate the effects of non-linear currents terms $J^\phi = \rho h k_{\rm pol} \xi \Psi$. Unfortunately we cannot treat configurations with only non-linear currents, because in this situation the Grad-Shafanov equation has always a trivial solution $\Psi = 0$, and our numerical algorithm always converges to it. It is not clear if non-trivial solutions of the Grad-Shafranov equation exist in any case, and it is just the numerical algorithm that fails to find them, or if they only exist for specific values of the background quantities (ρ, ϕ, α), and in this case it well could be that no self-consistent model can be build. So to model cases with $\xi \neq 0$, is it necessary to add a stabilizing linear current. This can be done either by adding a distributed current term $J^\phi = \rho h k_{\rm pol}$ or by introducing singular currents. For simplicity, we will not consider this latter possibility in the analysis of the parameter space and we will investigate configurations with distributed currents alone. The non-linear current terms may in principle produce multipolar magnetic configurations. Nevertheless, the symmetry of the magnetic field geometry is dictated by the stabilizing linear currents. Given that a current $J^\phi = \rho h k_{\rm pol}$, always gives *dipole-dominated* magnetic fields, this geometry will be preserved also by including non-linear terms. To obtain prevalent quadrupolar magnetic fields, one needs, for example, to introduce singular currents that are antisymmetric with respect to the equator as we will show later in this chapter (see Sub. 4.1.3).

In Fig. 4.6 we show the distribution of the linear and non-linear currents inside the star, both in the additive ($\xi = 20$) and subtractive ($\xi = -5$) cases with $\nu = 1$. Non-linear currents are more concentrated and they peak at larger radii. In the additive case, we succeeded in building models where non-linear currents are dominant in the outer stellar layers. On the contrary, for subtractive currents, we could not reach configurations with current inversions.

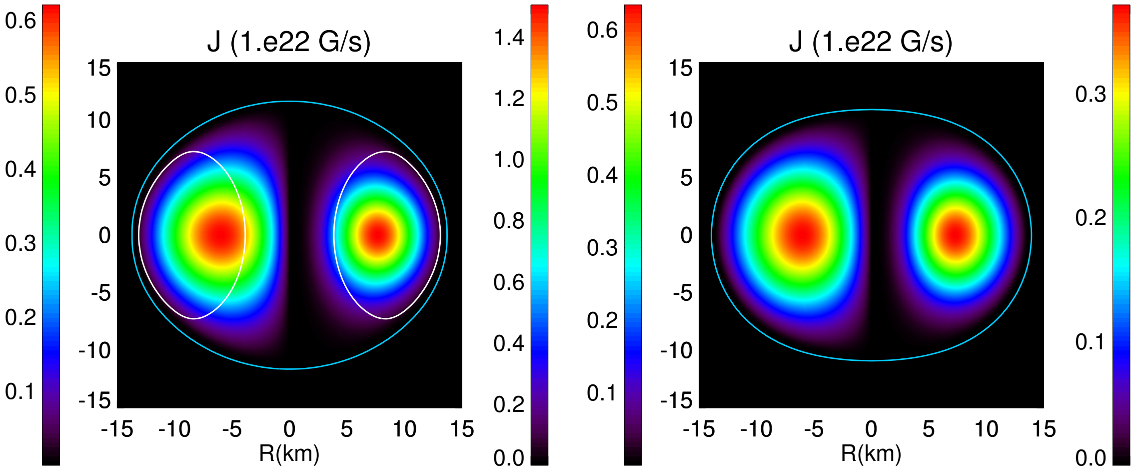

Figure 4.6: Comparison among models with different current distributions. Left panel: modulus of the zero-current term $J_0^\phi = \rho h k_{\rm pol}$ (left-half) and first-order one $J_1^\phi = \rho h k_{\rm pol}\xi\Psi$ (right-half) for an equilibrium configuration with $\xi = 20$, $M = 1.551 M_\odot$ and $\mu = 1.477 \times 10^{35}\,{\rm erg\,G^{-1}}$. Right panel: same as the left panel but for a model with $\xi = -5$, same mass $M = 1.550 M_\odot$ and magnetic dipole moment $\mu = 1.510 \times 10^{35}\,{\rm erg\,G^{-1}}$. The white line locates the points where $|J_1^\phi|/|J_0^\phi| \sim 1$. The blue line represents the stellar surface.

In Fig. 4.7 we compare how various global quantities change, as a function of the magnetic dipole moment μ for NSs with fixed gravitational mass $M = 1.551 M_\odot$, and for various values of the parameter $\xi \in \{-10, -5, 0, 20, 40\}$. We opted for a parametrization in terms of μ and M instead of $B_{\rm max}$ and M_0, because the former are in principle observable quantities, and as such of greater astrophysical relevance, while the latter are not.

Here we can note that, for a fixed dipole moment μ, the addition of negative current terms ($\xi < 0$) leads to less compact and more deformed configurations, conversely the presence of a positive current term ($\xi > 0$) makes the equilibrium configurations more compact and less oblate. This might appear as contradictory: increasing currents should make deformations more pronounced. However this comparison is carried out at fixed dipole moment μ. This means than any current added to the outer layers, must be compensated by a reduction of the current in the deeper ones (to keep μ constant). Giving that deformations are dominated by the core region, this explains why the star is less oblate. The opposite argument applies for subtractive currents.

4.1.2 Fully saturated current

In this subsection we extend the previous results obtained for $\nu = 1$, to more general current distributions in order to investigate also the role played by fully saturated non-linear currents. Because the convergence of our numerical code noticeably slows down with the introduction of non-linear current terms in the first part of this subsection we limit our analysis to weakly magnetized NSs (i.e. $H << M$). In this case one can safely assume that the metric

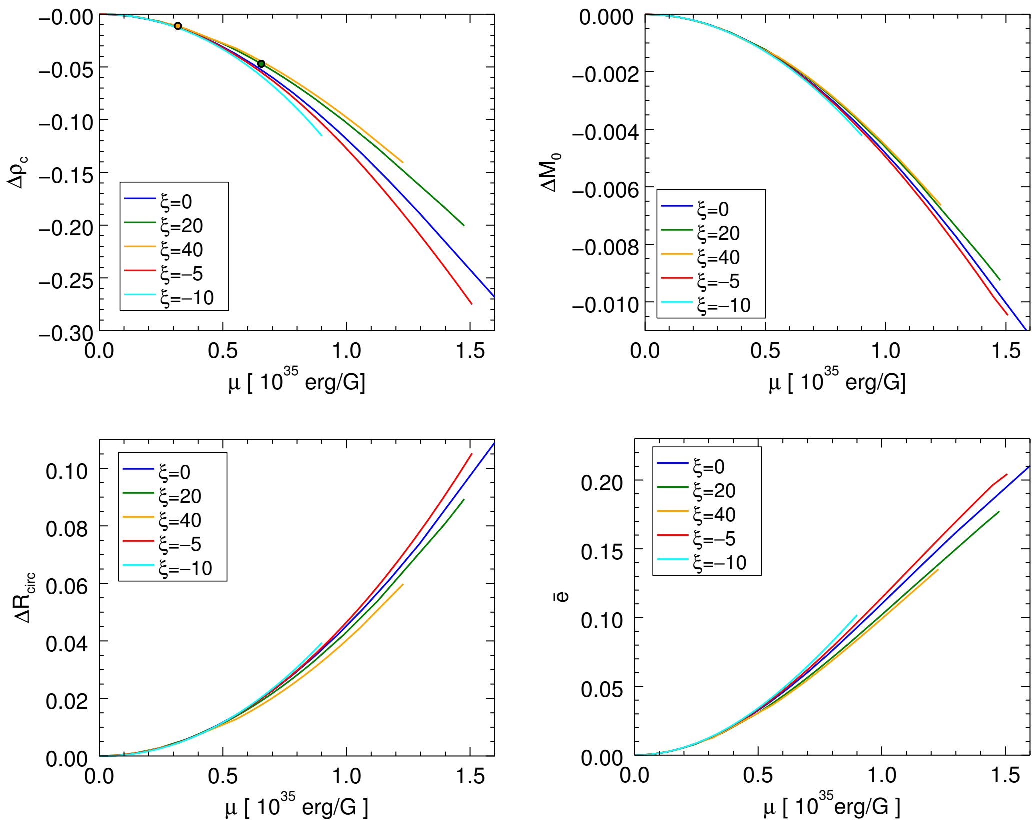

Figure 4.7: Variations of global quantities with respect to the non-magnetized configuration, as a function of the magnetic dipole moment, along an equilibrium sequence with fixed gravitational mass $M = 1.551 M_\odot$, and purely poloidal field. Notation is the same as in Fig. 3.2. Filled dots locate the points where the maximum strength of zeroth-order term $J_0^\phi = \rho h k_{\rm pol}$ is equal to the maximum strength of first-order term $J_1^\phi = \rho h k_{\rm pol} \xi A^\phi$. Details concerning these configurations and those which show the higher value of μ for each sequence are listed in Tab. 4.2.

Table 4.2: Global quantities of selected configurations belonging to the equilibrium sequences shown in Fig 4.7, at $M = 1.551 M_\odot$. For each value of ξ we show the details for the configuration with the maximal magnetic dipole moment. For cases with $\xi = 20, 40$ we also present those configurations where ratio $|J_1|/|J_0| \simeq 1$.

Model	ρ_c $[10^{14}\mathrm{g\,cm^{-3}}]$	M_0 $[M_\odot]$	R_{circ} [km]	r_p/r_e $[10^{-1}]$	$\bar{e}$ $[10^{-1}]$	H/W $[10^{-2}]$	$B_{\max}$ $[10^{17}\mathrm{G}]$	μ $[10^{35}\mathrm{erg\ G^{-1}}]$	$\lvert J_1\rvert/\lvert J_0\rvert$
$\xi = 20$	8.149	1.678	14.48	9.656	0.468	1.443	2.692	0.629	0.989
	6.810	1.665	15.54	8.420	1.773	6.656	4.595	1.477	2.421
$\xi = 40$	8.426	1.680	14.35	9.827	0.127	0.979	1.417	0.118	0.990
	7.320	1.670	15.11	8.857	1.352	4.837	3.964	1.230	4.023
$\xi = -5$	6.176	1.663	15.75	7.774	2.067	7.482	6.243	1.510	0.585
$\xi = -10$	7.543	1.674	14.79	8.996	1.014	3.099	4.782	0.911	0.691

terms α and ψ are the same as in the unmagnetized case (up to corrections of the order of H/M). Moreover, also the structure of the NS is weakly affected by the magnetic field and one has to solve only the GS Eq. 2.125 on top of the TOV solution. The solution of the GS equation, in turn, does not depend on the specific value of the magnetic field strength: if Ψ is a solution of the GS equation for given values of $k_{\mathrm{pol}}, \xi, \nu, \alpha, \psi, \rho$, then $\eta\Psi$ will be the solution for $\eta k_{\mathrm{pol}}, \xi, \nu, \alpha, \psi, \rho$. This implies that the strength of the magnetic field can be renormalized to any values for which the weak magnetization regime holds. In particular we have chosen to display our solutions by normalizing the strength of the magnetic field at the pole to 10^{14}G. We have verified that the limit of weak fields holds with high level of accuracy up to a maximum strength $\sim 10^{16}$G, corresponding to a typical surface magnetic field of a few 10^{15}G. Indeed, for higher fields we observe non-linear variations higher that the overall accuracy of our numerical scheme ($\sim 10^{-3}$, see also Appx. A). In the following, we adopt a slightly different form of the current function $\mathcal{M}(\Psi)$ that allows us to renormalize the current and to avoid divergences related to the iterative nature of our solver. In particular:

$$\mathcal{M}(\Psi) = k_{\mathrm{pol}}\Psi\left[1 + \frac{\hat{\xi}}{\nu+1}\left(\frac{\Psi}{\Psi_{\max}}\right)^{\nu}\right], \tag{4.2}$$

where $\Psi_{\max}$ is the maximum value of the magnetic potential.

In Fig. 4.8 we show the magnetic field and the current distribution for a series of models computed with different values of $\hat{\xi} < 0$ and different values for the poloidal index ν. The effect of the nonlinear term is to suppress the currents in the outer part of the star, and to concentrate them in the inner region. The same holds for the magnetic field. As $\hat{\xi}$ decreases, the interior of the star becomes progressively less magnetized, and the magnetic field is confined toward the axis. It is interesting to note that this effect becomes significative only as $\hat{\xi}$ approaches -1.0 (for values of $\hat{\xi}$ closer to 0 deviations are marginal). Moreover it is evident that in the case of subtractive currents the magnetic field geometry that one finds is almost independent on the magnetization index ν. Indeed the change in poloidal index seems only to produce marginal effects in the magnetic field distribution, with configurations that are slightly more concentrated toward the axis for smaller values of ν. In particular we find that the unmagnetized and current free region extends to fill the outer half of the star (the magnetic field at the equator drops to zero at about half the stellar radius). One also finds, in general, that the ratio of the strength of the magnetic field at the pole, with respect to the one at the centre, increases by about 30 to 50%, as $\hat{\xi}$ approaches -1.

Interestingly, we were not able to obtain models with $\hat{\xi} < -1$. This implies that we cannot find configurations where there is a current inversion (the sign of the current is always the same inside the star). Our relaxation scheme for the GS equation seems at first to converge to a metastable equilibrium with accuracy $\sim 10^{-4}$, but then the solution diverges. We want to stress here that the Grad-Shafranov equation, in cases where the currents are nonlinear in the vector potential Ψ, becomes a nonlinear Poisson-like equation, that in principle might admit multiple solutions and bifurcations (local uniqueness is not guaranteed). This is a known problem (Ilgisonis and Pozdnyakov 2003), and suggests that a very small tolerance (we adopt 10^{-8}) is required to safely accept the convergence of a solution. As discussed in Sec 2.3, a nonlinear Poisson equations of the kind $\nabla^2\psi = k\psi^a$ satisfy local uniqueness only if $ka \geq 0$. It is evident that this depends on the relative sign of the coefficient and exponent of the nonliner source term: in our case the relative sign of $\hat{\xi}$ and ν. Given that ν is always positive, what matters is just the sign of ξ. This explains why we can obtain solutions with additive currents ($\xi > 0$) even in the regime dominated by the nonlinear term, while solutions with subtractive currents ($\xi < 0$) can only be built up to $\xi > -1$, where the contribution of the nonlinear current is still smaller than the linear one which acts as a stabilizing term. However we want to recall here that the GS equation is not a Poisson equation, and it is not proved that the same uniqueness criteria apply.

In Fig. 4.9 we show the opposite case of additive currents, $\hat{\xi} > 0$. The value of ν in this case establishes how much concentrated these currents are, and plays a major role in determining the properties of the resulting magnetic field. Rising the value of $\hat{\xi}$ the nonlinear currents become progressively more important. We can define a nonlinear dominated regime in the limit of high $\hat{\xi}$, where the magnetic field structure and distribution converge to a solution that is independent of $\hat{\xi}$. The values of $\hat{\xi}$, at which this limit is reached, depends on ν. For $\nu = 1$ the limit is achieved already at $\hat{\xi} = 20$ as can be inferred from Fig. 4.9, while for $\nu = 10$ the limit is reached at $\hat{\xi} \sim 1000$.

In contrast with the case $\nu = 1$, where the presence of the non-linear current does not alter significantly the morphology of the magnetic field, at higher values of ν the magnetic field geometry in the nonlinear dominated regime changes substantially. The overall current is strongly concentrated around the neutral point. The location of the neutral point itself shifts toward the surface of the NS, from about 0.7 stellar radii at $\xi = 0$ to about 0.8 stellar radii in the nonlinear dominated limit. Moreover the maximum in the strength of the magnetic field is not reached at the centre any longer, but at intermediate radii where the nonlinear current is located. In this case the value of this local maximum can be a factor a few higher than the value at the centre. Configurations with two local maxima are also possible. This

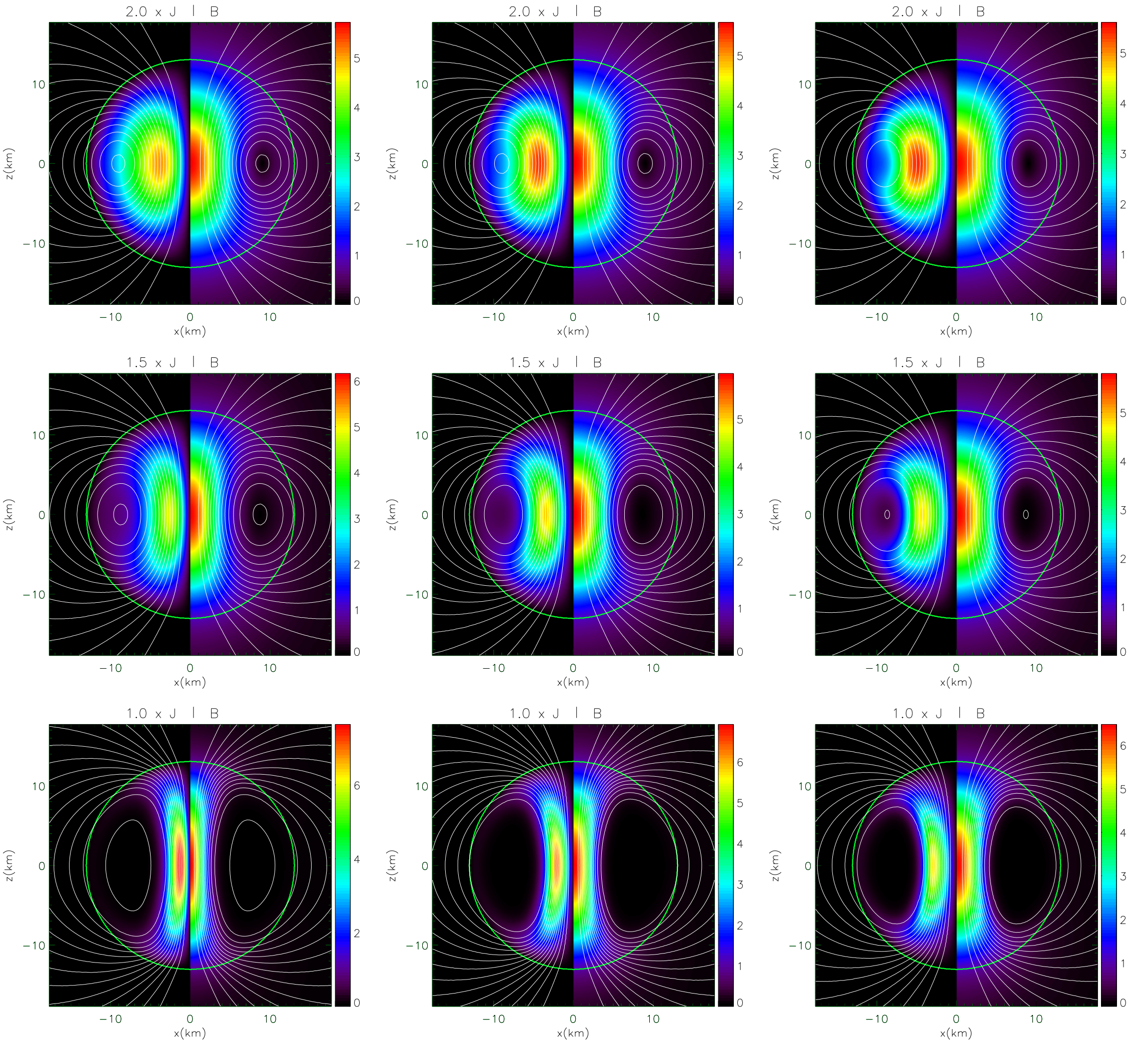

Figure 4.8: Strength of the azimuthal current in units of 10^{19}G s^{-1} (left half of each panel) and strength of the poloidal magnetic field in units 10^{14} G (right half of each panel). White contours represent magnetic field surfaces (isocontours of $\tilde{\Psi}$). The left column represents cases with $\nu = 1$, the central one those with $\nu = 4$, the right one those with $\nu = 10$. From top to bottom, rows represent cases with $\hat{\xi} = -0.5, -0.9, -1.0$. The thick green line is the stellar surface. In all cases the surface magnetic field at the pole is 10^{14} G.

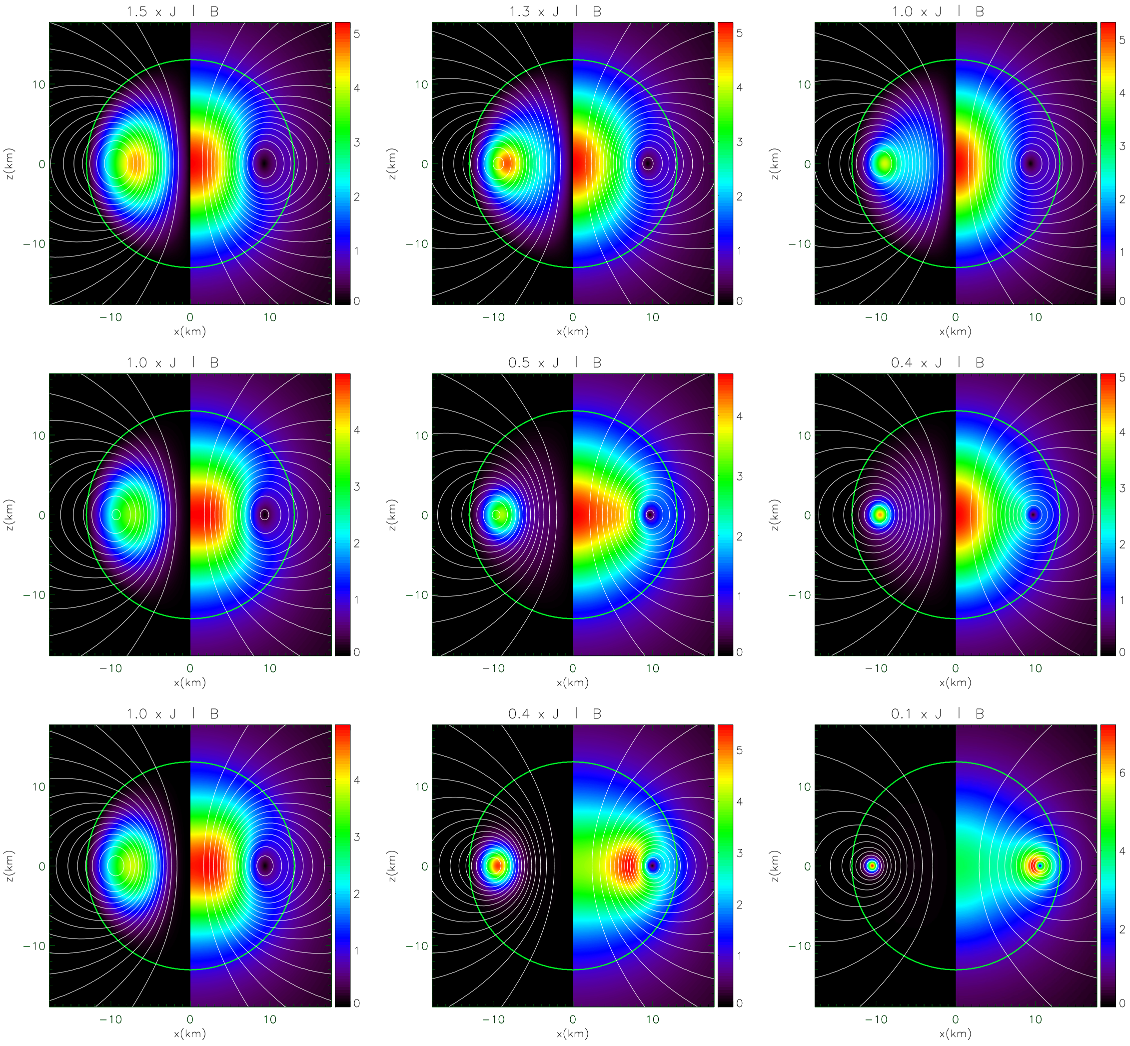

Figure 4.9: Strength of the azimuthal current in units of 10^{19}G s^{-1} (left half of each panel) and strength of the poloidal magnetic field in units 10^{14} G (right half of each panel). White contours represent magnetic field surfaces (isocontours of $\tilde{\Psi}$). The left column represents cases with $\nu = 1$, the central one those with $\nu = 4$, the right one those with $\nu = 10$. From top to bottom, rows represent cases with $\hat{\xi} = 2.0, 10.0, 200.0$. The thick green line is the stellar surface. In all cases the surface magnetic field at the pole is 10^{14} G.

behavior is strongly reminiscent of what is found for the so-called TT configurations, where a toroidal component of the magnetic field is also present, inducing a current that behaves as the nonlinear term we have introduced here (see the next Chap. 5).

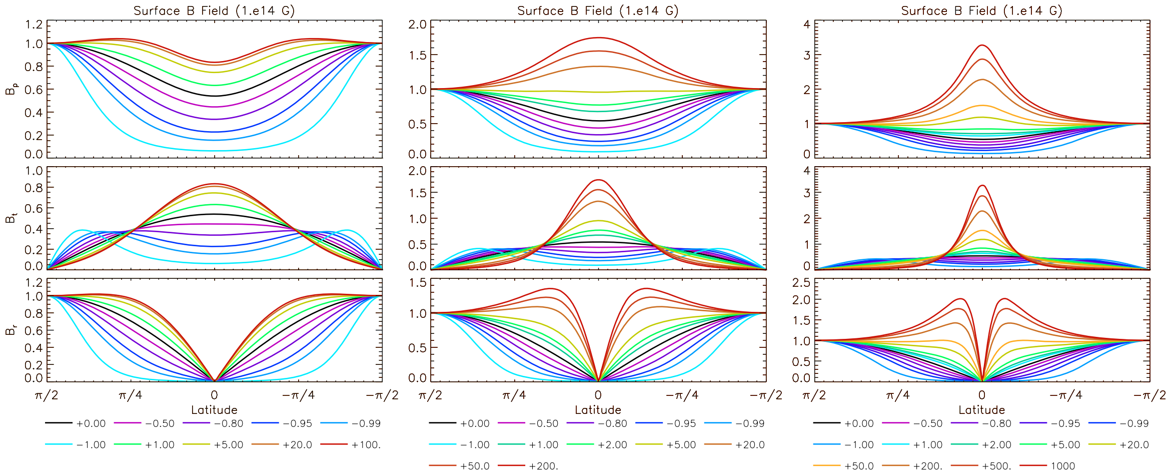

Figure 4.10: Magnetic field at the surface normalized to the value at the pole, for various values of $\hat{\xi}$. Left column represents cases with $\nu = 1$, central column cases with $\nu = 4$ and right column cases with $\nu = 10$. Upper panels display the total strength of the poloidal magnetic field, middle panels the strength of the parallel θ component, and lower panels the radial one.

One can also look at the strength and distribution of the surface magnetic field, shown in Fig. 4.10. For decreasing values of $\xi < 0$ the magnetic field tends to concentrate at the pole, in a region that is $\sim 30°$ for $\xi = -1$. The radial magnetic field in the equatorial region is strongly suppressed, the field is almost parallel to the stellar surface, and the overall strength of the poloidal field is a factor 10 smaller with respect to the case with $\xi = 0$. In general these results are weakly dependent on the value of ν, with higher values of ν leading to configurations where the field is slightly less concentrated toward the poles. A quite different behavior is seen for the cases of additive currents $\xi > 0$. For $\nu = 1$, the radial component of the magnetic field tends to be higher than in the case $\xi = 0$, and it tends to be uniform in the polar region. The θ component of the magnetic field increases in the equatorial region by about a factor 2. The overall strength of the magnetic field becomes quite uniform over the stellar surface in the nonlinear dominated regime. These effects are further enhanced for increasing values of ν. At $\nu = 4$, in the nonlinear dominated regime, the radial component of the magnetic field reaches its maximum at $\sim \pm 25°$ from the equator. The θ component, parallel to the NS surface, is instead strongly enhanced by about a factor 3 at the equator. The result is that for increasing ξ there is a transition from configurations where the poloidal field strength is higher at the poles, to configurations where it is higher (by about 40%) at the equator, with intermediate cases where it can be almost uniform. At $\nu = 10$ these effects are even stronger: the radial field now peaks very close to the equator, at $\sim \pm 10°$, and the overall strength of the magnetic field can be higher at the equator by a factor ~ 3 with respect to the poles. This is the clear manifestation of a concentrated and localized peripheral current close to the surface of the star.

Strong field regime

Let us come back to strongly magnetized equilibria in order to characterize the deformation induced by the different current distributions with $\nu > 1$. In Fig. 4.11 we plot the deformation ratio $\bar{e}$, and the relative variation of the circumferential radius $\Delta R_{\rm circ}$ for various values of ν, and with $\hat{\xi}$ chosen such that the fully non linear regime is reached, both for subtractive and additive terms. Note that, for subtractive currents, the deformation ratio is insensitive to the values of ν, because, as we have shown, in the subtractive case, the resulting magnetic field is only very weakly dependent on ν. On the other hand, substantial differences are observed in the case of additive currents.

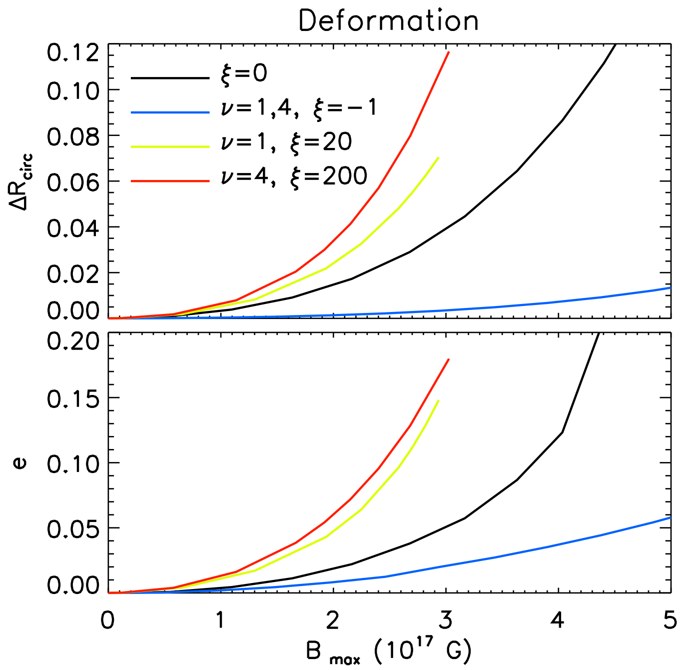

Figure 4.11: Upper panel: relative variation of the circumferential radius as a function of the maximum strength of the magnetic field inside the star, for various values of ν and $\hat{\xi}$. Lower panel: deformation rate as a function of the maximum strength of the magnetic field inside the star. These sequences are done for a constant gravitational mass $M = 1.4 M_{\odot}$.

Subtractive currents tend to concentrate the field toward the center. This leads to significative changes of the rest mass density distribution limited to the core (structures with two rest mass density peaks can be reached) without affecting the rest of the star. As a consequence, the deformation rate, being related to the moment of inertia, changes less than in the case $\hat{\xi} = 0$, where a more uniformly distributed magnetic field affects also the outer layers. On the contrary, additive non linear currents tend to concentrate the field toward the edge of the star, and thus to produce a stronger deformation. This trend is evident in the circularization radius. This radius is almost unchanged for $\hat{\xi} = -1$, while for $\hat{\xi} > 0$ the field causes a larger expansion of the outer layers of the star. Note that for $\hat{\xi} = 0, -1$ and for $\nu = 1$ the maximum magnetic field strength is reached at the center. For $\nu = 4$ and $\hat{\xi} >> 1$ it is reached half way through the star (see Fig. 4.9).

4.1.3 Antisymmetric solutions

As we already discussed in Sect.4.1, the parity of the magnetic field, with respect to the equator, depends on the parity of the linear current term in the magnetization function $\mathcal{M}$. All the solutions that we have shown previously are symmetric (for Ψ) with respect to the equator because this linear current term is proportional to the rest mass density. This is a requirement built into the integrability condition leading to the Bernoulli integral of Euler equation that fixes the possible functional forms of $\mathcal{M}$. If one is willing to relax the global integrability condition, by allowing for example singular surface currents, it is possible to obtain antisymmetric solutions. Due to the presence of a surface current, there will be a jump in the parallel component of the magnetic field at the surface. However, introducing non linear current terms in $\mathcal{M}$, one can go to the fully non linear saturated regime, where the contribution of the linear current term becomes negligible, and makes the residual jump in the magnetic field at the surface arbitrarily small. The non linear current term will preserve the parity of the surface current. We stress that, in this case, equilibrium and integrability hold inside the star, except at the surface itself.

If we choose for $\mathcal{M}$ the following functional form:

$$\mathcal{M}(\Psi) = k_{\rm pol}\Psi\left[\frac{\hat{\xi}}{\nu+1}\left(\frac{\Psi}{\Psi_{\rm max}}\right)^{\nu}\right], \tag{4.3}$$

and add to the current J^{ϕ}, that enters the Grad-Shafranov Eq. 2.125, a singular current term:

$$k_{\rm pol}\cos\theta\,\delta(r-R_{NS}), \tag{4.4}$$

by rising the value of $\hat{\xi}$ one can find solutions that are independent of the strength of the surface current. We show in Fig. 4.12 the result in the case $\nu = 1$, $\hat{\xi} = 50$. The jump at the surface is much smaller than the value of the magnetic field, and the solution can be assumed to be smooth. The result is dominated by the quadrupolar component.

Notice that the symmetry of the current term only fixes the symmetry of the final solution. Every symmetric current will lead to the same symmetric field, which depends only on ν, while every antisymmetric function will lead to the same antisymmetric field, which again depends on ν alone. With this approach it is not possible to produce for example octupolar models (where the dipole and quadrupole components are absent). Even the use of an octupolar surface current leads to dipolar configurations, in the fully saturated nonlinear regime. In the presence of non linear current term, multipoles are not eigenfunctions of the Grad Shafranov, and mode mixing is introduced. For the values of ν that we investigated, there is always a leading dipole component in the symmetric case, and a leading quadrupole component in the antisymmetric case, even if the strength of higher order multipoles at the surface can be relevant.

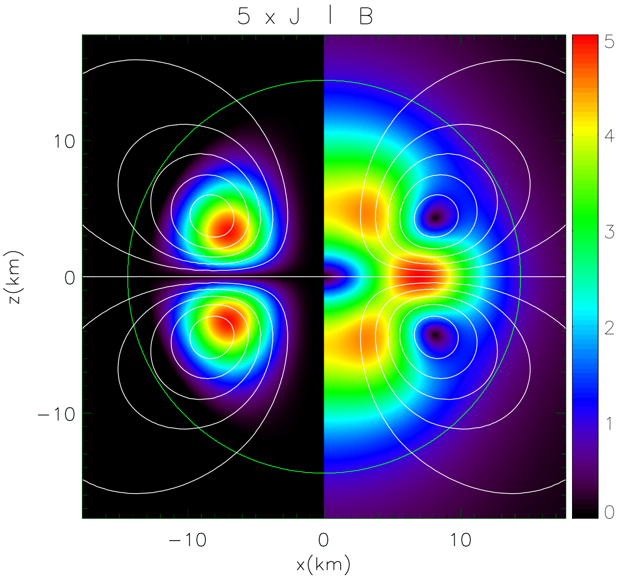

Figure 4.12: Antisymmetric solution, with $\nu = 1$. Left panel: azimuthal current density normalized to 0.2 times its maximum. Right panel: magnetic field strength, normalized to the value at the pole. White contours represent magnetic field surfaces (isocontours of Ψ). The thick green line is the stellar surface.

4.2 Rotating models

In this section we will characterize the effects of the poloidal magnetic field on the equilibrium structure of rotating NSs. As far as the current distribution is concerned we will focus on the simplest choice with $\xi = 0$ in Eq. 2.100 requiring the solutions to have a vanishing net electric charge. As in the toroidal field case (see Sec. 3.2) we will limit our investigation to $\Omega = 5.1 \times 10^3\ \mathrm{s}^{-1}$ since at this frequency, given our choice for the EoS, the parameter space is substantially reduced because of mass shedding. The parameter space of our models is shown in Fig. 4.14, in terms of the central density ρ_c and the gravitational mass M, at fixed rotational frequency Ω. In each plot we show equilibrium sequences at fixed baryonic mass M_0, magnetic dipole moment μ, maximum field strength $B_{\rm max}$, or deformation $\bar{e}$. As expected, in analogy with the toroidal case, both the gravitational and baryon mass rise with the magnetization (or equivalently with the magnetic dipole moment μ) and with the rotational frequency Ω. Here, however, the magnetic field deforms the equilibrium in the same way of the centrifugal force, flattening the star in the direction of the equatorial plane. As a consequence all the configurations are oblate and the surface ellipticity $e_{\rm s}$ is always positive. The majority of stellar surfaces can be well approximated with standard ellipsoids having $n_{\rm s} \sim 2$. The differences between the deformation induced by the rotation and the one due to the poloidal field are clearly evident in the low density region of the parameter space ($\rho_{\rm c} \lesssim 5 \times 10^{15}\mathrm{g/cm^3}$) where the superellipsoid index ranges from ~ 1.6 for the configuration at the mass-shedding limit, to $n_{\rm s} \sim 2.8$ for the most magnetized NSs with $B_{\rm max} \gtrsim 7 \times 10^{17}$G. Indeed, while rigid rotation acts preferentially on the external equatorial layers of the star,

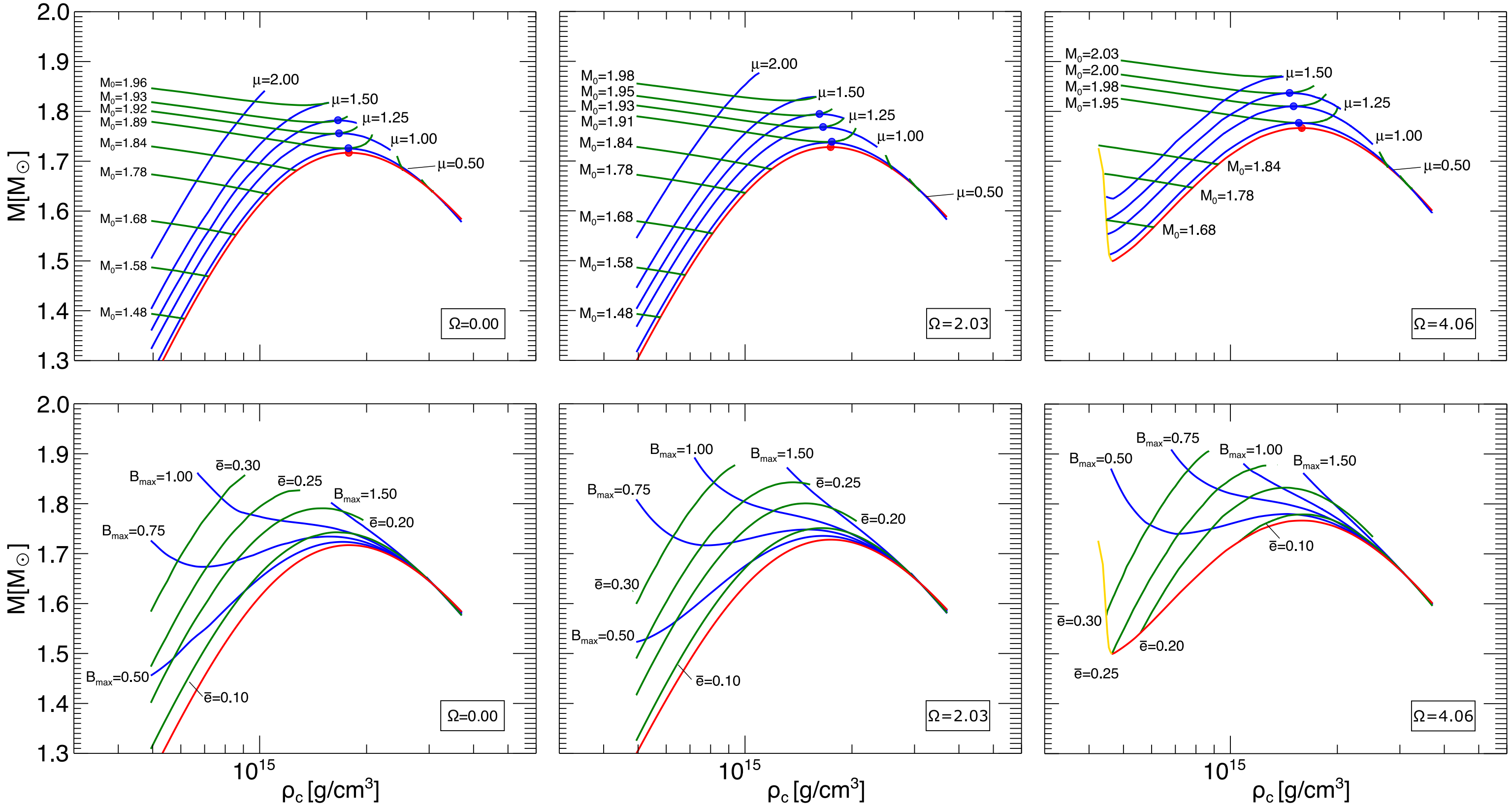

Figure 4.14: Space of physical solution for rigidly rotating NSs endowed with purely poloidal magnetic field obtained assuming a current distribution with $\xi = 0$ in Eq. 2.100. Top row: equilibrium sequences with fixed baryonic mass M_0 (green lines) and fixed magnetic dipole moment μ (blue lines). Bottom row: equilibrium sequences with fixed matter deformation $\bar{e}$ (green lines) or with fixed maximum magnetic strength $B_{\max}$ (blue lines). The yellow lines trace the mass shedding limit while the red lines represent the unmagnetized equilibria. The baryonic mass is expressed in unit of $M_\odot$, μ is expressed in unit of 10^{35} erg G^{-1}, $B_{\max}$ is expressed in unit of 10^{18} G and finally the rotational rate Ω is in unit of 10^3s^{-1}.

originating hypoellipsoidal with $n_s < 2$, the Lorentz force associated to the poloidal magnetic field globally flattens the star, from the core to the external layers, reducing the polar radius and favouring the occurrence of hyperellipsoids with $n_s > 2$. Two representative equilibrium configurations are shown in Fig. 4.13 and Tab. 4.3. They both share the same value of the gravitational mass but, because of the different degree of magnetization and rotation rate, they have $n_s \sim 2.5$ (left panel) and $n_s \sim 1.8$ (right panel). Notice that, as discussed before in Sec. 4.1 the poloidal field does not inflate the outer layers of the star so that the central density at the mass shedding, for a given Ω, does not change with respect to the unmagnetized case, as shown in the right panels of Fig. 4.14. Our finding suggests that the poloidal field enhances the stability of the configuration close to the Keplerian limit: indeed while the equatorial Lorentz force in the core region points outward causing the flattening of the star, in the outer layers it is directed inward playing a confining role.

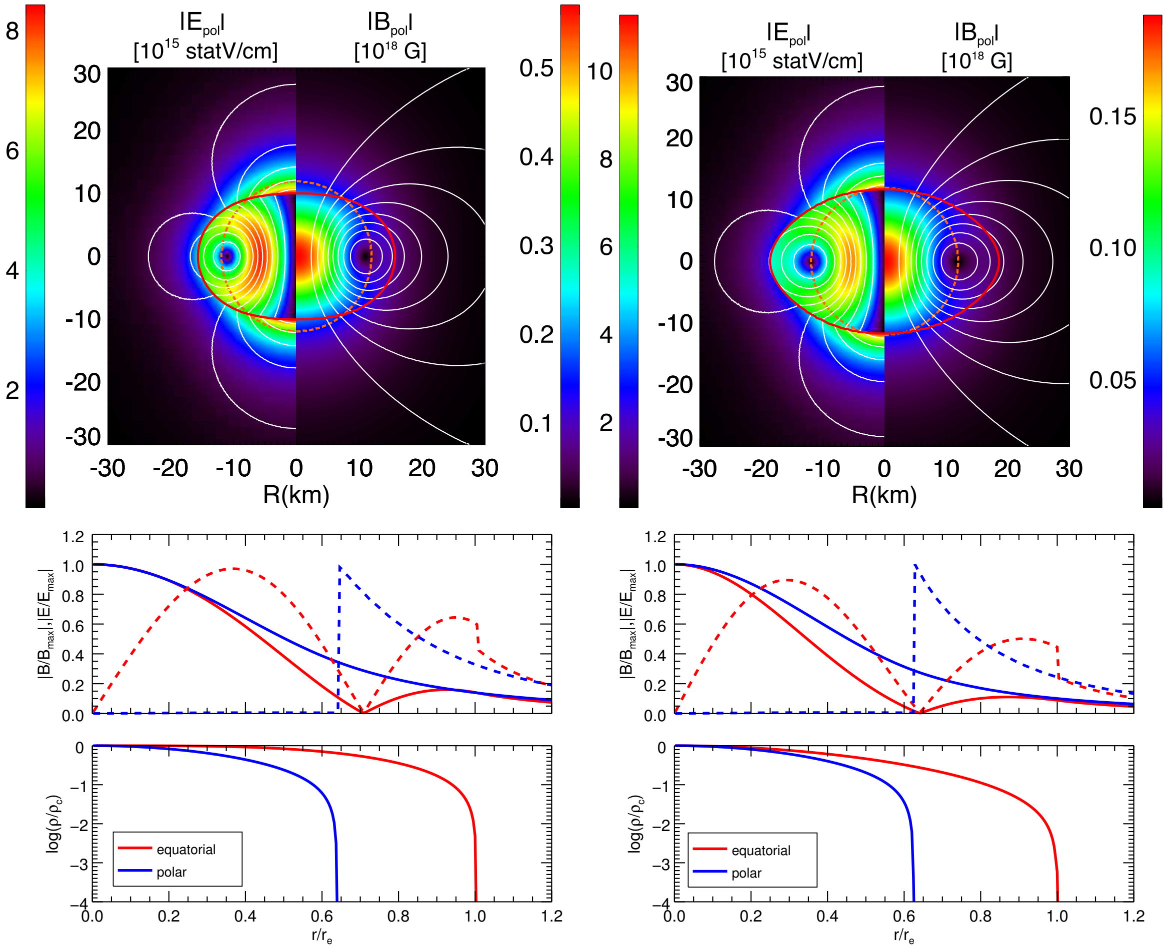

Figure 4.13: Top row: electric (left half panel) and magnetic (right half panel) field distribution together with the contours of the electric potential Φ (left half panel) and of the magnetic potential Ψ (right half panel) for two configurations sharing the same gravitational mass but with different B_{max} and Ω. Numerical details are shown in Tab. 4.3. Middle row: profile of the magnetic field strength (solid lines) and of the electric field strength (dashed lines) in the equatorial (red lines) and polar (blue lines) direction. Bottom rows: polar and equatorial radial profiles of the baryon density ρ_c.

In Fig. 4.13 we show the morphology of the magnetic and electric field together with the isocontours of the magnetic potential Ψ and the electric potential Φ. Inside the star, Φ traces the magnetic field lines Ψ = cost in agreement with the ideal MHD requirement $\partial_i\Phi = -\Omega\partial_i\Psi$ (Eq. 2.88). Outside the star the structure of the electric potential is mainly quadrupolar reflecting the fact that the monopolar component has been filtered out in order to achieve a globally uncharged configuration. The resulting internal electric field strength reaches its maximum value between the rotational axis and the neutral line, where it vanishes together with the magnetic field strength. The exterior electric field instead reaches its maximum strength in correspondence of the pole of the star. Obviously, different prescriptions on the total electric charge of the star lead to different morphologies for the exterior electric field. The interior one instead remains unchanged. Hence, in our models, the structure of the star is only marginally affected by the choice for the electrosphere, and the associated global quantities do not change within the accuracy of the code.

Table 4.3: Global quantities for the configuration shown in Fig. 4.13 with gravitational mass $M = 1.55\mathrm{M}_\odot$.

$B_{\rm max}$ 10^{17} G	Ω $10^3\mathrm{s}^{-1}$	$\rho_{\rm c}$ $10^{14}\mathrm{g/cm}^3$	M_0 $M_\odot$	$R_{\rm circ}$ km	$r_{\rm p}/R_{\rm e}$	$\bar{e}$	$n_{\rm s}$	H/W 10^{-2}	T/W 10^{-2}	H/M 10^{-2}	T/M 10^{-2}
1.88	1.02	4.79	1.65	20.7	0.62	0.267	1.80	1.60	8.67	0.19	1.02
5.72	4.06	4.30	1.64	17.7	0.64	-0.328	2.20	14.0	0.49	1.79	0.06

4.2.1 The structure of the electrosphere

As discussed in Sec. 2.5 the electric field outside the star is not fully determined by the ideal MHD condition Eq. 2.89, due to the arbitrary constant in the definition of the harmonic function Φ_a. This degree of freedom corresponds to an arbitrary net surface charge that can always be added to an the equilibrium configuration, and which manifests itself in the global structure of the electrosphere. The choice for this arbitrary constant is usually motivated on physical grounds. In the literature a typical choice is to assume a vanishing net charge (Goldreich and Julian 1969, Bocquet et al. 1995, Franzon and Schramm 2015, Franzon et al. 2016a), based on the assumption that any charged astrophysical object can pull opposite charges from the interstellar medium (ISM), till it neutralizes. This argument however is strictly valid only for non-rotating systems. The charge is not a relativistic invariant, and it is debatable in which reference frame (the ISM or the rotating NS) charge neutrality should hold. It is indeed well known that a neutrally charged rotating NS, while not able to attract charges from infinity, can easily pull them from its surface, thus creating a magnetosphere and charging itself Goldreich and Julian (1969). Other different choices have been presented even if less often. One can assume a net charge, in order to minimize the electric field, responsible for the extraction of charges from the surface (Michel 1974), or in order to minimize the electromagnetic energy in the space outside the star (Ruffini and Treves 1973). In the following we esplore these possibilities in order to characterize the structure of the external electric field, the surface charge distribution, and the associated Lorentz force. For

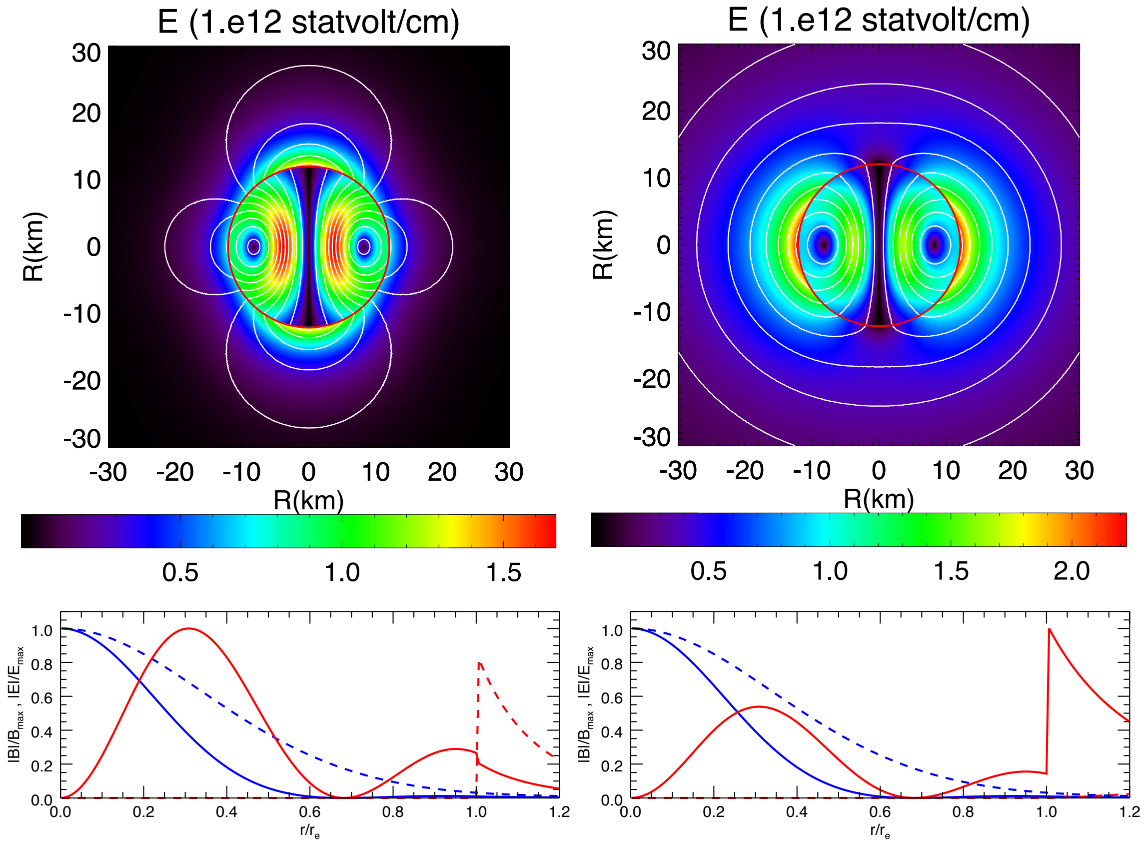

Figure 4.15: Top panels: distribution of the electric field strength $E = \sqrt{E^r E_r + E^\theta E_\theta}$ together with the iso-contour of the potential Φ for configurations with vanishing net electric charge (left panels) and vanishing polar electric field (right panels). Bottom panels: radial profiles of the magnetic (blue lines) and electric (red lines) field strength along the equatorial (solid lines) and the polar direction (dashed lines).

convenience, we restrict our investigation in the weak magnetization and slow rotation limit assuming, for our fiducial model with $M = 1.55\mathrm{M}_\odot$ (see Sec. 2.8) a polar magnetic field $B_\mathrm{pole} \sim 10^{14}$ G, and a rotation frequency $\Omega = 2 \times 10^2 \mathrm{s}^{-1}$.

Let us begin, discussing the left panel of Fig. 4.15 where we show the electric field distribution for a globally uncharged star. The external electric field peaks at the pole, in the so called *polar cap*, i.e. the region of magnetic field lines potentially extending at radii beyond the Light Cylinder. This electric field is capable of lifting charges from the stellar surface in the magnetosphere and beyond.

In the right panel of Fig. 4.16 we show the electric field distribution for a star where the external electric field vanishes at the poles. The star is endowed with a non vanishing net electric charge which, in this case, corresponds to $Q_\mathrm{e} = 3 \times 10^{24}$statC, still far below the critical value $\sim 10^{29}$statC (i.e. $\sim 0.1\sqrt{G}M_0$ in cgs units) capable to induce substantial effects in the stellar structure (Ghezzi 2005). The electric field peaks at the stellar equator, where it is about a factor ~ 2 stronger than the internal one. This star while unable to extract charges from the polar cap, can pull them from the ISM.

We have also analyzed the energetics of the electrosphere: the configuration that minimize the electromagnetic energy of the system is the uncharged one. This is in contrast with the results obtained in Ruffini and Treves (1973), where the minimum energy configuration has a negative net charge. In that work however, the structure of the magnetic field was chosen to depend on the specific value of the electric charge.

In either case, the electric field has a discontinuous normal component at the surface, corresponding to a surface charge given by:

$$\sigma_e = E^r_\mathrm{out} - E^r_\mathrm{in}, \tag{4.5}$$

and shown in Fig. 4.16 normalized to the Goldreich-Julian value $\sigma_\mathrm{GJ} = \Omega B_\mathrm{pole} r_\mathrm{p} = 9.5 \times 10^{10}$statC cm^{-2}. Notice that the sign of the surface charge, as well as the sign of the electric field, depends on the relative orientation of the magnetic dipole moment and the angular momentum. As a result the sign of the Lorenz force acting on such surface charge does not. Our results are shown for the aligned case.

In Fig. 4.16 we also plot the orthogonal and parallel component (with respect to the magnetic field) of the Lorentz force acting on the surface charge density given by $L^i = \sigma_e E^i$. It is possible to see that inside the star the MHD condition guarantees that the parallel component of the Lorentz force vanishes.

In the uncharged configurations the charge surface density is maximal at the pole. The Lorentz force with respect to the internal electric field vanishes on the rotation axis, reaches its maximum strength at latitude $\sim \pm 50$ deg and points always toward the equator, remaining mainly tangential to the stellar surface. The Lorentz force with respect to the external electric field instead is mainly parallel to the magnetic field in the polar region, and becomes mainly orthogonal in the equatorial region where it points inward. In the case of a negative surface charge, (an electron excess if angular momentum and dipole moment are aligned), the Lorentz force is able to extract electrons. In the case of a positive surface charge (an ion excess if angular momentum and dipole moment are counter-aligned) the Lorentz force will be unable to extract ions. Assuming a cohesive energy $\sim$ 350keV for an iron chain with spacing $\sim 10^{-9}$cm at $B = 10^{14}$G (Medin and Lai 2006, 2007), the critical electric field capable to directly rip iron ions off the stellar crust is of the order of $\sim 10^{13-14}$statV/cm which is larger than the electric fields of our model ($\sim 10^{12}$). In this case, instead of driving a magnetospheric current, the overall Lorentz force will stretch the stellar crust outward in the polar region and inward in the equatorial one, favoring a prolate deformation of the crust itself, that might counterbalance the oblateness of the underlying star.

The configuration with a vanishing polar Lorentz force is instead characterized by a surface charge density of opposite sign, with respect to the uncharged case, with a maximum at the equator. By consequence, the action of the surface Lorentz force is reversed: the maximum strength is reached in the equatorial region, and the force always points toward the exterior of the star. If the surface charge is made of electrons (counter-aligned case) such force could pull them out from the surface and fill the closed magnetosphere within the Light Cylinder. If instead it is made of ions (aligned case) this could lead to an oblate crustal deformation, that adds to the oblateness of the underlying star.

Let us point here that once one allows the presence of a singular surface charge (and the related Lorentz force) in the Maxwell Equations Eq. 2.78, then there is no reason to impose the absence of any singular surface current. This is however usually done in building equilibrium models, because it guarantees the integrability for non rotating system and avoids the problem to consider arbitrary crustal currents that in general are not well constrained by physical arguments. On the other hand the extra degree of freedom associated with a surface current, can be used to modify the magnetic field structure, and the net Lorentz force at the surface. In particular if one chooses the following surface current:

$$J_{\rm surf} = \sigma_e \frac{\Omega - \omega}{\alpha} \delta(r - r_e), \tag{4.6}$$

corresponding to the assumption that the surface charge corotates with the star, then a discontinuity in the azimuthal component of the magnetic field arises:

$$J_{\rm surf} = \frac{B^\theta_{\rm in} - B^\theta_{\rm out}}{\psi^2 \sin\theta}. \tag{4.7}$$

and both the radial and azimuthal component of the Lorentz force at the surface, with respect to the internal electromagnetic field vanish. The surface charge and currents are now in equilibrium with respect to the internal field. Note however that no current can suppress the component of the Lorentz force parallel to the magnetic field, outside the star. Moreover, the new current term induces only small deviation $\lesssim 10^{-5}$ on the global structure of the electromagnetic field. The relevant effect is on the Lorentz force itself.

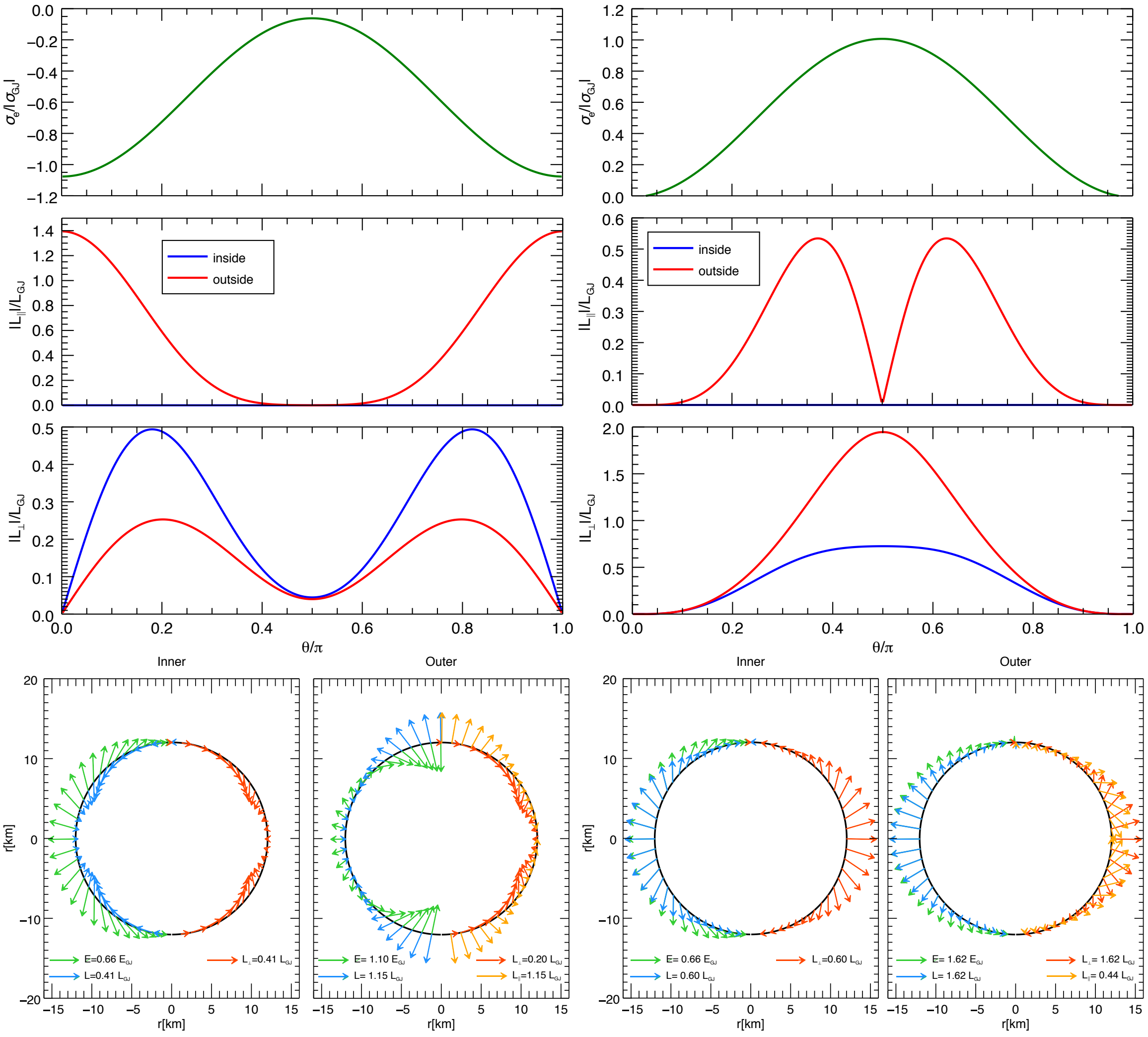

Figure 4.16: Top rows: surface charge density, parallel component $|L_{\parallel}|$ and perpendicular component $|L_{\perp}|$ of the surface Lorentz force as a function of the colatitude (parallel and perpendicular refer to the direction of the magnetic field). Bottom row: vector plots of the surface electric field $E^{\hat{i}}$, of the Lorentz force $L^{\hat{i}}$ and its perpendicular and parallel component. Numerical values are normalized to $\sigma_{\rm GJ} = E_{\rm GJ} = \Omega B_{\rm pole} r_{\rm p}$ and $L_{\rm GJ} = \rho_{\rm GJ} E_{\rm GJ}$ (corresponding respectively to $\sigma_{\rm GJ} = 9.5 \times 10^{10}$statC cm^{-2}, $E_{\rm GJ} = 1.2 \times 10^{12}$statVolt cm^{-1} and $L_{\rm GJ} = 1.1 \times 10^{23}$dyne cm^{-2}). Panels on the left refer to the uncharged equilibrium configuration while panels on the right refer to the configuration with vanishing polar electric field.

4.3 Global trends

4.3.1 Results at fixed gravitational mass

In analogy to what has been done in the toroidal field case (see Sec. 3.2) we present a detailed analysis of models at fixed gravitational mass $M = 1.551\mathrm{M}_\odot$. In Fig. 4.17 we show the variation of ρ_c, M_0 and R_c, with respect to the non rotating and unmagnetized equilibrium configuration, as function of the maximum magnetic field strength $B_{\max}$ and the magnetic dipole moment μ along equilibrium sequences with constant rotation frequency Ω. Just as in the toroidal case, the qualitative effects of the poloidal magnetic field remain the same independently of the rotational rate: both the baryonic mass M_0 and the central density ρ_c decrease with $B_{\max}$ while the circumferential radius R_{circ} and the deformation rate $\bar{e}$ grow. Interestingly, independently of Ω, the configuration at the turning point shows a circumferential radius R_{circ} about 20% larger than the unmagnetized model, corresponding to $\bar{e} \sim 0.3$.

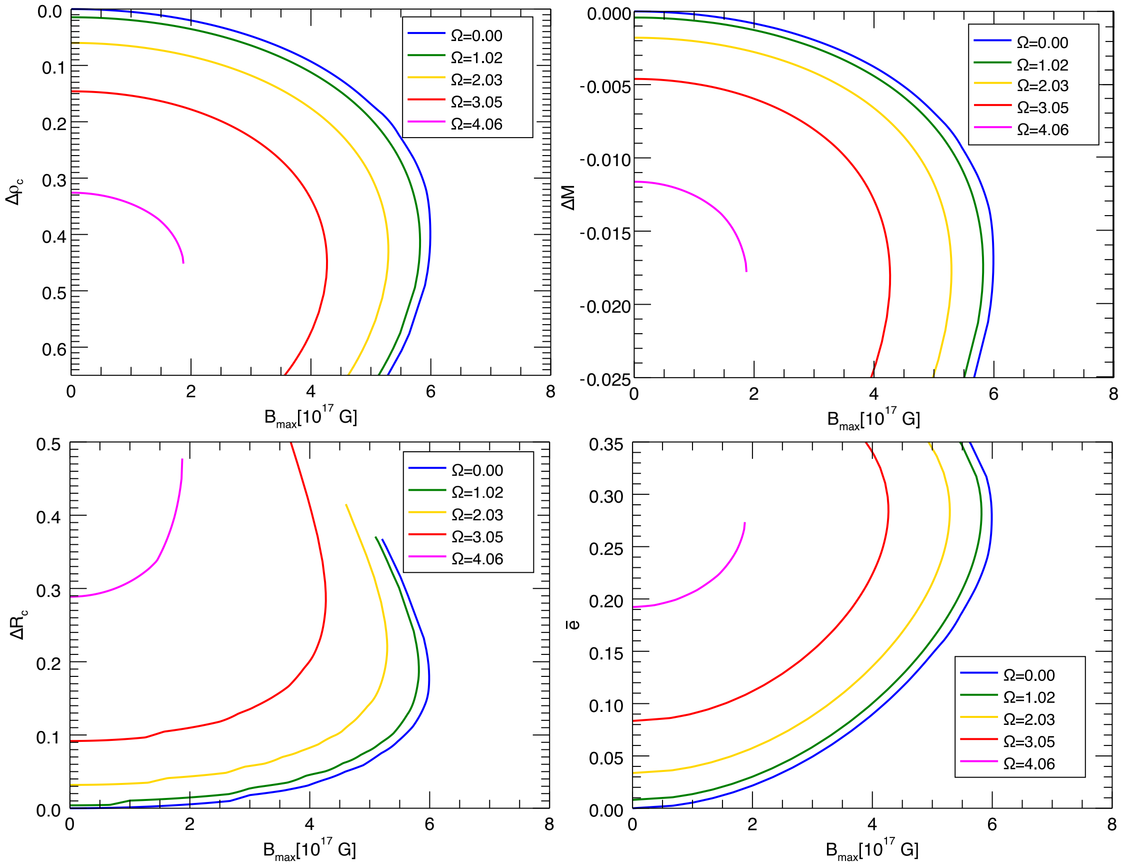

Figure 4.17: Variation of the baryon mass M_0, central density ρ_c and circumferential radius R_c and of the deformation ratio $\bar{e}$ with respect to the unmagnetized and static reference model along sequences of constant gravitational mass $M = 1.55\ \mathrm{M}_\odot$ for different values of the rotational rate Ω as a function of the maximum strength of the poloidal magnetic field $B_{\max}$.

The role of the rotation can be factored out as an offset, plus an enhancement of the effectiveness of the magnetic field, and it is still possible to find a self-similarity scaling,

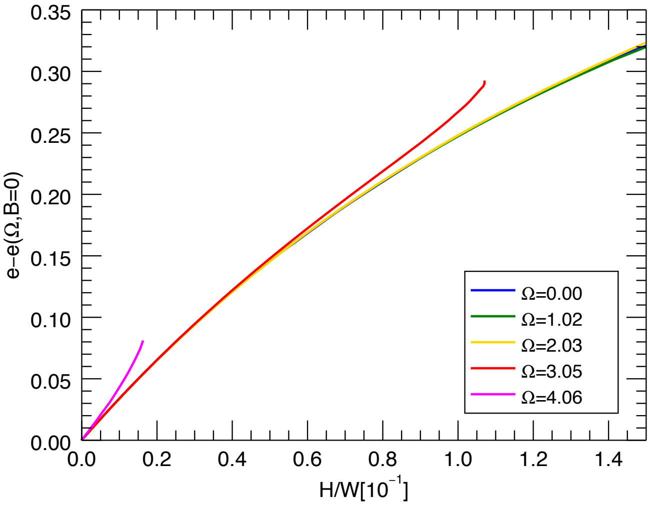

Figure 4.18: Variation of the deformation rate $\bar{e}$ with respect to the unmagnetized rotating reference configuration as a function of the magnetic to binding energy ratio along sequences with fixed mass $M = 1.55 M_\odot$.

as for the toroidal field case. In particular Eqs. 3.2 and 3.3 are still valid with $a_{\bar{e}} = -0.15$ and $b_{\bar{e}} = 0.27$ respectively, in the range $\Omega \lesssim 3 \times 10^3 \mathrm{s}^{-1}$ and $T/M \lesssim 5 \times 10^{-3}$ as shown in Fig. 4.18. With respect to the toroidal case, the sign of $b_{\bar{e}}$ changes from negative to positive, while the sign of $a_{\bar{e}}$ remains the same. Therefore, if parametrized in terms of H/W the rotation coupling term acts to reduce the deformation of the star. This because at given H/W, the configurations with slower rotation, have larger magnetic energy H resulting in a more evident deformation. We stress here that H, which now includes also the electric energy that contributes at most within few percent on the total energy even for the fastest rotator, is not entirely confined inside the star as in the toroidal field case. Indeed $\sim 25\%$ of the total energy is located outside the star.

In the range $B_{\mathrm{max}} \lesssim 3{\times}10^{17}$G and $\Omega \lesssim 4{\times}10^3 \mathrm{s}^{-1}$ (corresponding to $H/W \lesssim 3.5{\times}10^{-2}$ and $T/W \lesssim 5.1 \times 10^{-2}$ or $H/M \lesssim 2.5 \times 10^{-3}$ and $T/M \lesssim 4.1 \times 10^{-3}$), which is comparable with the bilinear regime for the purely toroidal field case (see Eqs. 3.4 and 3.5), the deformation rate $\bar{e}$ is approximated with an accuracy $\lesssim 10\%$ by the relation

$$\bar{e} = d_\Omega \, \Omega_{\mathrm{ms}}^2 + d_{\mathrm{B}} \, B_{17}^2 \tag{4.8}$$

where $d_{\mathrm{B}} \simeq 5.4 \times 10^{-3}$ and $d_\Omega \simeq 0.3$. Analogously, for the surface ellipticity we find:

$$e_s = s_\Omega \, \Omega_{\mathrm{ms}} + s_{\mathrm{B}} \, B_{17}^2 \tag{4.9}$$

with $s_{\mathrm{B}} \simeq 5 \times 10^{-3}$ and $s_\Omega \simeq 0.4$.

These scaling laws can be also given in term of the magnetic dipole moment μ that, in contrast with B_{max}, is a measurable quantity. We obtain, in the same range as before, that:

$$\bar{e} = d_\Omega \, \Omega_{\mathrm{ms}}^2 + d_\mu \, \mu_{35}^2 \tag{4.10}$$

where $d_\mu = 0.14$ and

$$e_s = s_\Omega\,\Omega_{\rm ms}^2 + s_\mu\,\mu_{35}^2 \tag{4.11}$$

with $s_\mu \simeq 0.11$ (μ_{35} is the value of the magnetic dipole moment in unity of 10^{35}erg G^{-1}). In Fig 4.19 we show the variations of different stellar quantities as functions of μ. Notice that, just as the magnetic energy, μ is a monotonic function of the magnetization $k_{\rm pol}$. Moreover, in the case of ΔM_0, a parametrization in terms of μ reduces the non-linear coupling between rotation and magnetic field.

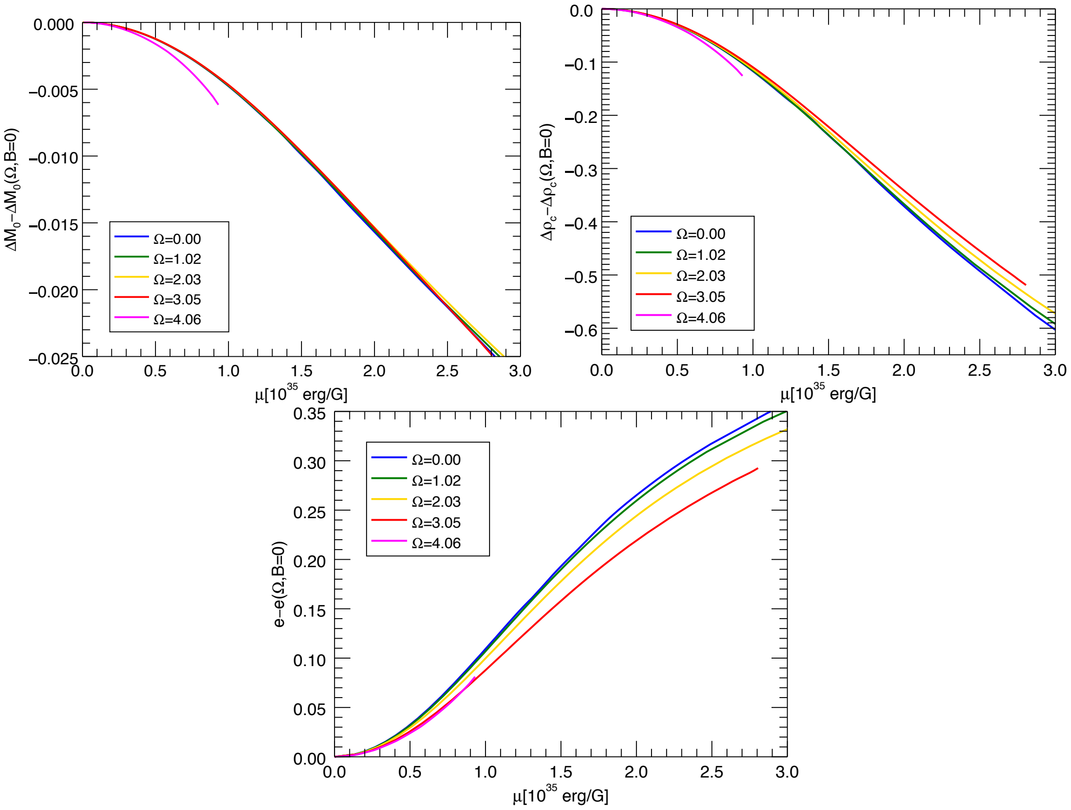

Figure 4.19: Variation of the baryonic mass M_0, central density ρ_c and deformation rate $\bar{e}$ as a function of the magnetic dipole moment μ along equilibrium configurations with fixed gravitational mass $M = 1.55{\rm M}_\odot$.

4.3.2 The effects of the current distribution

An extensive investigation of the parameter space in the case of rotating models, using different prescriptions for the current distribution, is computationally expensive. Indeed, as anticipated in Sec. 4.1.2, the non-linear current term substantially slows down the convergence of the scheme even in the static case, where we have just to solve the Grad-Shafranov equation. In order to get some handling on the effects of the current distribution on the deformation of the star, as we have done in the toroidal field case, we have just analyzed the simple static case with $\nu = 1$, confident that in the bilinear regimes the effects of the magnetic field and the rotation can be separated. We have found that in the range $|\xi| \lesssim 30$, away from the fully saturated regime, the effects of the non-linear currents terms can be effectively reabsorbed with a parametrisation in terms of H/W (or equivalently H/M) with an accuracy of $\sim 5\%$, using an effective energy ratio

$$\bar{e} \simeq \mathcal{F}\left([1 + a_\xi \xi]\frac{H}{W}\right) \tag{4.12}$$

where $a_\xi = -2.8 \times 10^{-3}$. In the linear regime with $B_{\rm max} \lesssim 2. \times 10^{17}$ G, the parametrisation in term of the magnetic field strength can be generalized as

$$\bar{e} = d_{\rm B}[1 + d_\xi\, \xi]\, B_{17}^2. \tag{4.13}$$

with $d_\xi = 4.1 \times 10^{-3}$.

The difference between the signs of a_ξ and d_ξ may appear contradictory. This discrepancy is however only apparent since, for a fixed value of H/W, the configuration with $\xi < 0$ has a larger value of $B_{\rm max}$ than the configuration with $\xi > 0$. This is because subtractive currents demagnetize to outer layer of the star and, in order to achieve higher value of H/W, one has to increase the maximum strength of the magnetic field which in turn largely affects the core. This holds also in the fully saturated regime where, however, it is not possible to find a simple parametrization of the current distribution effects neither in term of energy ratios or other global quantities such as the magnetic dipole moment. Interestingly however, if parametrized in terms of H/W the deformation of the fully saturated regime ranges just within a factor 2. This suggests that the morphology of the current distribution, rather than its global magnetic energy content, may play a relevant role in affecting the structure of the star.

4.3.3 Dependency from the gravitational mass

As expected, also for a purely poloidal field, the effect of magnetization and of rotation depends on the compactness of the star. To generalize the trends found in the previous sections, to different gravitational masses, we again make use of an effective energy ratio:

$$\left[\frac{H}{W}\right]_{\rm eff} = \frac{1.55 M_\odot}{M}\frac{H}{W}. \tag{4.14}$$

By using this quantity the quadrupole deformation can be parametrized as in the Eq. 3.11, where the coupling term is now given by

$$a_{\bar{e},{\rm eff}} = -\left(2.5 - 2.4\frac{M}{1.55 M_\odot}\right). \tag{4.15}$$

and the functional form for $\mathcal{F}$ is

$$\mathcal{F}(x) = 3.8x - 4.3x^{1.5}. \tag{4.16}$$

This parametrization is able to describe the trends of the quadrupole deformation with an accuracy less than 5% up to $\bar{e} \sim 0.15$ as shown in the left panel of Fig. 4.20. Notice that here, as in the toroidal field case, for a fixed value of H/W the coupling term $a_{\bar{e},\mathrm{eff}}$ reduces the absolute value of $\bar{e}$.

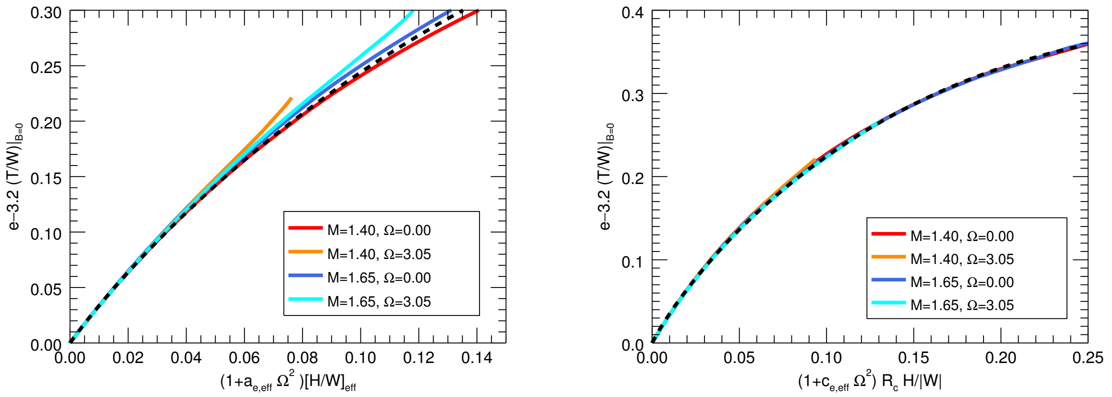

Figure 4.20: Deformation $\bar{e}$ with respect to the unmagnetized model as a function of the effective mass energy ratio H/W in the left panel or HR_c/W (where R_c is normalized to 14 km) in the right panel for configurations with mass between $1.40\mathrm{M}_\odot - 1.65\mathrm{M}_\odot$ and rotational frequency $\Omega = 0.0 - 3.05 \times 10^3\mathrm{s}^{-1}$. The dashed black lines shows Eq. 4.16 and Eq. 4.19.

Interestingly a more accurate parametrization of $\bar{e}$ can be obtained including, as a parameter, the reciprocal of the circumferential radius in place of the gravitational mass. In particular we obtain that, by using the relation

$$\bar{e} \simeq 3.2\frac{T}{W}\bigg|_{B=0} + \mathcal{G}\left(\left[1 + c_{\bar{e},\mathrm{eff}}\Omega_{\mathrm{ms}}^2\right]\frac{H}{W}R_{14}\right), \tag{4.17}$$

where R_{14} is the circumferential radius normalized to 14km, the coupling therm is given by

$$c_{\bar{e},\mathrm{eff}} = -3.6 + 3.0\frac{M}{1.55\mathrm{M}_\odot} \tag{4.18}$$

and the functional form of $\mathcal{G}$ is

$$\mathcal{G} = 4.8\,x - 5.1\,x^{1.3}, \tag{4.19}$$

we can fit with high accuracy the variation of $\bar{e}$ for all the value of Ω and M even in the strong magnetization regime as shown in Fig. 4.20.

Limited to the bilinear regime, the coefficients appearing in the Eqs. 4.8-4.11 are listed in Tab. 4.4 as a function of the gravitational mass. Interestingly the coefficients d_μ and s_μ are only weakly affected by the specific value of the gravitational mass and they remain almost constant within $\sim 5\%$.

In the perturbative regime of $H, T \to 0$ the relation in Eq. 3.11, with Eq. 4.15 and Eq. 4.16, gives:

$$\bar{e} = \frac{C_{\bar{e}}}{W_0}\left[T + 1.8\frac{H}{M/M_\odot}\right], \tag{4.20}$$

Table 4.4: Mass dependency for the expansion coefficients for both $\bar{e}$ and e_s in the case of purely poloidal magnetic fields.

M $M_\odot$	d_Ω 10^{-1}	d_B 10^{-3}	d_μ 10^{-1}	s_Ω 10^{-1}	s_B 10^{-3}	s_μ 10^{-1}
1.40	4.2	9.8	1.4	6.0	8.0	1.2
1.45	3.8	8.1	1.4	5.1	7.1	1.2
1.50	3.4	6.7	1.4	4.6	5.6	1.2
1.55	3.0	5.4	1.4	3.8	4.0	1.2
1.60	2.6	4.4	1.4	3.5	3.6	1.2
1.65	2.2	3.2	1.4	3.1	3.0	1.2

which is the analogous of Eq. 3.13 for the toroidal magnetic field. The main difference between the two relations is that in the poloidal field case the sign of the magnetic term is positive. This reflects the fact that a poloidal field induces an oblate deformation. An analogous relation is found also for the apparent ellipticity:

$$e_s = \frac{C_{e_s}}{W_0}\left[T + 1.1\frac{H}{M/M_\odot}\right]. \tag{4.21}$$

4.4 Summary

In this chapter we have analyzed a large sample of axisymmetric equilibrium models with purely poloidal magnetic field either rotating or static, and for the latter we have also investigated different current distributions. For rotators we have assumed an outer vacuum and shown how different prescriptions for the global charge translate into the properties of the electrospheres.

Just as in the toroidal field case, along sequences of constant gravitational mass or constant baryonic mass there exists a maximum strength that the magnetic field can reach inside the star: a further increase of magnetization leads to a rapid drop in the central density in conjunction with a rapid expansion of the equatorial radius and a contraction of the polar radius. As in Cardall et al. (2001), this finally results in doughnut-like configurations where the magnetic stresses move the maximum of the density off-center. Contrary to the toroidal field case where rotation counterbalances the effects of the magnetic field here the centrifugal effects act in the same direction of the magnetic field. On the other hand the non linear coupling is analogous, with rotation enhancing the effectiveness of magnetic field in deforming the star. As a consequence, the surface shape of star changes depending on the dominant effect: strongly magnetized configurations appear as hyperellipsoids, while configurations dominated by rotations appear as hypoellipsoids. Interestingly, since the poloidal magnetic field does not produce an inflation of the outer layers of the star, where the density distribution remains similar to the unmagnetized case, the mass-shedding limit is only weakly affected by the presence of the magnetic field itself. In particular, in line with what has been found by Franzon and Schramm (2015), at fixed central density the Lorentz force induced by the poloidal field stabilizes the star against mass shedding.

Since we are not interested in modeling the pulsar magnetospheres we obtain our models under the electrovacuum assumption. We have however analyzed the structure of the electrosphere arising in consequence of the rotation. Since the electric field outside the star is not fully determined by ideal MHD inside the star but there is an additional degree of freedom that corresponds to the net charge of the star, we have considered either configurations with vanishing net electric charge or configurations where we neutralize the Lorentz force at the pole. While the interior configuration is not influenced by this choice, differences emerge in the surface distribution of the charge density and the associated Lorentz force. For globally uncharged star the electric field peaks in the polar caps, in the other case at the equator. In both cases, depending on the alignment/counter-alignment between the rotation and the magnetic dipole, the Lorentz force is able to extract negative charges from the surface of the star (at polar cap for the uncharged star, at the equator in the other case) or to induce crustal stresses that are directed toward the equator for globally uncharged star or toward the pole if the polar Lorentz force is neutralized.

Analyzing different current distributions we have seen that: additive currents tend to concentrate the field in the outer layer of the star, where in the most extreme cases the magnetic field assumes its maximum strength; instead subtractive currents confine the magnetic field toward the axis, leaving in the the fully saturated non-linear regime a large unmagnetized region inside the star. These latter configurations appear similar to what has recently been found in full time-dependent MHD simulations of proto-NS formation in supernovae by Obergaulinger et al. (2014) (see the bottom panel of their Fig. 14). The reason is due to the fact that turbulent eddies tend to expel magnetic field (Moffatt 1978) which concentrates towards the axis, and becomes almost tangential at the proto-NS surface. Finally, the interior distribution of currents reflects on the multipolar structure of the surface magnetic field: in the case of subtractive currents the magnetic field is mainly concentrated along the axis and it can be strongly suppressed at the equator; for additive currents located at the edge of the star, the situation is reversed. Notice that, independently from the specific choice for currents, all our configurations are dominated by the dipolar component of the magnetic field. Moreover they retains the same equatorial simmetry of the density distribution. This is because, in order to numerically solve the GS equation, we need to maintain a stabilizing term, proportional to the density distribution, in the expression of the current function. Antisymmetric solutions can be obtained only replacing this stabilizing term with a singular surface current.

As for purely toroidal field, it is possible to parametrize the deformation of the star in terms of a balance between the rotational energy, the magnetic energy and the binding energy (or analogously the gravitational mass). In particular it is possible to reabsorb the effects related to the current distribution and the compactness in a unique functional form that is able to fit the induced deformation in our parameter space up to the non linear regime of strong magnetization and fast rotation. We have seen that the deformation of the star is mainly indicative of the energy content of the system rather than the distribution of the currents inside the star. The latter becomes relevant only in the fully saturated regime.

5

Mixed magnetic field

It is well known that purely toroidal or purely poloidal magnetic fields are both unstable on an Alfvén crossing time (Tayler 1973, Flowers and Ruderman 1977, Wright 1973, Lander and Jones 2011a,b, Kiuchi et al. 2011, Ciolfi et al. 2011) and it has been suggested that only a combination of the two is capable to stabilize the system on much longer timescales (Braithwaite and Spruit 2006, Akgün et al. 2013, Mitchell et al. 2015). Axisymmetric configurations with both poloidal and toroidal fields are generically referred as Twisted-Torus (TT) configurations. The main characteristic of this morphology is that the toroidal fields threads the closed field line region of the poloidal field, remaining confined to a torus like region under the surface of the star. Such kinds of configurations have been investigated by different authors (see Sec. 1.4) because previous dynamical studies (in particular Braithwaite and Nordlund 2006, Braithwaite and Spruit 2006, Braithwaite 2009) have shown that a magnetic field inside a fluid star tends to relax toward a TT geometry that, in turn, can be considered 'stable' if the toroidal component is energetically dominant with respect to the poloidal counterpart (see also Secs. 1.3 and 1.4 for a discussion). Despite several attempts in various regimes (Ciolfi et al. 2009, Lander and Jones 2009), only equilibrium configurations where the energetics was dominated by the poloidal component could be found. Recently Ciolfi and Rezzolla (2013) and Fujisawa and Eriguchi (2015) have shown that very peculiar current distributions might be required in order to obtain toroidally dominated systems. This raises questions about the importance of the specific choice of the form of the free currents $\mathcal{I}$ and $\mathcal{M}$. More precisely one would like to know if previous failure to get toroidally dominated geometries is due to a limited sample of the parameter space, or if only very *ad hoc* choices for the current distribution and/or boundary conditions satisfy this requirement. Most of the efforts have focused on understanding how this magnetic field acts on the star and the amount of deformation that it induces, using however only a limited set of models and current distributions.

In this Chapter, that is based on Pili et al. (2014) and Bucciantini et al. (2015a), we will consider simple 'canonical' TT models in order to discuss the effects of a mixed geometry on the structure of the NS. Then in Sec 5.2 we extend our results to more general current distributions, in order to check if and under which conditions equipartition of the toroidal and poloidal component can be achieved.

5.1 Twisted Torus models: the effects on the stellar structure

To generate mixed field configurations, we add to the current function $\mathcal{M}$, used in purely poloidal models, i.e.

$$\mathcal{M}(\Psi) = k_{\rm pol}\Psi(1 + \xi\Psi^{\nu}), \tag{5.1}$$

a current function $\mathcal{I}$, with the following functional form:

$$\mathcal{I} = \frac{a}{\zeta + 1}\Theta[\Psi - \Psi_{\rm sur}](\Psi - \Psi_{\rm sur})^{\zeta+1} \tag{5.2}$$

where $\Theta[.]$ is the Heaviside function and $\Psi_{\rm sur}$ is the maximum the magnetic potential Ψ reaches on the stellar surface. The above choice guarantees that the currents are all confined within the star with components given by

$$J^r = \alpha^{-1}B^r a\,\Theta[\Psi - \Psi_{\rm sur}](\Psi - \Psi_{\rm sur})^{\zeta}, \tag{5.3}$$

$$J^\theta = \alpha^{-1}B^\theta a\,\Theta[\Psi - \Psi_{\rm sur}](\Psi - \Psi_{\rm sur})^{\zeta}, \tag{5.4}$$

$$J^\phi = \rho h k_{\rm pol}(1 + \xi\Psi^{\nu}) + \frac{a^2}{(\zeta + 1)\alpha^2 R^2}\Theta[\Psi - \Psi_{\rm sur}](\Psi - \Psi_{\rm sur})^{2\zeta+1}. \tag{5.5}$$

Let us start with the simplest case, assuming $\xi = 0$ and $\zeta = 0$. Notice that the presence of the current term linked to $\mathcal{I}$ is actually equivalent to the existence of an effective non-linear current term. In Fig. 5.1 we present a typical TT model, and in particular this configuration corresponds to the one with the highest toroidal magnetic field among all our models. As anticipated, the structure of the poloidal magnetic field closely resembles what was found in the previous chapter, on purely poloidal models: it threads the entire star, reaches its maximum value at the center, vanishing only in a ring-like region in the equatorial plane, and crosses smoothly the stellar surface. The magnetic field outside the star is dominated by its dipole component. The toroidal field distribution is reminiscent of purely toroidal field cases with large $m > 10$: it does not fill completely the interior of the star, but it is confined in a torus tangent to the stellar surface at the equator. It reaches its maximum exactly in the ring-like region where the poloidal component vanishes. Of course this behaviour is related to our choice of the poloidal current distribution, and to our requirement that they should be confined within the star.

In the same Fig. 5.1 we also show the distribution of the baryonic density. It is evident that the poloidal component of the magnetic field, which is also energetically dominant, is mostly responsible for the deformation of the star in our TT configurations: the baryonic density distribution in fact resembles closely what we obtained in the purely poloidal configurations,

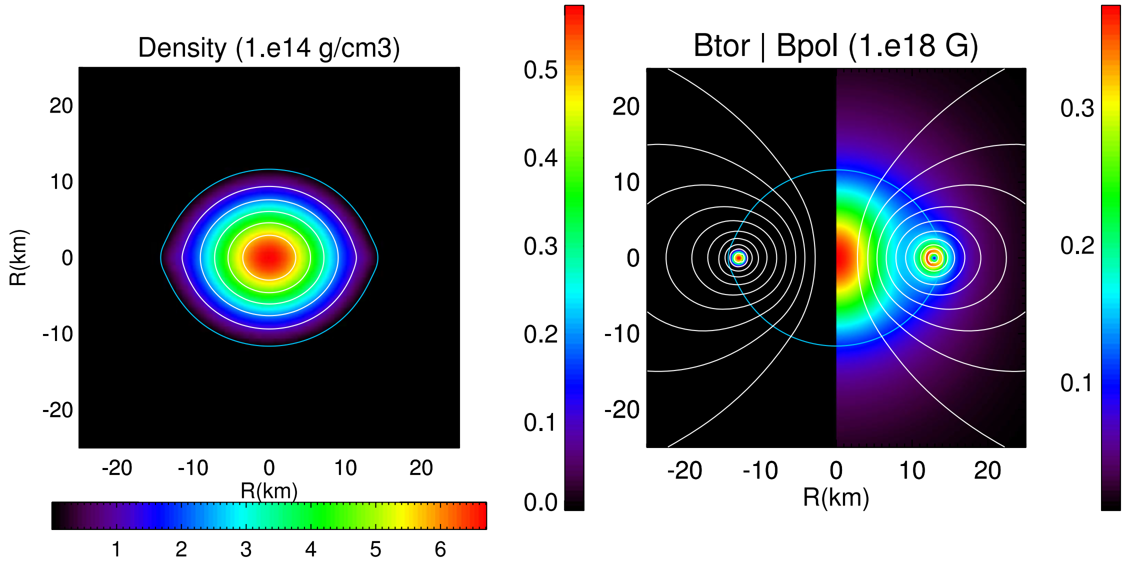

Figure 5.1: TT configuration with a gravitational mass $M = 1.551 M_\odot$, a baryonic mass $M_0 = 1.660$, a maximum field strength $B_{\rm max} = 5.857 \times 10^{17}$ G. Left panel: baryonic density distribution. Right panel: strength of the toroidal (left half) and poloidal (right half) magnetic field components, superimposed to *magnetic field surfaces* (isocontours of Ψ). The blue curve locates the stellar surface. The other global physical quantities of this configuration are listed in the last line of Table 5.1.

the stellar shape is oblate and the external layers have a *lenticular* aspect, with only small deviation $\sim 5\%$ form the typical superellipsoidal shape.

Table 5.1: Global quantities for various TT models with the same gravitational mass $M = 1.551 M_\odot$ but different values of both $B_{\rm max}$ and a (see Fig. 5.2). In the last three lines we present the models with the highest maximum magnetic field that we could build, for each value of a.

a	ρ_c $[10^{14}{\rm g\,cm^{-3}}]$	M_0 $[M_\odot]$	$R_{\rm circ}$ [km]	r_e/r_p	$\bar{e}$ $[10^{-1}]$	H/W $[10^{-1}]$	$B_{\rm c}$ $[10^{17}{\rm G}]$	$B_{\rm tor,max}$ $[10^{17}{\rm G}]$	μ $[10^{35}\,{\rm erg\,G^{-1}}]$	$H_{\rm tor}/H$ $[10^{-2}]$
0.5	8.488	1.680	14.24	1.000	0.033	0.011	0.745	0.194	0.173	2.893
0.5	7.890	1.675	14.70	0.935	0.715	0.251	3.338	0.944	0.862	3.228
0.5	5.373	1.650	16.88	0.723	2.636	1.285	5.344	1.974	2.308	4.082
1.0	5.545	1.647	17.41	0.733	2.510	1.455	4.409	3.983	2.790	7.262
1.5	5.454	1.645	18.11	0.711	2.552	1.566	4.134	5.582	3.199	7.282
2.0	6.713	1.660	16.40	0.816	1.636	0.880	3.758	5.857	2.152	6.696

Fig. 5.2 shows a comparison between the strength of the toroidal and poloidal magnetic field in the equatorial direction with different values of the magnetization constants $k_{\rm pol}$ and a. We found that, at a fixed value of a, the strength of both the toroidal and poloidal field grows with $k_{\rm pol}$, while if one keeps fixed the maximum strength of the poloidal field, then the region occupied by the torus shrinks as a grows.

In Fig.5.3 we show the relation between the magnetic dipole moment and the value of the magnetic field strength in the centre $B_{\rm c}$ along equilibrium sequences where the gravitational mass has been kept fixed, $M = 1.551 M_\odot$, for various values of $a = \{0.0, 0.5, 1.0, 1.5, 2.0\}$. It is evident that at fixed magnetic dipole moment, the field strength decreases with a. This can be understood if one recalls that at higher values of a there is an increasing contribution to the magnetic dipole moment from currents associated to the toroidal field (the same value

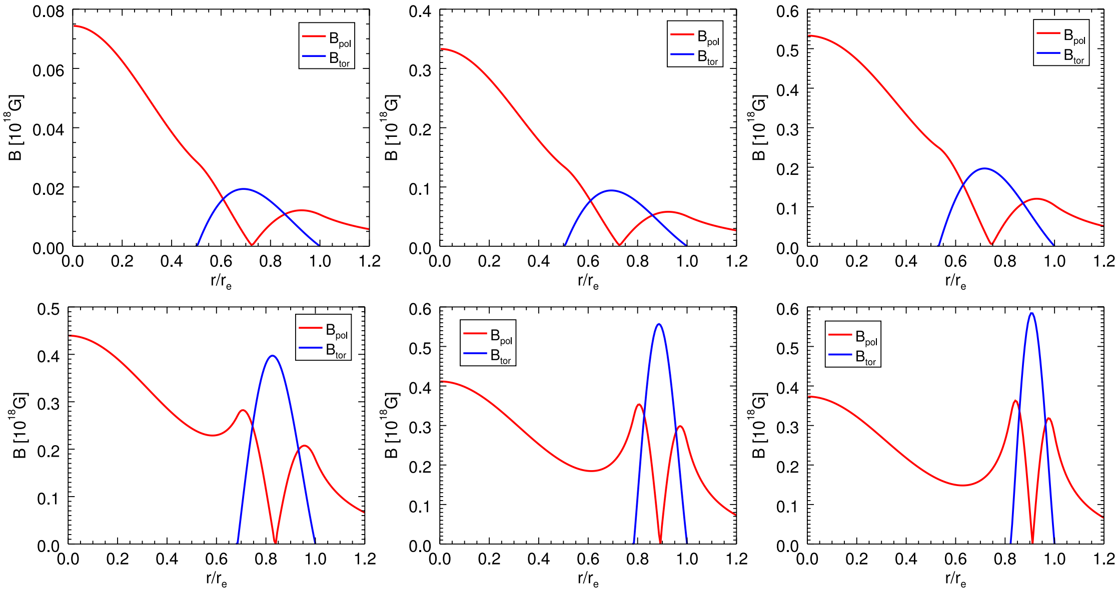

Figure 5.2: Profiles of the strength of the poloidal and toroidal components of the magnetic field, along the equator. r_e is the equatorial radius. All models have the same gravitational mass $M = 1.551 M_\odot$. Top panels show three models with $a = 0.5$ and $k_{\rm pol} = 0.04$ (left), $k_{\rm pol} = 0.18$ (center) or $k_{\rm pol} = 0.31$ (right). The left bottom panel shows a model with $a = 1.0$ and $k_{\rm pol} = 0.23$, the central bottom panel with $a = 1.5$ and $k_{\rm pol} = 0.22$, and the right bottom panel with $a = 2.0$ and $k_{\rm pol} = 0.19$. The global physical quantities of these configuration are listed in Table 5.1.

of μ corresponds to a lower value of $k_{\rm pol}$). As a result the value of the magnetic field at the center, which is mostly determined by the current term $\rho h k_{\rm pol}$, drops. This is the same behaviour that we have already discussed for purely poloidal field in Sec. 4.1.1. Moreover, it is also evident that there is a maximum asymptotic value that the central magnetic field $B_{\rm c}$ can reach inside the star, and that it is smaller for higher values of a. As shown in Fig. 4.4 in the previous chapter, in the case $a = 0$ this asymptotic value is actually an inversion point for the magnetic field. Even if we have not computed models with higher μ for $a \neq 0$, it is reasonable to expect that this behaviour remains the same also at higher a.

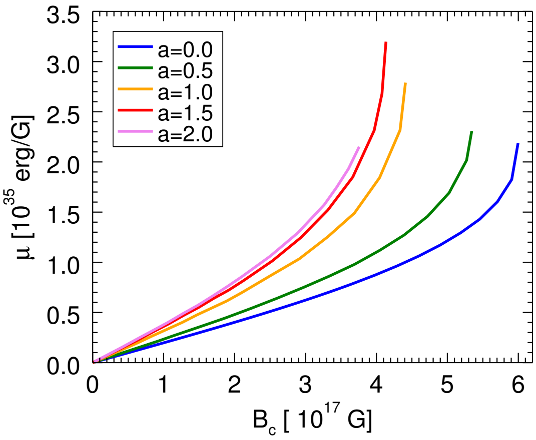

Figure 5.3: Magnetic dipole moment μ as a function of $B_{\rm c}$ for various values of the parameter a. All models have the same gravitational mass $M = 1.551 M_\odot$.

In Fig. 5.4 we display, along the same sequences, how selected global quantities change as a function of the magnetic dipole moment μ. We stress here that this parametrization is not equivalent to the one in terms of the strength of the magnetic field. We can notice that for a fixed value of μ the deviation from the unmagnetized case is progressively less pronounced at increasing values of a. This is related to the same behaviour discussed above for B_c. Peripheral currents, that contribute to the magnetic dipole moment, have minor effects on the magnetic field at the center. On the other hand it is the poloidal field that penetrates the core and dominates the energetics which is mostly responsible for these deviations. Moving to higher values of μ along the TT sequences in Fig. 5.4 the mean deformation rate $\bar{e}$ and the circumferential radius $R_{\rm circ}$ increase whereas the central density ρ_c diminishes, just as in the purely poloidal configurations.

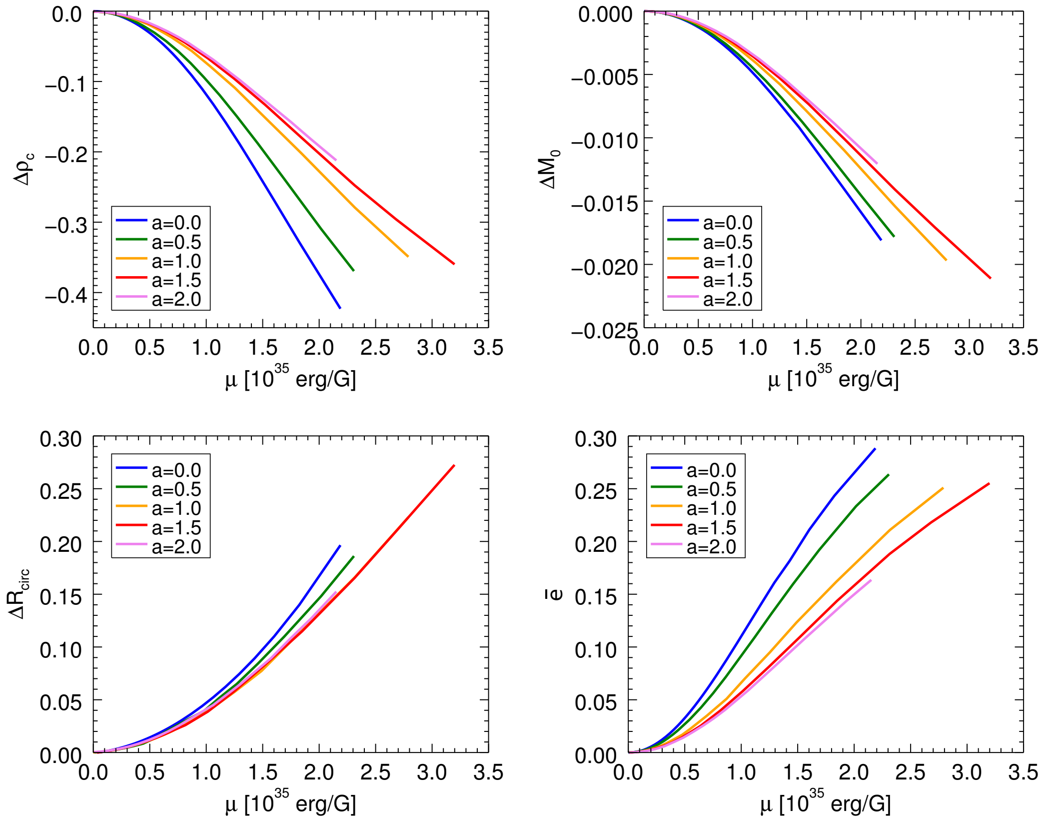

Figure 5.4: Behaviour of the baryonic central density ρ_c, of the baryonic mass M_0, of the circumferential radius $R_{\rm circ}$ and the mean deformation rate for TT equilibrium sequences with a fixed gravitational mass $M = 1.551 M_\odot$. All quantities are shown as a function of the magnetic dipole moment μ. The models corresponding to the extreme cases for each sequence are presented in details in the last four lines in Table 5.1.

It is also interesting to look at the same quantities as parametrized in terms of the strength of the magnetic field and the associated energy content, either for the toroidal or the poloidal component. In our models, for $a < 1$, the maximum magnetic field inside the star is associated with the poloidal component, and it is coincident with the central value B_c, while for $a > 1$ the maximum strength of the magnetic field is associated to the toroidal component. This does not seem to depend on the overall strength of the magnetic field. For the high-

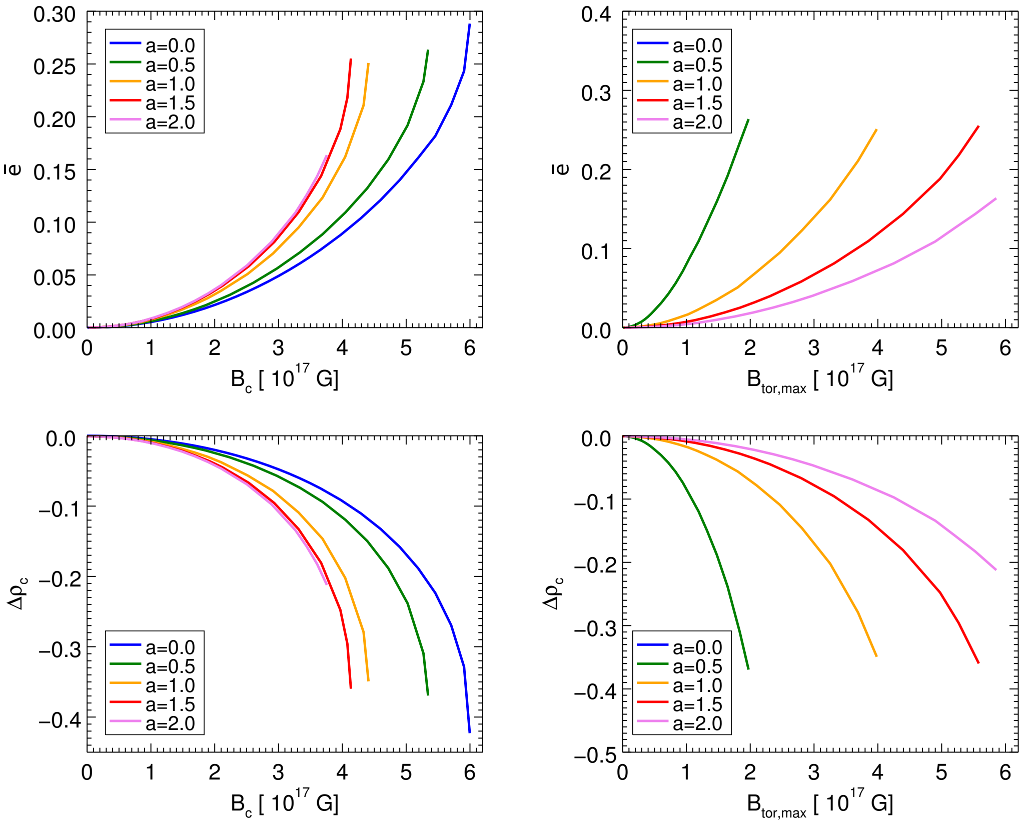

Figure 5.5: Mean deformation rate $\bar{e}$ (top) and $\Delta\rho_c$ (bottom) displayed as a function of B_c and $B_{\rm tor,max}$ along the same sequences shown in Fig. 5.4.

est values of a the strength of the poloidal component of the magnetic field might reach its maximum in the torus region rather then at the centre of the star (see the trend in Fig. 5.2).

In Fig. 5.5 we show $\Delta\rho_c$ and $\bar{e}$ as a function of B_c and $B_{\rm tor,max}$. We can notice that for a fixed B_c the trend with a is exactly the opposite than the one shown previously for fixed μ. This might seem counter-intuitive, given that both quantities are parametrizations of the strength of the poloidal field. However, models with higher a, at fixed μ, have weaker central fields, and smaller deviations, while models with higher a, at fixed B_c have higher total magnetic energy, and as such larger deviations. The effects due to the tension of the toroidal field (that would lead to a less deformed star), are dominated by the drop in the central density due to the increase of magnetic energy. For the same reason, when shown as a function of the maximum strength of the toroidal magnetic field, models show that higher values of a imply smaller deviations from the unmagnetized case.

In Fig. 5.6 these same sequences are shown in terms of their energy content. We note that, at fixed B_c, the equilibrium configurations with higher a are characterized by a higher value of both the total toroidal magnetic field energy $H_{\rm tor}$, and the poloidal magnetic field energy $H_{\rm pol}$, as expected. It is also evident that the parameter a regulates the ratio of energy between the toroidal and poloidal components of the magnetic field, $H_{\rm tor}/H$. We see that the ratio $H_{\rm tor}/H$ tends to a constant in the limit of a negligible magnetic field. In the last panel in Fig. 5.6 we also show the relation between B_c and the maximum strength of the toroidal magnetic field $B_{\rm tor,max}$. The ratio $H_{\rm tor}/H$ shows a clear maximum at ~ 0.07 for $a \simeq 1.5$. For smaller values of a this ratio increases because the strength of the toroidal field increases, however, for $a \gtrsim 1$, the volume taken by the torus, where the toroidal field is confined, diminishes substantially, reducing the energy of the toroidal component. The net effect of the torus shrinkage on $H_{\rm tor}/H$ is also evident from Fig. 5.7 where the magnetic energy ratio is shown as a function of the parameter a along a sequence with fixed $B_{\rm c} = 2 \times 10^{17}$ G.

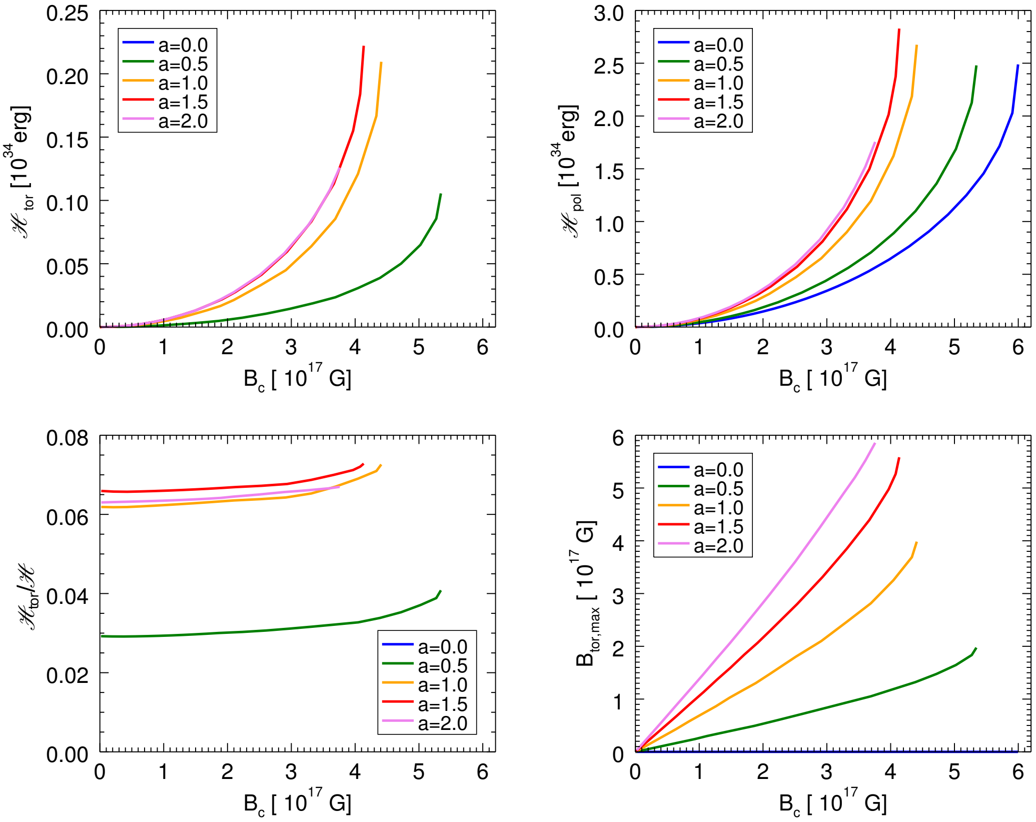

Figure 5.6: Top left panel: toroidal magnetic energy $H_{\rm tor}$. Top right panel: poloidal magnetic energy $H_{\rm pol}$. Bottom left panel: ratio of the toroidal magnetic energy $H_{\rm tor}$ to the total magnetic energy H. Right bottom panel: maximum value of the toroidal magnetic field strength $B_{\rm tor,max}$. All quantities are plotted as a function of the central magnetic field strength $B_{\rm c}$ along the same sequences shown in Fig. 5.4.

Summarizing our results, in this section we have seen that while the magnetization constant $k_{\rm pol}$ regulates the strength of both the toroidal and poloidal magnetic field (up to the inversion point, where $B_{\rm c}$ reaches its maximum value along the equilibrium sequence), the parameter a controls the magnetic energy ratio $H_{\rm tor}/H_{\rm pol}$, modifying the profiles of the magnetic distribution inside the star. As the parameter a grows the amplification of the toroidal component is accompanied by a growth of the poloidal component in the outer layer of the star and its morphology strictly resembles the one obtained with fully saturated additive currents discussed in Sec. 4.1.2 (compare Fig. 5.2 and Fig. 4.9). As a consequence, at a given $H_{\rm pol}$, configurations with higher a have a larger total magnetic energy, corresponding to a larger toroidal field, but a smaller value of the central magnetic field strength. This not only reflects on the peculiar trends observed for μ, but it has also important consequences on the

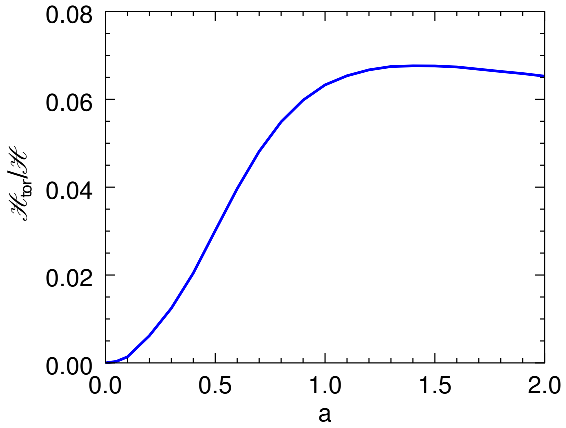

Figure 5.7: Ratio of the toroidal magnetic energy $H_{\rm tor}$ to the total magnetic energy H as a function of the parameter a along a sequence with fixed gravitational mass $M = 1.551 M_{\odot}$ and central magnetic field strength $B_{\rm c} = 2 \times 10^{17}$ G.

effects of mixed field on the stellar deformation: in our equilibrium models, the growth of the toroidal field strength, requires a redistribution of the poloidal energy toward the stellar surface that manifests as a reduction of the effectiveness of the poloidal field in affecting the deformation of the star (see Sec. 4.3.2). This implies that our previous results in Eqs. 3.13 and 4.20, obtained separately for a purely toroidal or a purely poloidal magnetic field respectively, can not be used together to infer the induced deformation even in the linear regime, where differences are already of the order of 40% for the higher values of a. Nevertheless, the previous parametrizations of $\bar{e}$ can be generalized to

$$\bar{e} \simeq \frac{C_{\bar{e}}}{W_0}\left[-(1.3 + q_{\rm tor}\, a)\frac{H_{\rm tor}}{M/{\rm M}_{\odot}} + (1.8 + q_{\rm pol}\, a)\frac{H_{\rm pol}}{M/{\rm M}_{\odot}}\right], \tag{5.6}$$

where $q_{\rm tor}$ and $q_{\rm pol}$ are corrective coefficients accounting for the current redistribution. Since the contribution of the toroidal magnetic field energy $H_{\rm tor}$ to $\bar{e}$ is $\lesssim 5\%$ and since we expect that the poloidal current redistribution is less efficient in deforming the star than fully saturated toroidal currents (see Secs 3.5 and 4.3.2), we assume $q_{\rm tor} = 0$. For weak magnetic fields $B \lesssim 10^{17}$ G and $a \lesssim 2$ the linear trend of $\bar{e}$ is fitted by Eq. 5.6 with an accuracy $\lesssim 10\%$ assuming $q_{\rm pol} = 0.33$.

5.2 The role of the current distribution

Let us discuss in this section the role played by a different current distribution regulated by the parameter ζ in the Eq. 5.2. As in Sec. 4.1.2 for the purely poloidal field case, we limit our study to the weak magnetization regime adopting a different renormalization for the current term $\mathcal{I}$. Eq. 4.2 is used for $\mathcal{M}$ while for the current function $\mathcal{I}$ we use the following prescription

$$\mathcal{I} = \frac{\hat{a}}{\zeta + 1}\Theta[\Psi - \Psi_{\rm sur}]\frac{(\Psi - \Psi_{\rm sur})^{\zeta+1}}{(\Psi_{\rm sur})^{\zeta}}. \tag{5.7}$$

where $\hat{a}$ plays the same role of a. As discussed in Sec. 4.1.2, with these choices in the low magnetization limit ($H << M$), the solution of the GS equation does not depend on the magnetic field strength and our solution can be rescaled to any value of $B_{\rm max}$ up to $10^{16}G$ (corresponding to $B_{\rm pole} \sim 10^{15}$), when the influence by the magnetic field itself on fluid and metric quantities becomes relevant.

The role of ζ is to regulate the shape of the current distribution inside the torus. For $\zeta \to -0.5$ the current becomes uniformly distributed within the torus, while for $\zeta > 0$ it concentrates in the vicinity of the neutral line, where the poloidal field vanishes. As was pointed out by Ciolfi and Rezzolla (2013) and Fujisawa and Eriguchi (2015) the role of the current distribution inside the torus region plays an important role in establishing the maximum allowed magnetic energy ratio $H_{\rm tor}/H$. In particular they both show that it is the integrated current associated with $\mathcal{I}$ that prevents TT configurations to reach the toroidal dominated regime: as the strength of this current increases the toroidal field rises, but the torus-like region shrinks toward the surface of the star so that its volume diminishes.

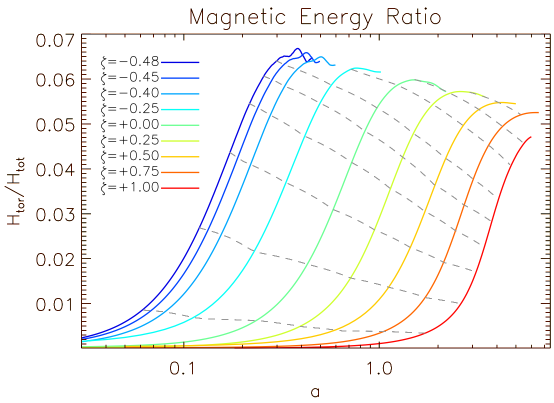

Figure 5.8: Value of the ratio $H_{\rm tor}/H$ for TT sequences characterized by different values for ζ as a function of $\hat{a}$. The dashed lines correspond to configurations where the ratio between the maximum strength of the toroidal magnetic field $B^{\rm tor}_{\rm max}$, and the maximum strength of the poloidal component $B^{\rm pol}_{\rm max}$ is constant. From bottom to top $B^{\rm tor}_{\rm max}/B^{\rm pol}_{\rm max} = 0.1, 0.2, 0.3, 0.4, 0.5, 0.6, 0.8, 1.0, 1.25$.

In Fig. 5.8 we show how the ratio of magnetic energy associated to the toroidal field $H_{\rm tor}$ over the total magnetic energy H changes with the parameters a and ζ. The maximum value of this ratio is always ~ 0.06, slightly higher for smaller values of ζ. In all cases we verified that at high values of $\hat{a}$ the volume of the region containing the toroidal magnetic field is strongly reduced. For $\zeta = 1$ we could not find equilibrium models (solution of the GS equation) all the way to the maximum (the algorithm failed to converge). Given that, for Eq. 5.7, both the energy of toroidal magnetic field and the associated current scale with $\mathcal{I}$, one cannot increase the former without increasing the latter. The systems seem always to self-regulate, with a maximum allowed current, implying a maximum allowed toroidal magnetic energy. The value of ζ affects the local value and distribution of the magnetic field, but does not play a relevant role for integrated quantities like currents and magnetic energy. Indeed by looking at Fig. 5.8 and Fig. 5.11, it is evident that for $\zeta < 0$ it is not possible to have configurations where the maximum strength of the toroidal field exceeds the one of the poloidal field. For smaller ζ the same toroidal magnetic field energy, corresponds in general to weaker toroidal magnetic fields. For $\zeta > 0$ instead we could reach configurations with a toroidal field stronger than the poloidal one. Interestingly the volume of the torus, for configurations where the ratio $H_{\rm tor}/H$ is maximal, does not depend on ζ.

One can also look at the magnetic field distribution on the surface of the star. Given our previous results for purely poloidal configurations in Sec. 4.1.2, we expect strong deviations from the standard dipole, where the strength of the magnetic field at the pole is twice the one at the equator. In Fig. 5.11 we show the total strength of the magnetic field at the surface (where the field is purely poloidal), for configurations where the ratio $H_{\rm tor}/H$ is maximal. The presence of a current torus, just underneath the surface, is evident in the peak of the field strength at the equator. The peak is even narrower than what was found for purely poloidal cases with $\xi = 10$ (compare with Fig. 4.9 in Sec. 4.1.2) and the strength of the equatorial field can be more than twice the polar one. Again, there is little difference among cases with different ζ. Higher values of ζ correspond to currents that are more concentrated around the neutral line, located at $\sim 0.85 R_{\rm NS}$, and as such buried deeper within the star. Indeed the strength of the magnetic field at the equator with respect to the value at the pole, is higher for smaller ζ.

5.2.1 Twisted Ring Configurations

In the previous part of this section we have shown that in the case of TT geometry it is not possible to reach toroidally dominated configurations. This result is also independent on the particular shape of the current distribution $\mathcal{I}$. The system always self-regulates. As was pointed out by Ciolfi and Rezzolla (2013) this is due to the one to one correspondence between integrated quantities, like the net current and magnetic field energy. Motivated by this, we can look for different forms for the equation $\mathcal{I}$ that allow a larger toroidal field, with a smaller net integrated current. The current given by Eq. 5.7 has always the same sign and, as shown, acts as an additive term. On the other hand, we can adopt another form for $\mathcal{I}$ such that the current associated with the new choice changes its sign within the toroidal region where it is defined. In particular we set

$$\mathcal{I}(\Psi) = \frac{\hat{a}}{\zeta + 1}\Theta[\Psi - \Psi_{\rm sur}]\frac{(\Psi - \Psi_{\rm sur})^{\zeta+1}(\Psi_{\rm max} - \Psi)^{\zeta+1}}{(\Psi_{\rm sur}\Psi_{\rm max})^{2\zeta+1/2}} \tag{5.8}$$

where $\Psi_{\rm max}$ is the maximum value assumed by the magnetic potential inside the star. The field in this case has a geometry reminiscent of a *Twisted Ring* (TR): its strength vanishes on the neutral line, where also the poloidal field goes to zero, and reaches a maximum in a shell around it. This can be clearly seen in Fig. 5.9. The net integrated currents in this case, is much less than in the case of Eq. 5.2, and it is globally subtractive.

In Fig. 5.10 we show how the ratio of magnetic energy associated to the toroidal field $H_{\rm tor}$ over the total magnetic energy H changes with the parameter $\hat{a}$ and ζ. Again we find that it is not possible to build models that are toroidally dominated. The maximum value of

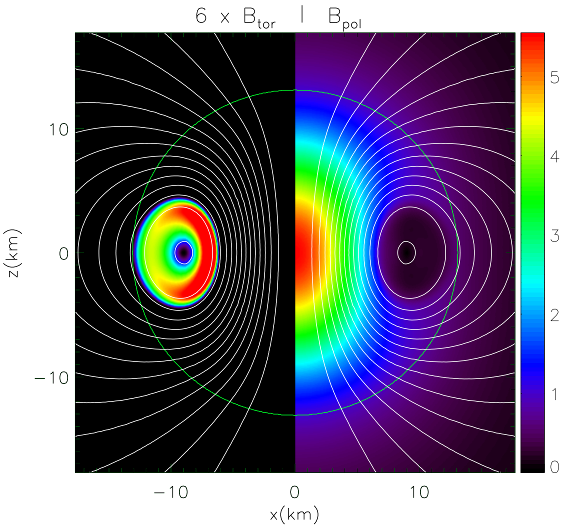

Figure 5.9: Magnetic field for a TR configuration with $\zeta = 0$ and $a = 12.6$ (corresponding to a ratio $B^{tor}_{max}/B^{pol}_{max} = 0.15$ close to the maximum). Strength of the toroidal magnetic field (left) multiplied times a factor 6 for convenience, and poloidal magnetic field (right) normalized to the surface value at the pole. White contours represent magnetic field surfaces. The thick green line is the stellar surface.

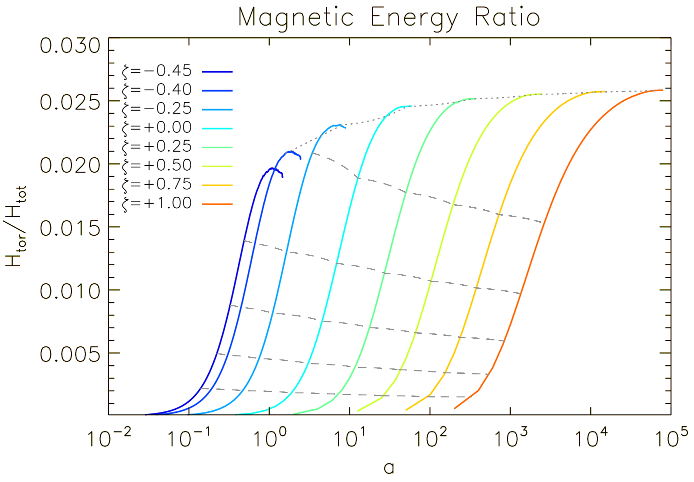

Figure 5.10: Value of the ratio H_{tor}/H for TR sequences characterized by different values for ζ as a function of $\hat{a}$. The dashed lines correspond to configurations where the ratio between the maximum strength of the toroidal magnetic field B^{tor}_{max}, and the maximum strength of the poloidal component B^{pol}_{max} is constant. From bottom to top $B^{tor}_{max}/B^{pol}_{max} = 0.05, 0.075, 0.10, 0.125, 0.150$. The dotted line corresponds to configurations where $B^{tor}_{max}/B^{pol}_{max} = 0.14$, indicating that the ratio of the magnetic field component is not monotonic.

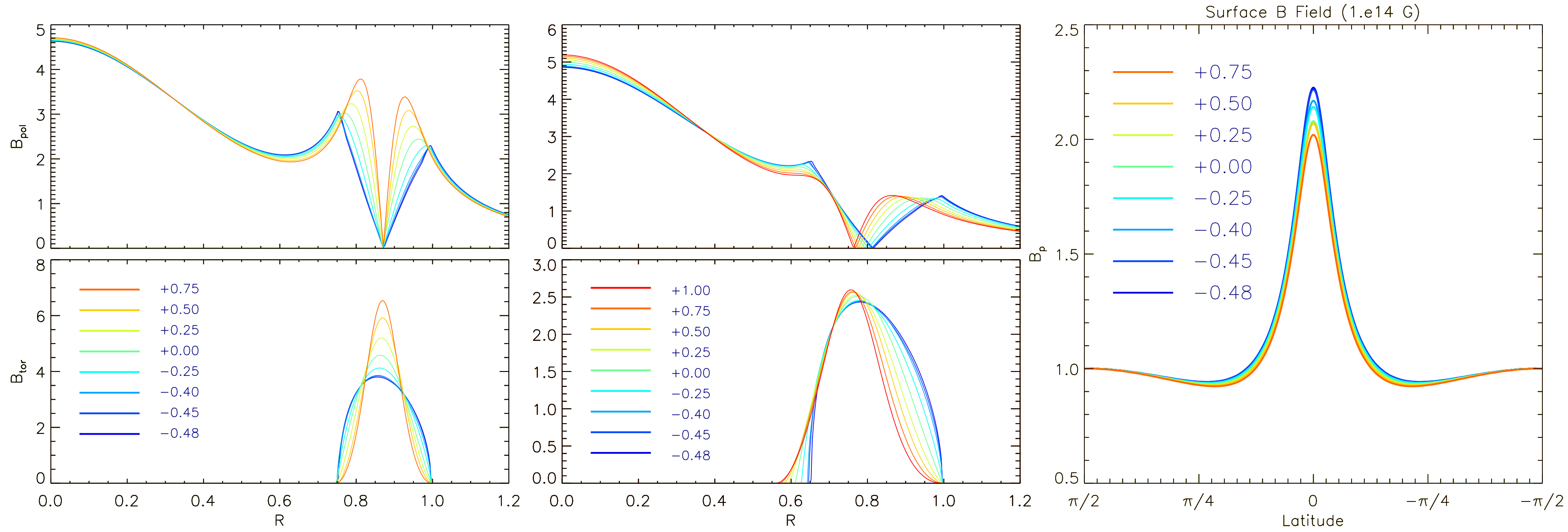

Figure 5.11: Left panel: strength of the poloidal magnetic field (top) and toroidal magnetic field (bottom) inside the star on the equatorial plane as a function of r, normalized to the equatorial radius r_e, for models corresponding to the maximum of $H_{\rm tor}/H$ for various values of ζ. Middle panel:strength of the poloidal magnetic field (top) and toroidal magnetic field (bottom) inside the star, on the equatorial plane, as a function of r, for models corresponding to $B^{\rm tor}_{\rm max}/B^{\rm pol}_{\rm max} = 0.5$. Right panel: strength of the magnetic field at the surface for models corresponding to the maximum of $H_{\rm tor}/H$. In all cases the strength is normalized to the surface value at the pole.

the ratio $H_{\rm tor}/H$ never exceeds 0.03 for all the values of ζ that we have investigated. The reason now is exactly the opposite of the one for TT configurations. The current of TR geometry, as anticipated, is subtractive. It acts like the nonlinear terms in the purely poloidal configurations with $\xi < 0$ (see Sec. 4.1.2). Its effect is to remove current from the interior of the star. This means that in the region where $\mathcal{I} \neq 0$, the vector potential Ψ becomes shallower: the quantity $[\Psi_{\rm max} - \Psi_{\rm sur}]$ diminishes. However, the strength of the toroidal magnetic field itself scales as $[\Psi_{\rm max} - \Psi_{\rm sur}]$. The nonlinearity of the problem manifests itself again as a self-regulating mechanism. Increasing $\hat{a}$, in principle, implies a higher subtractive current, but this reduces the value of $[\Psi_{\rm max} - \Psi_{\rm sur}]$, and the net result is that subtractive current saturates, and the same holds for the toroidal magnetic field. This saturation is reached at small values of $H_{\rm tor}/H$. Indeed, in Fig. 5.10, a clear maximum is only visible for $\zeta < 0$, while for $\zeta \geq 0$ the curves seem to saturate to an asymptotic value. Again we find that the value of ζ leads to small variations, with higher values of ζ leading to configurations with slightly higher value of $H_{\rm tor}/H$.

In all the parameter space we have investigated the strength of the toroidal magnetic field never exceeds the one of the poloidal component. At most, the toroidal magnetic field reaches values that are ~ 0.15 times the maximum value of the poloidal field. This is in sharp contrast with what was found for TT cases. Moreover, while in the TT cases the maximum strength of the toroidal field $B^{\rm tor}_{\rm max}$ was found to be a monotonically increasing function of the parameter a, along sequences at fixed ζ, now $B^{\rm tor}_{\rm max}$ reaches a maximum $\sim 0.15 B^{\rm pol}_{\rm max}$, and then slowly diminishes, as can be seen from Fig. 5.10. Interestingly, the region occupied by the toroidal magnetic field does not shrink as a increases. The saturation of the toroidal magnetic energy is not due to a reduction of the volume filled by the toroidal field, but to a depletion of the currents.

As was done for the TT cases, we can also look at the distribution of magnetic field inside the star. In Fig. 5.12, we show the strength of the poloidal and toroidal components of the magnetic field along an equatorial cut. The effect of subtractive currents is evident in the suppression of the poloidal field in the TR region that extends from about half the star radius to its outer edge. It is also evident that the value of ζ plays only a minor role, and that differences are stronger at saturation than for intermediate values. Interestingly, there are very marginal effects concerning the strength of the magnetic field at the surface, which is essentially the same as the standard dipole. Again this can be partially understood recalling the behaviour of purely poloidal configurations with $\xi < 0$. In those cases, substantial deviations from the dipolar case were achieved only in the limit $\xi \rightarrow 1$, when a large part of the star was unmagnetized. Here the size of the unmagnetized ring region remains more or less constant, and it does not affect the structure of the field at the surface. The global effect of the subtractive currents is small, and this reflects in the trend of the magnetic dipole moment, which diminishes only slightly by about 30-40%.

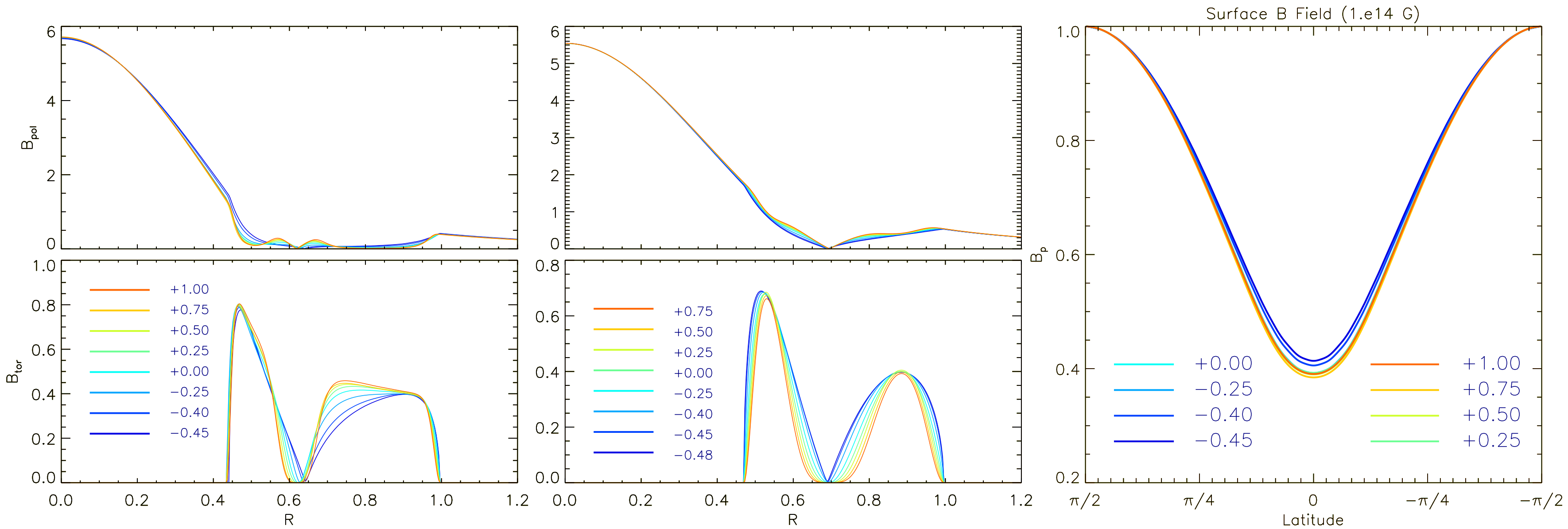

Figure 5.12: Left panel: strength of the poloidal magnetic field (top) and toroidal magnetic field (bottom) inside the star, on the equatorial plane, as a function of r, normalized to $R_{\rm NS}$,for models corresponding to the maximum of $H_{\rm tor}/H$, for various values of ζ. Middle panel:strength of the poloidal magnetic field (top) and toroidal magnetic field (bottom) inside the star, on the equatorial plane, as a function of r, for models corresponding to $B^{\rm tor}_{\rm max}/B^{\rm pol}_{\rm max} = 0.5$. Right panel: strength of the magnetic field at the surface for models corresponding to the maximum of $H_{\rm tor}/H$. In all cases the strength is normalized to the surface value at the pole.

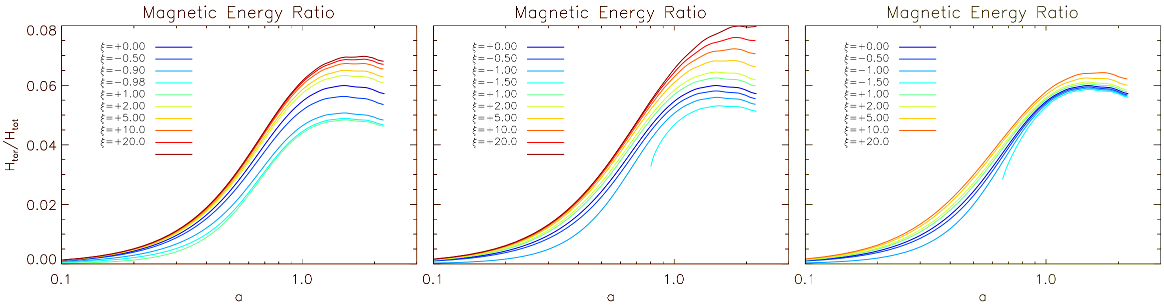

Figure 5.13: Values of the ratio $H_{\rm tor}/H$ for TT configurations with $\zeta = 0$, in the presence of nonlinear terms in the definition of $\mathcal{M}$. Left panel: cases with $\nu = 1$. Middle panel: cases with $\nu = 4$. Right panel: cases with $\nu = 10$.

5.2.2 Mixed nonlinear currents

It was suggested by Ciolfi and Rezzolla (2013) that a possible reason why TT configurations, computed using $\xi = 0$ in $\mathcal{M}$, could not achieve the toroidally dominated regime, was due to the fact that the contribution to the azimuthal current from $\mathcal{I}$ soon dominates. As a consequence, the resulting poloidal configuration enters the nonlinear regime in which the size of the torus region, where the toroidal field is confined, shrinks. They show that, by introducing a current term in $\mathcal{M}$ to compensate for $\mathcal{I}$, it was possible to avoid this behaviour. However they also stressed the fact that a very peculiar form for $\mathcal{M}$ was needed to achieve significative results.

Here we investigate what happens to TT models, using for $\mathcal{I}$ the form of Eq. 5.7, if we retains nonlinear terms in the definition of $\mathcal{M}$, and what happens in cases where $\xi \neq 0$. In Fig. 5.13 we show how $H_{\rm tor}/H$ changes for TT configurations with $\zeta = 0$ for various values of the parameter ξ and for selected values of $\nu = 1, 4, 10$. Naively, based on the idea that compensating currents are needed to achieve toroidally dominated configurations, one would expect that higher values of $H_{\rm tor}/H$ should be reached for $\xi < 0$ (subtractive currents). Fig. 5.13 shows instead that the trend is the opposite. In general, lower values of $H_{\rm tor}/H$ are found for $\xi < 0$ and higher for $\xi > 0$, even if this is just a minor difference. The value of ν seems not to play a major role. Interestingly the effect is maximal for intermediate values of $\nu = 4$, and marginal for $\nu = 10$. This counter-intuitive trend is due to the fact that both the effects of the current term $\mathcal{I}$ and the contribution of nonlinear terms in $\mathcal{M}$, become important only in the fully nonlinear regime. For values of $\xi \sim 0$ the effect of the nonlinear current term in $\mathcal{M}$ is negligible. For higher values of ξ this nonlinear term becomes more important. In the case $\xi < 0$ they give rise to a compensating current (the net dipole grows less) but, as discussed, they also tend to suppress the vector potential and this effect is stronger, leading to a overall decrease of the magnetic field. In the case $\xi > 0$, one would expect this additive current to lead to an even more pronounced reduction in the torus volume, however, this is not so. The net dipole increases but this additive currents enhance the vector potential and the net result is a higher $H_{\rm tor}/H$ (up to 30% higher for $\nu = 4$ and $\xi = 20$). The highly non trivial behaviour of the nonlinear regime is apparent. It is however possible that different

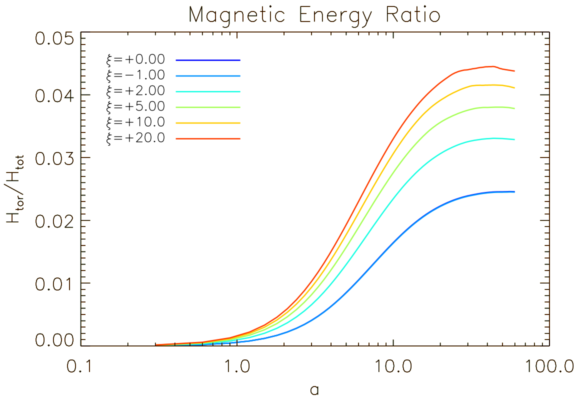

Figure 5.14: Values of the ratio $H_{\rm tor}/H$ for TR configurations with $\zeta = 0$, in the presence of nonlinear terms in the definition of $\mathcal{M}$, with $\nu = 4$.

forms for the compensating current might lead to different results.

Interestingly, again we are not able to construct equilibrium model with current inversion. It is possible, for higher values of ν, to build models with $\xi < -1$, but only as long as the current in the domain is always of the same sign. Indeed, cases with $\xi < -1$ are allowed by the presence of a current due to $\mathcal{I}$, given by Eq. 5.7, that is always additive. There appears to be a threshold value for a below which cases with $\xi < -1$ are not realized. Solutions with subctractive currents can be built only as long as the nonlinear current term is subdominant, and other currents enforce stability. Given the presence of an extra current due to $\mathcal{I}$, associated with the toroidal magnetic field, now it is possible to build solutions with $\xi < -1$.

Similar results apply for the cases of TR configuration where $\mathcal{I}$ is given by Eq. 5.8. In Fig. 5.14 we show these results. For values of $\xi < 0$ the ratio $H_{\rm tor}/H$ is essentially unchanged (it looks like the ratio is marginally smaller). For positive values of ξ we found a substantial increase: $H_{\rm tor}/H$ can be a factor 2 higher than in the simple TR case. In this case, the additive non linear term in $\mathcal{M}$ compensates the subtractive current due to $\mathcal{I}$, and stronger values for the magnetic field are achieved. However, in the range of parameter investigated here, the ratio $H_{\rm tor}/H$ never exceeds 0.05. The energetics is still dominated by the poloidal magnetic field.

Given the opposite behaviour of the currents associated with $\mathcal{I}$, respectively from Eq. 5.7, and Eq. 5.8, we also investigated configurations where the current associated with $\mathcal{I}$, is given by a combination of TT and TR configurations. Based on the results discussed above, we expect that the additive term associated with the component of $\mathcal{I}$ from Eq. 5.7, should lead to results similar to what we found for TR configurations with nonlinear terms in $\mathcal{M}$ with $\xi > 0$. Indeed this is confirmed. In general we find that the ratio $H_{\rm tor}/H$ is smaller than for the TT case, but larger than for TR case, even by a factor 2. It seems that additive currents, at least for the functional form adopted here, tend to dominate over subtractive ones.

5.3 Dependence on the stellar model

In the previous sections we have investigated in detail the role of two families of currents for $\mathcal{I}$, that can be considered quite representative of a large class of current configurations. Our results show that in neither case we could obtain magnetic field distributions where the energetics was dominated by the toroidal component.

In this section we try to investigate the importance of the underlying stellar model. In general, previous studies have mainly focused on the distribution of currents, assuming a reference model for the NS with $M = 1.4M_\odot$ (Ciolfi et al. 2009, 2010, Ciolfi and Rezzolla 2013, Lander and Jones 2009). Only Glampedakis et al. (2012a) have partly investigated how the stellar structure might affect the energetics properties of the magnetic field. In particular they focused on the role of stable stratification, and showed that this might change the maximum amount of magnetic energy associated to the toroidal magnetic field, in standard TT configurations.

In Fig. 5.15 we show how the ratio $H_{\rm tor}/H$ changes as a function of a for standard TT models with $\zeta = 0$, but for NSs with different masses. For the EoS in Sec. 2.8 the maximum mass for a NS is found to be $\sim 1.7M_\odot$. It is clear that models with a higher mass have a higher value of the ratio $H_{\rm tor}/H$, for the same value of a. Interestingly, the maximum value reached by $H_{\rm tor}/H$ for a $1.7M_\odot$ NS, is about 0.08, compared to 0.06 for a $\sim 1.4M_\odot$ NS. This is a substantial relative increase, even if the magnetic energy is still dominated by the poloidal component. Moreover this increasing trend is stronger at higher masses.

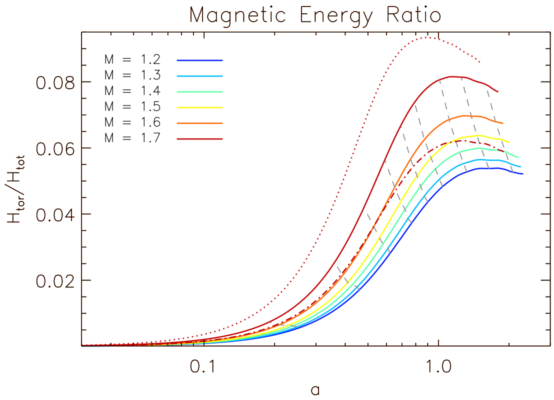

Figure 5.15: Value of the ratio $\mathcal{H}_{\rm tor}/\mathcal{H}$ for TT sequences with $\zeta = 0$, characterized by different values for the gravitational mass as a function of a. The dashed grey lines corresponds to configurations where the ratio between the maximum strength of the toroidal magnetic field $B^{\rm tor}_{\rm max}$, and the maximum strength of the poloidal component $B^{\rm pol}_{\rm max}$ is constant. From bottom to top $B^{\rm tor}_{\rm max}/B^{\rm pol}_{\rm max} = 0.1, 0.2, 0.3, 0.4, 0.5, 0.6, 0.8, 1.0, 1.25$. The dotted red line corresponds to a configuration with $M = 2.0M_\odot$, and the same central rest mass density as the $1.7M_\odot$ case. The dot-dashed red line corresponds to a configuration with $M = 1.7M_\odot$, but a lower central rest mass density with respect to the $K_{\rm a} = 110$ case.

We also investigated how much of this trend is related just to the total stellar mass (i.e. the compactness of the system) and how much it depends on the value of rest mass density in the core of the NS. Indeed it was previously found the NSs with higher masses can harbor in principle stronger magnetic fields (see Chaps. 3 and 4). On the other hand, the current associated with $\mathcal{M}$, responsible for the structure of the poloidal field, scales as the rest mass density. For models built by keeping constant $K_{\rm a} = 110$, a higher mass implies a higher central rest mass density, so that it is hard to disentangle them. In Fig. 5.15 we show also two models with different EoS: one that has the same central rest mass density as the $1.7 M_{\odot}$ NS, but different values of the adiabatic constant $K_{\rm a}$, such that is total gravitational mass is $2.0 M_{\odot}$; the other has the same mass of $1.7 M_{\odot}$, but a lower central rest mass density (about one third). It is evident that models with a smaller total mass, given the same central rest mass density, correspond to lower maximum value for $\mathcal{H}_{\rm tor}/\mathcal{H}$. On the other hand, given the same central rest mass density, the ratio $\mathcal{H}_{\rm tor}/\mathcal{H}$ clearly increases with total mass. It appears that the rest mass density stratification (how much concentrated is the rest mass density distribution in the core and how much shallow is it in the outer layers), regulates the relative importance of $\mathcal{I}$ and $\mathcal{M}$, and the net outcome in terms of energetics of the toroidal and poloidal components.

5.4 Summary

In this Chapter we have analyzed several equilibrium configurations for NSs endowed with a mixed magnetic field. This allowed us to investigate general trends and to sample the role of various current distributions both in the strong and weak field regime.

Our findings are in qualitative agreement with previous results (Lander and Jones 2009, Ciolfi et al. 2009, 2010, Armaza et al. 2015), concerning the shape, the deformation, and the expected distribution of the poloidal and toroidal components. In particular we confirm the difficulties in finding TT models based on a simple choice for the current distribution. Even if the toroidal component can reach a strength comparable with the poloidal one it remains always energetically subdominant. The main reason for this is that to increase the toroidal magnetic field, one needs to rise also the toroidal currents that in turn reduce the volume occupied by the toroidal field itself. As a consequence the deformation of all our TT models is always controlled by the poloidal component.

Recent results by Ciolfi and Rezzolla (2013) and Fujisawa and Eriguchi (2013, 2015) have however shown that specific choices for the current distribution can lead to configurations that are energetically dominated by the toroidal magnetic field, where the ratio $H_{\rm tor}/H$ can reach values close to unity. In particular Fujisawa and Eriguchi (2013, 2015) have shown, through an analytic study, that a necessary condition to obtain such TT configuration is the coexistence of oppositely flowing toroidal currents inside the NS. On the basis of these results we have investigated different current distribution, but we always find that the system saturates to configurations where the energy of the toroidal component is at most 10% of the total magnetic energy.

Unfortunately, a precise comparison with Ciolfi and Rezzolla (2013), is non trivial. For example, using the definition of current in their Eq.3, does not lead to converged solutions in the purely poloidal case. This because their formulation of Eq.3, with a non-linear term which introduces a subtractive currents with respect to the linear one, can lead to current inversions inside the NS. As we pointed out in the previous chapter (see Sec. 4.1.2), our algorithm fails (diverges) every time we attempt to model systems with current inversions, and this might be related to uniqueness issues of the elliptical GS equation. If this is indeed an issue with uniqueness then different numerical approaches might be more or less stable, and the robustness of the solution becomes questionable. Moreover Ciolfi and Rezzolla (2013) impose that the field at the surface is a pure dipole, setting all other multipoles to zero. This might probably filter out and suppress the formation of localized currents at the edge of the NS and any effect associated to small scale structures, like the increase of the value of $\Psi_{\rm sur}$. As we have shown above and in Sec. 4.1.2 for purely poloidal magnetic fields, the structure of the magnetic field at the surface, can dramatically differ from a pure dipole, depending on the current distribution. Even using the functional form by Ciolfi and Rezzolla (2013), in the range where our code converges, we found that at the surface of the NS the magnetic field is far from a pure dipole. Imposing a purely dipolar field outside the stellar surface may have been determinant in the results of Ciolfi and Rezzolla (2013), but because our algorithm is structured in such a way that it is not possible to specify such surface boundary condition, further independent verification is needed to resolve this issue.

The failure to get toroidally dominated configurations, that are expected for stability in barotropic stars, might even point to the possibility that barotropicity does not hold in NSs, and the entire stability problem is just related to entropy stratification (Reisenegger 2009, Akgün et al. 2013), and not to the current distribution. Indeed, as pointed out in Glampedakis and Lasky (2016), axisymmetric MHD equilibria in non-barotropic or multifluid NSs can be freely prescribed. It is worth to mention that stratification may also play a fundamental role in stabilizing the equilibrium configuration as shown in Lander and Jones (2012) and Mitchell et al. (2015). Finally, TT configurations may also be unstable on a spindown timescale because of the spin-lag between the crust and core rotation induced by the presence of a closed field-line region inside the core of the NS (Glampedakis and Lasky 2015).

In view of the results obtained in Chaps. 3 and 4, we have also verified that, in general, the deformation induced by a mixed field can not be trivially described as a direct sum of the deformations obtained for the toroidal magnetic field and for the poloidal magnetic field separately. This is because the interplay between the toroidal field and the magnetic field causes a rearrangement of the current distributions inside the star. In our particular case, where the two components of the magnetic field are linked together by the integrability requirement of the GS equation, the growth of the toroidal component implies that the toroidal current distribution moves from the center of the star toward the stellar surface, resembling the morphology presented for fully saturated additive current in Sec. 4.1.2. As a result even a weakly energetic toroidal field (with $H_{\rm tor} \lesssim 10\% H$) is able to induce, at a given total energy H, a substantial reduction (of the order of 40%) of the oblateness of the star. The role of the current distribution was already highlighted by Mastrano et al. (2015). Through the computation of TT models for non-barotropic NSs, they show how, augmenting the weight of the quadrupolar component of the poloidal magnetic field or enlarging the volume occupied by the toroidal field, it is possible to reduce the effectiveness of the poloidal magnetic field or, analogously, to increase the efficiency of the toroidal field in deforming the star. Hence, in general, the condition $\bar{e} = 0$ is not reached at equipartition $H_{\rm pol} = H_{\rm tor}$ but it strongly depends on the current distribution.

6

Twisted Magnetosphere models

The phenomenology and the spectral properties of SGRs and AXPs strongly support the fact that magnetar magnetospheres are tightly twisted in the vicinity of the star. Previous studies on equilibrium configurations have so far focused on either the internal or the external magnetic field, without considering a real coupling between the two fields, apart from a few very recent studies by Glampedakis et al. (2014), Fujisawa and Kisaka (2014), Ruiz et al. (2014). Here, extending the TT models analyzed in the previous Chapter, we investigate numerical equilibrium models of magnetized neutron stars endowed with a confined twisted magnetosphere. Our approach is hence based on the solution of the relativistic GS equation both in the interior and in the exterior of the compact object. A comprehensive study of the parameters space is provided, to investigate the effects of different current distributions on the overall magnetic field structure. This Chapter is based on Pili et al. (2015).

6.1 Generalizing TT models

Known magnetars show dipole spin down magnetic field below a few 10^{15}G. For this reason, and in view of the results shown in Chap. 5 we will mainly consider models obtained in the weak magnetization regime (i.e. $H << M$). The strong field regime will be briefly discussed in Sec. 6.2 in order to investigate how the magnetospheric distribution of currents acts on the stellar deformation. Moreover, given the slow rotation rate of magnetars, in the range $\sim 2-12$s, we limit our study to static cases. Here ideal GRMHD is supposed to hold not only in the interior of the star but also outside in the external magnetosphere, where plasma inertia is certainly negligible (this actually corresponds to the so called force-free regime, see again Sec. 2.5 for a detailed discussion).

We search for a solution of the GS equation (Eq. 2.125) allowing currents to flow outside the star. This can be obtained generalizing the analytical form used for TT models to

$$\mathcal{I}(\Psi) = \frac{a}{\zeta+1}\Theta[\Psi-\Psi_{\rm ext}]\frac{(\Psi-\Psi_{\rm ext})^{\zeta+1}}{(\Psi_{\rm max})^{\zeta+1/2}}, \tag{6.1}$$

where, here, $\Psi_{\rm ext}$ is the maximum value the magnetic potential reaches at a distance $r = \lambda r_{\rm e}$

from the star, while $\Psi_{\rm max}$ is, as in the previous chapters, the maximum value assumed over the entire domain. For the current function $\mathcal{M}$ we retain the simplest form given by:

$$\mathcal{M}(A_\phi) = k_{\rm pol} A_\phi. \tag{6.2}$$

Note that these choices are analogous to the ones made in Glampedakis et al. (2014). The new parameter λ, that enters in the definition of $\Psi_{\rm ext}$, allows us to control the size of the twisted magnetosphere outside the star. Results for TT models can be recovered assuming $\lambda = 1$. On the other hand, for $\lambda > 1$ the toroidal magnetic field is not confined within the star but extends smoothly outside the stellar surface, just like the poloidal component.

Given our choice for the free functions $\mathcal{M}$ and $\mathcal{I}$, the components of the conduction currents become

$$J^r = \alpha^{-1} B^r a\Theta[\Psi - \Psi_{\rm ext}] \frac{(\Psi - \Psi_{\rm ext})^\zeta}{(\Psi_{\rm max})^{\zeta+1/2}}, \tag{6.3}$$

$$J^\theta = \alpha^{-1} B^\theta a\Theta[\Psi - \Psi_{\rm max}] \frac{(\Psi - \Psi_{\rm ext})^\zeta}{(\Psi_{\rm max})^{\zeta+1/2}}, \tag{6.4}$$

$$J^\phi = \rho h\, k_{\rm pol} + \frac{a^2}{(\zeta+1)\sigma} \Theta[\Psi - \Psi_{\rm ext}] \frac{(\Psi - \Psi_{\rm ext})^{2\zeta+1}}{(\Psi_{\rm max})^{2\zeta+1}}. \tag{6.5}$$

Thanks to the renormalization by $\Psi_{\rm max}$, the ϕ component of the conduction current is independent from the absolute value of the magnetic flux function (it does not depend on the field strength), while it is directly controlled only by the magnetization parameter $k_{\rm pol}$ and a. This choice allows us to stabilize the convergence of our numerical scheme preventing the non-linear term from diverging at the highest value for a and λ. This, in turn, allows us to obtain also configurations with a complex magnetospheric field geometry.

We adopt the reference model of Sec. 2.8 and concentrate only on the magnetic properties of the equilibrium configurations. In particular in the low magnetization limit, as discussed also Secs. 4.1.2 and 5.2, with our choice for the current functions it is possible to recast the current term in a self-similar way, such that the resulting magnetic field configuration remains unchanged, modulo its strength. If J^ϕ is rescaled with a numerical factor η sending $k_{\rm pol} \mapsto \eta k_{\rm pol}$ and $a \mapsto \sqrt{\eta} a$, the solution of the GS equation itself is rescaled by the same numerical factor. The self similar parameter can be thus defined in terms of the strength of the magnetic field as

$$\hat{a} = a \left(\frac{B_{\rm pole}}{10^{14}{\rm G}} \right)^{-\frac{1}{2}}, \tag{6.6}$$

where $B_{\rm pole}$ is the magnetic field at the pole, that we have decided to always normalize to 10^{14} G. Then the quantity $\hat{a}$ parametrizes the magnetic configurations, independently from the strength of the magnetic field.

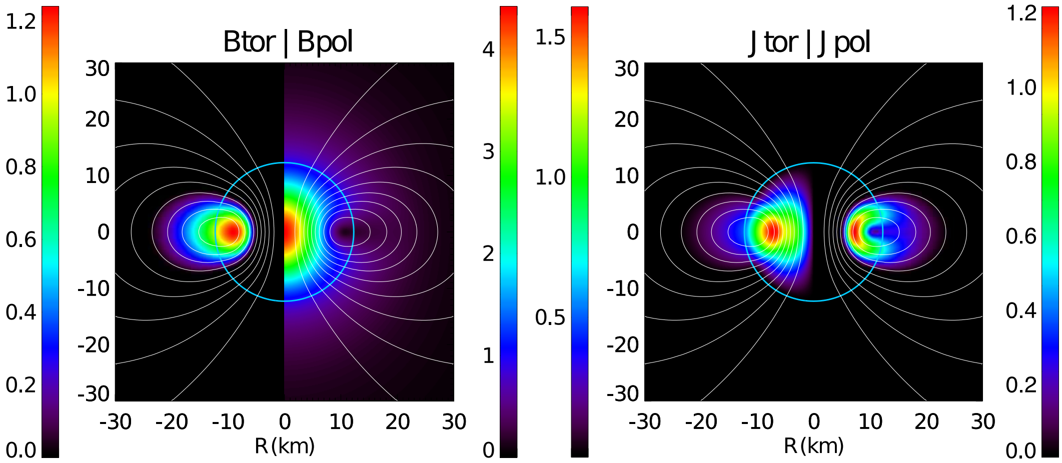

Figure 6.1: Left: strength of the toroidal (left half) and poloidal (right half) magnetic field in units of $B_{\rm pole}$. Contours represent magnetic field surfaces. Right: same as the left panel for the toroidal (left half) and poloidal (right half) current density . Current densities are expressed in units of 10^{18} statAmp cm^{-2}. In both panels the blue curves represents the surface of the star. This configuration has $\lambda = 2$ and $\hat{a} = 2.5$, corresponding the highest value for the magnetic energy ratio $H_{\rm tor}/H = 11.29 \times 10^{-2}$.

6.1.1 Models with $\zeta = 0$

We begin by discussing the simple case with $\zeta = 0$ in Eq. 6.1. In Fig. 6.1 we show a typical example of an equilibrium model with a twisted magnetosphere. This specific configuration corresponds to $\lambda = 2$ and $\hat{a} = 2.5$. The poloidal magnetic field extends through the whole domain and reaches its maximum strength $B^{\rm pol}_{\rm max} = 4.422\, B_{\rm pole}$ at the centre of the star. The toroidal component of the magnetic field is, by construction, confined inside a closed region that extends in the radial direction from the interior of the star up to twice the stellar radius, and in latitude it is contained within a wedge about $\pm\pi/6$ around the equator. The maximum value of the toroidal magnetic field $B^{\rm pol}_{\rm max} = 1.256\, B_{\rm pole}$ is reached inside the star in correspondence to the neutral line where the poloidal magnetic field vanishes. The right panel of Fig. 6.1 shows that the poloidal current density peaks inside the star, and extends smoothly outside the stellar surface along the magnetic field surfaces. The toroidal current, on the other hand, results from the sum of the linear current term in $\mathcal{M}$, $J^\phi = \rho h k_{\rm pol}$, fully confined within the star, and of the non-linear term in $\mathcal{I}$, that extends outside the star over the same region where the poloidal currents are confined. The magnetospheric equilibria of the type shown in Fig. 6.1, and discussed above, are qualitatively similar to previous results (Mikic and Linker 1994, Viganò et al. 2011, Parfrey et al. 2013). However, in those cases the equilibria were obtained by the relaxation of an initially sheared dipolar configuration, while here we directly solve the GS equation. Such configurations, for a moderate shear of the magnetic footpoints, are expected to be stable. On the other hand, our approach based on the GS equation allows us to derive equilibrium models but, of course, it does not provide any hint about their stability. A more direct comparison can be made with Glampedakis et al. (2014): in spite of a different value $\zeta = 0.5$ employed, our solutions qualitatively agree with the ones presented in more detail in the cited work.

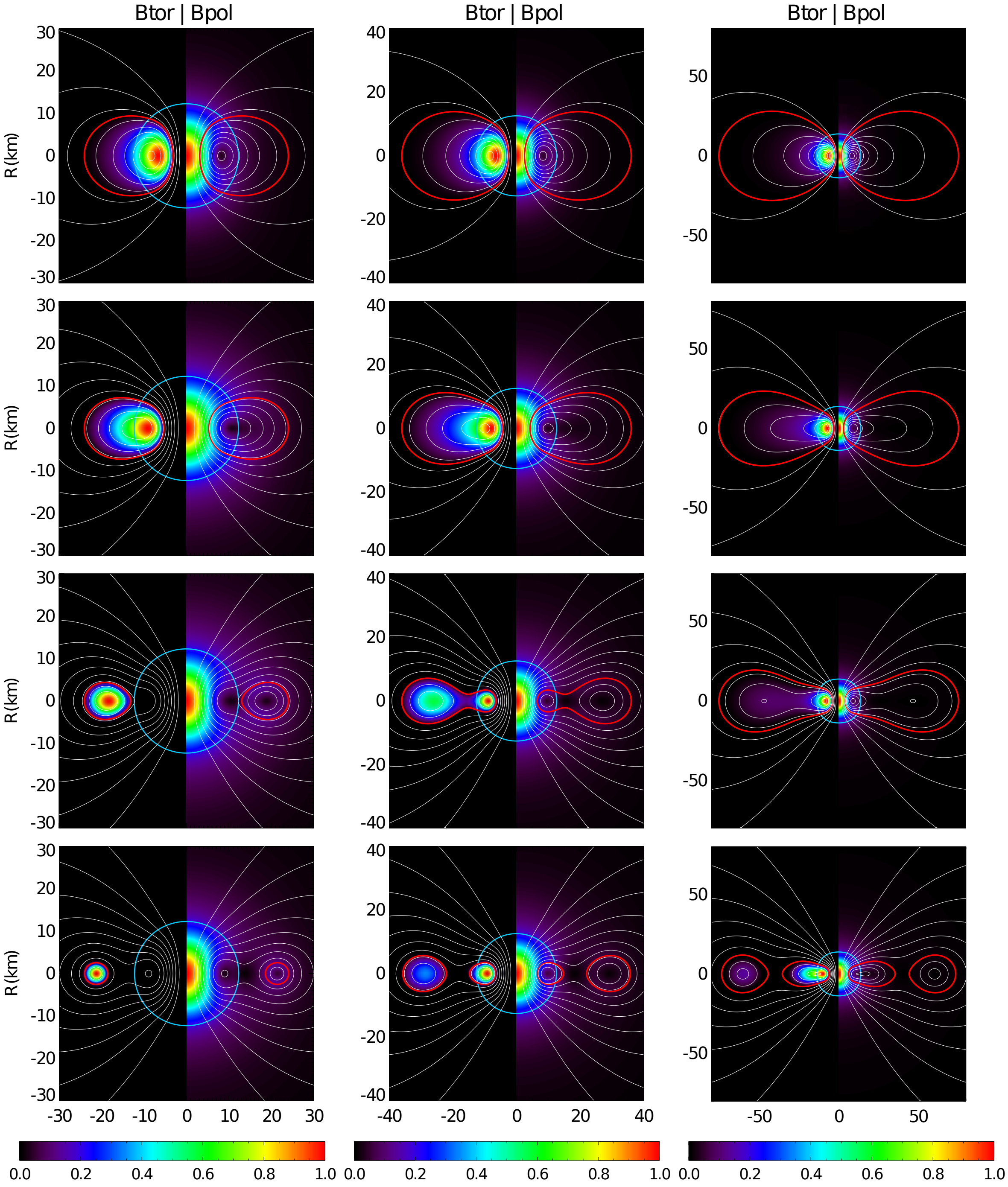

Figure 6.2: TT magnetosphere configurations: strength of the toroidal (left half of each panel) and poloidal (right half of each panel) magnetic field. The left column shows models with $\lambda = 2$, the central column those with $\lambda = 3$, and the right column those with $\lambda = 6$. Contours represent magnetic field surfaces. From top to bottom each row corresponds to increasing values of $\hat{a}$, given in Tab. 6.1. For each panel the colour code is normalized to the maximum value of the magnetic field components that are listed in Tab. 6.1. The blue line represents the surface of the star. The red line locates the boundary of the region where the toroidal component of the magnetic field is present.

Table 6.1: Values of the maximum strength of the toroidal and poloidal components of the magnetic field for the configuration shown in Fig. 6.2. Magnetic fields are expressed in unity of B_{pole}.

λ	$\hat{a}$ [10^{-3}]	$B^{\text{tor}}_{\text{max}}$	$B^{\text{pol}}_{\text{max}}$
2	0.4	0.359	5.629
	2.5	1.256	4.422
	5.6	0.938	4.576
	10	1.087	4.373
3	0.4	0.435	5.581
	1.5	1.004	4.577
	3.3	0.676	4.767
	4.2	1.170	4.618
6	0.4	0.491	5.352
	0.9	0.782	4.874
	1.3	0.822	4.842
	2.7	0.753	4.277

In Fig. 6.2 we present sequences of models computed for various values of the parameters λ and $\hat{a}$. The main characteristics of those configurations are stated in Table 6.1. These results illustrate the key features and trends of the equilibrium configurations that we were able to obtain. For small values of the parameter $\hat{a}$ (first row of Fig. 6.2), all configurations share the same overall topology and a similar magnetic field distribution. The toroidal magnetic field fills a region that smoothly extends from the interior of the star to the maximum allowed radius λr_e. As it can be seen also from Fig. 6.3, the toroidal field component reaches, in this case, a maximum inside the star and then decreases monotonically in the magnetosphere. For small values of $\hat{a}$, the non-linear current terms associated to $\mathcal{I}$ outside the star are still too weak to significantly alter the magnetic field structure below the surface.

As the contribution of the non-linear currents becomes more important, with increasing $\hat{a}$, the toroidal field increases and its peak moves toward the stellar surface together with the poloidal neutral line. This is the same behaviour that we have discussed in the case of TT models in Chap. 5. As the toroidal magnetic field increases, the ratio of the magnetic energy associated to the toroidal field H_{tor} with respect to the total magnetic energy H increases too, until it reaches a maximum. These maximal configurations are shown in the second row of Fig. 6.2. The structure and topology of the magnetic field is analogous to the small $\hat{a}$ cases (see also Fig. 6.3), however the presence of stronger magnetospheric currents now affects the field geometry outside the star. While the outer magnetic field in the small $\hat{a}$ regime still resembles closely a dipole, this is no longer true for the maximal energy configurations, where magnetic surfaces appear to be stretched, especially for high values of λ. Note, moreover, that for higher λ, the configurations of maximum energy ratio are reached for smaller values of $\hat{a}$. This because the energy is an integrated quantity that depends not just on the

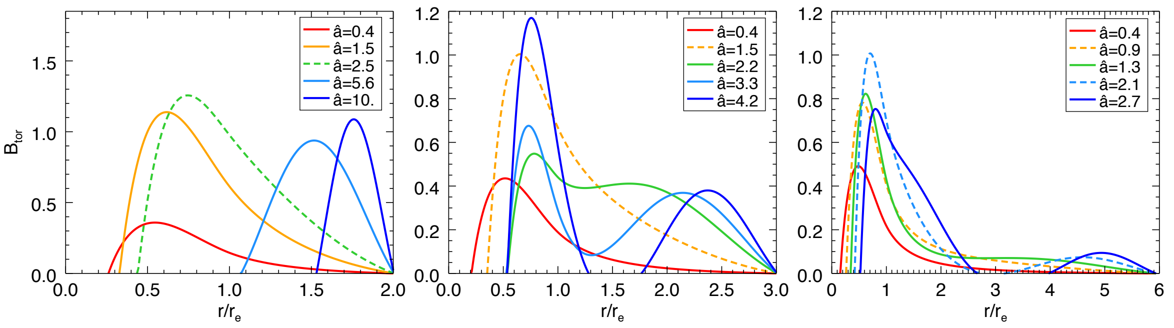

Figure 6.3: Profiles of the toroidal magnetic field strength (in units of $B_{\rm pole}$) for selected models ($\hat{a}$ is expressed in units of 10^{-3}) along the equilibrium sequences with $\lambda = 2$ (left), $\lambda = 3$ (centre) and $\lambda = 6$ (right). The dashed lines represent models where the value of $H_{\rm tor}/H$ reaches a maximum.

strength of the currents but also on the volume they fill.

After the maximum value of $H_{\rm tor}/H$ has been reached, solutions react differently to a further increase of $\hat{a}$, depending on the value of the parameter λ. This can be seen in the third row in Fig. 6.2 and in Fig. 6.3. In the case of $\lambda \leq 2$ the toroidal magnetic field migrates completely outside the star and the final outcome strictly resembles that of the TT case with $\lambda = 1$ discussed in Sec. 5.1: the toroidal magnetic field strength grows but its support progressively shrinks toward the maximum allowed radius. Here the toroidal magnetic field shows a single maximum. On the other hand, for $\lambda \geq 3$, as the neutral line approaches the stellar surface, a second peak in the strength of the toroidal magnetic field develops. This second peak moves with increasing $\hat{a}$ at larger radii in the magnetosphere, while the first peak remains inside the star, approximately at the same position, independently of $\hat{a}$. The formation of a second peak indicates a topological change in the structure of the magnetic field, where an X-point arises, usually in the vicinity of the stellar surface, and where there are magnetic regions (surfaces) in the magnetosphere disconnected from the star. A further increase in the value of $\hat{a}$ leads to solutions that show two completely disconnected magnetic regions, one inside the star, and the other outside (see the fourth row of Fig. 6.2). Note also that the maximum value of the strength of the toroidal magnetic field $B^{\rm tor}_{\rm max}$ does not grow monotonically with $\hat{a}$.

These types of equilibria, with disconnected magnetic regions, are likely to be highly unstable. Indeed, those kind of equilibria resemble the solutions find in time-dependent numerical simulation by Mikic and Linker (1994) in the context of magnetic field arcades in the solar corona, and *plasmoid* formation: our disconnected regions in the NS magnetosphere could be seen as the equivalent of the plasmoids in the solar case.

While a full 3D study of the stability and/or evolution, of the various topological configurations, is beyond the scope of the present work, it is possible to roughly evaluate the magnetospheric conditions, in relation to known stability criteria. We need also to recall here that the physical regime, to which our models apply, is typical of the late phases of the proto-NS evolution. Indeed, after ~ 100 s since the formation of the NS the neutrino wind ceases (Pons et al. 1999), a force free magnetosphere can be established and a crust begin to form freezing the poloidal magnetic field lines on the surface of the NS.

In each of our models the energy of the external toroidal magnetic field is, at most, 25% of the total magnetic energy in the magnetosphere which is, thus, dominated by the poloidal field. It is important, at this point, to distinguish between those configurations, where all field lines thread the crust, and those with disconnected regions. In the first case, if the poloidal component can be stabilized by the crust (which can be the case for weak fields $\sim 10^{14}$G), then it is unlikely that the toroidal one, being subdominant, could drive major changes in the magnetospheric structure. It is possible to compare our results to those by Parfrey et al. (2013), where a study of the magnetospheric stability was done using a time dependent shearing algorithm. We find in our models (those with no disconnected regions) that the twist amplitude, defined as the azimuthal angular displacement of the magnetospheric footpoints, does not exceed 2 radians. This value is below the critical value of 3.65 radians estimated in Parfrey et al. (2013) as a stability limit for the magnetosphere.

In the other cases, when a disconnected toroidal current loop develops in the magnetosphere around the neutral line, since some of the magnetic field lines do not cross the crust, the twist amplitude is not an indicative parameter for the stability, and one cannot invoke for this disconnected region a stabilizing effect of the crust. However the stability of this flux rope, can be determined from the Kruskal-Shafranov condition for the development of kink instability (Shafranov 1956, Kruskal and Tuck 1958). The application of this condition implies that only small detached flux ropes contained inside $1.3r_{\rm e}$ are marginally stable, while disconnected regions that extends further out from the star are unstable.

The reason why the GS equation, for large $\hat{a}$, admits solutions with multiple peaks can be easily understood. The solution of the GS equation can be seen as an eigenvalue problem for a second order non-linear PDE. For small values of $\hat{a}$ the source terms in the currents are dominated by $\mathcal{M}$: they are fully confined within the star and have a single peak. Thus the solution reflects the properties of the source, and only single-peak eigenmodes are selected. However, for higher values of $\hat{a}$, non-linear terms dominates, and other possible eigenmodes can be selected. Eigenmodes that, in principle, for a second order non-linear PDE will admit multiple radial nodes (this is the reason why two peaks develop). Indeed, as can be seen from Fig. 6.2 and 6.3, there is some hint that the more extreme case at $\lambda = 6$ might develop into a third peak. Unfortunately, we could not investigate higher values of $\hat{a}$ because the convergence of the GS solver becomes highly oscillatory, and ultimately fails.

In Fig. 6.4 we show the profiles of the poloidal and toroidal components of the magnetic field along the stellar surface. In the small $\hat{a}$ regime, the poloidal field at the surface is essentially dipolar. The toroidal magnetic field extends over a region $\pm 45^\circ$ in latitude around the equator, slightly bigger for larger values of λ. Trends are different depending if the structure evolves to a single peak or double peak. For $\lambda \leq 2$ (single peak), as $\hat{a}$ increases, the magnetic field becomes slightly higher in the polar region but decreases substantially at the equator. As the peak moves outwards, so does the poloidal neutral line (where the poloidal field vanishes). This is the reason why the equatorial field drops. The magnetic field at the surface becomes closer to a split monopole: the curvature of magnetic field surfaces

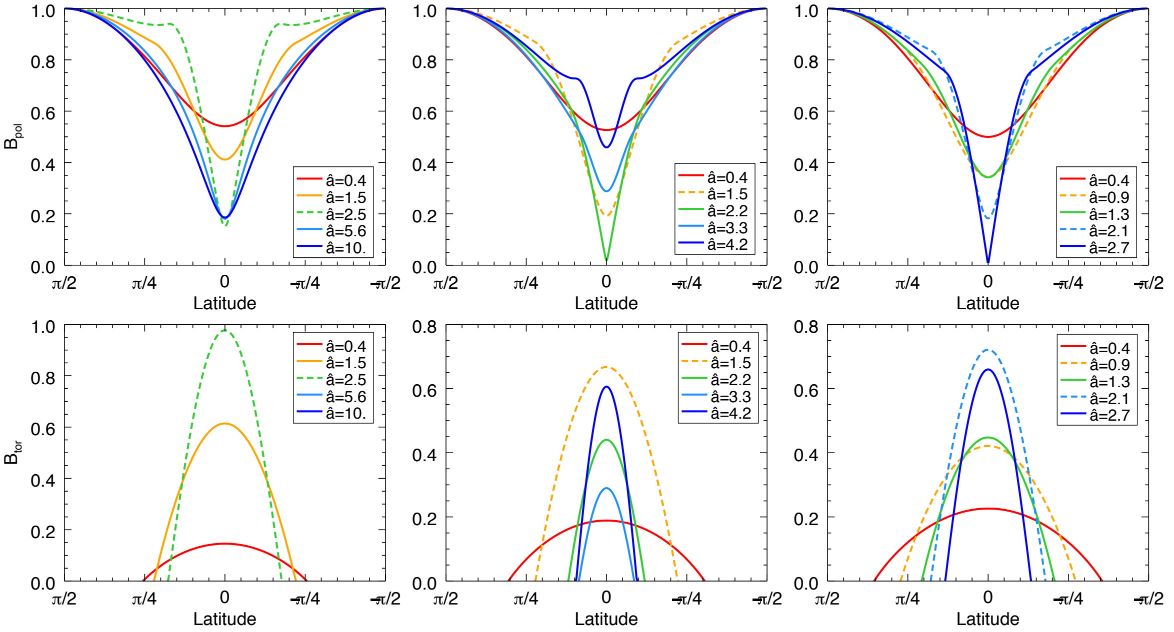

Figure 6.4: Profiles of the strength (expressed in units of $B_{\rm pole}$) of the poloidal (top panel) and toroidal (bottom panel) magnetic field on the stellar surface for selected models ($\hat{a}$ is expressed in units of 10^{-3}) along the equilibrium sequences with $\lambda = 2$ (left), $\lambda = 3$ (centre) and $\lambda = 6$ (right). The dashed lines represent models where the value of $H_{\rm tor}/H$ reaches a maximum.

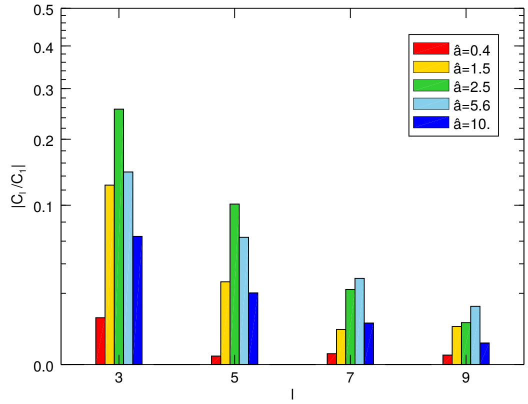

Figure 6.5: Harmonic content C_l/C_1 of the magnetic field at the surface of the star in the case $\lambda = 2$ for the selected models shown in the upper left panel of Fig. 6.4.

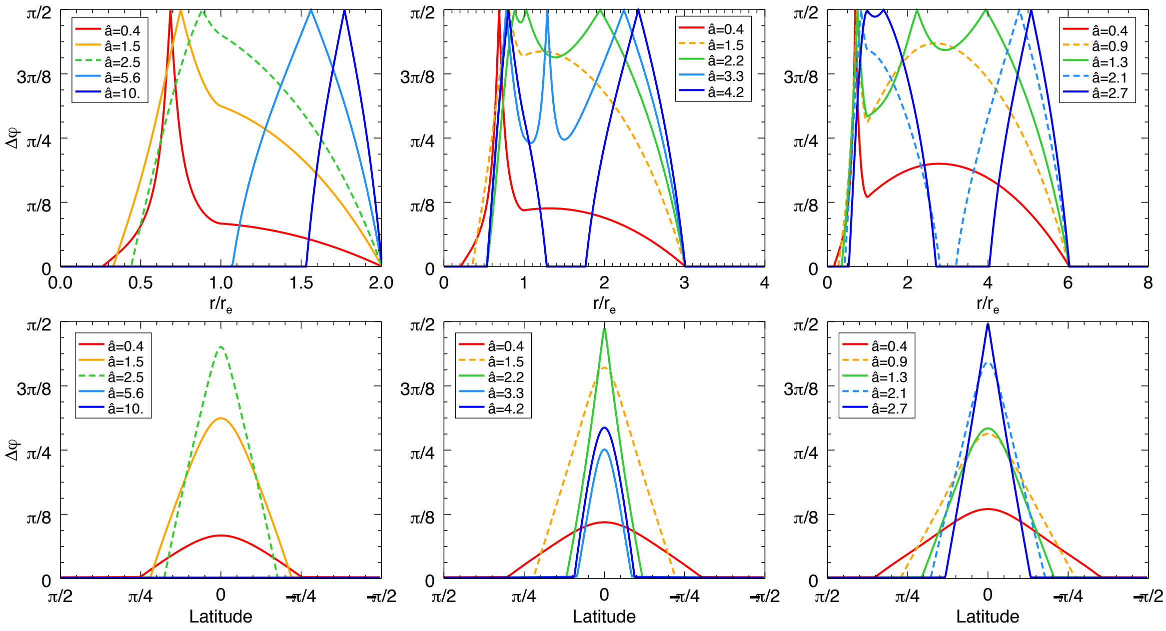

Figure 6.6: Profiles of the twist angle $\Delta\varphi$ at the equator as a function of distance (normalized to the stellar radius r_e) (upper panels), and as a function of latitude on the stellar surface (bottom panels), for selected models ($\hat{a}$ is expressed in units of 10^{-3}) along the equilibrium sequences with $\lambda = 2$ (left), $\lambda = 3$ (centre) and $\lambda = 6$ (right). The dashed lines represent models with maximum value of $H_{\rm tor}/H$ along the same sequences.

diminishes, the radial component becomes more uniform, except very close to the equator. The portion of the surface where $B_{\rm tor} \neq 0$ instead shrinks, and vanishes completely once the twisted region gets out of the star. In Fig. 6.5 we show the harmonic content C_l/C_1 of the surface magnetic field for different models, in the case $\lambda = 2$. As expected the dipole term is always the dominant one. Multipole terms become more important in correspondence to configurations with the highest $H_{\rm tor}/H$, when the toroidal field is stronger and the neutral line is located just underneath the stellar surface. Finally, as the twisted magnetospheric torus moves away from the star, the multipolar content of the surface field drops.

For higher values of $\lambda \geq 3$ the appearance of multiple peaks and disconnected magnetic regions leads to a more complex behaviour of the magnetic field at the surface. In the polar regions at high latitude $> 45°$ the value of the poloidal field does not change much with increasing $\hat{a}$. What changes is the poloidal magnetic field at the equator that drops with $\hat{a}$. In this case, however, this is not due to the neutral line moving outwards, but because an X-point forms in the vicinity of the surface. Indeed, as can be seen in Fig.s 6.4 and 6.2, in the $\lambda = 3$ case the values of $\hat{a}$ for which the poloidal field vanishes at the equator is the same at which a second peak forms. For higher values of $\hat{a}$, the equatorial poloidal field rises again. The portion of the surface where $B_{\rm tor} \neq 0$ shrinks again, though for these cases it never vanishes completely. In all cases we find that the strength of the toroidal component of the magnetic field at the surface tends to grow becoming comparable to, or even exceeding, the strength of the poloidal one.

Another parameter that it is useful to show is the angle between the magnetic field and the meridional plane, to which we refer as twist angle $\Delta\varphi$. For convenience it can be defined as the complementary of the angle that the magnetic field forms with respect to the azimuthal direction

$$\Delta\varphi = \arcsin\left[\left(B_\phi B^\phi / B_i B^i\right)^{1/2}\right]. \tag{6.7}$$

The value of $\Delta\varphi$ ranges from 0 to $\pi/2$, assuming the latter when the magnetic field is purely azimuthal, and 0 when the magnetic field lies in the meridional plane. In Fig. 6.6 we show this angle, measured at the equator, as a function of radial distance r. Since our models are not rotating, all the magnetic field lines are eventually closed. The location where $\Delta\varphi = \pi/2$ corresponds to the location of either the neutral line (O-point) or the X-point, where the poloidal component of the magnetic field vanishes. For cases with $\lambda \leq 2$ the profile of $\Delta\varphi$ shows a unique peak where the θ-component of the poloidal field reverses sign in the twisted region. Again we see that at higher values of $\hat{a}$ the toroidal field is completely outside the star.

As expected, in the case $\lambda \geq 3$ the behavior is more complex. For the smallest value of $\hat{a}$ the trend of $\Delta\varphi$ resembles that of the analogous configuration at $\lambda = 2$: the twist is prominent in the vicinity of the neutral line and extends outside the star remaining well below $\sim \pi/4$. Moving at higher $\hat{a}$, the presence of two peaks in the toroidal magnetic field strength inside the twisted region means that $\Delta\varphi$ reaches $\pi/2$ in three locations. In particular the first and the third of those locations are always associated with O-points, the second one with an X-point. At the higher value of $\hat{a}$, the formation of two detached twisted regions is also evident. In this cases, however, the trend of $\Delta\varphi$ reveals only the position of the two O-point because the ϕ-component of the magnetic field vanishes in correspondence with the X-point. Here we note that in the most extreme case at $\lambda = 6$ the trend of $\Delta\varphi$ strengthen the hypothesis concerning the development of a third peak in the toroidal magnetic field strength. Indeed the second peak in $\Delta\varphi$ corresponds to an O-point and an unresolved X-point.

The bottom row of Fig. 6.6 displays the profile of $\Delta\varphi$ along the stellar surface. As pointed out before, in the limit of small $\hat{a}$ the twist at the surface increases. However, for higher values of $\hat{a}$ the trend is not uniform, depending on the formation of a second peak, and the related location of the X-point.

In Fig. 6.7 we plot the maximum value of the strength of the toroidal magnetic field $B^{\rm tor}_{\rm max}$, and the poloidal one $B^{\rm pol}_{\rm max}$, for different values of λ, as a function of $\hat{a}$. In all our models the poloidal field reaches its maximum at the centre. Initially, in the small $\hat{a}$ regime, $B^{\rm tor}_{\rm max}$ grows, while $B^{\rm pol}_{\rm max}$ decreases. This happens because the strength of the magnetic field at the pole is always kept fixed in all models. As one enhances the contribution to the total current by increasing $\mathcal{I}$, one must decrease the contribution from $\mathcal{M}$, causing a drop in the strength of the field at the centre of the star. This effect depends also on the location of the current, as this term moves to larger radii the poloidal field begins to grow again. Configurations with $\lambda \geq 3$ show several inversions of this trend, which again are a manifestation of the change in the field topology.

Analogously to the TT case, all the equilibrium models we obtain are energetically dominated by the poloidal magnetic field. In Fig. 6.8 we show the same equilibrium sequences

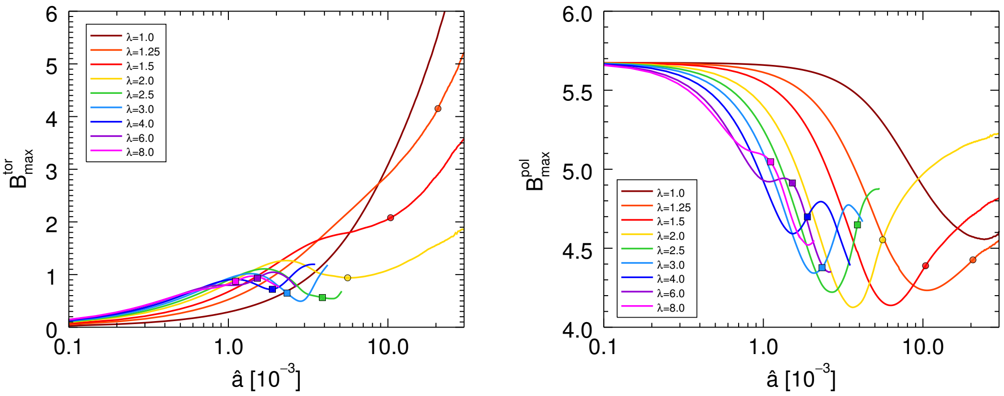

Figure 6.7: Maximum value of the toroidal (left) poloidal (right) magnetic field along equilibrium sequences with different values of λ. Dots indicate configurations where the toroidal magnetic field component is completely outside the star. Squares indicate configurations which show two maxima of the toroidal magnetic field.

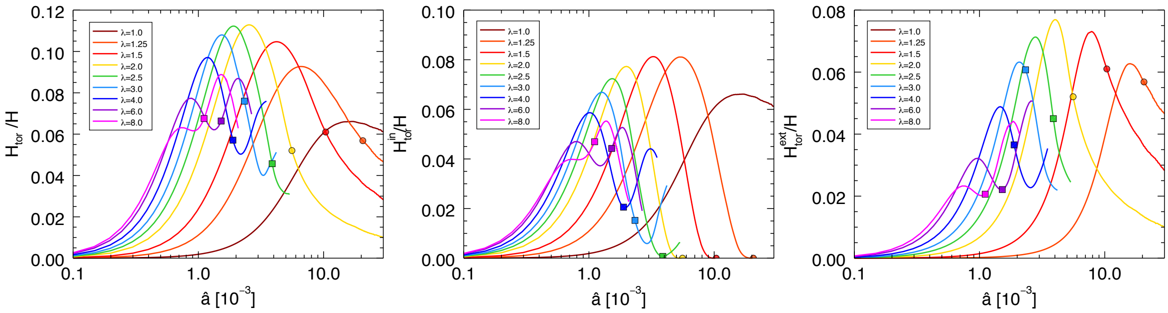

Figure 6.8: Profiles of the ratio of total magnetic energy of the toroidal component $H_{\rm tor}$, external one $H_{\rm tor}^{\rm ext}$ and internal one $H_{\rm tor}^{\rm in}$, with respect to the total magnetic energy H. Curves show sequences as a function of $\hat{a}$ for various values of λ. Dots and squares as in Fig. 6.7.

in terms of the ratio of magnetic energy of the toroidal magnetic field $H_{\rm tor}$ over the total magnetic energy H. Generally the magnetic energy ratio initially grows with $\hat{a}$ reaching a first maximum that corresponds to a configuration still characterized by a single peak (see the first rows of fig 6.1). Again the trend for higher values of $\hat{a}$ depends on the value of λ. While sequences with $\lambda \leq 2$ show a decreasing monotonic trend, sequences with $\lambda \geq 3$ reach a minimum and then the magnetic energy ratio begin to grow again. For configurations with $\lambda \gtrsim 6$ we could reach a second local maximum. It is possible in principle that other maxima and minima could be reached at higher values of $\hat{a}$, but we could not compute those models. The magnetic energy is an integrated quantity, as such it also depends on the size of the twisted region. The formation of an X-point, followed by the formation of two detached magnetic twisted domains, is associated to a decrease of the net volume taken by the toroidal field, and to the drop of $H_{\rm tor}$ after the first maximum. In Fig. 6.8 we also compare the toroidal magnetic energy confined inside $H_{\rm tor}^{\rm in}$ and outside $H_{\rm tor}^{\rm ext}$ the star. The two are in general comparable except for cases with $\lambda \leq 2$ where the interior toroidal field vanishes at high $\hat{a}$. Note also that the ratio $H_{\rm tor}/H$ is at most 8-10%. The net poloidal and toroidal currents follow a similar behavior.

Finally in Fig. 6.9 we show the variation of the magnetic dipole moment μ as a function

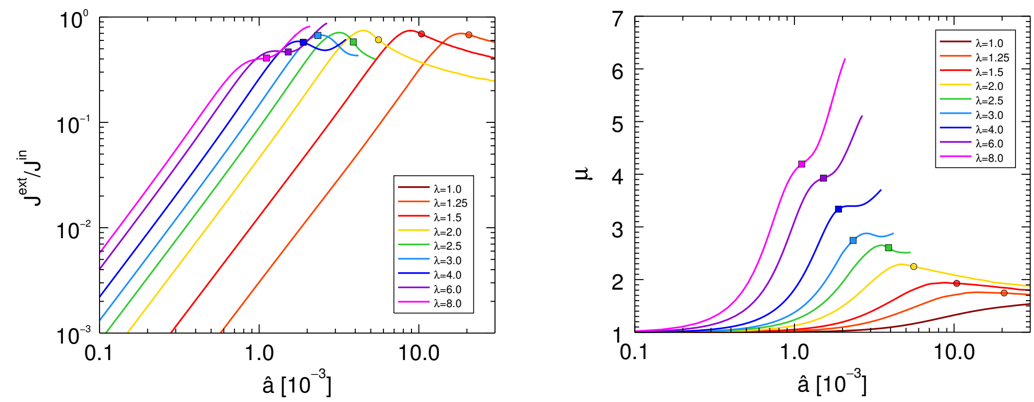

Figure 6.9: Left panel: ratio between the toroidal current density outside the star $\mathcal{J}_\mathrm{e}^\mathrm{ext}$ and the toroidal current density inside $\mathcal{J}_\mathrm{e}^\mathrm{in}$, as a function of $\hat{a}$ along equilibrium sequences with different value of λ. Right: magnetic dipole moment μ along the same sequences expressed in units of the magnetic dipole moment of the fiducial configuration $\mu = 1.114 \times 10^{32}$ erg/G. Dots and squares as in Fig. 6.7.

of $\hat{a}$. We see that the magnetic dipole, for fixed values of $\hat{a}$, grows with λ. This is because the total integrated toroidal current, defined as

$$\mathcal{J}_\mathrm{e} = \int \sqrt{J^\phi J_\phi} \psi^6 r^2 \sin\theta dr d\theta d\phi \tag{6.8}$$

is bigger for larger magnetospheres with higher values of λ. Very interestingly, for large values of λ the net magnetic dipole moment can be even 4-5 times higher, given the same strength of the field at the pole. External currents contribute to the net dipole without affecting too much the strength of the magnetic field at the surface. This is a known property of twisted magnetospheres (Thompson et al. 2002).

For all the configurations computed here the internal linear current $\mathcal{J}_\mathrm{e}^\mathrm{in}$ is always greater than the external one $\mathcal{J}_\mathrm{e}^\mathrm{ext}$, reaching similar values only for configurations where the energy ratio reaches a maximum. At first, as expected, the external current, due only to the term $\mathcal{I}$, grows linearly with $\hat{a}^2$, while the internal one dominated by $\mathcal{M}$ remains more or less constant. For higher values of $\hat{a}$ the ratio decreases exactly for the same volume effect that was discussed for the trend of H_tor/H.

6.1.2 Models with $\zeta = 1$

The toroidal magnetization index ζ controls the shape of the current distribution inside the torus-like region of the twisted field. With respect to the $\zeta = 0$ case, choosing higher value for ζ entails stronger currents mostly concentrated in the proximity of the neutral line. In this subsection we will consider the $\zeta = 1$ case in order to show which are the possible qualitative and quantitative differences that can arise if a different value of ζ is chosen.

In order to compare the results with those at $\zeta = 0$, let us focus to those configurations where H_tor/H is maximal. In Fig. 6.10 we show the strength of the magnetic field, both at the surface and along the equator, in the cases $\lambda = 2, 3$ and 6, compared with that of the

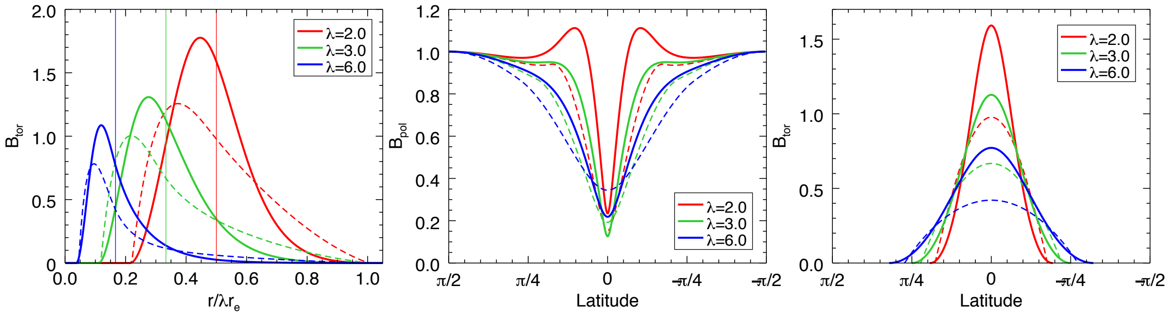

Figure 6.10: The left panel shows the profile of the toroidal magnetic field strength (in units of B_{pole}) for the configuration with the first maximum value of the magnetic energy ratio H_{tor}/H along sequences with fixed λ =2,3 and 6. Solid lines refer to configurations with $\zeta = 1$, while dashed ones refer to the equivalent configurations with $\zeta = 0$. The thin vertical lines indicate the location of the stellar surface for each λ. The remaining panels show, for the same configurations, the profile of the magnetic field strength, evaluated at the surface of the star, for the poloidal (center) and the toroidal component (right) as a function of latitude.

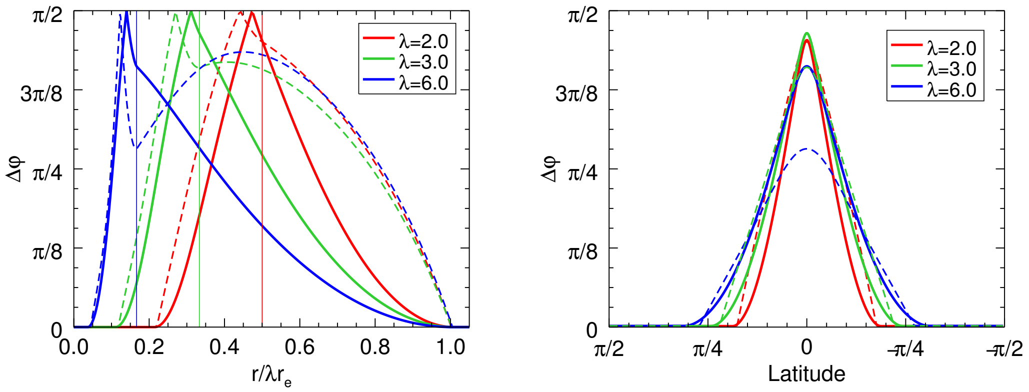

Figure 6.11: Profiles of the twist angle $\Delta\varphi$ in the magnetosphere (left) and at the stellar surface (right) for the same equilibrium configurations whose magnetic field profiles have been shown in Fig. 6.10. Solid lines (dashed lines) refer to configurations with $\zeta = 1$ ($\zeta = 0$).

equivalent configurations at $\zeta = 0$. In the $\zeta = 1$ case the toroidal magnetic field reaches higher values than in the $\zeta = 0$ case. However, even though the geometry and shape of the twisted region remains almost the same, the distribution of the magnetic field is more concentrated around the peak and the magnetic field decays more rapidly to zero in the magnetosphere.

Looking at the distribution of the poloidal and toroidal field at the surface of the star (central and right panel in Fig. 6.10) it is evident that the multipolar terms of the magnetic field become more important in the $\zeta = 1$ cases: while the strength of the poloidal magnetic field at the equator decreases marginally, it increases in the neighboring region where it can also exceed the value of B_{pole} within a wedge of about $\pm\pi/4$ around the equator. While the portion of the surface where $B_{\text{tor}} \neq 0$ remains approximately the same the toroidal field is now more concentrated around the equator where its strength can be a factor ~ 2 higher than for $\zeta = 0$.

The effects of the new current distribution on the twist angle $\Delta\varphi$ are shown in Fig. 6.11 where we plot the trend of $\Delta\phi$ for the same equilibria discussed above. While the growth of

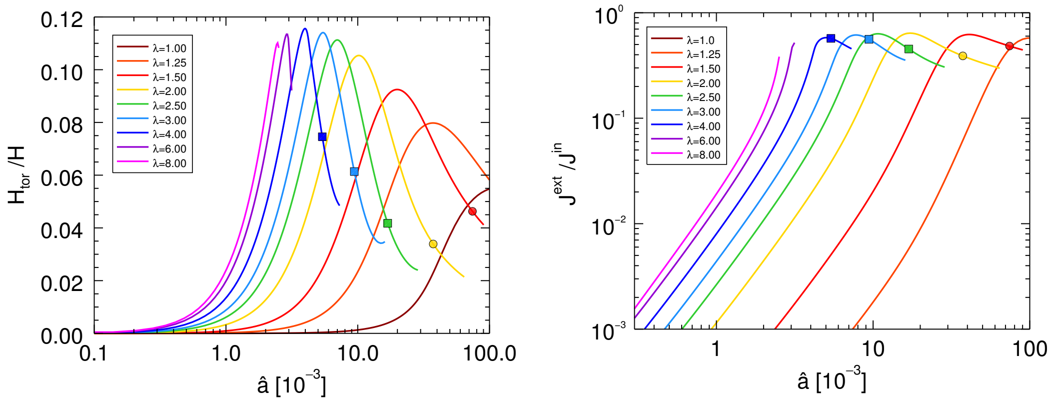

Figure 6.12: Profiles of the toroidal energy ratio $H_{\rm tor}/H$ (left) and of the current ratio $\mathcal{J}_{\rm e}^{\rm ext}/\mathcal{J}_{\rm e}^{\rm in}$ as a function of $\hat{a}$ along equilibrium sequences with constant λ. Dots and squares as in Fig. 6.7.

the surface $\Delta\phi$ is a direct consequence of the stronger toroidal field obtained for the $\zeta = 1$ configurations, the analysis of trends in the magnetosphere deserves more attention. In fact, even though the toroidal field in the new configurations is stronger in the proximity of the stellar surface, the twist angle in the magnetosphere decreases monotonically and it is highly suppressed with respect to that obtained in the $\zeta = 0$ models. This is due, on the one hand, to the fact that $B_{\rm tor}$ goes more rapidly to zero in the magnetosphere but, on the other hand, also to the presence of a stronger equatorial poloidal field in the vicinity of the star.

The structure of the magnetic field is however only slightly affected by the value of the magnetic index ζ. This is also evident from Fig. 6.12 where we plot the profile of both the magnetic energy ratio $H_{\rm tor}/H$ and the current ratio $\mathcal{J}_{\rm e}^{\rm ext}/\mathcal{J}_{\rm e}^{\rm in}$ as a function of $\hat{a}$ for the various sequences. The trends strictly reflect those obtained in the $\zeta = 0$ case (see Fig. 6.8 and 6.9) and it is interesting to notice that sequences with equal λ behave, from the point of view of the field topology, in the same way: for sequences with $\lambda \lesssim 2$ the twisted region moves outside the star; for sequences with $\lambda \gtrsim 2.5$ the configuration at higher $\hat{a}$ are characterized by a more complex topology and part of the toroidal field remains always confined in the star. Also a more quantitative comparison shows little differences. In the $\zeta = 1$ case the maximum allowed $H_{\rm tor}/H$ is lower if $\lambda \lesssim 2.5$ and higher if $\lambda > 2.5$. The major differences regard the sequences with $\lambda = 6$ and 8 where the higher value of $B_{\rm tor}$ and a more regular topology of the solution (i.e. there is no formation of an X-point) allow one to reach higher value for the magnetic energy ratio. Finally in both cases, when $\mathcal{J}_{\rm e}^{\rm ext} \sim 0.7\mathcal{J}_{\rm e}^{\rm in}$, the system self regulates inducing a change in the topology of the distribution of the magnetic field and the associated external current.

6.2 Strong field regime

Newly born magnetars, with their fast rotation (with period of the order of $\sim$ 1 s) and their strong magnetic deformation, can power a significant emission of gravitational waves and, during the first few seconds of their life, they could be a promising target for the next

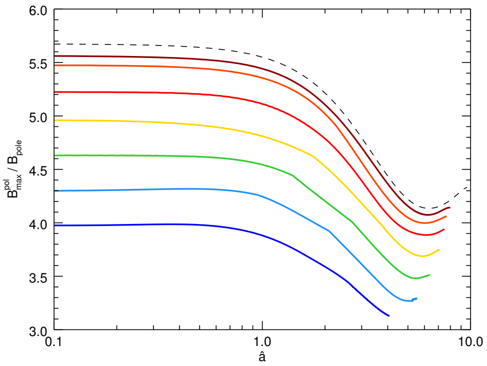

Figure 6.13: Profiles of the maximum value of the poloidal magnetic field $B^{\rm pol}_{\rm max}$ along sequences with $\lambda = 1.5$ and constant value of $B_{\rm pole}$. Solid lines from top to bottom $B_{\rm pole} = 0.2, 0.4, 0.6, 0.8, 1.0, 1.2, 1.4 \times 10^{17}$ G. The black dashed line corresponds to the weak field limit.

generation of ground-based GW-interferometers (Mastrano et al. 2011). After this lapse of time, because of the spin-down induced by the strong poloidal field ($\sim 10^{14}$ G) the strain amplitude reduces considerably and the GW emission is hardly detectable. However, even though our assumption of a force-free magnetosphere only applies to the late phases of a proto-NS, when GW emission will be quenched, it is still interesting to consider the strong field regime and how a magnetospheric distribution of currents acts on the stellar deformation. In the following we will limit our discussion to sequences with $\lambda = 1.5$, considering only configurations with a simple topology with no detached magnetic flux rope outside the star. As discussed in Sec. 6.1.1 this kind of configurations, whose properties are weakly affected by λ, are possibly the only stable ones.

In the strong field regime the solutions of the GS Eq. 2.125 depend on the specific value of the magnetic field strength and they do not rescale as in the weak-field limit. This is evident from Fig. 6.13 where we show the value of the ratio $B^{\rm pol}_{\rm max}/B_{\rm pole}$ as a function of $\hat{a}$ along sequences with constant value of $B_{\rm pole}$ (from the weak field limit to $\sim 10^{17}$ G) and fixed gravitational mass $M = 1.551 M_\odot$. Just like in the weak-field regime, along each sequence the trend of $B^{\rm pol}_{\rm max}$ is not monotonic. Here, however, the ratio $B^{\rm pol}_{\rm max}/B_{\rm pole}$ is smaller for stronger magnetic fields. This can be explained in term of the deformation of the star: as in the weak-field limit our equilibrium configurations are energetically dominated by the poloidal field (the magnetic energy ratio $H_{\rm tor}/H$ depends weakly on the strength of the field) and they show an oblate deformation. Therefore, if the star is more magnetized, the deformation is stronger and the pole is closer to the center of the star implying a smaller $B^{\rm pol}_{\rm max}/B_{\rm pole}$.

Fig. 6.14 shows the deformation rate $\bar{e}$ (Kiuchi and Yoshida 2008, Pili et al. 2014) as a function of $B^{\rm pol}_{\rm max}$. Here the black lines trace the configurations with constant $\hat{a}$. Moving from the purely poloidal case with $\hat{a} = 0$ to higher value of $\hat{a}$ the toroidal magnetic field strengthen up to $\sim 2 \times 10^{17}$ G and the deformation rate increases by a factor ~ 2. The presence of a toroidal field in the system, seems to increase, rather then reduce, the oblate deformation. However, as discussed in Chaps. 4 and 5, neither the maximum strength of the

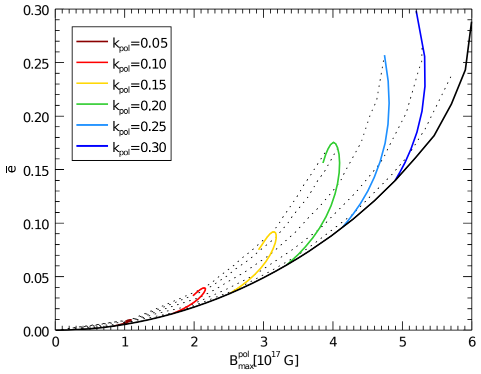

Figure 6.14: Profiles of the deformation rate $\bar{e}$ along sequences with constant value of $k_{\rm pol}$, $\lambda = 1.5$, and gravitational mass $M = 1.551 M_\odot$ as a function of the maximum value of the poloidal magnetic field $B^{\rm pol}_{\rm max}$. The black solid line represents the sequence with $\hat{a} = 0$ (purely poloidal configurations). The dotted lines correspond to sequences with fixed value of $\hat{a}$ equispaced from $\hat{a} = 1.0 \times 10^{-3}$ to $\hat{a} = 5.0 \times 10^{-3}$.

magnetic field nor the magnetic energy alone are, in general, good indicators of the possible deformations of the NS in the case of poloidal fields. The distribution of the currents play an important role and the effects of magnetic field located in the outer layers of the star are less important than those of comparable strength situated in the core region. Therefore the trend of $\bar{e}$ can be explained in terms of the strength of the poloidal magnetic field, which resides deeper inside the star. Moving along sequences with fixed $k_{\rm pol}$ (without constraints on $B_{\rm pole}$) from the purely poloidal configurations to higher $\hat{a}$, both the poloidal and the toroidal field grow in strength while the neutral line moves toward the surface of the star. Finally, as soon as the radius of the neutral line reaches a value of $\sim 0.8 r_{\rm e}$, the poloidal field begins to drop leading to an inversion point in the sequences and a reduction of the deformation rate $\bar{e}$.

6.3 Summary

We have computed numerical equilibrium models of general relativistic magnetized NSs with twisted magnetospheres, allowing for electric currents extending smoothly from the interior of the star to the exterior. The work presented in this Chapter extends the study by Glampedakis et al. (2012a) limited to the Newtonian regime. Our models, indeed, represent a straightforward generalization of typical Twisted-Torus configurations, where the twist is allowed to extend also outside the NS. In particular, we focused on the low-magnetization non-rotating limit, since this limit is appropriate for real physical systems like AXPs and SGRs. In this case the morphology of the magnetic field can be fully parametrized in terms of a single quantity $\hat{a}$, independently of the strength of the magnetic field. We have shown that the extent of the magnetosphere (our parameter λ) plays an important role and defines the possible existence of different topological classes of solutions.

In the low $\hat{a}$ regime, when the non-linear current terms are weak, the magnetic field lines are inflated outward by the toroidal magnetic field pressure and the twist of the field lines extends also to higher latitude. The result is a single magnetically connected region. As $\hat{a}$ increases, the effects of the non-linearity of the equation appears. This not only reduces the twist of the near-surface magnetic field but also leads to the formation of a disconnected magnetic island, reminiscent of the so-called plasmoids often found in simulations of the solar corona. This regime and these topologies are very likely to be unstable.

Regarding the current distribution, for all the configurations that we have computed, the internal linear current is always greater than the external one reaching similar values only for configurations where the energy ratio reaches a maximum. Apparently, as one tries to rise the external currents, the system self-regulates inducing a change in the topology of the distribution of the magnetic field and the associated external current. As a consequence there is a maximum twist that can be imposed to the magnetosphere, before re-connection and plasmoid formation sets in. We found moreover that the external currents contribute to the net dipole without affecting too much the strength of the magnetic field at the surface. Similar results have been recently obtained by Fujisawa and Kisaka (2014), which consider also the effects of a crust (requiring MHD equilibrium in the core and Hall equilibrium in the crust), and Akgün et al. (2016). In the latter case, even if they do not find disconnected morphology, they find a critical twist amplitude $\sim 1.2-1.5$ beyond which they can not obtain solutions. This is compatible with our estimation ~ 2 rad for the maximum twist amplitude before the developments of X-points.

Our approach to NS magnetospheric equilibrium has allowed us to obtain complex magnetic field morphologies. However with our choice for $\mathcal{I}$ we have focused our analysis on configurations with a magnetospheric confined twist, which is in turn located around the equatorial plane. Even though, as pointed out in Beloborodov (2011), the observations of shrinking hotspots on magnetar transient (Rea et al. 2009) seem to suggest that the twist is more probably located near the pole, similar magnetospheric geometries have been recently used to model SGR giant flares as flux rope eruptions (Huang and Yu 2014b,a).

Apart from a rough estimate based on known criteria, it is difficult to establish the stability of our models, especially with respect to non azimuthal perturbations. Moreover, since we treat the magnetosphere as force-free plasma, the physical regime to which our models apply, is characteristic of the late phases of a proto-NS, when a crust begins to form. Therefore, a meaningful modellization of the evolution of the system can not disregard the possible stabilizing role played by the crust, relaxing the ideal MHD hypothesis in order to include Hall evolution and Ohmic dissipation of the magnetic field (as in recent numerical simulations by Gourgouliatos et al. 2016), and considering the effects of strong magnetic field on the structure and the properties of the crystalline crust (Chamel and Haensel 2008, Chamel et al. 2015, Fantina et al. 2016). This is just indicative of the great complexity of the physics involved, and correspondingly of the extreme difficulties in the realistic modelling of NS structure.

7

Quark deconfinement in the proto-magnetar model of Long Gamma-Ray Bursts

The late time activity observed after the prompt emission of several GRBs can be interpreted, in the context of the *millisecond magnetar model*, as due to the continuous energy injection from a newly born magnetar (Usov 1992, Bucciantini et al. 2009, Metzger et al. 2011). Within this picture it is however difficult to explain late time bursts that are often observed in the light curve of many GRBs. Indeed, while the canonical millisecond magnetar model predicts a steady smooth energy injection in the form of a relativistic magnetically driven wind, bursts require a sudden reactivation of the central engine that may be due to fall-back accretion (Proga and Zhang 2006, Rosswog 2007, Bernardini et al. 2013, 2014, Bernardini 2015, Dall'Osso et al. 2017) or magnetic reconnection-driven explosions (Dai et al. 2006, Gao and Fan 2006). Other possibilities, that do not require a reactivation of the central engine, link late-time flares and rebrightening to the interactions between the outflows and the circumburst medium (Giannios 2006, Giannios et al. 2008, Shen et al. 2011).

In this chapter we investigate the possible implications of quark deconfinement on the phenomenology of LGRBs focusing, in particular, on the occurrence of multiple prompt emission phases in the context of the *proto-magnetar model*. Starting from numerical models of rotating Hadron Stars and Quark Stars we track the electromagnetic spin-down evolution in both the hadronic and quark phase, linking the two families through conservation of baryon number and angular momentum. We will give estimates of the timescales and the energetic involved in the spindown process deriving, in the relevant spin range, the relation between the initial and the final masses and rotational energies, whenever hadron-quark conversion is possible. We will show how these results can be used in relevant astrophysical cases such as the double burst GRB 110709B. This Chapter is based on Pili et al. (2016).

7.1 The two families scenario

The nature of the inner engine of Long Gamma-Ray Bursts (LGRBs) is still one of the most interesting and unsolved problems in astrophysics. While there is a compelling evidence that these events are associated with the core collapse of massive stars, it is not yet established whether the burst is produced by a disk accreting onto a black hole (within the so-called Collapsar model, Woosley 1993) or by the outflow emerging from a fast rotating and highly magnetized proto-neutron star (within the so-called proto-magnetar model, Metzger et al. 2011). It is also possible that both these systems contribute in producing LGRBs, depending on the initial conditions of the progenitor (in particular its mass, spin frequency and magnetic field). The discovery by Swift of a late time activity, lasting up to 10^4 s and present in a sizable fraction of LGRBs, is more naturally interpreted within the proto-magnetar model as due to the pulsar-like energy injection powered by the residual rotational energy left after the prompt emission (Dall'Osso et al. 2011).

Within the proto-magnetar model, an important ingredient which regulates the temporal evolution of the jet and its gamma-ray luminosity is the neutrino signal released by the star due to deleptonization (the gradual neutronization of matter) and cooling. In particular, neutrinos ablate baryonic matter from the surface and provide a tiny amount of baryonic load which is crucial for an efficient internal dissipation of the kinetic energy of the jet into gamma emission. When the neutrino luminosity drops below $\sim 10^{50}$ erg/s (after a few tens of seconds), the magnetization (or the Lorentz factor) is too large and the prompt emission ends. It is not easy within the proto-magnetar model to reactivate the inner engine and therefore to describe multi-episodes of the prompt emission of LGRBs (e.g. Zhang et al. 2012) or X-ray flares occurring during the afterglow (Zhang et al. 2006).

The proto-magnetar model has been developed assuming that the newly born Compact Star (CS) is and remains a nucleonic star. Motivated by the measurements of very massive CSs (Demorest et al. 2010, Antoniadis et al. 2013) and the hints of the existence of very compact stellar objects (with radii close to 10km, Guillot et al. 2013, Ozel and Freire 2016), a two-families scenario has been recently proposed where both Hadronic Stars (HSs) and Quark Stars (QSs) exist in nature (Drago et al. 2014, 2016b, Drago and Pagliara 2016). Within this picture, a conversion of a HS into a QS can take place. In the following sections we will discuss how this transition modifies the proto-magnetar model, revitalizing the inner engine. In particular, we will investigate the following scenario: i) a proto-magnetar is formed after a successful supernova explosion and its spinning down, which is responsible for the emission of a LGRB, leads to a gradual increase of the central density; ii) the increase of the density allows the formation of heavy hadrons such as Δ resonances and hyperons; iii) once a critical amount of strangeness is formed through hyperons at a density ρ_{crit}, the HS converts (on a time-scale $\lesssim$ 10 s) into a QS. This picture has been qualitatively discussed in Drago et al. (2014) for the case of non-rotating stars. Here we will improve that work by including rotation and spin-down evolution along the line of Haensel et al. 2016, and references therein.

A distinctive feature of the two-families model is that the formation of a QS is accompanied by a rather large amount of energy released in the conversion, of the order of 10^{53} erg. Moreover, we will show that since the final QS configuration has a larger radius than the initial HS configuration, the conversion is accompanied by a significant increase of the moment of inertia with a corresponding decrease of the rotational frequency. We will discuss possible phenomenological implications of the two-families scenario for the light curves of LGRBs in connection with late time activity. For the case of QSs there are two possible ways to produce a jet with the appropriate Lorentz factor. The first mechanism is based on the ablation of baryonic material from the surface of the star as long as the conversion front has not yet reached the surface (Drago and Pagliara 2016). A second mechanism is based on the rather large emission of electron-positron pairs from the surface of the bare quark star (Usov 1997, 2001, Page and Usov 2002). Both mechanisms can be at work to produce late time activities.

7.2 The quasi-stationary evolution

In order to investigate the possible implications of the two-families scenario for the phenomenology of GRBs we have computed a large set of rigidly rotating equilibrium models for both HSs and QSs. Given the typical cooling evolution of newly formed proto-neutron stars (Pons et al. 1999), the assumption of a cold star is justified at times larger than $\gtrsim 10$ s after formation (the radius is relaxed to its final value). These numerical models are then linked together to describe the quasi-stationary evolution of CSs under the effect of the magnetic braking. With this simple approach we can give a preliminary estimate of both the timescales and the energetics involved in the spin-down before and after quark deconfinement, which we assume to happen when the central baryon density ρ_c reaches a critical value of the order of 10^{15} g/cm^3 (Drago et al. 2014). Here we set $\rho_{\rm crit} = 1.34 \times 10^{15}$ g/cm^3. We also derive the range of initial masses for which a delayed HS to QS conversion is possible.

Numerical models have been obtained using the EoSs discussed in Drago et al. (2016b). Since the typical surface magnetic field invoked by the magnetar model for GRBs are of the order of 10^{15} G our models are computed neglecting the deformation due to magnetic field. Indeed, as discussed in Sub. 4.1.2, only central magnetic fields stronger than $\sim 10^{16}$ G, corresponding to surface magnetic fields stronger than a few 10^{15} G, are able to modify the stellar global properties to a level appreciable with respect to the overall accuracy of our numerical scheme ($\lesssim 10^{-3}$). Hence we can safely assume that the stellar structure and the associated global quantities such as the gravitational mass M, the baryonic mass M_0 (a proxy for the total baryon number), the circumferential radius $R_{\rm circ}$ and the Komar angular momentum $\mathcal{J}$ do not depend on the magnetic field strength.

In the millisecond magnetar model for GRBs the typical rotation periods invoked in the literature (Metzger et al. 2011, Bucciantini et al. 2012) can be as high as ~ 1 ms. The maximum rotation rate of compact stars at the end of deleptonization has been investigated in several papers (Goussard et al. 1998, Villain et al. 2004, Camelio et al. 2016). Its value depends on the initial physical conditions of the proto-neutron star (e.g. the entropy profile and a possible differential rotation) and on the compactness of the final cold and deleptonized configuration. If one adopts rather stiff EoS, the maximum rotational frequency ranges between 300 and 600 Hz (Goussard et al. 1998, Villain et al. 2004, Camelio et al. 2016). In

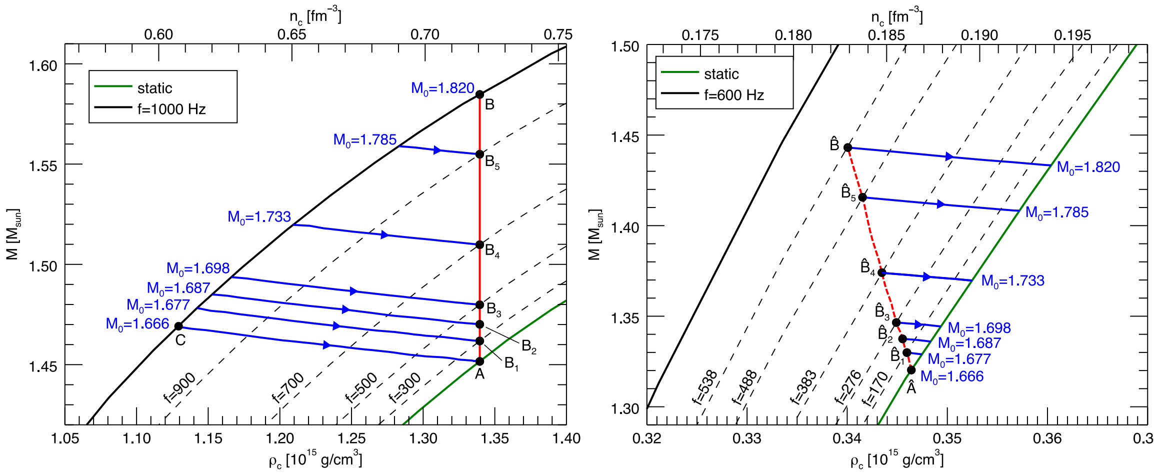

Figure 7.1: Gravitational mass against baryon central density for sequences of HSs (left panel) and QSs (right panel) with constant spin frequency. In both cases the green solid lines represent the non-rotating sequences while the black solid lines are sequences rotating at the maximum spin frequency considered in this work: 1000Hz for HSs and 600Hz for QSs. Dashed black lines are sequences with intermediate values of f while blue lines are equilibrium sequences at constant baryon mass M_0. The red solid line locates HSs with $\rho_c = \rho_{crit}$ while the red dashed line locates QSs originating from the conversion of HSs lying on the red solid line. Detailed results on the configurations labeled A and Bs are listed in Tab. 7.1.

our analysis we use a rather soft hadronic EoS due to the formation of Delta resonances and hyperons and the maximum rotation frequency is expected to be larger. In the following we limit the rotation of our HSs to a maximum frequency $f = 10^3$ Hz. On the other hand, for those QSs resulting from the conversion of a HS it is sufficient to limit the spin frequency to 600 Hz.

Models are shown in Fig. 7.1 in terms of central baryon density ρ_c and gravitational mass M for both HSs (left panel) and QSs (right panel). Here blue lines are sequences of equilibria for given baryonic mass and therefore they represent the evolutionary path of HSs and QSs undergoing spin-down. The same configurations are also shown in Fig. 7.2 where we plot the mass-radius relation for different sequences of CSs at constant spin frequency. There are two limiting configurations: the non-rotating configuration A with $M(\mathrm{A}) = 1.45 M_\odot$, $M_0(\mathrm{A}) = 1.67 M_\odot$ and $R = 10.9$ km; the 1 ms rotating configuration B with $M(\mathrm{B}) = 1.58 M_\odot$, $M_0(\mathrm{B}) = 1.82 M_\odot$ and $R = 12$ km. These define the mass range of interest for delayed quark deconfinement. The value of the critical mass of the configuration A cannot be determined with high precision not even in the scheme of the two families. The main uncertainties are due to the dynamics regulating the appearance of baryonic resonances and on the estimate of the nucleation time of the first droplet of quark matter (Bombaci et al. 2016).

Massive HSs, that after their initial cooling (lasting for at most ∼ 10 s after core collapse) end above the red line in Fig. 7.2, have $\rho_c \geq \rho_{crit}$ and they will decay immediately to a QS. On the other hand those HSs having $M_0 < M_0(\mathrm{A})$ will never experience this transition[1]. Since

---

[1] For simplicity, we are not considering here the process of nucleation of quark matter (Bombaci et al. 2016). In a more realistic case the red lines connecting the configurations A and B would transform in a strip whose width is connected to the nucleation time.

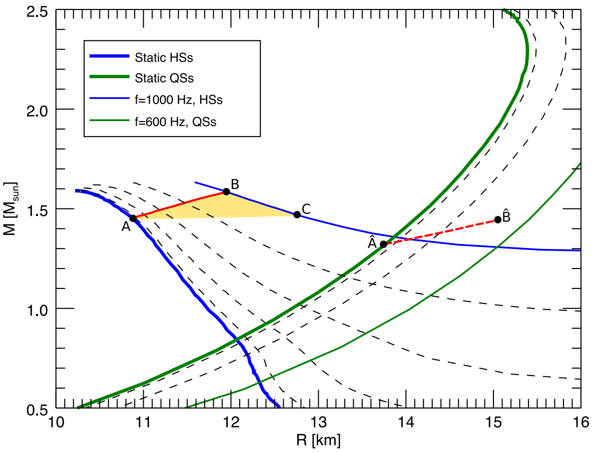

Figure 7.2: Gravitational mass as a function of the circumferential radius for both HSs and QSs. Thin dashed lines are sequences of stars at a fixed frequency from the non-rotating configurations (thick solid blue and green lines) to the configurations rotating at the maximum frequency (thin solid blue and green lines) and spaced by 200 Hz. The yellow region shows hadronic configurations centrifugally supported against deconfinement. Red lines and labels are the same as in Fig. 7.1.

for isolated CSs the baryonic mass is a conserved quantity, only those HSs having baryonic mass between M_0(A) and M_0(B) can migrate into the QS branch when their baryon central density rises to $\rho_{\rm crit}$ as a consequence of spin-down. The yellow shaded region of Fig. 7.2 shows these configurations. All the configurations having the same baryonic mass as A (for example the 1 ms rotator configuration C) take an infinite time to deconfine (deconfinement takes place at zero frequency). Notice that along the evolutionary paths the variation of the gravitational mass, and hence of the total energy, is at most of the order of $\sim 1\%$.

As soon as the central density reaches the critical value the HS decays into a QS in $\lesssim 10$ s. Given the typical spin-down timescales we assume that this transition is instantaneous and both the baryon number (baryonic mass) and the angular momentum $\mathcal{J}$ are conserved. The red dashed line in the right panel of Fig. 7.1 and in Fig. 7.2 maps upon the QS sequences the configurations which originate from quark deconfinement of HSs. With reference to our limiting configurations, the HS labeled with A migrates to the configuration Â with gravitational mass $M(\hat{\rm A}) = 1.32 M_\odot$, while the HS B migrates to the configuration B̂ with $M(\hat{\rm B}) = 1.44 M_\odot$. In both cases the total energy released in the transition is of the order of $\sim 0.1 M_\odot$. Finally, after the formation, QSs can spin-down following the evolutionary path of constant M_0 shown in the right panel of Fig. 7.1. Detailed results are presented in Tab. 7.1 where we list the variation of the spin frequency $\Delta f_{\rm d}$, of the gravitational mass $\Delta M_{\rm d}$ and of the rotational kinetic energy $\Delta K_{\rm d}$ (where $K := \frac{1}{2}\mathcal{J}\Omega$) during the phase transition for a set of selected models. Since QSs have larger radii and hence also a larger moment of inertia, conservation of the angular momentum implies a drop in spin frequency. Interestingly we found that the variation of the stellar radius is slightly larger ($\sim 10\%$ between cases A and B) at higher M_0. Hence transitions at higher M_0 are characterized by a bigger percent variation of the spin frequency and of the rotational energy. $\Delta K_{\rm d}$ only accounts for the variation of the kinetic energy while the total change of energy is given by the variation of the gravitational

Table 7.1: Global quantities at the phase transition for the configurations labeled in Fig. 7.1: gravitational mass M and spin frequency f of the hadronic configuration at deconfinement; difference between the spin frequency $\Delta f_{\rm d}$, the gravitational mass $\Delta M_{\rm d}$, and the rotational energy $\Delta K_{\rm d}$ before and after deconfinement.

Label	M_0 $[M_\odot]$	f [Hz]	$\Delta f_{\rm d}$ [Hz]	M $[M_\odot]$	$\Delta M_{\rm d}$ $[M_\odot]$	$\Delta K_{\rm d}$ $[10^{52}$ erg]
A	1.666	0.00	0.00	1.452	0.132	0.00
B_1	1.677	300	130	1.462	0.132	0.20
B_2	1.687	400	177	1.470	0.133	0.35
B_3	1.698	500	224	1.480	0.133	0.57
B_4	1.733	700	317	1.520	0.136	1.18
B_5	1.785	900	413	1.555	0.139	2.14
B	1.820	1000	462	1.585	0.142	2.80

mass ΔM_d and it will produce a reheating of the star. In the range of interest, $\Delta M_d \simeq 10^{53}$ erg and $\Delta K_d \simeq 10^{51-52}$ erg. This significant amount of energy released by quark deconfinement can be associated with a late time activity as we will discuss in the following.

In the magnetar GRB model the spin-down evolution is governed by magnetic torques. Therefore in order to evaluate the evolutionary timescales of our models we solve, for simplicity, the spin-down formula for an aligned dipole rotator (Spitkovsky 2006):

$$\frac{\mathrm{d}\mathcal{J}}{\mathrm{d}t} = -\frac{B^2R^6\Omega^3}{4}, \tag{7.1}$$

where B is the magnetic field strength at the pole and we assume that the magnetic flux $\Phi = BR^2$ is constant during the evolution. This choice gives only an upper limit to the timescale for deconfinement: oblique rotators or mass loaded winds can have higher torques (Metzger et al. 2011) that can lead to faster spin-down (up to a factor 10) in the first tens of seconds. Furthermore we neglect the possibility of late time mass accretion (Bernardini et al. 2014), because it introduces extra degree of freedom that cannot be easily constrained. We also neglect gravitational waves emission which is relevant only if the star owns a very strong internal toroidal field larger than $\sim 10^{16}$ G (Dall'Osso et al. 2009). In the mass range of interest we have evaluated the spin-down timescale up to deconfinement, which is shown in Fig. 7.3 and Tab. 7.2, for each equilibrium sequence of constant M_0 , assuming an initial surface magnetic field $B_0 = 10^{15}$ G. Note that the spin-down age scales with B_0^{-2}. Conservation of the magnetic flux Φ is also assumed to hold during the phase transition. The resulting magnetic field strength is of the order of $0.5B_0$ due to the change of the stellar radius.

The time evolution of the spin frequency f and of the rotational energy K is shown in Fig. 7.3 for the HS configurations labelled $B_1 - B_5$. It is evident that HSs with higher mass have a shorter lifetime before deconfinement, since they reach the critical density at higher spin frequencies. In Tab. 7.2 we list the time it takes to start deconfinement and the associated

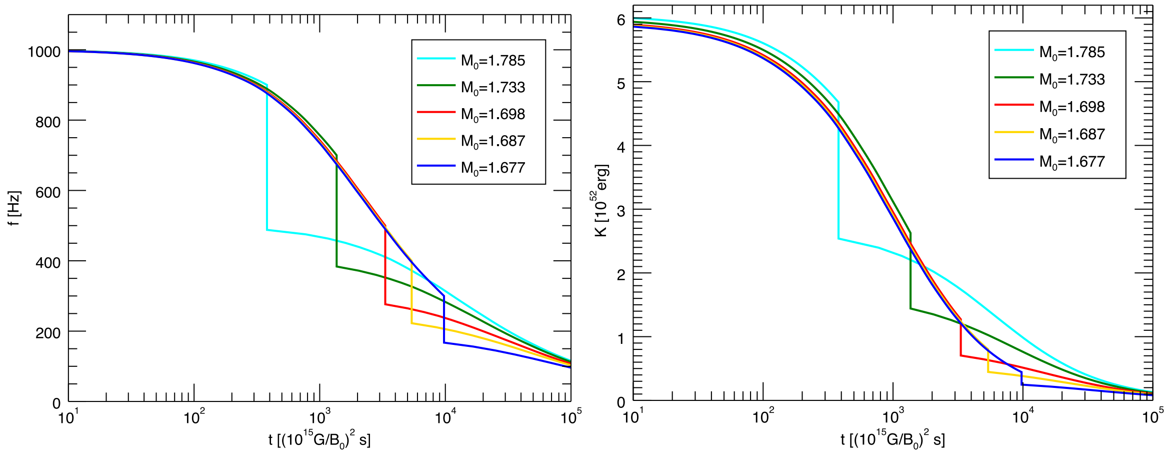

Figure 7.3: Time evolution of the spin-frequency (left panel) and of the rotational energy (right panel) for dipole magnetic field losses along sequences of constant baryonic mass M_0. Details about these sequences are listed in Tabs. 7.1 and 7.2.

Table 7.2: Spin-down timescales to start quark deconfinement $\Delta t_{\rm sd}$ together with the associated variation of the rotational kinetic energy $\Delta K_{\rm sd}$ starting from an initial spin period P_i for the equilibrium sequences shown in Fig. 7.3. We also show the spin-down timescales $\Delta t_{\rm q}$ (defined as the time needed to half the rotational frequency of the QS) and the corresponding rotational energy loss $\Delta K_{\rm q}$ after quark deconfinement. The initial magnetic field is 10^{15} G.

M_0 $[M_\odot]$	$P_i \to P_{\rm d}$ [ms]	$\Delta t_{\rm sd}$	$\Delta K_{\rm sd}$ [10^{52} erg]	$\Delta t_{\rm q}$	$\Delta K_{\rm q}$ [10^{52}erg]
1.666	$1.0 \to \infty$	∞	5.91	-	-
1.677	$1.0 \to 3.3$	2.7 hr	5.48	37 hr	0.19
	$2.0 \to 3.3$	1.8 hr	0.82		
	$3.0 \to 3.3$	37 min	0.13		
1.687	$1.0 \to 2.5$	1.5 hr	5.13	21 hr	0.33
	$2.0 \to 2.5$	36 min	0.46		
1.698	$1.0 \to 2.0$	55 min	4.68	14 hr	0.53
1.733	$1.0 \to 1.4$	23 min	3.37	8.2 hr	1.20
1.785	$1.0 \to 1.1$	6 min	1.37	5.4 hr	1.95
1.820	$1.0 \to 1.0$	0	0	4.6 hr	2.41

rotational spin-down energy loss $\Delta K_{\rm sd}$ for different values for the initial spin period.

7.3 Discussion and conclusions

Let us consider now the phenomenological implications of our scenario for the evolution of proto-magnetars. The variation of the rotational energy $\Delta K_{\rm sd}$ displayed in Tab. 7.2 gives an estimate of the energy reservoir available to the HS before deconfinement which occurs after a spin-down time scale $\Delta t_{\rm sd}$ that ranges from several minutes to hours. Comparing $\Delta K_{\rm sd}$ with the typical energetics of the millisecond magnetar model for GRBs (Fig. 19 of Metzger et al. 2011) one notices that the values shown in Tab. 7.2 are compatible with the requirement for classical GRBs, being $\Delta K_{\rm sd}$ much larger than 10^{50-51} erg, i.e. the typical energy emitted in X-rays and in gamma-rays during GRB events. We also remark that since $\Delta t_{\rm sd}$ is much larger than the typical duration of the prompt phase of LGRBs, deconfinement does not spoil the nice description of the prompt emission of LGRBs within the proto-magnetar model.

However, as discussed before, also the HS to QS transition is characterized by a huge release of energy (Tab. 7.1) that in principle could manifest itself as a second transient. Hence the time for deconfinement $\Delta t_{\rm sd}$ is indicative of the delay between the prompt GRB emission due to the HS and the possible flare or second prompt emission associated to quark deconfinement. Let us summarize how the deconfinement process proceeds and how is the energy released. As studied in Drago and Pagliara (2015), deconfinement can be described as a combustion process which can be separated in two phases. The first phase is very rapid due to turbulence and it converts the bulk of the star in a time scale of few ms (Drago et al. 2007, Herzog and Röpke 2011). The second phase is dominated by diffusion of strangeness and it is therefore much slower, typically lasting a few tens of seconds (Drago and Pagliara 2015). The huge energy associated to deconfinement is released via thermal neutrinos whose luminosity can similarly be divided into an initial peak associated with the deconfinement of the bulk of the star and a lower quasi-plateau emission associated with the burning of the external layer of the star. The interaction of neutrinos with the material of the crust of the star causes the ablation of baryons which plays a crucial role in the proto-magnetar model of GRBs. A distinctive feature of the formation of a QS is the rapid suppression of the baryonic flux once the conversion front reaches the surface of the star. This poses an upper limit to the duration of an event of the prompt emission if described within the proto-magnetar model and if associated with the baryonic emission from the surface of a star undergoing quark deconfinement. However, also the lepton emission from the surface of the bare QS (Usov 1997, 2001, Page and Usov 2002) can be used to produce a jet.

As an example we discuss the case of GRB 110709B characterized by two sub-bursts of observed duration respectively $\Delta t^{(1)} \sim 80$ s and $\Delta t^{(2)} \sim 300$ s, separated by a delay $\Delta t_{\rm delay} \sim 600$ s (Zhang et al. 2012, Penacchioni et al. 2013). Neither the cosmological redshift nor the energetics of the event are well determined and in the following we adopt values compatible with the analysis by Penacchioni et al. (2013), being in agreement with the pulse-wise Amati relation (Basak and Rao 2013). In particular we assume an isotropic energy $E_{\rm iso}^{(1)} = 2.6 \times 10^{53}$ erg for the first burst and $E_{\rm iso}^{(2)} = 4.4 \times 10^{52}$ erg for the second one at redshift $z = 1$. We further assume a beaming correction of $\sim 10^{-2}$ in line with average jet opening angle of LGRB (Guidorzi et al. 2014). Requiring that during the bursting events (radiatively-efficient phases) the mass loading enhances the spin-down by a factor 3 – 4 with respect to the force-free case (Metzger et al. 2011), we find that, assuming an initial magnetic field $B = 2 \times 10^{15}$ G, HSs with initial spin period in the range $1 - 1.6$ ms and baryon masses in $M_0 = 1.72 - 1.70 M_\odot$ have enough rotational energy to power the first event in a time $\Delta t^{(1)}$, deconfine with a delay $\Delta t_{\rm delay}$ and originate a QS rotating fast enough to power also the second event on the required time $\Delta t^{(2)}$. Notice that the requirements of short delays and fast rotating QS select for configurations with high baryon mass. On the contrary HSs with lower M_0 take longer to decay and form a slowly rotating QS that at most could power weak flaring events in the afterglows, on timescales of few hours (see Tab. 7.2), similarly to what is seen in GRB 050916 (Chincarini et al. 2007).

Finally, let us clarify how deconfinement can be responsible of rather long gamma emissions, as in the case of GRB 110709B, and also of the prompt phase of short GRBs, as discussed in Drago and Pagliara (2016), Drago et al. (2016a). The main differences are related to the neutrinos flux and energy which determine the baryonic mass ejection rate. In the case of short GRBs, the neutrino flux is significantly larger (of at least one order of magnitude) mainly because of the larger mass of the forming QS. Also the neutrino energy is larger roughly by a factor of three. This implies that the phase during which the QS forms cannot produce a large enough Lorentz factor in the case of short GRBs. At variance, in the case of LGRBs, the mass ejection rate is not too large and the prompt emission can start almost immediately at the beginning of deconfinement.

Although our model requires further investigation for a detailed assessment, our simple analysis of the spin-down evolution of CSs provides us with a new characterization, in terms of energetics and timescales, of the possible observational signatures associated with the two-families scenario. In particular we have shown, with reference to double GRBs, how, once the EoS of HSs and QSs are chosen, the associated phenomenology is constrained by the initial magnetic field strength, initial rotational period and the stellar mass. This implies that, in principle, new observations could validate the two-families hypothesis, gaining new insights in the physics of dense matter.

Conclusions

The simultaneous presence of high density, strong gravity, fast rotation and strong magnetic fields makes NSs a unique environment, where theories from different branches of physics can be tested under extreme conditions not achievable on Earth. Nevertheless, in order to investigate the physics of NSs, it is necessary to deeply understand their observational properties. These, in turn, depend dramatically on the structure and the properties of the magnetic field which plays a key role in the phenomenology of the emission of NSs. Even small differences in the morphology of the magnetic field can lead to changes in the physical processes that might be important for the way NSs manifest. Therefore, an accurate and detailed description of the morphology of the magnetic field is a necessary ingredient to develop a realistic physical model able to shed light on NSs phenomenology.

This thesis focuses on the development of a comprehensive numerical study of magnetized configurations, derived in full GR, taking into account different magnetic field geometries as well as the effects of rapid rotation. Equilibrium models have been obtained through the XNS code, which has been updated during this Ph.D. program to model barotropic NSs endowed with a general magnetic field configuration, including also rotation and realistic EoSs. Our code solves simultaneously, by means of semi-spectral methods, Einstein's equation for the metric, and Maxwell's equations for the electromagnetic potential, together with the Bernoulli integral to set the equilibrium. The main difficulties in solving for magnetized equilibrium models in GR are due to the complexity and the non-linearity of Einstein's equation. While in the case of purely toroidal or purely poloidal magnetic fields the exact metric has a simple form because of the circularity of spacetime, for a mixed magnetic field many metric terms must be retained and a large set of coupled elliptic partial differential equations has to be solved. Here we have chosen a different approach with respect to previous studies: instead of solving the exact equations or resorting to a perturbative approach, we approximate the spacetime metric to be conformally flat, using the recently developed XCFC formalism, which is indeed at the base of the XNS code. We have shown that differences with respect to the exact solutions are negligible (well within the typical discretization errors of numerical codes even under extreme conditions), with the benefit of a far more numerically stable and well conditioned system of equations. This has allowed us to sample a wide and general class of current distributions performing a vast parameter study (up to the fully non-linear regime), necessary to establish general trends and expectations regarding how different current distributions affect the structure of the star and the morphology of the associated magnetic field, considering also the coupling with centrifugal and compactness effects. The analysis of this large set of equilibria has provided us the opportunity to extend previous results presented in literature (assessing their robustness and generality) but also to derive new quantitative and qualitative relations between different stellar quantities (such as the induced deformation, the gravitational mass and the stellar radii), the energy content of the system and the multipolar structure of the magnetic field.

In this work we have analized purely toroidal, purely poloidal and mixed magnetic fields. In general we have seen that the effect of the magnetic field is more pronounced in less compact NSs. More massive configurations of higher central density, instead, show smaller deformations even if they can host a stronger magnetic field. Moreover at fixed gravitational/baryonic mass, and excluding supramassive configurations, there is always a maximum magnetic field strength that can be placed inside the star. This corresponds to the development of a highly non-linear regime, where the magnetic energy increases as a consequence of the expansion of the star, rather than a growth in the magnetic field strength. In principle, we might expect that the magnetic energy stored inside the star can be increased to be almost comparable with the gravitational mass of the NS. However we have verified that this is not the case: the inflation of the star (in the purely toroidal field case) or the topological change of the density distribution (in the poloidal field case) leads to a saturation of the magnetic field energy. Considering also rotation we have seen that, since it reduces the compactness of the star, it enhances the effectiveness of the magnetic field in changing the structure of the star itself. Interestingly, we have found that while a toroidal magnetic field reduces the maximum rotational rate below which the mass shedding occurs, the poloidal field does the opposite stabilizing the system against mass-shedding.

In our analysis we gave a particular emphasis to the parametrization of the induced deformation, which is the relevant quantity in the context of GWs astronomy. Previous studies have already provided such parametrizations both in terms of the magnetic field strength and the rotational frequency, or in terms of the associated energetics. In the majority of cases, however, such analyses were limited to the perturbative regime especially when considering complex magnetic field morphologies. Here, instead the analysis is always performed up to the fully non linear regime extrapolating then to a more realistic regime. This has allowed us to compare the interplay between different current distributions, even in the most extreme cases, in order to understand if the deformation of the star can be explained exclusively in terms of the energetics of the system or if one should also consider the specific profile of the magnetic field distribution inside the star. In general we have seen that, in the case of distributed currents, a parametrization in terms of the energetic allows us to obtain general scaling laws that take into account also the dependency on the compactness of the star, the current distribution and the coupling between the magnetic field and the rotation. This is indicative of the fact that the deformation of the star can be viewed as the result of the balance between the magnetic energy and the kinetic rotational energy versus the gravitational binding energy. However, while distributed currents have minor effects on the stellar deformation, the situation is reversed in the case of fully saturated and highly concentrated currents especially for poloidal magnetic fields: we noticed that, being the energetics equal, currents located in the outer layers of the stars are less important than currents located in the deeper interior. This is particularly evident in the case of TT configurations where, because of the equilibrium requirements in the GS equation, to increase the toroidal magnetic field it is also needed to rise the toroidal current in the outer layers of the star. This implies that at a given magnetic energy, even considering a configuration where the toroidal magnetic energy is sub-dominant, the rearrangement of the internal current causes a reduction of the efficiency of the poloidal magnetic field in the deformation of the star. This underlines the importance of the current distribution as a key parameter which, in turn, strongly depends of the details of the NS formation (the stratification of differential rotation, the location of the convective region, etc, ...). We stress here that in our mixed field configurations the deformation is indeed completely due to the poloidal magnetic field, since it is always energetically dominant. Even using several functional forms for the current, we have found that the system always saturates to configurations where the energy of the toroidal field is at most 10% of the total magnetic energy. Again, the reason is that the growth of the peripheral toroidal currents acts to change the structure of the poloidal field reducing the volume occupied by the toroidal one. A possible solution to this problem it to relax the equilibrium condition, at least in the outer layers of the star, or to consider non-barotropic NSs. Indeed, it seems that the energy ratio depends more on the stratification of the star rather than on the current distribution.

Investigating how the NS reacts to different current distributions, we have also analyzed how the external magnetic field reorganizes in response to strongly concentrated currents. Indeed, the choice of the current profile leads to different configurations where the magnetic field can be concentrated either toward the center or toward the edge of the star. It is possible to obtain configurations where the magnetic field at the surface can differ substantially from a simple dipole: by adopting different prescriptions, we can make it either higher at the equator, or concentrated toward the axis, in configurations where the bulk of the star is demagnetized. This means that the surface field can be easily dominated by multipoles higher than the dipole. It also implies that local processes, at or near the surface, might differ substantially in their signatures from the expectations of dipole dominated models. On the other hand, processes related to the large-scale field, as spin-down, will not.

In the last years there was a growth of observational evidences supporting the idea that the magnetospheres of magnetars are tightly twisted in the vicinity of the star. Investigating how this twisted magnetosphere is arranged, and what could be its equilibrium structure, is thus an important step for a more realistic description of these astrophysical sources. Extending previous results in literature, we have generalized TT configurations to model twisted magnetospheres allowing for electric currents to flow from the interior of the star to the magnetosphere. The resulting morphology of the magnetic field is then characterized by toroidal fields (and hence a twist) extending also in the exterior of the star. All the equilibrium models that we have obtained are energetically dominated by the poloidal component, which stores almost 75% of the total magnetic energy of the magnetosphere. This result is in line with what we have obtained for TT configurations. The amount of twist in the magnetosphere can be regulated modulating the poloidal non-linear current injected outside. When this current is weak the magnetic field is inflated outward by the toroidal magnetic field pressure and the twist extends also to higher latitudes. In this case the toroidal field is organized in a single magnetically connected region, where all the poloidal field lines are connected to the surface of the star. As the exterior current increases and reaches values similar to the ones buried inside the star, the system starts to self-regulate inducing a dramatic change in the topology of the magnetic field distribution. The resulting topologies are very likely to be unstable suggesting that there is a maximum twist that can be imposed to the magnetosphere, before reconnection and plasmoid formation sets in.

Newly born rapidly rotating magnetars have been suggested as engine candidates for GRBs. The energy losses due to the emission of a relativistic magnetically driven wind can explain the bulk of known events, but it requires in general a high efficiency to convert the rotational energy of the proto-neutron star into wind kinetic energy. The presence of strong magnetic fields $\geq 10^{15}$ G is however expected to induce deformations able to trigger such an intense GWs emission that can compete with the electromagnetic emission of the wind. Indeed if, as expected from stability requirements and evolutionary scenarios, the toroidal field is energetically dominant, it would induce a prolate deformation that enhances the efficiency of GWs production. As discussed above, a detailed investigation of the deformation due to mixed magnetic fields requires a precise analysis of the current distribution. However, a rough comparison between the results obtained separately for purely toroidal and poloidal fields suggests that, for a typical millisecond magnetar with a poloidal magnetic field of the order of 10^{16} G, a toroidal component of the magnetic field of about one order of magnitude stronger than the poloidal one is necessary to achieve a prolate deformation.

During the last years, the proto-magnetar model is gaining popularity because of the observations of the extended emission of GRBs that can be interpreted as the imprint of an ongoing energy injection from the rapidly spinning magnetar. Within this picture, it is however difficult to explain late time bursts often present in the light-curve of many long GRBs, since the standard picture predicts a steady smooth energy injection in the form of a relativistic magnetically driven wind. Among all the possible explanations, it has been proposed that late time bursts can be associated with quark deconfinement. As an application of the results and the numerical tools developed during this Ph.D. research, we have explored the possible implication of quark deconfinement on the phenomenology of GRBs. In particular, in the last part of this work we have shown that, on the basis of energetical arguments and timescale evaluations, the transition from a neutron star into a quark star can take place giving rise to peculiar observable features in long GRBs as demonstrated through an application to the double-burst GRB 110709B.

In the future we hope that our models can be used as a starting point toward a more realistic and accurate modelization of NSs. Indeed, our equilibrium models can serve as an initial condition to study the evolution of the magnetic field after the formation of the NS. This is an important task, necessary to constrain the stability and morphological properties of the magnetic field inside the star. In addition future possible observations of GWs from a newly-born magnetar can be used to obtain important information about the geometry of the magnetic field. Even though a precise comparison with the GW signal requires a detailed modelization of the initial evolution of the system to obtain realistic GW templates, our presents results (in particular Eqs. 3.11, 4.17 and 5.6) can be used to roughly evaluate how the magnetic energy is shared between the toroidal and poloidal component of the magnetic field, since the GW strain amplitude is directly proportional to the quadrupolar deformation of the NS.

In the future we hope to be able to include also the effects of superfluidity/superconductivity and the presence of a crust. Adding these effects will allow us to study the long-term evolution of the magnetic and thermal properties of the NS and to link the reactions of the magnetosphere to rearrangements of the internal magnetic field. As an example our models, and in particular those endowed with a twisted magnetosphere (see Chap. 6), can be used to compute the synthetic electromagnetic emission of magnetars (including light-curves, spectra and polarization patterns) to be compared with observations. In particular, future data collected with X-ray polarimeters, such as XIPE (X-ray Imaging Polarimetry Explorer, Soffitta et al. 2013) and IXPE (Imaging X-ray Polarimeter Explorer, Weisskopf et al. 2013, Jahoda et al. 2014), would be crucial to unveil the magnetic structure of such kind of stars.

A

The XNS code

The XNS code solves for axisymmetric equilibria of magnetized and rotating NSs in GR. The code is based on the metric module and routines developed for the X-ECHO code for GRMHD in dynamical spacetimes (Bucciantini and Del Zanna 2011), which in turn is an upgrade of the Eulerian Conservative High-Order code (ECHO Del Zanna et al. 2007), During this Ph.D. program, XNS has been updated to account for various magnetic field topologies (purely poloidal, mixed) for both static and rotating NSs. It is now also possible to build rotating models using realistic tabulated EoSs.

In this Appendix we will describe the numerical work-flow of XNS (Sec. A.1) together with the numerical techniques used to solve the equations (Sec. A.2). Finally in Sec. A.3 we will provide some tests of the performances and the accuracy of XNS.

A.1 The numerical scheme

The XNS code solves self-consistently the coupled Einstein-Maxwell equations in spherical coordinates for an axisymmetric and stationary spacetime under the so-called XCFC approximation (see Sec. 2.3). For the magnetic field configurations it is possible to chose among different morphologies, i.e. purely toroidal, purely poloidal or mixed field configurations, arising from different currents distributions that can be either totally confined inside the star or extended outside in the magnetosphere. For rotating NSs, we have considered only rigid rotation with Ω = cost and we do not solve for differential rotation or meridional flows (i.e. $v^r = v^\theta \neq 0$). However the code can solve also for differential rotation with a toroidal magnetic field.

Once the central density $\rho_{\rm c}$, the rotational frequency of the rigid rotation and the free parameters associated with the current distribution have been chosen XNS performs the following iterative algorithm:

1. the numerical domain is initialized with a guess for the metric terms, the fluid quantities and the electromagnetic field; in the first iteration, the initial guess is provided by solving the TOV equation in isotropic coordinates (Tolman 1939) for a NS with central density ρ_c through a shooting method;

2. the XCFC equations 2.60 - 2.63 are hierarchically solved for the metric functions W^{ϕ}, ψ, α and β^{ϕ} using a semi-spectral method;

3. the 3-velocity v^{ϕ} (Eq. 2.81) and the Lorentz factor Γ are obtained on top of the metric function;

4. depending on the morphology of the magnetic field the Lorentz force contribution to the Bernoulli integral $\mathcal{M}$ is evaluated throughout different approaches:
   - if the magnetic field configuration is purely toroidal the potential $\mathcal{M}$ is given by Eq. (3.1);
   - in the case of a static configuration endowed with a poloidal magnetic field (and hence also mixed magnetic field configuration), the magnetic potential Ψ is obtained from Eq. 2.78 and Eq.2.99, finally determining $\mathcal{M}$;
   - if the magnetic field is purely poloidal but the star is rotating we iteratively solve together both the Maxwell-Gauss equation (2.77) and the Ampère equation Eq. 2.78 (respectively for the potential Φ and Ψ), initializing the source terms using Eq. (2.100) and assuming vacuum outside the star;

5. the Bernoulli integral is finally solved via a Newton method and the fluid quantities are updated in order to start a new iterative cycle;

6. the previous steps, from 2 to 5 ,are repeated until convergence to a desired tolerance is achieved.

A.2 Solving equations

As discussed in Sec. 2.3, in the XCFC-formulation the Einstein's equation is turned into a system of two scalar Poisson-like PDEs, one for the conformal factor ϕ and the other for the lapse function α, and two vector Poisson-like equations, one for the shift vector β^{i} and one for W^{i}. These are fully decoupled and can be solved hierarchically (in the order: first the one for W^{i}, then ψ, α and finally β^{i}). Moreover they can be cast into a form that guarantees local uniqueness of the solution. In the case of purely rotating star only W^{ϕ}, and β^{ϕ} are different from zero.

The elliptic PDEs related to the vector quantities like W^{ϕ} and β^{ϕ} have the general form:

$$\Delta X^{\hat{\phi}} = H^{\hat{\phi}}, \tag{A.1}$$

where the $X^{\hat{\phi}} = X^{\hat{\phi}}(r, \theta)$ is the generic ϕ-component of the unknown vector field, while $H^{\hat{\phi}}$ is the associated source term. In the case of W^{φ}, the source term depends only on S^{ϕ}. While for $\omega = -\beta^{\phi}$ (the last equation solved), it depends also on the terms computed previously.

The elliptic PDEs for scalar quantities like ψ and α can be generally written as:

$$\Delta q = s q^p; \tag{A.2}$$

here again $q = q(r, \theta)$ is the generic unknown scalar function, and s is the scalar source term, which in turn depends on and the stress-energy content of the space-time, and on previously computed metric terms (recall that the metric solver has a hyerarchical structure).

Remarkably Maxwell Eqs. 2.77- 2.78 and the Grad Shafranov Eq. 2.125 share the same mathematical structure of the XCFC Einstein equations, in particular: the scalar equation for the electric potential Φ (Eq. 2.77) is a Poisson-like equation equivalent to Eq. A.2; the equation for Ψ (Eqs. 2.78 for rotating stars with purely poloidal field or Eq. 2.125 in the static case) are vector Poisson-like equation analogous to Eq. A.1 where $H = H(\Psi, \partial\Psi)$. The solutions of these elliptic PDEs are obtained through a semi-spectral method. The scalar functions ψ, $\alpha\psi$ and Φ are expanded as a linear combination of spherical harmonics $Y_\ell(\theta)$

$$q(r, \theta) = \sum_{\ell=0}^{\infty} K_\ell(r) Y_\ell(\theta), \tag{A.3}$$

while the vector quantities W^φ, β^φ and Ψ are expressed in terms of the ϕ-component of vector spherical harmonics

$$X^{\hat{\phi}}(r, \theta) = \sum_{\ell=0}^{\infty} C_\ell(r) Y'_\ell(\theta), \tag{A.4}$$

where $'$ stands for the derivative with respect to θ (notice that the assumption of axisymmetry excludes the harmonic degree $m \neq 0$). The harmonic expansion reduces each PDE to a set of radial ordinary differential equations, one for each coefficient K_ℓ (or analogously C_ℓ), with the form

$$\frac{\mathrm{d}^2 K_\ell}{\mathrm{d}r^2} + \frac{2}{r}\frac{\mathrm{d}K_\ell}{\mathrm{d}r} - \frac{\ell(\ell+1)}{r^2} K_\ell = q_\ell \tag{A.5}$$

where the source term is

$$q_l(r) := 2\pi \int q(r, \theta) Y_\ell(\theta) \sin\theta \mathrm{d}\theta. \tag{A.6}$$

Adopting a second order radial discretization the equation for each harmonic can be solved via a direct tridiagonal matrix inversion. The harmonics decomposition ensures also the correct behavior of the solution on the symmetry axis, at the centre and at the outer boundary of the domain which, in our case, is at a finite distance from the stellar surface. At the centre of the star the coefficients C_ℓ and K_ℓ go to zero with parity respectively $(-1)^\ell$ and $(-1)^{\ell-1}$, while at the outer radius the coefficients scale as $r^{-(\ell+1)}$.

In general, apart for rotating stars endowed with a poloidal magnetic field (see next Sec. A.2.1), we do not impose any condition at the surface of the star. Ideed, we solve all PDEs on the full numerical domain instead of using an interior grid, inside the star, and an exterior one, outside. This automatically guarantees that all solutions are continuous and smooth at the stellar surface, avoiding the onset of spurious surface currents. It also allows the stellar surface to adjust freely, and not to any imposed shape that is not known in advance in the case of strong field or rapid rotation.

A.2.1 Numerical resolution of Maxwell equation

In the case of rotating NSs with a purely poloidal field, we solve separately Eqs. 2.78-2.77 for the potentials Ψ and Φ respectively. These equations are solved iteratively computing the source terms from Eqs. 2.99-2.98 exploiting, at each step, the potential found from the previous one. Accordingly with the vacuum assumption, the current density J^ϕ and the charge density ρ_e are set to zero outside the star.

Since Eqs. 2.78-2.77 are solved, at once, on the entire numerical grid, both Ψ and Φ cross smoothly the the stellar surface. This is not consistent with the fact that a rotating perfect conductor, endowed with a poloidal magnetic field, naturally acquires a surface charge density, which in turn manifests as discontinuity of the component of the electric field and hence of the derivatives of Φ. Indeed, the obtained potential Φ does not satisfy the perfect conducting relation Eq. 2.89 inside the star, but differs from the MHD solution $\Phi_{\rm MHD} = -\Omega\Psi + C$ by an harmonic function Φ_a:

$$\Phi = \Phi_{\rm MHD} + \Phi_a \quad \text{with} \quad \Delta\Phi_a = 0. \tag{A.7}$$

This harmonic function Φ_a is set by requiring Eq. 2.89 to hold at the stellar surface $\mathcal{S}_{\rm NS}$:

$$\Phi_a|_{\mathcal{S}_{\rm NS}} = (\Phi - \Phi_{\rm MHD})|_{\mathcal{S}_{\rm NS}}. \tag{A.8}$$

Being an harmonic function, it can be expanded in spherical harmonics inside and outside the star as

$$\Phi_a = \sum_{l=0}^{N_\ell} Y_\ell(\theta) \times \begin{cases} a_\ell r^\ell & \text{inside the star,} \\ b_\ell r^{-(\ell+1)} & \text{outside the star,} \end{cases} \tag{A.9}$$

The coefficient a_ℓ and b_ℓ are found by solving a system of $N_\ell + 1$ equations that one obtains evaluating Eq. A.8 on $N_\ell + 1$ collocation points located along the surface $\mathcal{S}_{\rm NS}$. The spacing between these collocation points is chosen in order to improve the convergence and avoid aliasing effects. For highly oblate stars, it is important to redistribute differently the collocations points used to compute the interior solution and those used to compute the exterior one: while the collocations points for the interior solution are mainly distributed in the vicinity of the stellar equator (at larger radii), in the other case they are clustered near the pole. Moreover, if the collocation points are chosen to coincide with the grid-points locating $\mathcal{S}_{\rm NS}$, the development of high-frequency numerical noise can compromise the accuracy with which high-ℓ coefficients are computed. Given the iterative nature of the algorithm, this might compromise the overall convergence. To avoid this problem, collocation points are selected on top of the super-ellipse, with equation

$$r = \left[\left(\frac{\cos\theta}{r_{\rm p}} \right)^{n_{\rm s}} + \left(\frac{\sin\theta}{r_{\rm eq}} \right)^{n_{\rm s}} \right]^{-\frac{1}{n_{\rm s}}} , \tag{A.10}$$

that best fits the discretized stellar surface (see Eq. 2.118). Interestingly, in almost all cases the stellar surface can be approximated by a super-ellipse with $1.5 \lesssim n_{\rm s} \lesssim 3$, within at most one grid point. Once $\Phi_{\rm a}$ has been obtained, the potential Φ can be corrected to $\Phi_{\rm new} = \Phi - \Phi_{\rm a}$, that satisfies ideal MHD inside the star. The new function $\Phi_{\rm new}$ is now continuous but not differentiable across the surface as expected.

Note that the ideal MHD condition Eq. 2.89, does not completely set the scalar potential Φ, which inside the star is still defined minus an arbitrary constant C. As pointed out by Bocquet et al. (1995) this constant corresponds to an arbitrary charge, that can be added to the star. A common choice is to require the net charge $Q_{\rm e} = 0$ (see discussion is Sec. 4.2.1). This can be achieved by minimizing iteratively the monopolar content of $\Phi_{\rm new}$, with the same procedure discussed in Bocquet et al. (1995). The other possibility that we have considered is to assume a net global charge in order to minimize the Lorentz force at the pole. This can be done by simply minimizing the discontinuity of the electric field at the pole.

A.2.2 The numerical setup

The equilibrium models that we present in this thesis are computed on top of different numerical grids depending on the specific magnetic field morphology that we have investigated. The spherical grid typical adopted is uniformly spaced and covers the range $r = [0, R_{\rm max} = 40]$ (in geometrized units) and $\theta = [0, \pi]$ with 600 points in the radial direction and 300 in the azimuthal one (the star is typically resolved with $\sim$ 200 radial points). The radial domain has been chosen such that its outer boundary $R_{\rm max}$ is far enough from the stellar surface, so that the higher order multipoles in the various quantities (i.e. in the metric terms) become negligible and the asymptotic trend $\propto r^{-(l+1)}$ can be imposed properly. We have verified that solutions do not depend on the position of the outer boundary.

In the particular case of twisted magnetosphere, where the toroidal field can extend up to eight times the stellar radius, we have increased the radial domain up to $R_{\rm max} = 150$ and we have used a non uniform grid in order to reduce the computational time: in the range $r = [0, 40]$ the grid is uniformly spaced with 600 zones, while a geometrically stretched grid covers the domain $r = [40, 150]$ with 200 grid points and with the following spacing

$$\Delta r_i = (1 + 5.962 \times 10^{-3}) \Delta r_{i-1} . \tag{A.11}$$

This allows us to resolve the star together with the extended magnetosphere always with the same accuracy, without resorting to huge numerical grids.

The surface of the star (needed to compute apparent ellipticity and to locate the collocation points to solve Eq. A.8) is defined as the locus of points where the baryon density

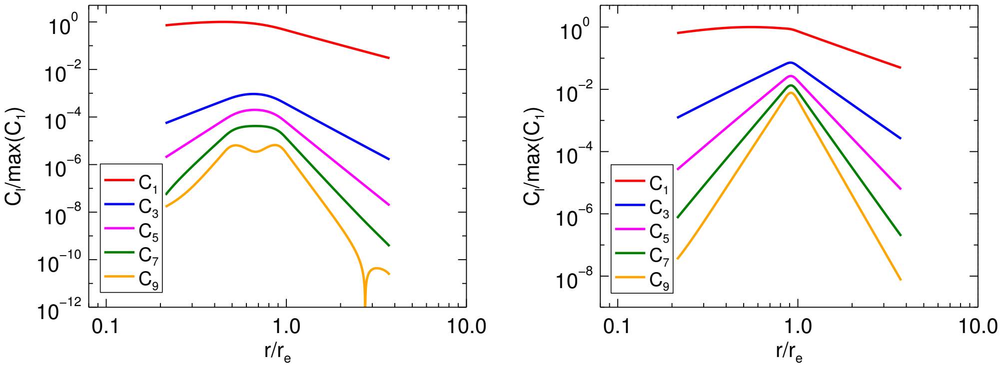

Figure A.1: Radial profiles of the norm of the $C_\ell(r)$ coefficients in the harmonic decomposition of the magnetic potential Ψ (see Eq. A.4), in the weak field limit. Values are normalized to the maximum of the $C_1(r)$, for convenience. Left panel: $a = 0.1$. Right panel: $a = 2.5$.

drops below $\sim 10^{-5} - 10^{-7}$ the value of the baryon density at the center of the star ρ_c. For numerical reasons, the value of the baryon density in the magnetosphere is set to a fiducial small value (typically $\sim 10^{-6} - 10^{-8}$ times ρ_c). The threshold value for the rest mass density is chosen such that lowering it further produces negligible changes (much smaller than the overall accuracy of our scheme).

In all these cases, the convergence tolerance for the iterative scheme and for the solution of the PDEs has been fixed to $10^{-7} - 10^{-8}$ (convergence is checked looking at the maximum deviation between successive solutions for the various quantities), however the overall accuracy of our solutions is 10^{-3} because of the discretization errors. This accuracy is typically achieved using 20 spherical harmonics. However for mixed field models or purely poloidal models with saturated currents (see Sec.4.1.2), the number of spherical harmonics has been increased up to 60 in some cases. In these cases, indeed, the magnetic field can be characterized by narrow features, corresponding to concentrated currents, that can be resolved only with an higher number of harmonics. This is shown in Fig. A.1. Here we compare the relative strength of the coefficients C_ℓ of the potential Ψ for two TT configurations characterized by different values of the parameter a (see Sec.5.1), in the regime of weak magnetization[1]. In the case $a = 0.1$, where the toroidal magnetic field is defined in a large torus extending in the outer half of the star (see Fig.A.2), the various multipoles are more than three to four orders of magnitude smaller than the dipole term, and in general each multipole of order ℓ is about one order of magnitude smaller than the preceding one of order $\ell - 1$ (for smaller values of a the various multipoles are so small that they are essentially compatible with being due to numerical noise). In the case $a = 2.5$, where the toroidal field is localized in a narrow torus under the surface of the star (see again Fig.A.2), the multipolar content of the magnetic field

---

[1] As discussed in Sec. 4.1.2 in the weak field regime, the metric terms are essentially independent of the magnetic field strength and we can directly compare the various multipole terms by looking at the relative strength of the C_ℓ terms in the expansion in Eq. A.4. This is not possible for stronger magnetic fields, because the metric is no longer just a function of r, and the C_ℓ will also contain a geometrical contribution from the metric, which we can not separate since spherical harmonics are not eigenfunctions of the angular part of the Laplacian in a generically curved spacetime.

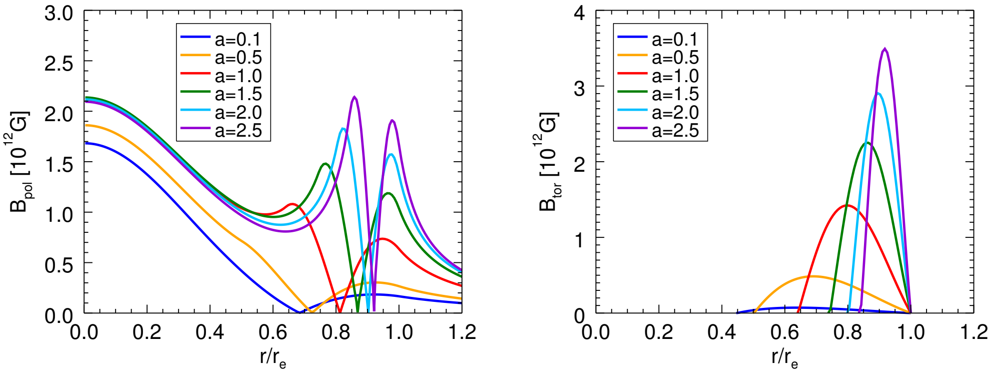

Figure A.2: The strength of the poloidal (left) and toroidal (right) magnetic field at the equator for various values of the parameter a (see Eq. 2.101).

is much higher: the $\ell = 3$ term is only a factor ~ 10 (at peak) smaller than the dipole term, and in general the ratio between two successive multipoles is only of the order of a few.

In the low magnetic field limit we have verified that in order to get converged solutions of the GS equation, we need to extend our decomposition of the vector potential Ψ into spherical harmonic, in Eq. A.4, up to $\ell_{\rm max}$ such that all the neglected multipoles have at least an amplitude $C_{\ell>\ell_{\rm max}}/C_1 < 10^{-5}$. Please note that, as said above, while the overall accuracy of our models is $\sim 10^{-3}$, the accuracy of elliptic solvers is 10^{-8}. In fact, multipoles with amplitude less than 10^{-7} times the leading dipole term are dominated by numerical noise (see e.g. the behaviour of the $C_{\ell=9}$ term in the left panel of Fig. A.1).

A.3 Accuracy of XCFC approximation

In this section we compare the results obtained with XNS with those of other codes presented in the literature in order to provide not only a test of the performances of our code, but also of the accuracy of the XCFC approximation.

A comparison between unmagnetized rotating equilibria is performed with reference to the RNS code (Stergioulas and Friedman 1995), which solves for equilibrium configurations of unmagnetized rotating NSs in the correct regime for the spacetime metric described by a quasi-isotropic form, for which we recall that $R \neq \psi^4 r^2 \sin^2\theta$. We have selected two classes of models presented in Dimmelmeier et al. (2006), which are computed using a polytropic EoS with $K_{\rm a} = 100$ and $n = 1$ for different rotational rates: the AU models are characterized by fixed baryonic mass $M_0 = 1.506 {\rm M}_\odot$; the BU models have fixed central density $\rho_{\rm c} = 1.280 \times 10^{-3}$ (in geometrized unit). We have computed these models in XNS on top of a computational grid defined in $r = [0, 20]$ and $\theta = [0, \pi]$ with 250 points in the radial direction and 100 in the angular one, and with 10 harmonics. As shown in Tab. A.1, the results obtained with the two codes agree within $\sim 5 \times 10^{-3}$ even for the BU9 model, which represents a configuration at the mass-shedding limit. In Fig. A.3 we compare in detail the models BU8 obtained with XNS and RNS, in terms of the radial profiles of the baryon density and

Table A.1: Comparison between the XNS code and RNS for rigidly rotating stars. AU models have fixed baryonic mass while BU equilibria are computed at fixed central density $\rho_c = 1.280 \times 10^{-3}$. The rotational rate is in unity of 10^{-2} while the central density is listed in unity of 10^{-3}. All quantities are expressed in geometrized units.

	ρ_c	Ω	M		r_e		r_p/r_e	
			XNS	RNS	XNS	RNS	XNS	RNS
AU0	1.280	0.000	1.403	1.400	8.12	8.13	1.000	1.000
AU1	1.164	1.293	1.407	1.404	8.68	8.71	0.917	0.919
AU2	1.072	1.656	1.411	1.407	9.25	9.30	0.853	0.852
AU3	0.978	1.888	1.414	1.411	10.04	10.06	0.777	0.780
AU4	0.883	2.029	1.419	1.415	11.80	11.14	0.697	0.698
AU5	0.799	2.084	1.427	1.420	13.35	13.43	0.573	0.575
BU0	1.280	0.000	1.403	1.400	8.12	8.13	1.000	1.000
BU1	1.280	1.075	1.435	1.432	8.29	8.33	0.952	0.950
BU2	1.280	1.509	1.469	1.466	8.52	8.58	0.898	0.900
BU3	1.280	1.829	1.507	1.503	8.76	8.82	0.854	0.850
BU4	1.280	2.084	1.547	1.543	9.08	9.13	0.797	0.800
BU5	1.280	2.290	1.590	1.585	9.48	9.50	0.747	0.750
BU6	1.280	2.452	1.631	1.627	9.88	9.95	0.700	0.700
BU7	1.280	2.569	1.669	1.666	10.44	10.51	0.648	0.650
BU8	1.280	2.633	1.695	1.692	11.24	11.26	0.594	0.600
BU9	1.280	2.642	1.699	1.695	11.56	11.63	0.578	0.580

of the metric functions. It is evident that XNS reproduces the matter distribution inside the star with a discrepancy of the order of 10^{-3} with respect to the RNS code. Analogously the metric terms are in agreement within the same accuracy of 10^{-3}, which is in turn comparable with the level of approximation introduced with the CFC assumption (see the green line in Fig. A.3).

In the case of non-rotating magnetized star with a purely toroidal magnetic field we compare our results with those obtained by Kiuchi and Yoshida (2008) and Frieben and Rezzolla (2012). They both solve for equilibrium in quasi-isotropic coordinates. Despite this, their results are significatively different. In particular they both compute a sequence of magnetized equilibrium models with fixed gravitational mass $M_0 = 1.680 \mathrm{M}_\odot$, using a polytropic EoS with $K_a = 110$ and $n = 1$. Therefore we have realized this same sequence with XNS adopting the same numerical grid as for the unmagnetized rotating models discussed previously. As shown in Fig. A.4 our results are in complete agreement with those of Frieben and Rezzolla (2012) (within again $\sim 5 \times 10^{-3}$), confirming the latter against Kiuchi and Yoshida (2008).

For purely poloidal magnetic field we refer to Bocquet et al. (1995). The polytropic index that they use is $n = 1$ while the polytropic constant is $K_a = 372$. For the model that we could reproduce, we found an agreement with deviations $\lesssim 1\%$ for all quantities, except the magnetic dipole moment, where the error is about a few per cent. We want, however,

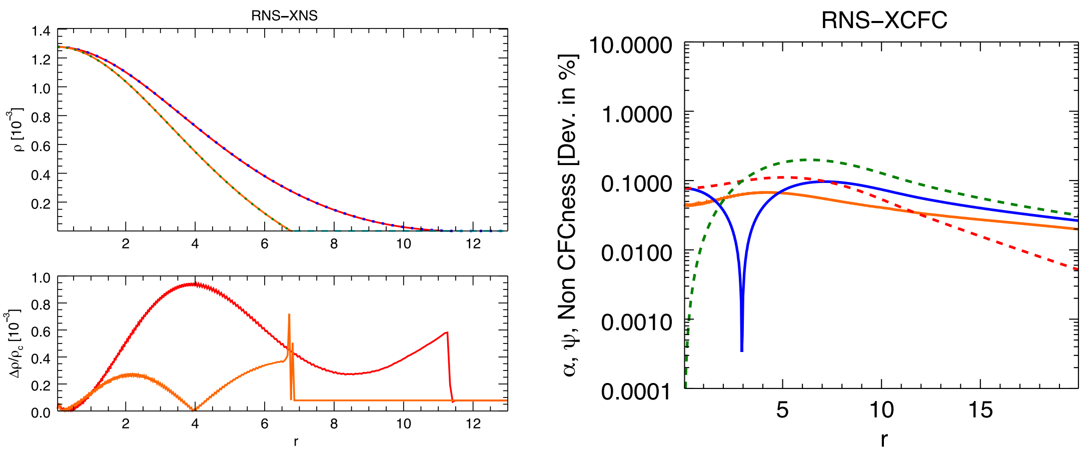

Figure A.3: Comparison between RNS and XNS solutions for model BU8. Left panels: density profiles derived with XNS (solid lines) and RNS (dotted lines) along the equatorial direction (solid-red and dotted-blue) and the polar direction (solid-orange and dotted-green). The bottom panel shows the residuals in the equatorial (red) and polar (orange) direction. Right panel: the orange line shows the relative error between the lapse computed with XNS and RNS. The blue and red curves are respectively the relative error between the conformal factor ψ of the CFC metric to the one in quasi-isotropic coordinates, and the quantity $[R/\sin\theta]^{-2}$. Finally the green line traces the difference between ψ and $[R/\sin\theta]^{-2}$ in quasi-isotropic coordinate, which can be considered as a measure of the non-conformal flatness of the RNS solution.

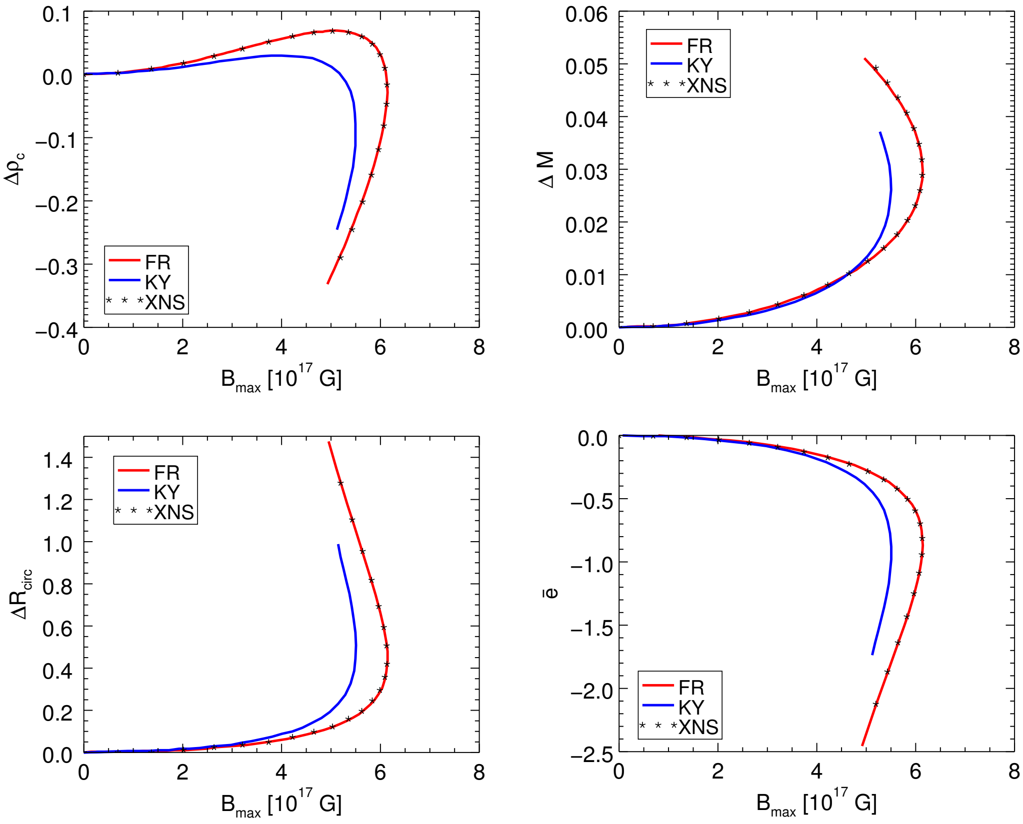

Figure A.4: Variation with respect to the unmagnetized equilibrium model of the central baryon density ρ_c, of the gravitational mass M, of the circumferential radius $R_{\rm circ}$ and of the deformation ratio along the equilibrium sequence of magnetized configuration with constant $M_0 = 1.680\mathrm{M}_\odot$ and $m = 1$. Lines represent the result from Frieben and Rezzolla (2012) (FR) and Kiuchi and Yoshida (2008) (KY); points are our results.

to point out that our operative definition of magnetic dipole moment (Eq. 2.116) is different than the one given by Bocquet et al. (1995), which is valid only in the asymptotically flat limit, where magnetic field vanishes.

Given that Dimmelmeier et al. (2006), Bocquet et al. (1995) and Frieben and Rezzolla (2012) solve in the correct quasi-isotropic metric, these comparisons are also a check on the accuracy of the XCFC approximation. It is evident that the XCFC approximation gives results that are in agreement with what is found in the correct full GR regime even in the magnetized case.

Finally, the XNS code has also been extensively validated in the Newtonian-limit (Das and Mukhopadhyay 2015, 2016, Subramanian and Mukhopadhyay 2015, Mukhopadhyay 2015). In particular, Bera and Bhattacharya (2015) have verified that our numerical scheme provides solutions that are indistinguishable, within the numerical accuracy, from those obtained with the LORENE code (`http://www.lorene.obspm.fr/`).

References

[**Aasi et al. 2014**] J. Aasi, J. Abadie, B. P. Abbott, R. Abbott, T. Abbott, M. R. Abernathy, T. Accadia, F. Acernese, C. Adams, T. Adams and et al., ‘Gravitational Waves from Known Pulsars: Results from the Initial Detector Era’. *ApJ*, April 2014, volume 785, 119, doi:10.1088/0004-637X/785/2/119, arXiv:1309.4027.

[**Aasi et al. 2015**] J. Aasi, B. P. Abbott, R. Abbott, T. Abbott, M. R. Abernathy, F. Acernese, K. Ackley, C. Adams, T. Adams, P. Addesso and et al., ‘Searches for Continuous Gravitational Waves from Nine Young Supernova Remnants’. *ApJ*, November 2015, volume 813, 39, doi:10.1088/0004-637X/813/1/39, arXiv:1412.5942.

[**Abbott et al. 2008**] B. Abbott, R. Abbott, R. Adhikari, P. Ajith, B. Allen, G. Allen, R. Amin, S. B. Anderson, W. G. Anderson, M. A. Arain and et al., ‘Beating the Spin-Down Limit on Gravitational Wave Emission from the Crab Pulsar’. *ApJLett*, August 2008, volume 683, L45, doi:10.1086/591526, arXiv:0805.4758.

[**Abbott et al. 2016a**] B. P. Abbott, R. Abbott, T. D. Abbott, M. R. Abernathy, F. Acernese, K. Ackley, C. Adams, T. Adams, P. Addesso, R. X. Adhikari and et al., ‘GW151226: Observation of Gravitational Waves from a 22-Solar-Mass Binary Black Hole Coalescence’. *Physical Review Letters*, June 2016a, volume 116(24), 241103, doi:10.1103/PhysRevLett.116.241103, arXiv:1606.04855.

[**Abbott et al. 2016b**] B. P. Abbott, R. Abbott, T. D. Abbott, M. R. Abernathy, F. Acernese, K. Ackley, C. Adams, T. Adams, P. Addesso, R. X. Adhikari and et al., ‘Observation of Gravitational Waves from a Binary Black Hole Merger’. *Physical Review Letters*, February 2016b, volume 116(6), 061102, doi:10.1103/PhysRevLett.116.061102, arXiv:1602.03837.

[**Abdikamalov et al. 2009**] E. B. Abdikamalov, H. Dimmelmeier, L. Rezzolla and J. C. Miller, ‘Relativistic simulations of the phase-transition-induced collapse of neutron stars’. *MNRAS*, January 2009, volume 392, 52–76, doi:10.1111/j.1365-2966.2008.14056.x, arXiv:0806.1700.

[**Akgün et al. 2016**] T. Akgün, J. A. Miralles, J. A. Pons and P. Cerdá-Durán, ‘The force-free twisted magnetosphere of a neutron star’. *MNRAS*, October 2016, volume 462, 1894–1909, doi:10.1093/mnras/stw1762, arXiv:1605.02253.

[**Akgün et al. 2013**] T. Akgün, A. Reisenegger, A. Mastrano and P. Marchant, ‘Stability of magnetic fields in non-barotropic stars: an analytic treatment’. *MNRAS*, August 2013, volume 433, 2445–2466, doi:10.1093/mnras/stt913, arXiv:1302.0273.

[**Akgün and Wasserman 2008**] T. Akgün and I. Wasserman, ‘Toroidal magnetic fields in type II superconducting neutron stars’. *MNRAS*, February 2008, volume 383, 1551–1580, doi:10.1111/j.1365-2966.2007.12660.x, arXiv:0705.2195.

[**Alcubierre 2008**] M. Alcubierre, *Introduction to 3+1 Numerical Relativity* (Oxford University Press 2008).

[**An et al. 2013**] H. An, R. Hascoët, V. M. Kaspi, A. M. Beloborodov, F. Dufour, E. V. Gotthelf, R. Archibald, M. Bachetti, S. E. Boggs, F. E. Christensen, W. W. Craig, B. W. Greffenstette, C. J. Hailey, F. A. Harrison, T. Kitaguchi, C. Kouveliotou, K. K. Madsen, C. B. Markwardt, D. Stern, J. K. Vogel and W. W. Zhang, ‘NuSTAR Observations of Magnetar 1E 1841-045’. *ApJ*, December 2013, volume 779, 163, doi:10.1088/0004-637X/779/2/163, arXiv:1310.6221.

[**Andersson et al. 2011**] N. Andersson, V. Ferrari, D. I. Jones, K. D. Kokkotas, B. Krishnan, J. S. Read, L. Rezzolla and B. Zink, 'Gravitational waves from neutron stars: promises and challenges'. *General Relativity and Gravitation*, February 2011, volume 43, 409–436, doi:10.1007/s10714-010-1059-4, arXiv:0912.0384.

[**Antoniadis et al. 2013**] J. Antoniadis, P. C. C. Freire, N. Wex, T. M. Tauris, R. S. Lynch, M. H. van Kerkwijk, M. Kramer, C. Bassa, V. S. Dhillon, T. Driebe, J. W. T. Hessels, V. M. Kaspi, V. I. Kondratiev, N. Langer, T. R. Marsh, M. A. McLaughlin, T. T. Pennucci, S. M. Ransom, I. H. Stairs, J. van Leeuwen, J. P. W. Verbiest and D. G. Whelan, 'A Massive Pulsar in a Compact Relativistic Binary'. *Science*, April 2013, volume 340, 448, doi:10.1126/science.1233232, arXiv:1304.6875.

[**Archibald et al. 2016**] R. F. Archibald, E. V. Gotthelf, R. D. Ferdman, V. M. Kaspi, S. Guillot, F. A. Harrison, E. F. Keane, M. J. Pivovaroff, D. Stern, S. P. Tendulkar and J. A. Tomsick, 'A High Braking Index for a Pulsar'. *ApJLett*, March 2016, volume 819, L16, doi:10.3847/2041-8205/819/1/L16, arXiv:1603.00305.

[**Armaza et al. 2015**] C. Armaza, A. Reisenegger and J. Alejandro Valdivia, 'On Magnetic Equilibria in Barotropic Stars'. *ApJ*, April 2015, volume 802, 121, doi:10.1088/0004-637X/802/2/121, arXiv:1412.1524.

[**Armaza et al. 2014**] C. Armaza, A. Reisenegger, J. A. Valdivia and P. Marchant, 'Magnetohydrodynamic equilibria in barotropic stars'. In P. Petit, M. Jardine and H. C. Spruit, editors, *Magnetic Fields throughout Stellar Evolution*, volume 302 of *IAU Symposium* (2014) pages 419–422, doi:10.1017/S1743921314002646, arXiv:1305.0592.

[**Arnowitt et al. 1962**] R. L. Arnowitt, S. Deser and C. W. Misner, *Canonical analysis of general relativity*, page 127 (1962).

[**Arons and Scharlemann 1979**] J. Arons and E. T. Scharlemann, 'Pair formation above pulsar polar caps - Structure of the low altitude acceleration zone'. *ApJ*, August 1979, volume 231, 854–879, doi:10.1086/157250.

[**Arras et al. 2004**] P. Arras, A. Cumming and C. Thompson, 'Magnetars: Time Evolution, Superfluid Properties, and the Mechanism of Magnetic Field Decay'. *ApJLett*, June 2004, volume 608, L49–L52, doi:10.1086/422337, arXiv:astro-ph/0401561.

[**Asai et al. 2016**] H. Asai, U. Lee and S. Yoshida, 'Non-axisymmetric magnetic modes of neutron stars with purely poloidal magnetic fields'. *MNRAS*, January 2016, volume 455, 2228–2241, doi:10.1093/mnras/stv2368, arXiv:1507.00314.

[**Asseo and Khechinashvili 2002**] E. Asseo and D. Khechinashvili, 'The role of multipolar magnetic fields in pulsar magnetospheres'. *MNRAS*, August 2002, volume 334, 743–759, doi:10.1046/j.1365-8711.2002.05481.x, arXiv:astro-ph/0203129.

[**Astashenok et al. 2015**] A. V. Astashenok, S. Capozziello and S. D. Odintsov, 'Magnetic neutron stars in f(R) gravity'. *Ap&SS*, February 2015, volume 355, 333–341, doi:10.1007/s10509-014-2182-6, arXiv:1405.6663.

[**Bai and Spitkovsky 2010**] X.-N. Bai and A. Spitkovsky, 'Uncertainties of Modeling Gamma-ray Pulsar Light Curves Using Vacuum Dipole Magnetic Field'. *ApJ*, June 2010, volume 715, 1270–1281, doi:10.1088/0004-637X/715/2/1270, arXiv:0910.5740.

[**Bakirova and Folomeev 2016**] E. Bakirova and V. Folomeev, 'Dipole magnetic field of neutron stars in f(R) gravity'. *General Relativity and Gravitation*, October 2016, volume 48, 135, doi:10.1007/s10714-016-2127-1, arXiv:1603.01936.

[**Basak and Rao 2013**] R. Basak and A. R. Rao, 'Pulse-wise Amati correlation in Fermi gamma-ray bursts'. *MNRAS*, December 2013, volume 436, 3082–3088, doi:10.1093/mnras/stt1790, arXiv:1309.5233.

[**Baumgarte et al. 1997**] T. W. Baumgarte, G. B. Cook, M. A. Scheel, S. L. Shapiro and S. A. Teukolsky, 'Binary Neutron Stars in General Relativity: Quasiequilibrium Models'. *Physical Review Letters*, August 1997, volume 79, 1182–1185, doi:10.1103/PhysRevLett.79.1182, arXiv:gr-qc/9704024.

[**Baumgarte et al. 1998**] T. W. Baumgarte, G. B. Cook, M. A. Scheel, S. L. Shapiro and S. A. Teukolsky, ‘General relativistic models of binary neutron stars in quasiequilibrium’. *Phys. Rev. D*, June 1998, volume 57, 7299–7311, doi:10.1103/PhysRevD.57.7299, arXiv:gr-qc/9709026.

[**Baumgarte and Shapiro 1999**] T. W. Baumgarte and S. L. Shapiro, ‘Evolution of Rotating Supermassive Stars to the Onset of Collapse’. *ApJ*, December 1999, volume 526, 941–952, doi:10.1086/308006, arXiv:astro-ph/9909237.

[**Baumgarte and Shapiro 2003**] T. W. Baumgarte and S. L. Shapiro, ‘General Relativistic Magnetohydrodynamics for the Numerical Construction of Dynamical Spacetimes’. *ApJ*, March 2003, volume 585, 921–929, doi:10.1086/346103, arXiv:astro-ph/0211340.

[**Baumgarte and Shapiro 2010**] T. W. Baumgarte and S. L. Shapiro, *Numerical Relativity: Solving Einstein’s Equations on the Computer* (2010).

[**Becker and Pavlov 2002**] W. Becker and G. G. Pavlov, ‘The Milky Way - Pulsars and Isolated Neutron Stars’. *ArXiv Astrophysics e-prints*, August 2002, arXiv:astro-ph/0208356.

[**Beloborodov 2011**] A. M. Beloborodov, ‘Activated Magnetospheres of Magnetars’. In D. F. Torres and N. Rea, editors, *High-Energy Emission from Pulsars and their Systems* (2011) page 299, doi:10.1007/978-3-642-17251-9_24, arXiv:1008.4388.

[**Beloborodov 2013**] A. M. Beloborodov, ‘On the Mechanism of Hard X-Ray Emission from Magnetars’. *ApJ*, January 2013, volume 762, 13, doi:10.1088/0004-637X/762/1/13, arXiv:1201.0664.

[**Beloborodov and Levin 2014**] A. M. Beloborodov and Y. Levin, ‘Thermoplastic Waves in Magnetars’. *ApJLett*, October 2014, volume 794, L24, doi:10.1088/2041-8205/794/2/L24, arXiv:1406.4850.

[**Beloborodov and Thompson 2007**] A. M. Beloborodov and C. Thompson, ‘Magnetar corona’. *Ap&SS*, April 2007, volume 308, 631–639, doi:10.1007/s10509-007-9318-x, arXiv:astro-ph/0608372.

[**Belyaev 2015**] M. A. Belyaev, ‘Dissipation, energy transfer, and spin-down luminosity in 2.5D PIC simulations of the pulsar magnetosphere’. *MNRAS*, May 2015, volume 449, 2759–2767, doi:10.1093/mnras/stv468, arXiv:1412.2819.

[**Bera and Bhattacharya 2015**] P. Bera and D. Bhattacharya, ‘Mass-Radius Relation of Strongly Magnetized White Dwarfs: Dependence on Field Geometry, GR effects and Electrostatic Corrections to the EOS’. *ArXiv e-prints*, August 2015, arXiv:1508.05521.

[**Bernardini 2015**] M. G. Bernardini, ‘Gamma-ray bursts and magnetars: Observational signatures and predictions’. *Journal of High Energy Astrophysics*, September 2015, volume 7, 64–72, doi:10.1016/j.jheap.2015.05.003.

[**Bernardini et al. 2013**] M. G. Bernardini, S. Campana, G. Ghisellini, P. D’Avanzo, D. Burlon, S. Covino, G. Ghirlanda, A. Melandri, R. Salvaterra, S. D. Vergani, V. D’Elia, D. Fugazza, B. Sbarufatti and G. Tagliaferri, ‘How to Switch a Gamma-Ray Burst On and Off through a Magnetar’. *ApJ*, September 2013, volume 775, 67, doi:10.1088/0004-637X/775/1/67, arXiv:1306.0013.

[**Bernardini et al. 2014**] M. G. Bernardini, S. Campana, G. Ghisellini, P. D’Avanzo, G. Calderone, S. Covino, G. Cusumano, G. Ghirlanda, V. La Parola, A. Maselli, A. Melandri, R. Salvaterra, D. Burlon, V. D’Elia, D. Fugazza, B. Sbarufatti, S. D. Vergani and G. Tagliaferri, ‘A magnetar powering the ordinary monster GRB 130427A?’ *MNRAS*, March 2014, volume 439, L80–L84, doi:10.1093/mnrasl/slu003, arXiv:1401.1972.

[**Bernuzzi and Hilditch 2010**] S. Bernuzzi and D. Hilditch, ‘Constraint violation in free evolution schemes: Comparing the BSSNOK formulation with a conformal decomposition of the Z4 formulation’. *Phys. Rev. D*, April 2010, volume 81(8), 084003, doi:10.1103/PhysRevD.81.084003, arXiv:0912.2920.

[**Bocquet et al. 1995**] M. Bocquet, S. Bonazzola, E. Gourgoulhon and J. Novak, ‘Rotating neutron star models with a magnetic field.’ *A&A*, September 1995, volume 301, 757, arXiv:gr-qc/9503044.

[**Bombaci et al. 2016**] I. Bombaci, D. Logoteta, I. Vidaña and C. Providência, ‘Quark matter nucleation in neutron stars and astrophysical implications’. *European Physical Journal A*, March 2016, volume 52, 58, doi:10.1140/epja/i2016-16058-5, arXiv:1601.04559.

[**Bona et al. 2003**] C. Bona, T. Ledvinka, C. Palenzuela and M. Žáček, ‘General-covariant evolution formalism for numerical relativity’. *Phys. Rev. D*, May 2003, volume 67(10), 104005, doi:10.1103/PhysRevD.67.104005, arXiv:gr-qc/0302083.

[**Bonanno et al. 2003**] A. Bonanno, L. Rezzolla and V. Urpin, ‘Mean-field dynamo action in protoneutron stars’. *A&A*, October 2003, volume 410, L33–L36, doi:10.1051/0004-6361:20031459, arXiv:astro-ph/0309783.

[**Bonazzola and Gourgoulhon 1996**] S. Bonazzola and E. Gourgoulhon, ‘Gravitational waves from pulsars: emission by the magnetic-field-induced distortion.’ *A&A*, August 1996, volume 312, 675–690, arXiv:astro-ph/9602107.

[**Bonazzola et al. 2004**] S. Bonazzola, E. Gourgoulhon, P. Grandclément and J. Novak, ‘Constrained scheme for the Einstein equations based on the Dirac gauge and spherical coordinates’. *Phys. Rev. D*, November 2004, volume 70(10), 104007, doi:10.1103/PhysRevD.70.104007, arXiv:gr-qc/0307082.

[**Bonazzola et al. 1999**] S. Bonazzola, E. Gourgoulhon and J.-A. Marck, ‘Numerical Models of Irrotational Binary Neutron Stars in General Relativity’. *Physical Review Letters*, February 1999, volume 82, 892–895, doi:10.1103/PhysRevLett.82.892, arXiv:gr-qc/9810072.

[**Bonazzola et al. 1993**] S. Bonazzola, E. Gourgoulhon, M. Salgado and J. A. Marck, ‘Axisymmetric rotating relativistic bodies: A new numerical approach for “exact” solutions’. *A&A*, November 1993, volume 278, 421–443.

[**Bonazzola et al. 2015**] S. Bonazzola, F. Mottez and J. Heyvaerts, ‘General solution for the vacuum electromagnetic field in the surroundings of a rotating star’. *A&A*, January 2015, volume 573, A51, doi:10.1051/0004-6361/201424659.

[**Borghese et al. 2015**] A. Borghese, N. Rea, F. Coti Zelati, A. Tiengo and R. Turolla, ‘Discovery of a Strongly Phase-variable Spectral Feature in the Isolated Neutron Star RX J0720.4-3125’. *ApJLett*, July 2015, volume 807, L20, doi:10.1088/2041-8205/807/1/L20, arXiv:1506.04206.

[**Braithwaite 2006a**] J. Braithwaite, ‘A differential rotation driven dynamo in a stably stratified star’. *A&A*, April 2006a, volume 449, 451–460, doi:10.1051/0004-6361:20054241, arXiv:astro-ph/0509693.

[**Braithwaite 2006b**] J. Braithwaite, ‘The stability of toroidal fields in stars’. *A&A*, July 2006b, volume 453, 687–698, doi:10.1051/0004-6361:20041282, arXiv:astro-ph/0512182.

[**Braithwaite 2007**] J. Braithwaite, ‘The stability of poloidal magnetic fields in rotating stars’. *A&A*, July 2007, volume 469, 275–284, doi:10.1051/0004-6361:20065903, arXiv:0705.0185.

[**Braithwaite 2009**] J. Braithwaite, ‘Axisymmetric magnetic fields in stars: relative strengths of poloidal and toroidal components’. *MNRAS*, August 2009, volume 397, 763–774, doi:10.1111/j.1365-2966.2008.14034.x, arXiv:0810.1049.

[**Braithwaite and Nordlund 2006**] J. Braithwaite and Å. Nordlund, ‘Stable magnetic fields in stellar interiors’. *A&A*, May 2006, volume 450, 1077–1095, doi:10.1051/0004-6361:20041980, arXiv:astro-ph/0510316.

[**Braithwaite and Spruit 2006**] J. Braithwaite and H. C. Spruit, ‘Evolution of the magnetic field in magnetars’. *A&A*, May 2006, volume 450, 1097–1106, doi:10.1051/0004-6361:20041981, arXiv:astro-ph/0510287.

[**Braithwaite and Spruit 2015**] J. Braithwaite and H. C. Spruit, ‘Magnetic fields in non-convective regions of stars’. *ArXiv e-prints*, October 2015, arXiv:1510.03198.

[**Bucciantini and Del Zanna 2011**] N. Bucciantini and L. Del Zanna, ‘General relativistic magnetohydrodynamics in axisymmetric dynamical spacetimes: the X-ECHO code’. *A&A*, April 2011, volume 528, A101, doi:10.1051/0004-6361/201015945, arXiv:1010.3532.

[**Bucciantini and Del Zanna 2013**] N. Bucciantini and L. Del Zanna, ‘A fully covariant mean-field dynamo closure for numerical 3 + 1 resistive GRMHD’. *MNRAS*, January 2013, volume 428, 71–85, doi:10.1093/mnras/sts005, arXiv:1205.2951.

[**Bucciantini et al. 2012**] N. Bucciantini, B. D. Metzger, T. A. Thompson and E. Quataert, ‘Short gamma-ray bursts with extended emission from magnetar birth: jet formation and collimation’. *MNRAS*, January 2012, volume 419, 1537–1545, doi:10.1111/j.1365-2966.2011.19810.x, arXiv:1106.4668.

[**Bucciantini et al. 2014**] N. Bucciantini, A. G. Pili and L. Del Zanna, ‘XNS: Axisymmetric equilibrium configuration of neutron stars’. Astrophysics Source Code Library, February 2014, arXiv:1402.020.

[**Bucciantini et al. 2015a**] N. Bucciantini, A. G. Pili and L. Del Zanna, ‘Modeling the structure of magnetic fields in Neutron Stars: from the interior to the magnetosphere’. *ArXiv e-prints*, November 2015a, arXiv:1511.02719.

[**Bucciantini et al. 2015b**] N. Bucciantini, A. G. Pili and L. Del Zanna, ‘The role of currents distribution in general relativistic equilibria of magnetized neutron stars’. *MNRAS*, March 2015b, volume 447, 3278–3290, doi:10.1093/mnras/stu2689, arXiv:1412.5347.

[**Bucciantini et al. 2009**] N. Bucciantini, E. Quataert, B. D. Metzger, T. A. Thompson, J. Arons and L. Del Zanna, ‘Magnetized relativistic jets and long-duration GRBs from magnetar spin-down during core-collapse supernovae’. *MNRAS*, July 2009, volume 396, 2038–2050, doi:10.1111/j.1365-2966.2009.14940.x, arXiv:0901.3801.

[**Burrows et al. 2007**] A. Burrows, L. Dessart, E. Livne, C. D. Ott and J. Murphy, ‘Simulations of Magnetically Driven Supernova and Hypernova Explosions in the Context of Rapid Rotation’. *ApJ*, July 2007, volume 664, 416–434, doi:10.1086/519161, arXiv:astro-ph/0702539.

[**Burrows and Lattimer 1986**] A. Burrows and J. M. Lattimer, ‘The birth of neutron stars’. *ApJ*, August 1986, volume 307, 178–196, doi:10.1086/164405.

[**Camelio et al. 2016**] G. Camelio, L. Gualtieri, J. A. Pons and V. Ferrari, ‘Spin evolution of a protoneutron star’. *Phys. Rev. D*, July 2016, volume 94(2), 024008, doi:10.1103/PhysRevD.94.024008, arXiv:1601.02945.

[**Cameron 1959**] A. G. Cameron, ‘Neutron Star Models.’ *ApJ*, November 1959, volume 130, 884, doi:10.1086/146780.

[**Cardall et al. 2001**] C. Y. Cardall, M. Prakash and J. M. Lattimer, ‘Effects of Strong Magnetic Fields on Neutron Star Structure’. *ApJ*, June 2001, volume 554, 322–339, doi:10.1086/321370, arXiv:astro-ph/0011148.

[**Carter 1970**] B. Carter, ‘The commutation property of a stationary, axisymmetric system’. *Communications in Mathematical Physics*, September 1970, volume 17, 233–238, doi:10.1007/BF01647092.

[**Carter 1973**] B. Carter, ‘Stationary-Axisymmetru, Circularity and the Papapetrou Theorem.’ In C. Dewitt and B. S. Dewitt, editors, *Black Holes (Les Astres Occlus)* (1973) pages 57–214.

[**Cerdá-Durán et al. 2005**] P. Cerdá-Durán, G. Faye, H. Dimmelmeier, J. A. Font, J. M. Ibáñez, E. Müller and G. Schäfer, ‘CFC+: improved dynamics and gravitational waveforms from relativistic core collapse simulations’. *A&A*, September 2005, volume 439, 1033–1055, doi:10.1051/0004-6361:20042602, arXiv:astro-ph/0412611.

[**Cerdá-Durán et al. 2008**] P. Cerdá-Durán, J. A. Font, L. Antón and E. Müller, ‘A new general relativistic magnetohydrodynamics code for dynamical spacetimes’. *A&A*, December 2008, volume 492, 937–953, doi:10.1051/0004-6361:200810086, arXiv:0804.4572.

[**Chadwick 1932**] J. Chadwick, ‘Possible Existence of a Neutron’. *Nature*, February 1932, volume 129, 312, doi:10.1038/129312a0.

[**Chamel and Haensel 2008**] N. Chamel and P. Haensel, ‘Physics of Neutron Star Crusts’. *Living Reviews in Relativity*, December 2008, volume 11, 10, doi:10.12942/lrr-2008-10, arXiv:0812.3955.

[**Chamel et al. 2015**] N. Chamel, Z. K. Stoyanov, L. M. Mihailov, Y. D. Mutafchieva, R. L. Pavlov and C. J. Velchev, ‘Role of Landau quantization on the neutron-drip transition in magnetar crusts’. *Phys. Rev. C*, June 2015, volume 91(6), 065801, doi:10.1103/PhysRevC.91.065801.

[**Chandrasekhar and Fermi 1953**] S. Chandrasekhar and E. Fermi, ‘Problems of Gravitational Stability in the Presence of a Magnetic Field.’ *ApJ*, July 1953, volume 118, 116, doi:10.1086/145732.

[**Chen and Beloborodov 2014**] A. Y. Chen and A. M. Beloborodov, ‘Electrodynamics of Axisymmetric Pulsar Magnetosphere with Electron-Positron Discharge: A Numerical Experiment’. *ApJLett*, November 2014, volume 795, L22, doi:10.1088/2041-8205/795/1/L22, arXiv:1406.7834.

[**Cheng et al. 1986**] K. S. Cheng, C. Ho and M. Ruderman, ‘Energetic radiation from rapidly spinning pulsars. I - Outer magnetosphere gaps. II - VELA and Crab’. *ApJ*, January 1986, volume 300, 500–539, doi:10.1086/163829.

[**Cheoun et al. 2013**] M.-K. Cheoun, C. Deliduman, C. Güngör, V. Keleş, C. Y. Ryu, T. Kajino and G. J. Mathews, ‘Neutron stars in a perturbative f(R) gravity model with strong magnetic fields’. *JCAP*, October 2013, volume 10, 021, doi:10.1088/1475-7516/2013/10/021, arXiv:1304.1871.

[**Chincarini et al. 2007**] G. Chincarini, A. Moretti, P. Romano, A. D. Falcone, D. Morris, J. Racusin, S. Campana, S. Covino, C. Guidorzi, G. Tagliaferri, D. N. Burrows, C. Pagani, M. Stroh, D. Grupe, M. Capalbi, G. Cusumano, N. Gehrels, P. Giommi, V. La Parola, V. Mangano, T. Mineo, J. A. Nousek, P. T. O’Brien, K. L. Page, M. Perri, E. Troja, R. Willingale and B. Zhang, ‘The First Survey of X-Ray Flares from Gamma-Ray Bursts Observed by Swift: Temporal Properties and Morphology’. *ApJ*, December 2007, volume 671, 1903–1920, doi:10.1086/521591, arXiv:astro-ph/0702371.

[**Chiu and Salpeter 1964**] H.-Y. Chiu and E. E. Salpeter, ‘Surface X-Ray Emission from Neutron Stars’. *Physical Review Letters*, April 1964, volume 12, 413–415, doi:10.1103/PhysRevLett.12.413.

[**Ciolfi 2014**] R. Ciolfi , ‘Magnetic field instabilities in neutron stars’. *Astronomische Nachrichten*, March 2014, volume 335, 285–290, doi:10.1002/asna.201312033, arXiv:1401.5276.

[**Ciolfi et al. 2010**] R. Ciolfi, V. Ferrari and L. Gualtieri, ‘Structure and deformations of strongly magnetized neutron stars with twisted-torus configurations’. *MNRAS*, August 2010, volume 406, 2540–2548, doi:10.1111/j.1365-2966.2010.16847.x, arXiv:1003.2148.

[**Ciolfi et al. 2009**] R. Ciolfi, V. Ferrari, L. Gualtieri and J. A. Pons, ‘Relativistic models of magnetars: the twisted torus magnetic field configuration’. *MNRAS*, August 2009, volume 397, 913–924, doi:10.1111/j.1365-2966.2009.14990.x, arXiv:0903.0556.

[**Ciolfi et al. 2011**] R. Ciolfi, S. K. Lander, G. M. Manca and L. Rezzolla, ‘Instability-driven Evolution of Poloidal Magnetic Fields in Relativistic Stars’. *ApJLett*, July 2011, volume 736, L6, doi:10.1088/2041-8205/736/1/L6, arXiv:1105.3971.

[**Ciolfi and Rezzolla 2012**] R. Ciolfi and L. Rezzolla, ‘Poloidal-field Instability in Magnetized Relativistic Stars’. *ApJ*, November 2012, volume 760, 1, doi:10.1088/0004-637X/760/1/1, arXiv:1206.6604.

[**Ciolfi and Rezzolla 2013**] R. Ciolfi and L. Rezzolla, ‘Twisted-torus configurations with large toroidal magnetic fields in relativistic stars’. *MNRAS*, August 2013, volume 435, L43–L47, doi:10.1093/mnrasl/slt092, arXiv:1306.2803.

[**Ciolfi and Siegel 2015**] R. Ciolfi and D. M. Siegel, ‘Short Gamma-Ray Bursts in the ”Time-reversal” Scenario’. *ApJLett*, January 2015, volume 798, L36, doi:10.1088/2041-8205/798/2/L36, arXiv:1411.2015.

[**Clark et al. 2005**] J. S. Clark, I. Negueruela, P. A. Crowther and S. P. Goodwin, ‘On the massive stellar population of the super star cluster Westerlund 1’. *A&A*, May 2005, volume 434, 949–969, doi:10.1051/0004-6361:20042413, arXiv:astro-ph/0504342.

[**Clark et al. 2014**] J. S. Clark, B. W. Ritchie, F. Najarro, N. Langer and I. Negueruela, ‘A VLT/FLAMES survey for massive binaries in Westerlund 1. IV. Wd1-5 - binary product and a pre-supernova companion for the magnetar CXOU J1647-45?’ *A&A*, May 2014, volume 565, A90, doi:10.1051/0004-6361/201321771, arXiv:1405.3109.

[**Comella et al. 1969**] J. M. Comella, H. D. Craft, R. V. E. Lovelace and J. M. Sutton, ‘Crab Nebula Pulsar NP 0532’. *Nature*, February 1969, volume 221, 453–454, doi:10.1038/221453a0.

[**Contopoulos et al. 1999**] I. Contopoulos, D. Kazanas and C. Fendt, ‘The Axisymmetric Pulsar Magnetosphere’. *ApJ*, January 1999, volume 511, 351–358, doi:10.1086/306652, arXiv:astro-ph/9903049.

[**Cordero-Carrión et al. 2009**] I. Cordero-Carrión, P. Cerdá-Durán, H. Dimmelmeier, J. L. Jaramillo, J. Novak and E. Gourgoulhon, ‘Improved constrained scheme for the Einstein equations: An approach to the uniqueness issue’. *Phys. Rev. D*, January 2009, volume 79(2), 024017, doi:10.1103/PhysRevD.79.024017, arXiv:0809.2325.

[**Counselman and Shapiro 1968**] C. C. Counselman, III and I. I. Shapiro, ‘Scientific Uses of Pulsars’. *Science*, October 1968, volume 162, 352–355, doi:10.1126/science.162.3851.352-a.

[**Cutler 2002**] C. Cutler, ‘Gravitational waves from neutron stars with large toroidal B fields’. *Phys. Rev. D*, October 2002, volume 66(8), 084025, doi:10.1103/PhysRevD.66.084025, arXiv:gr-qc/0206051.

[**D’Aì et al. 2016**] A. D’Aì, P. A. Evans, D. N. Burrows, N. P. M. Kuin, D. A. Kann, S. Campana, A. Maselli, P. Romano, G. Cusumano, V. La Parola, S. D. Barthelmy, A. P. Beardmore, S. B. Cenko, M. De Pasquale, N. Gehrels, J. Greiner, J. A. Kennea, S. Klose, A. Melandri, J. A. Nousek, J. P. Osborne, D. M. Palmer, B. Sbarufatti, P. Schady, M. H. Siegel, G. Tagliaferri, R. Yates and S. Zane, ‘Evidence for the magnetar nature of 1E 161348-5055 in RCW 103’. *MNRAS*, December 2016, volume 463, 2394–2404, doi:10.1093/mnras/stw2023, arXiv:1607.04264.

[**Dai et al. 2006**] Z. G. Dai, X. Y. Wang, X. F. Wu and B. Zhang, ‘X-ray Flares from Postmerger Millisecond Pulsars’. *Science*, February 2006, volume 311, 1127–1129, doi:10.1126/science.1123606, arXiv:astro-ph/0602525.

[**Dall’Osso et al. 2015**] S. Dall’Osso, B. Giacomazzo, R. Perna and L. Stella, ‘Gravitational Waves from Massive Magnetars Formed in Binary Neutron Star Mergers’. *ApJ*, January 2015, volume 798, 25, doi:10.1088/0004-637X/798/1/25, arXiv:1408.0013.

[**Dall’Osso et al. 2017**] S. Dall’Osso, R. Perna, T. L. Tanaka and R. Margutti, ‘Flares in gamma-ray bursts: disc fragmentation and evolution’. *MNRAS*, February 2017, volume 464, 4399–4407, doi:10.1093/mnras/stw2695, arXiv:1610.05302.

[**Dall’Osso et al. 2009**] S. Dall’Osso, S. N. Shore and L. Stella, ‘Early evolution of newly born magnetars with a strong toroidal field’. *MNRAS*, October 2009, volume 398, 1869–1885, doi:10.1111/j.1365-2966.2008.14054.x, arXiv:0811.4311.

[**Dall’Osso et al. 2011**] S. Dall’Osso, G. Stratta, D. Guetta, S. Covino, G. De Cesare and L. Stella, ‘Gamma-ray bursts afterglows with energy injection from a spinning down neutron star’. *A&A*, February 2011, volume 526, A121, doi:10.1051/0004-6361/201014168, arXiv:1004.2788.

[**Darmois 1927**] G. Darmois, *Les équations de la gravitation einsteinienne* (Gauthier-Villars 1927), URL `http://eudml.org/doc/192556`.

[**Das and Mukhopadhyay 2015**] U. Das and B. Mukhopadhyay, ‘GRMHD formulation of highly super-Chandrasekhar magnetized white dwarfs: stable configurations of non-spherical white dwarfs’. *JCAP*, May 2015, volume 5, 016, doi:10.1088/1475-7516/2015/05/016, arXiv:1411.5367.

[**Das and Mukhopadhyay 2016**] U. Das and B. Mukhopadhyay, ‘Highly super-Chandrasekhar white dwarfs in an extensive GRMHD framework’. *ArXiv e-prints*, February 2016, arXiv:1603.00115.

[**Del Zanna et al. 2007**] L. Del Zanna, O. Zanotti, N. Bucciantini and P. Londrillo, 'ECHO: a Eulerian conservative high-order scheme for general relativistic magnetohydrodynamics and magnetodynamics'. *A&A*, October 2007, volume 473, 11–30, doi:10.1051/0004-6361:20077093, arXiv:0704.3206.

[**Demorest et al. 2010**] P. B. Demorest, T. Pennucci, S. M. Ransom, M. S. E. Roberts and J. W. T. Hessels, 'A two-solar-mass neutron star measured using Shapiro delay'. *Nature*, October 2010, volume 467, 1081–1083, doi:10.1038/nature09466, arXiv:1010.5788.

[**Deutsch 1955**] A. J. Deutsch, 'The electromagnetic field of an idealized star in rigid rotation in vacuo'. *Annales d'Astrophysique*, January 1955, volume 18, 1.

[**Dimmelmeier et al. 2002a**] H. Dimmelmeier, J. A. Font and E. Müller, 'Numerical Studies of Rotational Core Collapse in Axisymmetry Using the Conformally Flat Metric Approach'. In V. G. Gurzadyan, R. T. Jantzen and R. Ruffini, editors, *The Ninth Marcel Grossmann Meeting* (2002a) pages 1695–1696, doi:10.1142/9789812777386_0357.

[**Dimmelmeier et al. 2002b**] H. Dimmelmeier, J. A. Font and E. Müller, 'Relativistic simulations of rotational core collapse II. Collapse dynamics and gravitational radiation'. *A&A*, October 2002b, volume 393, 523–542, doi:10.1051/0004-6361:20021053, arXiv:astro-ph/0204289.

[**Dimmelmeier et al. 2006**] H. Dimmelmeier, N. Stergioulas and J. A. Font, 'Non-linear axisymmetric pulsations of rotating relativistic stars in the conformal flatness approximation'. *MNRAS*, June 2006, volume 368, 1609–1630, doi:10.1111/j.1365-2966.2006.10274.x, arXiv:astro-ph/0511394.

[**Dirac 1958**] P. A. M. Dirac, 'The Theory of Gravitation in Hamiltonian Form'. *Proceedings of the Royal Society of London Series A*, August 1958, volume 246, 333–343, doi:10.1098/rspa.1958.0142.

[**Drago et al. 2016a**] A. Drago, A. Lavagno, B. D. Metzger and G. Pagliara, 'Quark deconfinement and the duration of short gamma-ray bursts'. *Phys. Rev. D*, May 2016a, volume 93(10), 103001, doi:10.1103/PhysRevD.93.103001, arXiv:1510.05581.

[**Drago et al. 2014**] A. Drago, A. Lavagno and G. Pagliara, 'Can very compact and very massive neutron stars both exist?' *Phys. Rev. D*, February 2014, volume 89(4), 043014, doi:10.1103/PhysRevD.89.043014, arXiv:1309.7263.

[**Drago et al. 2016b**] A. Drago, A. Lavagno, G. Pagliara and D. Pigato, 'The scenario of two families of compact stars. Part 1. Equations of state, mass-radius relations and binary systems'. *European Physical Journal A*, February 2016b, volume 52, 40, doi:10.1140/epja/i2016-16040-3, arXiv:1509.02131.

[**Drago et al. 2007**] A. Drago, A. Lavagno and I. Parenti, 'Burning of a Hadronic Star into a Quark or a Hybrid Star'. *ApJ*, April 2007, volume 659, 1519–1535, doi:10.1086/512112, arXiv:astro-ph/0512652.

[**Drago and Pagliara 2015**] A. Drago and G. Pagliara, 'Combustion of a hadronic star into a quark star: The turbulent and the diffusive regimes'. *Phys. Rev. C*, October 2015, volume 92(4), 045801, doi:10.1103/PhysRevC.92.045801, arXiv:1506.08337.

[**Drago and Pagliara 2016**] A. Drago and G. Pagliara, 'The scenario of two families of compact stars. Part 2: Transition from hadronic to quark matter and explosive phenomena'. *European Physical Journal A*, February 2016, volume 52, 41, doi:10.1140/epja/i2016-16041-2, arXiv:1509.02134.

[**Duncan and Thompson 1992**] R. C. Duncan and C. Thompson, 'Formation of very strongly magnetized neutron stars - Implications for gamma-ray bursts'. *ApJLett*, June 1992, volume 392, L9–L13, doi:10.1086/186413.

[**Dyks and Rudak 2003**] J. Dyks and B. Rudak, 'Two-Pole Caustic Model for High-Energy Light Curves of Pulsars'. *ApJ*, December 2003, volume 598, 1201–1206, doi:10.1086/379052, arXiv:astro-ph/0303006.

[**Elfritz et al. 2016**] J. G. Elfritz, J. A. Pons, N. Rea, K. Glampedakis and D. Viganò, 'Simulated magnetic field expulsion in neutron star cores'. *MNRAS*, March 2016, volume 456, 4461–4474, doi:10.1093/mnras/stv2963, arXiv:1512.07151.

[**Fantina et al. 2016**] A. F. Fantina, N. Chamel, Y. D. Mutafchieva, Z. K. Stoyanov, L. M. Mihailov and R. L. Pavlov, ‘Role of the symmetry energy on the neutron-drip transition in accreting and nonaccreting neutron stars’. *Phys. Rev. C*, January 2016, volume 93(1), 015801, doi:10.1103/PhysRevC.93.015801.

[**Ferdman et al. 2013**] R. D. Ferdman, I. H. Stairs, M. Kramer, R. P. Breton, M. A. McLaughlin, P. C. C. Freire, A. Possenti, B. W. Stappers, V. M. Kaspi, R. N. Manchester and A. G. Lyne, ‘The Double Pulsar: Evidence for Neutron Star Formation without an Iron Core-collapse Supernova’. *ApJ*, April 2013, volume 767, 85, doi:10.1088/0004-637X/767/1/85, arXiv:1302.2914.

[**Fernández and Thompson 2007**] R. Fernández and C. Thompson, ‘Resonant Cyclotron Scattering in Three Dimensions and the Quiescent Nonthermal X-ray Emission of Magnetars’. *ApJ*, May 2007, volume 660, 615–640, doi:10.1086/511810, arXiv:astro-ph/0608281.

[**Ferrario et al. 2015**] L. Ferrario, A. Melatos and J. Zrake, ‘Magnetic Field Generation in Stars’. *Space Sci. Rev.*, October 2015, volume 191, 77–109, doi:10.1007/s11214-015-0138-y, arXiv:1504.08074.

[**Ferrario and Wickramasinghe 2006**] L. Ferrario and D. Wickramasinghe, ‘Modelling of isolated radio pulsars and magnetars on the fossil field hypothesis’. *MNRAS*, April 2006, volume 367, 1323–1328, doi:10.1111/j.1365-2966.2006.10058.x, arXiv:astro-ph/0601258.

[**Ferrario and Wickramasinghe 2008**] L. Ferrario and D. Wickramasinghe, ‘Origin and evolution of magnetars’. *MNRAS*, September 2008, volume 389, L66–L70, doi:10.1111/j.1745-3933.2008.00527.x, arXiv:0807.2106.

[**Ferraro 1954**] V. C. A. Ferraro, ‘On the Equilibrium of Magnetic Stars.’ *ApJ*, March 1954, volume 119, 407, doi:10.1086/145838.

[**Flowers and Ruderman 1977**] E. Flowers and M. A. Ruderman, ‘Evolution of pulsar magnetic fields’. *ApJ*, July 1977, volume 215, 302–310, doi:10.1086/155359.

[**Fourès-Bruhat (Choquet-Bruhat) 1952**] Y. Fourès-Bruhat (Choquet-Bruhat), ‘Théorème d’existence pour certains systèmes d’équations aux dérivées partielles non linéaires.’ *Acta Mathematica*, 1952, volume 88(141).

[**Franzon et al. 2016a**] B. Franzon, V. Dexheimer and S. Schramm, ‘Internal composition of proto-neutron stars under strong magnetic fields’. *Phys. Rev. D*, August 2016a, volume 94(4), 044018, doi:10.1103/PhysRevD.94.044018, arXiv:1606.04843.

[**Franzon et al. 2016b**] B. Franzon, R. O. Gomes and S. Schramm, ‘Effects of the quark-hadron phase transition on highly magnetized neutron stars’. *MNRAS*, November 2016b, volume 463, 571–579, doi:10.1093/mnras/stw1967, arXiv:1608.02845.

[**Franzon and Schramm 2015**] B. Franzon and S. Schramm, ‘Effects of strong magnetic fields and rotation on white dwarf structure’. *Phys. Rev. D*, October 2015, volume 92(8), 083006, doi:10.1103/PhysRevD.92.083006, arXiv:1507.05557.

[**Frieben and Rezzolla 2012**] J. Frieben and L. Rezzolla, ‘Equilibrium models of relativistic stars with a toroidal magnetic field’. *MNRAS*, December 2012, volume 427, 3406–3426, doi:10.1111/j.1365-2966.2012.22027.x, arXiv:1207.4035.

[**Fujisawa 2015**] K. Fujisawa, ‘Magnetized stars with differential rotation and a differential toroidal field’. *MNRAS*, July 2015, volume 450, 4016–4024, doi:10.1093/mnras/stv905, arXiv:1504.05961.

[**Fujisawa and Eriguchi 2013**] K. Fujisawa and Y. Eriguchi, ‘Coexistence of oppositely flowing multi-φ currents: key to large toroidal magnetic fields within stars’. *MNRAS*, June 2013, volume 432, 1245–1263, doi:10.1093/mnras/stt541, arXiv:1304.0549.

[**Fujisawa and Eriguchi 2015**] K. Fujisawa and Y. Eriguchi, ‘Appearance of the prolate and the toroidal magnetic field dominated stars: Analytic approach’. *PASJ*, June 2015, volume 67, 53, doi:10.1093/pasj/psv024, arXiv:1504.00713.

[**Fujisawa and Kisaka 2014**] K. Fujisawa and S. Kisaka, 'Magnetic field configurations of a magnetar throughout its interior and exterior - core, crust and magnetosphere'. *MNRAS*, December 2014, volume 445, 2777–2793, doi:10.1093/mnras/stu1911, arXiv:1409.4547.

[**Fujisawa et al. 2013**] K. Fujisawa, R. Takahashi, S. Yoshida and Y. Eriguchi, 'Counter effects of meridional flows and magnetic fields in stationary axisymmetric self-gravitating barotropes under the ideal MHD approximation: clear examples - toroidal configurations'. *MNRAS*, May 2013, volume 431, 1453–1469, doi:10.1093/mnras/stt275, arXiv:1304.0548.

[**Fujisawa et al. 2012**] K. Fujisawa, S. Yoshida and Y. Eriguchi, 'Axisymmetric and stationary structures of magnetized barotropic stars with extremely strong magnetic fields deep inside'. *MNRAS*, May 2012, volume 422, 434–448, doi:10.1111/j.1365-2966.2012.20614.x, arXiv:1204.5830.

[**Gajjar et al. 2012**] V. Gajjar, B. C. Joshi and M. Kramer, 'A survey of nulling pulsars using the Giant Meterwave Radio Telescope'. *MNRAS*, August 2012, volume 424, 1197–1205, doi:10.1111/j.1365-2966.2012.21296.x, arXiv:1205.2550.

[**Gamow 1937**] G. Gamow, *Structure of Atomic Nuclei and Nuclear Transformations* (Oxford University Press 1937).

[**Gamow 1938**] G. Gamow, 'Nuclear Energy Sources and Stellar Evolution'. *Physical Review*, April 1938, volume 53, 595–604, doi:10.1103/PhysRev.53.595.

[**Gao and Fan 2006**] W.-H. Gao and Y.-Z. Fan, 'Short-living Supermassive Magnetar Model for the Early X-ray Flares Following Short GRBs'. *Chinese Journal of Astronomy and Astrophysics*, October 2006, volume 6, 513–516, doi:10.1088/1009-9271/6/5/01, arXiv:astro-ph/0512646.

[**Ghezzi 2005**] C. R. Ghezzi, 'Relativistic structure, stability, and gravitational collapse of charged neutron stars'. *Phys. Rev. D*, November 2005, volume 72(10), 104017, doi:10.1103/PhysRevD.72.104017, arXiv:gr-qc/0510106.

[**Giacconi et al. 1962**] R. Giacconi, H. Gursky, F. R. Paolini and B. B. Rossi, 'Evidence for x Rays From Sources Outside the Solar System'. *Physical Review Letters*, December 1962, volume 9, 439–443, doi:10.1103/PhysRevLett.9.439.

[**Giacconi et al. 1964**] R. Giacconi, H. Gursky and J. R. Waters, 'Two Sources of Cosmic X-rays in Scorpius and Sagittarius'. *Nature*, December 1964, volume 204, 981–982, doi:10.1038/204981a0.

[**Giacomazzo and Perna 2013**] B. Giacomazzo and R. Perna, 'Formation of Stable Magnetars from Binary Neutron Star Mergers'. *ApJLett*, July 2013, volume 771, L26, doi:10.1088/2041-8205/771/2/L26, arXiv:1306.1608.

[**Giacomazzo et al. 2015**] B. Giacomazzo, J. Zrake, P. C. Duffell, A. I. MacFadyen and R. Perna, 'Producing Magnetar Magnetic Fields in the Merger of Binary Neutron Stars'. *ApJ*, August 2015, volume 809, 39, doi:10.1088/0004-637X/809/1/39, arXiv:1410.0013.

[**Giannios 2006**] D. Giannios, 'Flares in GRB afterglows from delayed magnetic dissipation'. *A&A*, August 2006, volume 455, L5–L8, doi:10.1051/0004-6361:20065578, arXiv:astro-ph/0606441.

[**Giannios et al. 2008**] D. Giannios, P. Mimica and M. A. Aloy, 'On the existence of a reverse shock in magnetized gamma-ray burst ejecta'. *A&A*, February 2008, volume 478, 747–753, doi:10.1051/0004-6361:20078931, arXiv:0711.1980.

[**Gilkis 2016**] A. Gilkis, 'Asymmetric core-collapse of rapidly-rotating massive star'. *ArXiv e-prints*, August 2016, arXiv:1608.05320.

[**Glampedakis et al. 2012a**] K. Glampedakis, N. Andersson and S. K. Lander, 'Hydromagnetic equilibrium in non-barotropic multifluid neutron stars'. *MNRAS*, February 2012a, volume 420, 1263–1272, doi:10.1111/j.1365-2966.2011.20112.x, arXiv:1106.6330.

[**Glampedakis et al. 2011**] K. Glampedakis, N. Andersson and L. Samuelsson, 'Magnetohydrodynamics of superfluid and superconducting neutron star cores'. *MNRAS*, January 2011, volume 410, 805–829, doi:10.1111/j.1365-2966.2010.17484.x, arXiv:1001.4046.

[**Glampedakis et al. 2012b**] K. Glampedakis, D. I. Jones and L. Samuelsson, 'Gravitational Waves from Color-Magnetic "Mountains" in Neutron Stars'. *Physical Review Letters*, August 2012b, volume 109(8), 081103, doi:10.1103/PhysRevLett.109.081103, arXiv:1204.3781.

[**Glampedakis et al. 2014**] K. Glampedakis, S. K. Lander and N. Andersson, 'The inside-out view on neutron-star magnetospheres'. *MNRAS*, January 2014, volume 437, 2–8, doi:10.1093/mnras/stt1814, arXiv:1306.6881.

[**Glampedakis and Lasky 2015**] K. Glampedakis and P. D. Lasky, 'Persistent crust-core spin lag in neutron stars'. *MNRAS*, June 2015, volume 450, 1638–1650, doi:10.1093/mnras/stv638, arXiv:1501.05473.

[**Glampedakis and Lasky 2016**] K. Glampedakis and P. D. Lasky, 'The freedom to choose neutron star magnetic field equilibria'. *MNRAS*, August 2016, doi:10.1093/mnras/stw2115, arXiv:1607.05576.

[**Gold 1968**] T. Gold, 'Rotating Neutron Stars as the Origin of the Pulsating Radio Sources'. *Nature*, May 1968, volume 218, 731–732, doi:10.1038/218731a0.

[**Goldreich and Julian 1969**] P. Goldreich and W. H. Julian, 'Pulsar Electrodynamics'. *ApJ*, August 1969, volume 157, 869, doi:10.1086/150119.

[**Gotthelf and Halpern 2008**] E. V. Gotthelf and J. P. Halpern, 'CCO Pulsars as Anti-Magnetars: Evidence of Neutron Stars Weakly Magnetized at Birth'. In C. Bassa, Z. Wang, A. Cumming and V. M. Kaspi, editors, *40 Years of Pulsars: Millisecond Pulsars, Magnetars and More*, volume 983 of *American Institute of Physics Conference Series* (2008) pages 320–324, doi:10.1063/1.2900174, arXiv:0711.1554.

[**Gotthelf et al. 2013**] E. V. Gotthelf, J. P. Halpern and J. Alford, 'The Spin-down of PSR J0821-4300 and PSR J1210-5226: Confirmation of Central Compact Objects as Anti-magnetars'. *ApJ*, March 2013, volume 765, 58, doi:10.1088/0004-637X/765/1/58, arXiv:1301.2717.

[**Gourgoulhon 2010**] E. Gourgoulhon, 'An introduction to the theory of rotating relativistic stars'. *ArXiv e-prints*, March 2010, arXiv:1003.5015.

[**Gourgoulhon 2012**] É. Gourgoulhon, *3+1 Formalism in General Relativity: Bases of Numerical Relativity*. Lecture Notes in Physics (Springer Berlin Heidelberg 2012), URL `http://www.springer.com/us/book/9783642245244`.

[**Gourgoulhon et al. 2011**] E. Gourgoulhon, C. Markakis, K. Uryū and Y. Eriguchi, 'Magnetohydrodynamics in stationary and axisymmetric spacetimes: A fully covariant approach'. *Phys. Rev. D*, May 2011, volume 83(10), 104007, doi:10.1103/PhysRevD.83.104007, arXiv:1101.3497.

[**Gourgouliatos et al. 2013**] K. N. Gourgouliatos, A. Cumming, A. Reisenegger, C. Armaza, M. Lyutikov and J. A. Valdivia, 'Hall equilibria with toroidal and poloidal fields: application to neutron stars'. *MNRAS*, September 2013, volume 434, 2480–2490, doi:10.1093/mnras/stt1195, arXiv:1305.6269.

[**Gourgouliatos et al. 2016**] K. N. Gourgouliatos, T. S. Wood and R. Hollerbach, 'Magnetic field evolution in magnetar crusts through three-dimensional simulations'. *Proceedings of the National Academy of Science*, April 2016, volume 113, 3944–3949, doi:10.1073/pnas.1522363113, arXiv:1604.01399.

[**Goussard et al. 1998**] J.-O. Goussard, P. Haensel and J. L. Zdunik, 'Rapid differential rotation of protoneutron stars and constraints on radio pulsars periods'. *A&A*, February 1998, volume 330, 1005–1016, arXiv:astro-ph/9711347.

[**Grad and Rubin 1958**] H. Grad and H. Rubin, 'Hydromagnetic equilibria and force-free fields'. In *Proceedings of the 2nd UN Conf. on the Peaceful Uses of Atomic Energy (Geneva)*, volume 31 (IAEA 1958) page 190.

[**Gralla and Jacobson 2014**] S. E. Gralla and T. Jacobson, 'Spacetime approach to force-free magnetospheres'. *MNRAS*, December 2014, volume 445, 2500–2534, doi:10.1093/mnras/stu1690, arXiv:1401.6159.

[**Gralla et al. 2016**] S. E. Gralla, A. Lupsasca and A. Philippov, 'Pulsar Magnetospheres: Beyond the Flat Spacetime Dipole'. *ArXiv e-prints*, April 2016, arXiv:1604.04625.

[**Gregory and Fahlman 1980**] P. C. Gregory and G. G. Fahlman, 'An extraordinary new celestial X-ray source'. *Nature*, October 1980, volume 287, 805, doi:10.1038/287805a0.

[**Gualtieri et al. 2011**] L. Gualtieri, R. Ciolfi and V. Ferrari, 'Structure, deformations and gravitational wave emission of magnetars'. *Classical and Quantum Gravity*, June 2011, volume 28(11), 114014, doi:10.1088/0264-9381/28/11/114014, arXiv:1011.2778.

[**Guidorzi et al. 2014**] C. Guidorzi, C. G. Mundell, R. Harrison, R. Margutti, V. Sudilovsky, B. A. Zauderer, S. Kobayashi, A. Cucchiara, A. Melandri, S. B. Pandey, E. Berger, D. Bersier, V. D'Elia, A. Gomboc, J. Greiner, J. Japelj, D. Kopač, B. Kumar, D. Malesani, C. J. Mottram, P. T. O'Brien, A. Rau, R. J. Smith, I. A. Steele, N. R. Tanvir and F. Virgili, 'New constraints on gamma-ray burst jet geometry and relativistic shock physics'. *MNRAS*, February 2014, volume 438, 752–767, doi:10.1093/mnras/stt2243, arXiv:1311.4340.

[**Guillemot et al. 2013**] L. Guillemot, M. Kramer, T. J. Johnson, H. A. Craig, R. W. Romani, C. Venter, A. K. Harding, R. D. Ferdman, I. H. Stairs and M. Kerr, 'Fermi LAT Pulsed Detection of PSR J0737-3039A in the Double Pulsar System'. *ApJ*, May 2013, volume 768, 169, doi:10.1088/0004-637X/768/2/169, arXiv:1303.7352.

[**Guillot et al. 2013**] S. Guillot, M. Servillat, N. A. Webb and R. E. Rutledge, 'Measurement of the Radius of Neutron Stars with High Signal-to-noise Quiescent Low-mass X-Ray Binaries in Globular Clusters'. *ApJ*, July 2013, volume 772, 7, doi:10.1088/0004-637X/772/1/7, arXiv:1302.0023.

[**Gusakov and Dommes 2016**] M. Gusakov and V. Dommes, 'Relativistic dynamics of superfluid-superconducting mixtures in the presence of topological defects and the electromagnetic field, with application to neutron stars'. *ArXiv e-prints*, July 2016, arXiv:1607.01629.

[**Haensel et al. 2016**] P. Haensel, M. Bejger, M. Fortin and L. Zdunik, 'Rotating neutron stars with exotic cores: masses, radii, stability'. *European Physical Journal A*, March 2016, volume 52, 59, doi:10.1140/epja/i2016-16059-4, arXiv:1601.05368.

[**Halpern et al. 2013**] J. P. Halpern, S. Bogdanov and E. V. Gotthelf, 'X-Ray Measurement of the Spin-down of Calvera: A Radio- and Gamma-Ray-Quiet Pulsar'. *ApJ*, December 2013, volume 778, 120, doi:10.1088/0004-637X/778/2/120, arXiv:1310.6789.

[**Harding 2013**] A. K. Harding, 'The neutron star zoo'. *Frontiers of Physics*, December 2013, volume 8, 679–692, doi:10.1007/s11467-013-0285-0, arXiv:1302.0869.

[**Harding and Muslimov 2011**] A. K. Harding and A. G. Muslimov, 'Pulsar Pair Cascades in a Distorted Magnetic Dipole Field'. *ApJLett*, January 2011, volume 726, L10, doi:10.1088/2041-8205/726/1/L10, arXiv:1012.0451.

[**Harrison et al. 1958**] B. Harrison, M. Wakano and J. Wheeler, 'Matter-energy at high density: end point of thermonuclear evolution,'. volume Onzième Conseil de Physique Solvay, La Structure et l'Evolution de l'Univers (1958) .

[**Haskell et al. 2007**] B. Haskell, N. Andersson, D. I. Jones and L. Samuelsson, 'Are Neutron Stars with Crystalline Color-Superconducting Cores Relevant for the LIGO Experiment?' *Physical Review Letters*, December 2007, volume 99(23), 231101, doi:10.1103/PhysRevLett.99.231101, arXiv:0708.2984.

[**Haskell et al. 2008**] B. Haskell, L. Samuelsson, K. Glampedakis and N. Andersson, 'Modelling magnetically deformed neutron stars'. *MNRAS*, March 2008, volume 385, 531–542, doi:10.1111/j.1365-2966.2008.12861.x, arXiv:0705.1780.

[**Heger et al. 2005**] A. Heger, S. E. Woosley and H. C. Spruit, ‘Presupernova Evolution of Differentially Rotating Massive Stars Including Magnetic Fields’. *ApJ*, June 2005, volume 626, 350–363, doi:10.1086/429868, arXiv:astro-ph/0409422.

[**Herzog and Röpke 2011**] M. Herzog and F. K. Röpke, ‘Three-dimensional hydrodynamic simulations of the combustion of a neutron star into a quark star’. *Phys. Rev. D*, October 2011, volume 84(8), 083002, doi:10.1103/PhysRevD.84.083002, arXiv:1109.0539.

[**Hewish et al. 1968**] A. Hewish, S. J. Bell, J. D. H. Pilkington, P. F. Scott and R. A. Collins, ‘Observation of a Rapidly Pulsating Radio Source’. *Nature*, February 1968, volume 217, 709–713, doi:10.1038/217709a0.

[**Heyl and Kulkarni 1998**] J. S. Heyl and S. R. Kulkarni, ‘How Common Are Magnetars? The Consequences of Magnetic Field Decay’. *ApJLett*, October 1998, volume 506, L61–L64, doi:10.1086/311628, arXiv:astro-ph/9807306.

[**Huang and Yu 2014a**] L. Huang and C. Yu, ‘Magnetar Giant Flares in Multipolar Magnetic Fields. I. Fully and Partially Open Eruptions of Flux Ropes’. *ApJ*, April 2014a, volume 784, 168, doi:10.1088/0004-637X/784/2/168, arXiv:1402.3020.

[**Huang and Yu 2014b**] L. Huang and C. Yu, ‘Magnetar Giant Flares in Multipolar Magnetic Fields. II. Flux Rope Eruptions with Current Sheets’. *ApJ*, November 2014b, volume 796, 3, doi:10.1088/0004-637X/796/1/3, arXiv:1409.4488.

[**Hulse and Taylor 1975**] R. A. Hulse and J. H. Taylor, ‘Discovery of a pulsar in a binary system’. *ApJLett*, January 1975, volume 195, L51–L53, doi:10.1086/181708.

[**Ilgisonis and Pozdnyakov 2003**] V. Ilgisonis and Y. Pozdnyakov, ‘Bifurcational Solutions to Grad-Shafranov Equation’. In *APS Meeting Abstracts* (2003) page 1107P.

[**Isenberg 2008**] J. A. Isenberg, ‘Waveless Approximation Theories of Gravity’. *International Journal of Modern Physics D*, 2008, volume 17, 265–273, doi:10.1142/S0218271808011997, arXiv:gr-qc/0702113.

[**Jahoda et al. 2014**] K. M. Jahoda, J. K. Black, J. E. Hill, T. R. Kallman, P. E. Kaaret, C. B. Markwardt, T. Okajima, R. Petre, Y. Soong, T. E. Strohmayer, T. Tamagawa and Y. Tawara, ‘X-ray polarization capabilities of a small explorer mission’. In *Space Telescopes and Instrumentation 2014: Ultraviolet to Gamma Ray*, volume 9144 of *Proc. SPIE* (2014) page 91440N, doi:10.1117/12.2056719.

[**Janka 2012**] H.-T. Janka, ‘Explosion Mechanisms of Core-Collapse Supernovae’. *Annual Review of Nuclear and Particle Science*, November 2012, volume 62, 407–451, doi:10.1146/annurev-nucl-102711-094901, arXiv:1206.2503.

[**Janka and Moenchmeyer 1989**] H.-T. Janka and R. Moenchmeyer, ‘Hydrostatic POST bounce configurations of collapsed rotating iron cores - Neutrino emission’. *A&A*, December 1989, volume 226, 69–87.

[**Jones 1976**] P. B. Jones, ‘The secular variation of pulsar magnetic dipole moments’. *Ap&SS*, December 1976, volume 45, 369–381, doi:10.1007/BF00642671.

[**Just et al. 2016**] O. Just, M. Obergaulinger, H.-T. Janka, A. Bauswein and N. Schwarz, ‘Neutron-star Merger Ejecta as Obstacles to Neutrino-powered Jets of Gamma-Ray Bursts’. *ApJLett*, January 2016, volume 816, L30, doi:10.3847/2041-8205/816/2/L30, arXiv:1510.04288.

[**Kaspi 2010**] V. M. Kaspi, ‘Grand unification of neutron stars’. *Proceedings of the National Academy of Science*, April 2010, volume 107, 7147–7152, doi:10.1073/pnas.1000812107, arXiv:1005.0876.

[**Keane and Kramer 2008**] E. F. Keane and M. Kramer, ‘On the birthrates of Galactic neutron stars’. *MNRAS*, December 2008, volume 391, 2009–2016, doi:10.1111/j.1365-2966.2008.14045.x, arXiv:0810.1512.

[**Kiuchi et al. 2015**] K. Kiuchi, P. Cerdá-Durán, K. Kyutoku, Y. Sekiguchi and M. Shibata, ‘Efficient magnetic-field amplification due to the Kelvin-Helmholtz instability in binary neutron star mergers’. *Phys. Rev. D*, December 2015, volume 92(12), 124034, doi:10.1103/PhysRevD.92.124034, arXiv:1509.09205.

[**Kiuchi et al. 2009**] K. Kiuchi, K. Kotake and S. Yoshida, ‘Equilibrium Configurations of Relativistic Stars with Purely Toroidal Magnetic Fields: Effects of Realistic Equations of State’. *ApJ*, June 2009, volume 698, 541–557, doi:10.1088/0004-637X/698/1/541, arXiv:0904.2044.

[**Kiuchi et al. 2008**] K. Kiuchi, M. Shibata and S. Yoshida, ‘Evolution of neutron stars with toroidal magnetic fields: Axisymmetric simulation in full general relativity’. *Phys. Rev. D*, July 2008, volume 78(2), 024029, doi:10.1103/PhysRevD.78.024029, arXiv:0805.2712.

[**Kiuchi and Yoshida 2008**] K. Kiuchi and S. Yoshida, ‘Relativistic stars with purely toroidal magnetic fields’. *Phys. Rev. D*, August 2008, volume 78(4), 044045, doi:10.1103/PhysRevD.78.044045, arXiv:0802.2983.

[**Kiuchi et al. 2011**] K. Kiuchi, S. Yoshida and M. Shibata, ‘Nonaxisymmetric instabilities of neutron star with toroidal magnetic fields’. *A&A*, August 2011, volume 532, A30, doi:10.1051/0004-6361/201016242, arXiv:1104.5561.

[**Komissarov 2011**] S. S. Komissarov, ‘3+1 magnetodynamics’. *MNRAS*, November 2011, volume 418, L94–L98, doi:10.1111/j.1745-3933.2011.01150.x, arXiv:1108.3511.

[**Konno 2001**] K. Konno, ‘Moments of inertia of relativistic magnetized stars’. *A&A*, June 2001, volume 372, 594–600, doi:10.1051/0004-6361:20010556, arXiv:arXiv:gr-qc/0105015.

[**Kouveliotou et al. 1999**] C. Kouveliotou, T. Strohmayer, K. Hurley, J. van Paradijs, M. H. Finger, S. Dieters, P. Woods, C. Thompson and R. C. Duncan, ‘Discovery of a Magnetar Associated with the Soft Gamma Repeater SGR 1900+14’. *ApJLett*, January 1999, volume 510, L115–L118, doi:10.1086/311813, arXiv:astro-ph/9809140.

[**Kruskal and Tuck 1958**] M. Kruskal and J. L. Tuck, ‘The Instability of a Pinched Fluid with a Longitudinal Magnetic Field’. *Royal Society of London Proceedings Series A*, June 1958, volume 245, 222–237, doi:10.1098/rspa.1958.0079.

[**Kuiper et al. 2006**] L. Kuiper, W. Hermsen, P. R. den Hartog and W. Collmar, ‘Discovery of Luminous Pulsed Hard X-Ray Emission from Anomalous X-Ray Pulsars 1RXS J1708-4009, 4U 0142+61, and 1E 2259+586 by INTEGRAL and RXTE’. *ApJ*, July 2006, volume 645, 556–575, doi:10.1086/504317, arXiv:astro-ph/0603467.

[**Landau 1938**] L. Landau, ‘Origin of Stellar Energy’. *Nature*, February 1938, volume 141, 333–334, doi:10.1038/141333b0.

[**Lander 2016**] S. K. Lander, ‘Magnetar Field Evolution and Crustal Plasticity’. *ApJLett*, June 2016, volume 824, L21, doi:10.3847/2041-8205/824/2/L21, arXiv:1604.02972.

[**Lander et al. 2015**] S. K. Lander, N. Andersson, D. Antonopoulou and A. L. Watts, ‘Magnetically driven crustquakes in neutron stars’. *MNRAS*, May 2015, volume 449, 2047–2058, doi:10.1093/mnras/stv432, arXiv:1412.5852.

[**Lander and Jones 2009**] S. K. Lander and D. I. Jones, ‘Magnetic fields in axisymmetric neutron stars’. *MNRAS*, June 2009, volume 395, 2162–2176, doi:10.1111/j.1365-2966.2009.14667.x, arXiv:0903.0827.

[**Lander and Jones 2011a**] S. K. Lander and D. I. Jones, ‘Instabilities in neutron stars with toroidal magnetic fields’. *MNRAS*, April 2011a, volume 412, 1394–1400, doi:10.1111/j.1365-2966.2010.17998.x, arXiv:1009.2453.

[**Lander and Jones 2011b**] S. K. Lander and D. I. Jones, ‘Oscillations and instabilities in neutron stars with poloidal magnetic fields’. *MNRAS*, April 2011b, volume 412, 1730–1740, doi:10.1111/j.1365-2966.2010.18009.x, arXiv:1010.0614.

[**Lander and Jones 2012**] S. K. Lander and D. I. Jones, ‘Are there any stable magnetic fields in barotropic stars?’ *MNRAS*, July 2012, volume 424, 482–494, doi:10.1111/j.1365-2966.2012.21213.x, arXiv:1202.2339.

[**Lasky 2015**] P. D. Lasky, ‘Gravitational Waves from Neutron Stars: A Review’. *PASA*, September 2015, volume 32, e034, doi:10.1017/pasa.2015.35, arXiv:1508.06643.

[**Lasky and Glampedakis 2016**] P. D. Lasky and K. Glampedakis, 'Observationally constraining gravitational wave emission from short gamma-ray burst remnants'. *MNRAS*, May 2016, volume 458, 1660–1670, doi:10.1093/mnras/stw435, arXiv:1512.05368.

[**Lasky and Melatos 2013**] P. D. Lasky and A. Melatos, 'Tilted torus magnetic fields in neutron stars and their gravitational wave signatures'. *Phys. Rev. D*, November 2013, volume 88(10), 103005, doi:10.1103/PhysRevD.88.103005, arXiv:1310.7633.

[**Lasky et al. 2011**] P. D. Lasky, B. Zink, K. D. Kokkotas and K. Glampedakis, 'Hydromagnetic Instabilities in Relativistic Neutron Stars'. *ApJLett*, July 2011, volume 735, L20, doi:10.1088/2041-8205/735/1/L20, arXiv:1105.1895.

[**Lattimer 2012**] J. M. Lattimer, 'The Nuclear Equation of State and Neutron Star Masses'. *Annual Review of Nuclear and Particle Science*, November 2012, volume 62, 485–515, doi:10.1146/annurev-nucl-102711-095018, arXiv:1305.3510.

[**Lichnerowicz 1939**] A. Lichnerowicz, 'Sur certains problèmes globaux relatifs au système des équations d'einstein'. In *Thèses françaises de l'entre-deux-guerres* (1939) URL `http://www.numdam.org/item?id=THESE_1939__226__1_0`.

[**Lichnerowicz 1944**] A. Lichnerowicz, 'L'intégration des equations de la gravitation relativiste et la problème des n corps'. *J. Math. Pures et Appl.*, 1944.

[**Lyutikov and Gavriil 2006**] M. Lyutikov and F. P. Gavriil, 'Resonant cyclotron scattering and Comptonization in neutron star magnetospheres'. *MNRAS*, May 2006, volume 368, 690–706, doi:10.1111/j.1365-2966.2006.10140.x, arXiv:astro-ph/0507557.

[**Makishima et al. 2014**] K. Makishima, T. Enoto, J. S. Hiraga, T. Nakano, K. Nakazawa, S. Sakurai, M. Sasano and H. Murakami, 'Possible Evidence for Free Precession of a Strongly Magnetized Neutron Star in the Magnetar 4U 0142+61'. *Physical Review Letters*, May 2014, volume 112(17), 171102, doi:10.1103/PhysRevLett.112.171102, arXiv:1404.3705.

[**Makishima et al. 2016**] K. Makishima, T. Enoto, H. Murakami, Y. Furuta, T. Nakano, M. Sasano and K. Nakazawa, 'Evidence for a 36 ks phase modulation in the hard X-ray pulses from the magnetar 1E 1547.0-5408'. *PASJ*, June 2016, volume 68, S12, doi:10.1093/pasj/psv097, arXiv:1501.07684.

[**Margalit et al. 2015**] B. Margalit, B. D. Metzger and A. M. Beloborodov, 'Does the Collapse of a Supramassive Neutron Star Leave a Debris Disk?' *Physical Review Letters*, October 2015, volume 115(17), 171101, doi:10.1103/PhysRevLett.115.171101, arXiv:1505.01842.

[**Markey and Tayler 1973**] P. Markey and R. J. Tayler, 'The adiabatic stability of stars containing magneticfields-II. Poloidal fields'. *MNRAS*, 1973, volume 163, 77.

[**Markey and Tayler 1974**] P. Markey and R. J. Tayler, 'The adiabatic stability of stars containing magnetic fields-III. Additional results for poloidal fields'. *MNRAS*, September 1974, volume 168, 505–514.

[**Mastrano et al. 2013**] A. Mastrano, P. D. Lasky and A. Melatos, 'Neutron star deformation due to multipolar magnetic fields'. *MNRAS*, September 2013, volume 434, 1658–1667, doi:10.1093/mnras/stt1131, arXiv:1306.4503.

[**Mastrano et al. 2011**] A. Mastrano, A. Melatos, A. Reisenegger and T. Akgün, 'Gravitational wave emission from a magnetically deformed non-barotropic neutron star'. *MNRAS*, November 2011, volume 417, 2288–2299, doi:10.1111/j.1365-2966.2011.19410.x, arXiv:1108.0219.

[**Mastrano et al. 2015**] A. Mastrano, A. G. Suvorov and A. Melatos, 'Neutron star deformation due to poloidal-toroidal magnetic fields of arbitrary multipole order: a new analytic approach'. *MNRAS*, March 2015, volume 447, 3475–3485, doi:10.1093/mnras/stu2671, arXiv:1501.01134.

[**McLaughlin et al. 2006**] M. A. McLaughlin, A. G. Lyne, D. R. Lorimer, M. Kramer, A. J. Faulkner, R. N. Manchester, J. M. Cordes, F. Camilo, A. Possenti, I. H. Stairs, G. Hobbs, N. D'Amico, M. Burgay and

J. T. O'Brien, 'Transient radio bursts from rotating neutron stars'. *Nature*, February 2006, volume 439, 817–820, doi:10.1038/nature04440, arXiv:astro-ph/0511587.

[**Medin and Lai 2006**] Z. Medin and D. Lai, 'Density-functional-theory calculations of matter in strong magnetic fields. I. Atoms and molecules'. *Phys. Rev. A*, December 2006, volume 74(6), 062507, doi:10.1103/PhysRevA.74.062507, arXiv:astro-ph/0607166.

[**Medin and Lai 2007**] Z. Medin and D. Lai, 'Condensed surfaces of magnetic neutron stars, thermal surface emission, and particle acceleration above pulsar polar caps'. *MNRAS*, December 2007, volume 382, 1833–1852, doi:10.1111/j.1365-2966.2007.12492.x, arXiv:0708.3863.

[**Melrose and Yuen 2014**] D. B. Melrose and R. Yuen, 'Non-corotating models for pulsar magnetospheres'. *MNRAS*, January 2014, volume 437, 262–272, doi:10.1093/mnras/stt1876, arXiv:1310.1134.

[**Mereghetti 2011**] S. Mereghetti, 'X-ray emission from isolated neutron stars'. In D. F. Torres and N. Rea, editors, *High-Energy Emission from Pulsars and their Systems* (2011) page 345, doi:10.1007/978-3-642-17251-9_29, arXiv:1008.2891.

[**Mereghetti et al. 2015**] S. Mereghetti, J. A. Pons and A. Melatos, 'Magnetars: Properties, Origin and Evolution'. *Space Sci. Rev.*, October 2015, volume 191, 315–338, doi:10.1007/s11214-015-0146-y, arXiv:1503.06313.

[**Mestel and Takhar 1972**] L. Mestel and H. S. Takhar, 'The internal Dynamics of the Oblique Rotator'. *MNRAS*, 1972, volume 156, 419, doi:10.1093/mnras/156.4.419.

[**Metzger 2016**] B. D. Metzger, 'The Kilonova Handbook'. *ArXiv e-prints*, October 2016, arXiv:1610.09381.

[**Metzger et al. 2011**] B. D. Metzger, D. Giannios, T. A. Thompson, N. Bucciantini and E. Quataert, 'The protomagnetar model for gamma-ray bursts'. *MNRAS*, May 2011, volume 413, 2031–2056, doi:10.1111/j.1365-2966.2011.18280.x, arXiv:1012.0001.

[**Michel 1973a**] F. C. Michel, 'Pulsar Parameters.' In *Bulletin of the American Astronomical Society*, volume 5 of *BAAS* (1973a) page 425.

[**Michel 1973b**] F. C. Michel, 'Rotating Magnetospheres: an Exact 3-D Solution'. *ApJLett*, March 1973b, volume 180, L133, doi:10.1086/181169.

[**Michel 1974**] F. C. Michel, 'Comment on "Self-Consistent Solution for an Axisymmetric Pulsar Model"'. *Physical Review Letters*, December 1974, volume 33, 1521–1523, doi:10.1103/PhysRevLett.33.1521.

[**Michel and Li 1999**] F. C. Michel and H. Li, 'Electrodynamics of neutron stars'. *Phys. Rep.*, September 1999, volume 318, 227–297, doi:10.1016/S0370-1573(99)00002-2.

[**Migdal 1959**] A. B. Migdal, 'Superfluidity and the moments of inertia of nuclei'. *Nucl. Phys. A*, November 1959, volume 13, 655–674, doi:10.1016/0029-5582(59)90264-0.

[**Miketinac 1975**] M. J. Miketinac, 'Structure of polytropic models of stars containing poloidal magnetic fields'. *Ap&SS*, July 1975, volume 35, 349–362, doi:10.1007/BF00637003.

[**Mikic and Linker 1994**] Z. Mikic and J. A. Linker, 'Disruption of coronal magnetic field arcades'. *ApJ*, August 1994, volume 430, 898–912, doi:10.1086/174460.

[**Mitchell et al. 2015**] J. P. Mitchell, J. Braithwaite, A. Reisenegger, H. Spruit, J. A. Valdivia and N. Langer, 'Instability of magnetic equilibria in barotropic stars'. *MNRAS*, February 2015, volume 447, 1213–1223, doi:10.1093/mnras/stu2514, arXiv:1411.7252.

[**Moffatt 1978**] H. K. Moffatt, *Magnetic field generation in electrically conducting fluids* (1978).

[**Moiseenko et al. 2006**] S. G. Moiseenko, G. S. Bisnovatyi-Kogan and N. V. Ardeljan, 'A magnetorotational core-collapse model with jets'. *MNRAS*, July 2006, volume 370, 501–512, doi:10.1111/j.1365-2966.2006.10517.x.

[**Monaghan 1965**] J. J. Monaghan, 'Magnetic fields in stellar bodies. I, Magnetic fields in polytropes'. *MNRAS*, 1965, volume 131, 105.

[**Monaghan 1966**] J. J. Monaghan, ‘Magnetic fields in steller bodies III Distortion of polytropes’. *MNRAS*, 1966, volume 134, 275.

[**Moriya and Tauris 2016**] T. J. Moriya and T. M. Tauris, ‘Constraining the ellipticity of strongly magnetized neutron stars powering superluminous supernovae’. *MNRAS*, July 2016, volume 460, L55–L58, doi:10.1093/mnrasl/slw072, arXiv:1604.03983.

[**Mösta et al. 2015**] P. Mösta, C. D. Ott, D. Radice, L. F. Roberts, E. Schnetter and R. Haas, ‘A large-scale dynamo and magnetoturbulence in rapidly rotating core-collapse supernovae’. *Nature*, December 2015, volume 528, 376–379, doi:10.1038/nature15755, arXiv:1512.00838.

[**Mukhopadhyay 2015**] B. Mukhopadhyay, ‘Significantly super-Chandrasekhar limiting mass white dwarfs as progenitors for peculiar over-luminous type Ia supernovae’. *ArXiv e-prints*, September 2015, arXiv:1509.09008.

[**Müller 2016**] B. Müller, ‘The Status of Multi-Dimensional Core-Collapse Supernova Models’. *PASA*, September 2016, volume 33, e048, doi:10.1017/pasa.2016.40, arXiv:1608.03274.

[**Muno et al. 2006**] M. P. Muno, J. S. Clark, P. A. Crowther, S. M. Dougherty, R. de Grijs, C. Law, S. L. W. McMillan, M. R. Morris, I. Negueruela, D. Pooley, S. Portegies Zwart and F. Yusef-Zadeh, ‘A Neutron Star with a Massive Progenitor in Westerlund 1’. *ApJLett*, January 2006, volume 636, L41–L44, doi:10.1086/499776, arXiv:astro-ph/0509408.

[**Murguia-Berthier et al. 2014**] A. Murguia-Berthier, G. Montes, E. Ramirez-Ruiz, F. De Colle and W. H. Lee, ‘Necessary Conditions for Short Gamma-Ray Burst Production in Binary Neutron Star Mergers’. *ApJLett*, June 2014, volume 788, L8, doi:10.1088/2041-8205/788/1/L8, arXiv:1404.0383.

[**Nakamura et al. 2014**] K. Nakamura, T. Kuroda, T. Takiwaki and K. Kotake, ‘Impacts of Rotation on Three-dimensional Hydrodynamics of Core-collapse Supernovae’. *ApJ*, September 2014, volume 793, 45, doi:10.1088/0004-637X/793/1/45, arXiv:1403.7290.

[**Nakamura et al. 1987**] T. Nakamura, K. Oohara and Y. Kojima, ‘General Relativistic Collapse to Black Holes and Gravitational Waves from Black Holes’. *Progress of Theoretical Physics Supplement*, 1987, volume 90, 1–218, doi:10.1143/PTPS.90.1.

[**Nobili et al. 2008**] L. Nobili, R. Turolla and S. Zane, ‘X-ray spectra from magnetar candidates - II. Resonant cross-sections for electron-photon scattering in the relativistic regime’. *MNRAS*, September 2008, volume 389, 989–1000, doi:10.1111/j.1365-2966.2008.13627.x, arXiv:0806.3714.

[**Nousek 2006**] J. A. Nousek, ‘Swift Gamma-Ray Burst Explorer: The First Results’. *Chinese Journal of Astronomy and Astrophysics Supplement*, December 2006, volume 6(1), 357–360, doi:10.1088/1009-9271/6/S1/46.

[**Obergaulinger et al. 2014**] M. Obergaulinger, H.-T. Janka and M. A. Aloy, ‘Magnetic field amplification and magnetically supported explosions of collapsing, non-rotating stellar cores’. *MNRAS*, December 2014, volume 445, 3169–3199, doi:10.1093/mnras/stu1969, arXiv:1405.7466.

[**Oechslin et al. 2004**] R. Oechslin, K. Uryū, G. Poghosyan and F. K. Thielemann, ‘The influence of quark matter at high densities on binary neutron star mergers’. *MNRAS*, April 2004, volume 349, 1469–1480, doi:10.1111/j.1365-2966.2004.07621.x, arXiv:astro-ph/0401083.

[**Oppenheimer and Volkoff 1939**] J. R. Oppenheimer and G. M. Volkoff, ‘On Massive Neutron Cores’. *Physical Review*, February 1939, volume 55, 374–381, doi:10.1103/PhysRev.55.374.

[**Oron 2002**] A. Oron, ‘Relativistic magnetized star with poloidal and toroidal fields’. *Phys. Rev. D*, July 2002, volume 66(2), 023006, doi:10.1103/PhysRevD.66.023006.

[**Ostriker and Hartwick 1968**] J. P. Ostriker and F. D. A. Hartwick, ‘Rapidly Rotating Stars.IV. Magnetic White Dwarfs’. *ApJ*, September 1968, volume 153, 797, doi:10.1086/149706.

[**Ott et al. 2006**] C. D. Ott, A. Burrows, T. A. Thompson, E. Livne and R. Walder, ‘The Spin Periods and Rotational Profiles of Neutron Stars at Birth’. *ApJS*, May 2006, volume 164, 130–155, doi:10.1086/500832, arXiv:astro-ph/0508462.

[**Ott et al. 2007**] C. D. Ott, H. Dimmelmeier, A. Marek, H.-T. Janka, B. Zink, I. Hawke and E. Schnetter, ‘Rotating collapse of stellar iron cores in general relativity’. *Classical and Quantum Gravity*, June 2007, volume 24, S139–S154, doi:10.1088/0264-9381/24/12/S10, arXiv:astro-ph/0612638.

[**Owen 2005**] B. J. Owen, ‘Maximum Elastic Deformations of Compact Stars with Exotic Equations of State’. *Physical Review Letters*, November 2005, volume 95(21), 211101, doi:10.1103/PhysRevLett.95.211101, arXiv:astro-ph/0503399.

[**Ozel and Freire 2016**] F. Ozel and P. Freire, ‘Masses, Radii, and Equation of State of Neutron Stars’. *ArXiv e-prints*, March 2016, arXiv:1603.02698.

[**Pacini 1967**] F. Pacini, ‘Energy Emission from a Neutron Star’. *Nature*, November 1967, volume 216, 567–568, doi:10.1038/216567a0.

[**Paczynski 1986**] B. Paczynski, ‘Gamma-ray bursters at cosmological distances’. *ApJLett*, September 1986, volume 308, L43–L46, doi:10.1086/184740.

[**Page and Usov 2002**] D. Page and V. V. Usov, ‘Thermal Evolution and Light Curves of Young Bare Strange Stars’. *Physical Review Letters*, September 2002, volume 89(13), 131101, doi:10.1103/PhysRevLett.89.131101, arXiv:astro-ph/0204275.

[**Palapanidis et al. 2015**] K. Palapanidis, N. Stergioulas and S. K. Lander, ‘Magnetized neutron stars with superconducting cores: effect of entrainment’. *MNRAS*, September 2015, volume 452, 3246–3255, doi:10.1093/mnras/stv1536, arXiv:1503.00972.

[**Parfrey et al. 2013**] K. Parfrey, A. M. Beloborodov and L. Hui, ‘Dynamics of Strongly Twisted Relativistic Magnetospheres’. *ApJ*, September 2013, volume 774, 92, doi:10.1088/0004-637X/774/2/92, arXiv:1306.4335.

[**Parker 1966**] E. N. Parker, ‘The Dynamical State of the Interstellar Gas and Field’. *ApJ*, September 1966, volume 145, 811, doi:10.1086/148828.

[**Parker 1955**] J. M. Parker, ‘The Rotational Temperature of the Lower Solar Chromosphere.’ *ApJ*, May 1955, volume 121, 731, doi:10.1086/146038.

[**Passamonti et al. 2016**] A. Passamonti, T. Akgün, J. A. Pons and J. A. Miralles, ‘The relevance of ambipolar diffusion for neutron star evolution’. *ArXiv e-prints*, July 2016, arXiv:1608.00001.

[**Pavan et al. 2009**] L. Pavan, R. Turolla, S. Zane and L. Nobili, ‘Topology of magnetars external field - I. Axially symmetric fields’. *MNRAS*, May 2009, volume 395, 753–763, doi:10.1111/j.1365-2966.2009.14600.x, arXiv:0902.0720.

[**Penacchioni et al. 2013**] A. V. Penacchioni, R. Ruffini, C. L. Bianco, L. Izzo, M. Muccino, G. B. Pisani and J. A. Rueda, ‘GRB 110709B in the induced gravitational collapse paradigm’. *A&A*, March 2013, volume 551, A133, doi:10.1051/0004-6361/201220679, arXiv:1301.6014.

[**Perera et al. 2014**] B. B. P. Perera, C. Kim, M. A. McLaughlin, R. D. Ferdman, M. Kramer, I. H. Stairs, P. C. C. Freire and A. Possenti, ‘Realistic Modeling of the Pulse Profile of PSR J0737-3039A’. *ApJ*, May 2014, volume 787, 51, doi:10.1088/0004-637X/787/1/51, arXiv:1404.1458.

[**Perna and Gotthelf 2008**] R. Perna and E. V. Gotthelf, ‘Constraints on the Emission and Viewing Geometry of the Transient Anomalous X-Ray Pulsar XTE J1810-197’. *ApJ*, July 2008, volume 681, 522–529, doi:10.1086/588211, arXiv:0803.2042.

[**Perna and Pons 2011**] R. Perna and J. A. Pons, ‘A Unified Model of the Magnetar and Radio Pulsar Bursting Phenomenology’. *ApJLett*, February 2011, volume 727, L51, doi:10.1088/2041-8205/727/2/L51, arXiv:1101.1098.

[**Pétri 2015**] J. Pétri, ‘Multipolar electromagnetic fields around neutron stars: exact vacuum solutions and related properties’. *MNRAS*, June 2015, volume 450, 714–742, doi:10.1093/mnras/stv598, arXiv:1503.05307.

[**Pétri 2016a**] J. Pétri, ‘General-relativistic force-free pulsar magnetospheres’. *MNRAS*, February 2016a, volume 455, 3779–3805, doi:10.1093/mnras/stv2613, arXiv:1511.01337.

[**Pétri 2016b**] J. Pétri, ‘Quantum electrodynamical corrections to a magnetic dipole in general relativity’. *MNRAS*, March 2016b, volume 456, 4455–4460, doi:10.1093/mnras/stv2967, arXiv:1512.05805.

[**Pfeiffer and York 2003**] H. P. Pfeiffer and J. W. York, ‘Extrinsic curvature and the Einstein constraints’. *Phys. Rev. D*, February 2003, volume 67(4), 044022, doi:10.1103/PhysRevD.67.044022, arXiv:gr-qc/0207095.

[**Philippov et al. 2014**] A. Philippov, A. Tchekhovskoy and J. G. Li, ‘Time evolution of pulsar obliquity angle from 3D simulations of magnetospheres’. *MNRAS*, July 2014, volume 441, 1879–1887, doi:10.1093/mnras/stu591, arXiv:1311.1513.

[**Philippov et al. 2015a**] A. A. Philippov, B. Cerutti, A. Tchekhovskoy and A. Spitkovsky, ‘Ab-initio pulsar magnetosphere: the role of general relativity’. *ArXiv e-prints*, October 2015a, arXiv:1510.01734.

[**Philippov and Spitkovsky 2014**] A. A. Philippov and A. Spitkovsky, ‘Ab Initio Pulsar Magnetosphere: Three-dimensional Particle-in-cell Simulations of Axisymmetric Pulsars’. *ApJLett*, April 2014, volume 785, L33, doi:10.1088/2041-8205/785/2/L33, arXiv:1312.4970.

[**Philippov et al. 2015b**] A. A. Philippov, A. Spitkovsky and B. Cerutti, ‘Ab Initio Pulsar Magnetosphere: Three-dimensional Particle-in-cell Simulations of Oblique Pulsars’. *ApJLett*, March 2015b, volume 801, L19, doi:10.1088/2041-8205/801/1/L19, arXiv:1412.0673.

[**Pili et al. 2014**] A. G. Pili, N. Bucciantini and L. Del Zanna, ‘Axisymmetric equilibrium models for magnetized neutron stars in General Relativity under the Conformally Flat Condition’. *MNRAS*, April 2014, volume 439, 3541–3563, doi:10.1093/mnras/stu215, (PBD14), arXiv:1401.4308.

[**Pili et al. 2015**] A. G. Pili, N. Bucciantini and L. Del Zanna, ‘General relativistic neutron stars with twisted magnetosphere’. *MNRAS*, March 2015, volume 447, 2821–2835, doi:10.1093/mnras/stu2628, arXiv:1412.4036.

[**Pili et al. 2017**] A. G. Pili, N. Bucciantini and L. Del Zanna, ‘General relativistic models for rotating magnetized neutron stars’, October 2017, in prep.

[**Pili et al. 2016**] A. G. Pili, N. Bucciantini, A. Drago, G. Pagliara and L. Del Zanna, ‘Quark deconfinement in the proto-magnetar model of long gamma-ray bursts’. *MNRAS*, October 2016, volume 462, L26–L30, doi:10.1093/mnrasl/slw115, arXiv:1606.02075.

[**Pons and Geppert 2007**] J. A. Pons and U. Geppert, ‘Magnetic field dissipation in neutron star crusts: from magnetars to isolated neutron stars’. *A&A*, July 2007, volume 470, 303–315, doi:10.1051/0004-6361:20077456, arXiv:astro-ph/0703267.

[**Pons et al. 2009**] J. A. Pons, J. A. Miralles and U. Geppert, ‘Magneto-thermal evolution of neutron stars’. *A&A*, March 2009, volume 496, 207–216, doi:10.1051/0004-6361:200811229, arXiv:0812.3018.

[**Pons et al. 1999**] J. A. Pons, S. Reddy, M. Prakash, J. M. Lattimer and J. A. Miralles, ‘Evolution of Proto-Neutron Stars’. *ApJ*, March 1999, volume 513, 780–804, doi:10.1086/306889, arXiv:astro-ph/9807040.

[**Popov 2015**] S. B. Popov, ‘Origin of magnetars in binary systems’. *ArXiv e-prints*, July 2015, arXiv:1507.08192.

[**Popov and Prokhorov 2006**] S. B. Popov and M. E. Prokhorov, ‘Progenitors with enhanced rotation and the origin of magnetars’. *MNRAS*, April 2006, volume 367, 732–736, doi:10.1111/j.1365-2966.2005.09983.x, arXiv:astro-ph/0505406.

[**Potekhin et al. 2015**] A. Y. Potekhin, J. A. Pons and D. Page, 'Neutron Stars - Cooling and Transport'. *Space Sci. Rev.*, July 2015, doi:10.1007/s11214-015-0180-9, arXiv:1507.06186.

[**Prendergast 1956**] K. H. Prendergast, 'The Equilibrium of a Self-Gravitating Incompressible Fluid Sphere with a Magnetic Field. I.' *ApJ*, May 1956, volume 123, 498, doi:10.1086/146186.

[**Proga and Zhang 2006**] D. Proga and B. Zhang, 'The late time evolution of gamma-ray bursts: ending hyperaccretion and producing flares'. *MNRAS*, July 2006, volume 370, L61–L65, doi:10.1111/j.1745-3933.2006.00189.x, arXiv:astro-ph/0601272.

[**Punturo et al. 2010**] M. Punturo, M. Abernathy, F. Acernese, B. Allen, N. Andersson, K. Arun, F. Barone, B. Barr, M. Barsuglia, M. Beker, N. Beveridge, S. Birindelli, S. Bose, L. Bosi, S. Braccini et al., 'The third generation of gravitational wave observatories and their science reach'. *Classical and Quantum Gravity*, April 2010, volume 27(8), 084007, doi:10.1088/0264-9381/27/8/084007.

[**Rea et al. 2016**] N. Rea, A. Borghese, P. Esposito, F. Coti Zelati, M. Bachetti, G. L. Israel and A. De Luca, 'Magnetar-like Activity from the Central Compact Object in the SNR RCW103'. *ApJLett*, September 2016, volume 828, L13, doi:10.3847/2041-8205/828/1/L13, arXiv:1607.04107.

[**Rea and Esposito 2011**] N. Rea and P. Esposito, 'Magnetar outbursts: an observational review'. In D. F. Torres and N. Rea, editors, *High-Energy Emission from Pulsars and their Systems* (2011) page 247, doi:10.1007/978-3-642-17251-9_21, arXiv:1101.4472.

[**Rea et al. 2009**] N. Rea, G. L. Israel, R. Turolla, P. Esposito, S. Mereghetti, D. Götz, S. Zane, A. Tiengo, K. Hurley, M. Feroci, M. Still, V. Yershov, C. Winkler, R. Perna, F. Bernardini, P. Ubertini, L. Stella, S. Campana, M. van der Klis and P. Woods, 'The first outburst of the new magnetar candidate sgr0501+4516'. *MNRAS*, July 2009, volume 396, 2419–2432, doi:10.1111/j.1365-2966.2009.14920.x, arXiv:0904.2413.

[**Reisenegger 2009**] A. Reisenegger, 'Stable magnetic equilibria and their evolution in the upper main sequence, white dwarfs, and neutron stars'. *A&A*, May 2009, volume 499, 557–566, doi:10.1051/0004-6361/200810895, arXiv:0809.0361.

[**Rezzolla and Kumar 2015**] L. Rezzolla and P. Kumar, 'A Novel Paradigm for Short Gamma-Ray Bursts With Extended X-Ray Emission'. *ApJ*, April 2015, volume 802, 95, doi:10.1088/0004-637X/802/2/95, arXiv:1410.8560.

[**Rheinhardt and Geppert 2005**] M. Rheinhardt and U. Geppert, 'The proto-neutron-star dynamo. Viability and impediments'. *A&A*, May 2005, volume 435, 201–206, doi:10.1051/0004-6361:20042062, arXiv:arXiv:astro-ph/0502277.

[**Roberts 1955**] P. H. Roberts, 'The Equilibrium of Magnetic Stars.' *ApJ*, November 1955, volume 122, 508, doi:10.1086/146112.

[**Rodríguez Castillo et al. 2016**] G. A. Rodríguez Castillo, G. L. Israel, A. Tiengo, D. Salvetti, R. Turolla, S. Zane, N. Rea, P. Esposito, S. Mereghetti, R. Perna, L. Stella, J. A. Pons, S. Campana, D. Götz and S. Motta, 'The outburst decay of the low magnetic field magnetar SWIFT J1822.3-1606: phase-resolved analysis and evidence for a variable cyclotron feature'. *MNRAS*, March 2016, volume 456, 4145–4155, doi:10.1093/mnras/stv2490, arXiv:1510.09157.

[**Rosswog 2007**] S. Rosswog, 'Fallback accretion in the aftermath of a compact binary merger'. *MNRAS*, March 2007, volume 376, L48–L51, doi:10.1111/j.1745-3933.2007.00284.x, arXiv:astro-ph/0611440.

[**Roumeliotis et al. 1994**] G. Roumeliotis, P. A. Sturrock and S. K. Antiochos, 'A Numerical Study of the Sudden Eruption of Sheared Magnetic Fields'. *ApJ*, March 1994, volume 423, 847, doi:10.1086/173862.

[**Rowlinson et al. 2014**] A. Rowlinson, B. P. Gompertz, M. Dainotti, P. T. O'Brien, R. A. M. J. Wijers and A. J. van der Horst, 'Constraining properties of GRB magnetar central engines using the observed plateau luminosity and duration correlation'. *MNRAS*, September 2014, volume 443, 1779–1787, doi:10.1093/mnras/stu1277, arXiv:1407.1053.

[**Rowlinson et al. 2013**] A. Rowlinson, P. T. O'Brien, B. D. Metzger, N. R. Tanvir and A. J. Levan, 'Signatures of magnetar central engines in short GRB light curves'. *MNRAS*, April 2013, volume 430, 1061–1087, doi:10.1093/mnras/sts683, arXiv:1301.0629.

[**Roxburgh 1966**] I. W. Roxburgh, 'Magnetostatic equilibrium of polytropes'. *MNRAS*, 1966, volume 132, 347.

[**Ruderman 1972**] M. Ruderman, 'Pulsars: Structure and Dynamics'. *ARA&A*, 1972, volume 10, 427, doi:10.1146/annurev.aa.10.090172.002235.

[**Ruderman and Sutherland 1975**] M. A. Ruderman and P. G. Sutherland, 'Theory of pulsars - Polar caps, sparks, and coherent microwave radiation'. *ApJ*, February 1975, volume 196, 51–72, doi:10.1086/153393.

[**Ruffini and Treves 1973**] R. Ruffini and A. Treves, 'On a Magnetized Rotating Sphere'. *Astrophys. Lett.*, February 1973, volume 13, 109.

[**Ruiz et al. 2014**] M. Ruiz, V. Paschalidis and S. L. Shapiro, 'Pulsar spin-down luminosity: Simulations in general relativity'. *Phys. Rev. D*, April 2014, volume 89(8), 084045, doi:10.1103/PhysRevD.89.084045, arXiv:1402.5412.

[**Saijo 2004**] M. Saijo, 'The Collapse of Differentially Rotating Supermassive Stars: Conformally Flat Simulations'. *ApJ*, November 2004, volume 615, 866–879, doi:10.1086/424700, arXiv:astro-ph/0407621.

[**Scharlemann and Wagoner 1973**] E. T. Scharlemann and R. V. Wagoner, 'Aligned rotating magnetospheres. general analysis'. *ApJ*, jun 1973, volume 182, 951–960, doi:10.1086/152195.

[**Seyffert et al. 2014**] A. S. Seyffert, C. Venter, A. K. Harding and T. J. Johnson, 'Modelling the γ-ray and radio light curves of the double pulsar system'. *ArXiv e-prints*, November 2014, arXiv:1411.0881.

[**Shabaltas and Lai 2012**] N. Shabaltas and D. Lai, 'The Hidden Magnetic Field of the Young Neutron Star in Kesteven 79'. *ApJ*, April 2012, volume 748, 148, doi:10.1088/0004-637X/748/2/148, arXiv:1110.3129.

[**Shafranov 1956**] V. D. Shafranov. *The Soviet Journal of Atomic Energy*, 1956, volume 1(5), 709–713.

[**Shafranov 1966**] V. D. Shafranov, 'Plasma Equilibrium in a Magnetic Field'. *Reviews of Plasma Physics*, 1966, volume 2, 103.

[**Shen et al. 2011**] R. Shen, P. Kumar and T. Piran, 'The late jet in gamma-ray bursts and its interactions with a supernova ejecta and a cocoon'. *MNRAS*, December 2011, volume 418, 2106–2108, doi:10.1111/j.1365-2966.2011.19432.x.

[**Shibata and Nakamura 1995**] M. Shibata and T. Nakamura, 'Evolution of three-dimensional gravitational waves: Harmonic slicing case'. *Phys. Rev. D*, November 1995, volume 52, 5428–5444, doi:10.1103/PhysRevD.52.5428.

[**Shibata and Sekiguchi 2005**] M. Shibata and Y.-I. Sekiguchi, 'Magnetohydrodynamics in full general relativity: Formulation and tests'. *Phys. Rev. D*, August 2005, volume 72(4), 044014, doi:10.1103/PhysRevD.72.044014, arXiv:astro-ph/0507383.

[**Shklovskii 1967**] I. S. Shklovskii, 'The Nature of the X-Ray Source Sco X-1.' *AZh*, 1967, volume 44, 930.

[**Skyrme 1959**] T. Skyrme, 'The effective nuclear potential'. *Nucl. Phys. A*, 1959, volume 9, 615–634, doi:10.1016/0029-5582(58)90345-6.

[**Soffitta et al. 2013**] P. Soffitta, X. Barcons, R. Bellazzini, J. Braga, E. Costa, G. W. Fraser, S. Gburek, J. Huovelin, G. Matt, M. Pearce, J. Poutanen, V. Reglero, A. Santangelo, R. A. Sunyaev, G. Tagliaferri et al., 'XIPE: the X-ray imaging polarimetry explorer'. *Experimental Astronomy*, December 2013, volume 36, 523–567, doi:10.1007/s10686-013-9344-3, arXiv:1309.6995.

[**Spitkovsky 2006**] A. Spitkovsky, 'Time-dependent Force-free Pulsar Magnetospheres: Axisymmetric and Oblique Rotators'. *ApJLett*, September 2006, volume 648, L51–L54, doi:10.1086/507518, arXiv:astro-ph/0603147.

[**Spruit 2008**] H. C. Spruit, ‘Origin of neutron star magnetic fields’. In C. Bassa, Z. Wang, A. Cumming and V. M. Kaspi, editors, *40 Years of Pulsars: Millisecond Pulsars, Magnetars and More*, volume 983 of *American Institute of Physics Conference Series* (2008) pages 391–398, doi:10.1063/1.2900262, arXiv:0711.3650.

[**Spruit 2009**] H. C. Spruit, ‘The source of magnetic fields in (neutron-) stars’. In K. G. Strassmeier, A. G. Kosovichev and J. E. Beckman, editors, *Cosmic Magnetic Fields: From Planets, to Stars and Galaxies*, volume 259 of *IAU Symposium* (2009) pages 61–74, doi:10.1017/S1743921309030075.

[**Stabler 1960**] R. C. Stabler, *Energy Loss Mechanisms from Very Dense Stars*. Ph.D. thesis, CORNELL UNIVERSITY., 1960.

[**Staff et al. 2006**] J. E. Staff, R. Ouyed and P. Jaikumar, ‘Quark Deconfinement in Neutron Star Cores: The Effects of Spin-down’. *ApJLett*, July 2006, volume 645, L145–L148, doi:10.1086/506255, arXiv:astro-ph/0603743.

[**Stella et al. 2005**] L. Stella, S. Dall’Osso, G. L. Israel and A. Vecchio, ‘Gravitational Radiation from Newborn Magnetars in the Virgo Cluster’. *ApJLett*, December 2005, volume 634, L165–L168, doi:10.1086/498685, arXiv:astro-ph/0511068.

[**Stergioulas and Friedman 1995**] N. Stergioulas and J. L. Friedman, ‘Comparing models of rapidly rotating relativistic stars constructed by two numerical methods’. *ApJ*, May 1995, volume 444, 306–311, doi:10.1086/175605, arXiv:astro-ph/9411032.

[**Subramanian and Mukhopadhyay 2015**] S. Subramanian and B. Mukhopadhyay, ‘GRMHD formulation of highly super-Chandrasekhar rotating magnetized white dwarfs: stable configurations of non-spherical white dwarfs’. *MNRAS*, November 2015, volume 454, 752–765, doi:10.1093/mnras/stv1983, arXiv:1507.01606.

[**Takiwaki et al. 2016**] T. Takiwaki, K. Kotake and Y. Suwa, ‘Three-dimensional simulations of rapidly rotating core-collapse supernovae: finding a neutrino-powered explosion aided by non-axisymmetric flows’. *MNRAS*, September 2016, volume 461, L112–L116, doi:10.1093/mnrasl/slw105, arXiv:1602.06759.

[**Tauris et al. 2015**] T. M. Tauris, V. M. Kaspi, R. P. Breton, A. T. Deller, E. F. Keane, M. Kramer, D. R. Lorimer, M. A. McLaughlin, A. Possenti, P. S. Ray, B. W. Stappers and P. Weltevrede, ‘Understanding the Neutron Star Population with the SKA’. *Advancing Astrophysics with the Square Kilometre Array (AASKA14)*, 2015, 39, arXiv:1501.00005.

[**Taverna et al. 2014**] R. Taverna, F. Muleri, R. Turolla, P. Soffitta, S. Fabiani and L. Nobili, ‘Probing magnetar magnetosphere through X-ray polarization measurements’. *MNRAS*, February 2014, volume 438, 1686–1697, doi:10.1093/mnras/stt2310, arXiv:1311.7500.

[**Tayler 1973**] R. J. Tayler, ‘The adiabatic stability of stars containing magnetic fields-I.Toroidal fields’. *MNRAS*, 1973, volume 161, 365, doi:10.1093/mnras/161.4.365.

[**Tchekhovskoy et al. 2013**] A. Tchekhovskoy, A. Spitkovsky and J. G. Li, ‘Time-dependent 3D magnetohydrodynamic pulsar magnetospheres: oblique rotators’. *MNRAS*, August 2013, volume 435, L1–L5, doi:10.1093/mnrasl/slt076, arXiv:1211.2803.

[**Thompson and Duncan 1993**] C. Thompson and R. C. Duncan, ‘Neutron star dynamos and the origins of pulsar magnetism’. *ApJ*, May 1993, volume 408, 194–217, doi:10.1086/172580.

[**Thompson and Duncan 2001**] C. Thompson and R. C. Duncan, ‘The Giant Flare of 1998 August 27 from SGR 1900+14. II. Radiative Mechanism and Physical Constraints on the Source’. *ApJ*, November 2001, volume 561, 980–1005, doi:10.1086/323256, arXiv:astro-ph/0110675.

[**Thompson et al. 2002**] C. Thompson, M. Lyutikov and S. R. Kulkarni, ‘Electrodynamics of Magnetars: Implications for the Persistent X-Ray Emission and Spin-down of the Soft Gamma Repeaters and Anomalous X-Ray Pulsars’. *ApJ*, July 2002, volume 574, 332–355, doi:10.1086/340586, arXiv:astro-ph/0110677.

[**Thorne and MacDonald 1982**] K. S. Thorne and D. MacDonald, ‘Electrodynamics in Curved Spacetime - 3+1 Formulation’. *MNRAS*, January 1982, volume 198, 339, doi:10.1093/mnras/198.2.339.

[**Tiengo et al. 2013**] A. Tiengo, P. Esposito, S. Mereghetti, R. Turolla, L. Nobili, F. Gastaldello, D. Götz, G. L. Israel, N. Rea, L. Stella, S. Zane and G. F. Bignami, ‘A variable absorption feature in the X-ray spectrum of a magnetar’. *Nature*, August 2013, volume 500, 312–314, doi:10.1038/nature12386, arXiv:1308.4987.

[**Timokhin 2006**] A. N. Timokhin, ‘On the force-free magnetosphere of an aligned rotator’. *MNRAS*, May 2006, volume 368, 1055–1072, doi:10.1111/j.1365-2966.2006.10192.x, arXiv:astro-ph/0511817.

[**Tolman 1939**] R. C. Tolman, ‘Static Solutions of Einstein’s Field Equations for Spheres of Fluid’. *Physical Review*, February 1939, volume 55, 364–373, doi:10.1103/PhysRev.55.364.

[**Tomimura and Eriguchi 2005**] Y. Tomimura and Y. Eriguchi, ‘A new numerical scheme for structures of rotating magnetic stars’. *MNRAS*, May 2005, volume 359, 1117–1130, doi:10.1111/j.1365-2966.2005.08967.x.

[**Troja et al. 2007**] E. Troja, G. Cusumano, P. T. O’Brien, B. Zhang, B. Sbarufatti, V. Mangano, R. Willingale, G. Chincarini, J. P. Osborne, F. E. Marshall, D. N. Burrows, S. Campana, N. Gehrels, C. Guidorzi, H. A. Krimm, V. La Parola, E. W. Liang, T. Mineo, A. Moretti, K. L. Page, P. Romano, G. Tagliaferri, B. B. Zhang, M. J. Page and P. Schady, ‘Swift Observations of GRB 070110: An Extraordinary X-Ray Afterglow Powered by the Central Engine’. *ApJ*, August 2007, volume 665, 599–607, doi:10.1086/519450, arXiv:astro-ph/0702220.

[**Truemper et al. 1978**] J. Truemper, W. Pietsch, C. Reppin, W. Voges, R. Staubert and E. Kendziorra, ‘Evidence for strong cyclotron line emission in the hard X-ray spectrum of Hercules X-1’. *ApJLett*, February 1978, volume 219, L105–L110, doi:10.1086/182617.

[**Tsuruta and Cameron 1966**] S. Tsuruta and A. G. W. Cameron, ‘Cooling and detectability of neutron stars’. *Canadian Journal of Physics*, 1966, volume 44, 1863, doi:10.1139/p66-156.

[**Turolla 2009**] R. Turolla, ‘Isolated Neutron Stars: The Challenge of Simplicity’. In W. Becker, editor, *Astrophysics and Space Science Library*, volume 357 of *Astrophysics and Space Science Library* (2009) page 141, doi:10.1007/978-3-540-76965-1_7.

[**Turolla and Esposito 2013**] R. Turolla and P. Esposito, ‘Low-Magnetic-Field Magnetars’. *International Journal of Modern Physics D*, November 2013, volume 22, 1330024, doi:10.1142/S0218271813300243, arXiv:1303.6052.

[**Turolla et al. 2015**] R. Turolla, S. Zane and A. L. Watts, ‘Magnetars: the physics behind observations. A review’. *Reports on Progress in Physics*, November 2015, volume 78(11), 116901, doi:10.1088/0034-4885/78/11/116901, arXiv:1507.02924.

[**Urpin 2010**] V. Urpin, ‘Magnetorotational instability in proto-neutron stars’. *A&A*, January 2010, volume 509, A35, doi:10.1051/0004-6361/200912887, arXiv:0911.0309.

[**Uryū et al. 2014**] K. Uryū, E. Gourgoulhon, C. M. Markakis, K. Fujisawa, A. Tsokaros and Y. Eriguchi, ‘Equilibrium solutions of relativistic rotating stars with mixed poloidal and toroidal magnetic fields’. *Phys. Rev. D*, November 2014, volume 90(10), 101501, doi:10.1103/PhysRevD.90.101501, arXiv:1410.3913.

[**Uryū et al. 2016**] K. Uryū, A. Tsokaros, L. Baiotti, F. Galeazzi, N. Sugiyama, K. Taniguchi and S. Yoshida, ‘Do triaxial supramassive compact stars exist?’ *Phys. Rev. D*, November 2016, volume 94(10), 101302, doi:10.1103/PhysRevD.94.101302, arXiv:1606.04604.

[**Usov 1992**] V. V. Usov, ‘Millisecond pulsars with extremely strong magnetic fields as a cosmological source of gamma-ray bursts’. *Nature*, June 1992, volume 357, 472–474, doi:10.1038/357472a0.

[**Usov 1997**] V. V. Usov, ‘Low-Mass Normal-Matter Atmospheres of Strange Stars and Their Radiation’. *ApJLett*, June 1997, volume 481, L107–L110, doi:10.1086/310657, arXiv:astro-ph/9703037.

[**Usov 2001**] V. V. Usov, ‘Thermal Emission from Bare Quark Matter Surfaces of Hot Strange Stars’. *ApJLett*, April 2001, volume 550, L179–L182, doi:10.1086/319639, arXiv:astro-ph/0103361.

[**Viganò et al. 2011**] D. Viganò, J. A. Pons and J. A. Miralles, ‘Force-free twisted magnetospheres of neutron stars’. *A&A*, September 2011, volume 533, A125, doi:10.1051/0004-6361/201117105, arXiv:1106.5934.

[**Viganò et al. 2015**] D. Viganò, J. A. Pons, J. A. Miralles and N. Rea, ‘Magnetic fields in Neutron Stars’. In A. J. Cenarro, F. Figueras, C. Hernández-Monteagudo, J. Trujillo Bueno and L. Valdivielso, editors, *Highlights of Spanish Astrophysics VIII* (2015) pages 90–101, arXiv:1501.06735.

[**Viganò et al. 2013**] D. Viganò, N. Rea, J. A. Pons, R. Perna, D. N. Aguilera and J. A. Miralles, ‘Unifying the observational diversity of isolated neutron stars via magneto-thermal evolution models’. *MNRAS*, September 2013, volume 434, 123–141, doi:10.1093/mnras/stt1008, arXiv:1306.2156.

[**Villain et al. 2004**] L. Villain, J. A. Pons, P. Cerdá-Durán and E. Gourgoulhon, ‘Evolutionary sequences of rotating protoneutron stars’. *A&A*, April 2004, volume 418, 283–294, doi:10.1051/0004-6361:20035619, arXiv:astro-ph/0310875.

[**von Zeipel 1924**] H. von Zeipel, ‘The radiative equilibrium of a rotating system of gaseous masses’. *MNRAS*, June 1924, volume 84, 665–683, doi:10.1093/mnras/84.9.665.

[**Weisskopf et al. 2013**] M. C. Weisskopf, L. Baldini, R. Bellazini, A. Brez, E. Costa, R. Dissly, R. F. Elsner, S. Fabiani, G. Matt, M. Minuti, F. Muleri, S. O’Dell, M. Pinchera, B. Ramsey, A. Rubini, C. Sgro’, P. Soffitta and G. Spandre, ‘A small mission featuring an imaging x-ray polarimeter with high sensitivity’. In *UV, X-Ray, and Gamma-Ray Space Instrumentation for Astronomy XVIII*, volume 8859 of *Proc. SPIE* (2013) page 885908, doi:10.1117/12.2024473.

[**Wilson and Mathews 1989**] J. R. Wilson and G. J. Mathews, *Relativistic hydrodynamics.*, pages 306–314 (1989).

[**Wilson and Mathews 2003**] J. R. Wilson and G. J. Mathews, *Relativistic Numerical Hydrodynamics* (2003).

[**Woltjer 1960**] L. Woltjer, ‘A Magnetostatic Model for a Compressible Star.’ *ApJ*, January 1960, volume 131, 227, doi:10.1086/146823.

[**Woods 2008**] P. M. Woods, ‘Observations of Magnetars’. In C. Bassa, Z. Wang, A. Cumming and V. M. Kaspi, editors, *40 Years of Pulsars: Millisecond Pulsars, Magnetars and More*, volume 983 of *American Institute of Physics Conference Series* (2008) pages 227–233, doi:10.1063/1.2900149.

[**Woods et al. 2007**] P. M. Woods, C. Kouveliotou, M. H. Finger, E. Göğüş, C. A. Wilson, S. K. Patel, K. Hurley and J. H. Swank, ‘The Prelude to and Aftermath of the Giant Flare of 2004 December 27: Persistent and Pulsed X-Ray Properties of SGR 1806-20 from 1993 to 2005’. *ApJ*, January 2007, volume 654, 470–486, doi:10.1086/507459, arXiv:astro-ph/0602402.

[**Woosley 1993**] S. E. Woosley, ‘Gamma-ray bursts from stellar mass accretion disks around black holes’. *ApJ*, March 1993, volume 405, 273–277, doi:10.1086/172359.

[**Wright 1973**] G. A. E. Wright, ‘Pinch instabilities in magnetic stars’. *MNRAS*, 1973, volume 162, 339.

[**Yakovlev et al. 2008**] D. G. Yakovlev, O. Y. Gnedin, A. D. Kaminker and A. Y. Potekhin, ‘Theory of cooling neutron stars versus observations’. In C. Bassa, Z. Wang, A. Cumming and V. M. Kaspi, editors, *40 Years of Pulsars: Millisecond Pulsars, Magnetars and More*, volume 983 of *American Institute of Physics Conference Series* (2008) pages 379–387, doi:10.1063/1.2900259, arXiv:0710.2047.

[**Yakovlev et al. 2013**] D. G. Yakovlev, P. Haensel, G. Baym and C. Pethick, ‘Lev Landau and the concept of neutron stars’. *Physics Uspekhi*, March 2013, volume 56, 289-295, doi:10.3367/UFNe.0183.201303f.0307, arXiv:1210.0682.

[**Yakovlev and Pethick 2004**] D. G. Yakovlev and C. J. Pethick, ‘Neutron Star Cooling’. *ARA&A*, September 2004, volume 42, 169–210, doi:10.1146/annurev.astro.42.053102.134013, arXiv:astro-ph/0402143.

[**Yang et al. 1986**] W. H. Yang, P. A. Sturrock and S. K. Antiochos, ‘Force-free magnetic fields - The magnetofrictional method’. *ApJ*, October 1986, volume 309, 383–391, doi:10.1086/164610.

[**Yasutake et al. 2010**] N. Yasutake, K. Kiuchi and K. Kotake, ‘Relativistic hybrid stars with super-strong toroidal magnetic fields: an evolutionary track with QCD phase transition’. *MNRAS*, January 2010, volume 401, 2101–2112, doi:10.1111/j.1365-2966.2009.15813.x, arXiv:0910.0327.

[**Yazadjiev 2012**] S. S. Yazadjiev, ‘Relativistic models of magnetars: Nonperturbative analytical approach’. *Phys. Rev. D*, February 2012, volume 85(4), 044030, doi:10.1103/PhysRevD.85.044030, arXiv:1111.3536.

[**Yoon 2015**] S.-C. Yoon, ‘Evolutionary Models for Type Ib/c Supernova Progenitors’. *PASA*, April 2015, volume 32, e015, doi:10.1017/pasa.2015.16, arXiv:1504.01205.

[**York 1971**] J. W. York, ‘Gravitational Degrees of Freedom and the Initial-Value Problem’. *Physical Review Letters*, June 1971, volume 26, 1656–1658, doi:10.1103/PhysRevLett.26.1656.

[**York 1972**] J. W. York, ‘Role of Conformal Three-Geometry in the Dynamics of Gravitation’. *Physical Review Letters*, April 1972, volume 28, 1082–1085, doi:10.1103/PhysRevLett.28.1082.

[**York 1973**] J. W. York, Jr., ‘Conformally invariant orthogonal decomposition of symmetric tensors on Riemannian manifolds and the initial-value problem of general relativity’. *Journal of Mathematical Physics*, April 1973, volume 14, 456–464, doi:10.1063/1.1666338.

[**York 1979**] J. W. York, Jr., ‘Kinematics and dynamics of general relativity’. In L. L. Smarr, editor, *Sources of Gravitational Radiation* (1979) pages 83–126.

[**York 1999**] J. W. York, Jr., ‘Conformal “Thin-Sandwich” Data for the Initial-Value Problem of General Relativity’. *Physical Review Letters*, February 1999, volume 82, 1350–1353, doi:10.1103/PhysRevLett.82.1350, arXiv:gr-qc/9810051.

[**Yoshida et al. 2006**] S. Yoshida, S. Yoshida and Y. Eriguchi, ‘Twisted-Torus Equilibrium Structures of Magnetic Fields in Magnetized Stars’. *ApJ*, November 2006, volume 651, 462–474, doi:10.1086/507513.

[**Zhang 2006**] B. Zhang, ‘Astrophysics: A burst of new ideas’. *Nature*, December 2006, volume 444, 1010–1011, doi:10.1038/4441010a, arXiv:astro-ph/0612614.

[**Zhang et al. 2012**] B.-B. Zhang, D. N. Burrows, B. Zhang, P. Mészáros, X.-Y. Wang, G. Stratta, V. D’Elia, D. Frederiks, S. Golenetskii, J. R. Cummings, J. P. Norris, A. D. Falcone, S. D. Barthelmy and N. Gehrels, ‘Unusual Central Engine Activity in the Double Burst GRB 110709B’. *ApJ*, April 2012, volume 748, 132, doi:10.1088/0004-637X/748/2/132, arXiv:1111.2922.

[**Zhang et al. 2006**] F. Zhang, J. Qu, C. M. Zhang, W. Chen and T. P. Li, ‘Timing Features of the Accretion-driven Millisecond X-Ray Pulsar XTE J1807-294 in the 2003 March Outburst’. *ApJ*, August 2006, volume 646, 1116–1124, doi:10.1086/502673, arXiv:astro-ph/0602529.

–